



**Peer Reviewed**

**Title:**

Theory of Topological Phenomena in Condensed Matter Systems

**Author:**

[Zhang, Yi](#)

**Acceptance Date:**

2012

**Series:**

[UC Berkeley Electronic Theses and Dissertations](#)

**Degree:**

Ph.D., [Physics](#)[UC Berkeley](#)

**Advisor(s):**

[Vishwanath, Ashvin](#)

**Committee:**

[Moore, Joel](#), [Whaley, Birgitta](#)

**Permalink:**

<http://escholarship.org/uc/item/8ss5q2td>

**Abstract:**

**Copyright Information:**

All rights reserved unless otherwise indicated. Contact the author or original publisher for any necessary permissions. eScholarship is not the copyright owner for deposited works. Learn more at [http://www.escholarship.org/help\\_copyright.html#reuse](http://www.escholarship.org/help_copyright.html#reuse)



eScholarship  
University of California

eScholarship provides open access, scholarly publishing services to the University of California and delivers a dynamic research platform to scholars worldwide.

**Theory of Topological Phenomena in Condensed Matter Systems**

by

Yi Zhang

A dissertation submitted in partial satisfaction  
of the requirements for the degree of

Doctor of Philosophy

in

Physics

in the

GRADUATE DIVISION

of the

UNIVERSITY OF CALIFORNIA, BERKELEY

Committee in charge:

Professor Ashvin Vishwanath, Chair

Professor Joel E. Moore

Professor K. Birgitta Whaley

Spring 2012

## Abstract

Theory of Topological Phenomena in Condensed Matter Systems

by

Yi Zhang

Doctor of Philosophy in Physics

University of California, Berkeley

Professor Ashvin Vishwanath, Chair

Topological phenomena in physical systems are determined by topological structures and are thus universal and protected against perturbations. We theoretically establish exotic topological phenomena and their consequences for experiments in crystalline systems such as topological insulators and topologically ordered phases. We show that protected one-dimensional fermionic modes may be associated with the line defects such as dislocations in three-dimensional topological insulators, and strong electron-electron repulsion may lead to topological Mott insulators via spontaneous spin-orbit correlations in three dimensions. We also predict anomalous Aharonov Bohm conductance oscillations maximized at half integer multiples of a flux quantum in a topological insulator nanowire with strong surface disorder, arising from surface curvature induced Berry phase. In addition, we classify three-dimensional inversion symmetric insulators and their quantized responses.

Quantum entanglement provides a promising probe to the properties of many-body systems, especially topological phases not captured by local order parameters. We present a characterization of topological insulators using entanglement spectrum based only on bulk ground-state wave function. Further, by studying entanglement of trivial partitions, we establish topological order in candidate Gutzwiller projected wave functions for gapped spin liquids and Laughlin states; and with entanglement's dependence on the ground states for bipartition of a torus into two cylinders, we demonstrate a method to extract the modular matrices and statistics and braiding of quasiparticle excitations. Our method helps to determine the topological order with only the set of ground-state wave functions on a torus. Our variational Monte Carlo calculations of topological entanglement entropy agree well with theory. We also find a violation of the boundary law for a critical spin liquid of Gutzwiller projected Fermi sea on the triangular lattice, where the entanglement entropy's enhancement by a logarithmic factor reflects the presence of emergent fermions in a bosonic wave function.

# Contents

<b>Contents</b>	<b>i</b>
<b>List of Figures</b>	<b>v</b>
<b>List of Tables</b>	<b>xii</b>
<b>Acknowledgements</b>	<b>xiii</b>
<b>1 Introduction</b>	<b>1</b>
1.1 Motivation . . . . .	1
1.2 Review of Topological Phases . . . . .	3
1.3 Summary of Contents . . . . .	8
<b>2 Helical Metal Inside a Topological Insulator</b>	<b>11</b>
2.1 Introduction . . . . .	11
2.2 Dislocations in the Diamond Lattice Topological Insulator . . . . .	13
2.3 Dislocations in a General Topological Insulator . . . . .	16
2.4 Experimental Consequences . . . . .	18
2.5 Methods . . . . .	20
<b>3 Topological Insulators in Three Dimensions from Spontaneous Symmetry Breaking</b>	<b>22</b>
3.1 Introduction . . . . .	22
3.2 Topological Mott Insulators and Order Parameter Textures in Three Dimensions	24
3.3 Electronic Structure of a Line Defect: Numerical and Analytical Results . . .	27
3.4 Shankar Monopole in Three Dimensions . . . . .	31
3.5 Topological Mott Insulator in an Extended Hubbard Model on Diamond Lattice	32

3.6	Towards Experimental Realizations . . . . .	36
3.7	Conclusion . . . . .	39
<b>4</b>	<b>Anomalous Aharonov-Bohm Conductance Oscillations from Topological Insulator Surface States</b>	<b>40</b>
4.1	Introduction . . . . .	40
4.2	Surface Dirac Theory and Curvature Induced Berry Phase . . . . .	42
4.3	Numerical Experiments on Disordered Topological Insulator Cylinders . . . . .	44
4.4	Experimental Realizations . . . . .	48
4.5	Conclusion . . . . .	49
<b>5</b>	<b>Quantized Response and Topology of Magnetic Insulators with Inversion Symmetry</b>	<b>50</b>
5.1	Introduction . . . . .	50
5.2	Summary of Results . . . . .	53
5.3	Classifying Inversion Symmetric Insulators . . . . .	58
5.4	Physical Properties and Inversion Parities . . . . .	63
5.5	Parities and the Entanglement Spectra . . . . .	69
5.6	Conclusion . . . . .	74
<b>6</b>	<b>Entanglement And Inversion Symmetry in Topological Insulators</b>	<b>76</b>
6.1	Introduction . . . . .	76
6.2	Topological Band Insulators . . . . .	78
6.3	The Entanglement Spectrum . . . . .	79
6.4	From the Entanglement Spectrum to the Edge Modes . . . . .	82
6.5	Topological Insulator with only Inversion Symmetry . . . . .	88
6.6	Inversion Symmetry and Many-body Spectrum . . . . .	91
6.7	Preserved Distinctions against Interactions . . . . .	95
6.8	Conclusion . . . . .	96
<b>7</b>	<b>Entanglement Entropy of Critical Spin Liquids</b>	<b>97</b>
7.1	Introduction . . . . .	97
7.2	Renyi Entanglement Entropy and Monte Carlo Evaluation . . . . .	99
7.3	Entanglement Entropy of Gutzwiller Projected Wave Functions . . . . .	101

7.4	Conclusion . . . . .	104
<b>8</b>	<b>Topological Entanglement Entropy of Spin Liquids and Lattice Laughlin States</b>	<b>106</b>
8.1	Introduction . . . . .	106
8.2	Topological Entanglement Entropy and Variational Monte Carlo Method . .	109
8.3	Topological Entanglement Entropy for a Chiral Spin Liquid . . . . .	111
8.4	Lattice Version of the Laughlin State . . . . .	114
8.5	Topological Entanglement Entropy of a $Z_2$ Spin Liquid . . . . .	115
8.6	Conclusion . . . . .	117
<b>9</b>	<b>Quasi-particle Statistics and Braiding from Ground State Entanglement</b>	<b>118</b>
9.1	Introduction . . . . .	118
9.2	Ground State Dependence of Topological Entanglement Entropy . . . . .	121
9.2.1	Strong Subadditivity and the ‘Uncertainty’ Principle of TEE . . . . .	123
9.2.2	Ground State Dependence of TEE in a Chiral Spin Liquid . . . . .	124
9.2.3	Ground State Dependence of TEE in the Toric Code Model . . . . .	129
9.3	Extracting Statistics from Topological Entanglement Entropy . . . . .	135
9.3.1	Modular $\mathcal{S}$ Matrix of CSL from TEE . . . . .	135
9.3.2	Algorithm for Extracting Modular $\mathcal{S}$ Matrix from TEE . . . . .	136
9.3.3	Extracting Other Modular Matrices from TEE . . . . .	138
9.4	Conclusion . . . . .	138
<b>Bibliography</b>		<b>140</b>
<b>A</b>	<b>Effective Hamiltonian on a Curved Topological Insulator Surface</b>	<b>155</b>
<b>B</b>	<b>Inversion Symmetry Models and Related Properties</b>	<b>158</b>
B.1	Inversion Symmetric Tight Binding Models . . . . .	158
B.2	“Frozen” Crystals . . . . .	159
B.3	Monopoles and Weyl Points . . . . .	160
B.4	Inversion Symmetry in Entanglement Spectra . . . . .	162
<b>C</b>	<b>Algorithms and Benchmarks for Variational Monte Carlo Method</b>	<b>164</b>

C.1	Benchmarks . . . . .	164
C.2	Marshall Sign Rule for Gutzwiller Projected Wave Functions . . . . .	164
C.3	Sign Trick for Entanglement Entropy Calculation . . . . .	166
C.4	Method for Linear Combinations of Wave Functions . . . . .	167
<b>D</b>	<b>Minimum Entropy States and Modular Matrices of <math>Z_2</math> Gauge Theory</b>	<b>169</b>
D.1	Minimum Entropy States of the Toric Code Model on Dividing Torus . . . . .	169
D.2	Modular Transformations . . . . .	171
D.3	Modular Matrices of $Z_2$ Gauge Theory from Minimum Entropy States . . . . .	173

# List of Figures

1.1	The continuous evolution from a cup into a torus suggests that they are topologically equivalent. . . . .	2
1.2	The $\tilde{\mathbf{v}}$ parameter surface for a trivial insulator (left), a gapless model (center) and a nontrivial insulator with $\nu = 1$ (right). . . . .	4
1.3	Illustrations of time reversal symmetric topological insulator surface dispersions: while the backscattering within a Kramers pair of a Dirac node is forbidden, it is possible between different Kramers pairs or Dirac nodes. . . .	6
2.1	Screw Dislocations: [a] Cubic lattice screw dislocation with Burger's vector $\vec{B}$ ; [b] Diamond lattice screw dislocation along $\vec{B} = a(1, 1, 0)$ direction (shown as a cylinder with red ends), studied in the text. The two diamond sublattices are shown as yellow and white spheres. A cutting plane P plane that was used to generate the dislocation is shown, orthogonal to the strength $t$ nearest neighbor bond along $a/2(1, -1, -1)$ . . . . .	12
2.2	Dislocation Induced Electronic States: spectrum of the diamond lattice strong TI ( $\vec{M}_\nu = \frac{\pi}{2a}(1, 1, 1)$ ) in the presence of a pair of screw dislocations. Electronic states are shown as a function of $k$ , the wavevector along the dislocation. For [a][b][c], the dislocations are oriented along the $\vec{a}_3 = a(1, 1, 0)$ axis. [a] Spectrum, when the dislocation Burgers vector $\vec{B} = \vec{a}_3$ and satisfies $\vec{B} \cdot \vec{M}_\nu = \pi$ . A pair of counter-propagating modes per dislocation is found, that span the band gap (each midgap level happens to be doubly degenerate). [b] Spectrum when $\vec{B} = 2\vec{a}_3$ and $\vec{B} \cdot \vec{M}_\nu = 0 \pmod{2\pi}$ . No dislocation modes occur. [c] Probability distribution of a pair of midgap modes shown in the $\vec{a}_1, \vec{a}_2$ plane that intersects the dislocations. The modes are bound near the dislocations. [d] The dislocations are oriented along $\vec{B} = a(0, 1, -1)$ and $\vec{B} \cdot \vec{M}_\nu = 0$ . No dislocation modes occur. Calculations were done on a 36x36x18 unit cell system with periodic boundary condition along $\vec{a}_1, \vec{a}_2, \vec{B}$ directions, and dislocations separated by a half system size. The hopping parameters used in Eqn. 2.2 are $t = 1$ , $t + \delta t = 2$ , and $\lambda_{SO} = 0.125$ . . . . .	15
2.3	Screw dislocation in a weak topological insulator: the unpaired edge modes (one member of the edge mode pair is shown in red) of the top and bottom layer must propagate through the dislocation by continuity. . . . .	17

2.4	Surface density of states in the presence of dislocations: LDOS as measured by STM, for various dislocation configurations, in the diamond lattice strong TI with parameters as in Figure 2.2. In all cases dislocation pairs (and are directed along $\vec{a}_3$ ) are separated by a half system size. Topography of the integrated LDOS in the energy window $[-0.1, 0.1]$ is shown, with insets displaying energy dependent LDOS at special points on the surface. [a] The $(111)'$ surface intersecting a pair of screw dislocations with $\vec{B} = a(1, 1, 0)$ . These carry one-dimensional modes which give rise to a peak in the integrated LDOS. In [b] and [c], edge dislocations on the $(\bar{1}\bar{1}1)$ surface. In [b], the dislocation satisfies $\vec{B} \cdot \vec{M}_\nu = \pi$ , and has one-dimensional modes visible in the LDOS while in [c] the dislocation has $\vec{B} \cdot \vec{M}_\nu = 0$ , hence no one-dimensional line mode and no enhanced LDOS. In [a][b][c] only the top layer of atoms is shown, and calculations are done on $36 \times 36 \times 18$ unit cell system, with periodic boundary conditions in the $\vec{a}_1, \vec{a}_2$ directions. . . . .	19
3.1	An illustration of order parameter $\mathbf{R}$ of a nontrivial line defect in the $x - y$ plane, $\hat{z}$ direction is translation-invariant. The hollow and solid arrow are the $\hat{x}$ and $\hat{y}$ axes of local coordinate, the $\hat{z}$ axis points out of the paper for proper rotation. . . . .	26
3.2	Up: The density distribution of a midgap mode ( $k = 1.05, E = 0.25$ ) in the $\vec{a}_1, \vec{a}_2$ plane, the mode is well localized at the $l = 1$ vortex, the other state ( $k = 1.05, E = -0.25$ ) is well localized at the $l = -1$ antivortex; Down: Electronic spectrum of diamond lattice strong TMI along $p_z$ in the presence of a pair of defects. The parameters used in the Hamiltonian are $t = 1.0, \delta t = 1.0$ , and $\lambda_{SO} = 0.125$ . . . . .	28
3.3	Illustration for the model on an effective Hamiltonian on a curved surface we study. The radius of the cylinder is $R$ with strong TMI outside and vacuum inside. $p_z$ and $p_\varphi$ are momentum along $\hat{z}$ and the azimuthal direction, respectively. $\theta$ is the angle between $\vec{\sigma}'$ and $\vec{p}$ . . . . .	30
3.4	A three-dimensional plot of diamond lattice. Each unit cell contains two sublattices, denoted by $A$ and $B$ respectively, which each forms an FCC crystal. The repulsive interactions $V_2$ and $V_3$ between the second neighbor and third neighbor are shown. They are both between the atoms of the same sublattice. . . . .	33
3.5	Phase diagram for an extended Hubbard model on three-dimensional diamond lattice. The phase transitions from semimetal to SDW, CDW and TMI are all second order transitions. Other parameters are $V_3 = V_2/2$ and $J = 0.3t$ . The system size is $L = 40$ for calculation. . . . .	36
3.6	Phase diagram for an extended Hubbard model on two-dimensional diamond lattice layer including both sublattices (essentially honeycomb lattice). Note its difference from Ref. [142]. The TMI is limited to the center of the phase diagram and only partially breaks the $SU(2)$ SRS. The system size is $L = 40$ for calculation. . . . .	38

4.1	(a) proposed geometry, with (weak) magnetic field applied along the wire axis, with flux $\varphi = 2\pi\Phi/\Phi_0$ enclosed. (b) Quantization of transverse momenta $k_\theta$ for a cylinder, as a function of applied flux. The shaded area boundary in the Fermi surface. For $\varphi = 0$ , an even number of one-dimensional mode pairs occurs; but with $\varphi = \pi$ flux, an odd number of pairs, protected by time reversal symmetry, is expected. Demonstration in a microscopic model: spectrum of a cuboid of clean topological insulator, with cross section 10x10 unit cells (geometry shown in inset), as a function of momentum $k_z$ along its length. (c) Spectrum for $\varphi = 0$ , each band shown is doubly degenerate (d) For flux $\varphi = \pi$ , all modes except the linear one are doubly degenerate; hence an odd number of one-dimensional mode pairs is present. . . . .	43
4.2	(a), (b) and (c): Localization length $\lambda$ in the quasi-one-dimensional geometry, for different widths $L$ (measured in unit cells) and disorder strengths $W$ (in units of the bulk gap $\Delta$ ). Error bars are smaller than the symbol size. (a) and (b) Strong disorder: variation has flux-period $hc/e$ and $\lambda$ is maximum at flux $\varphi = \pi$ . Inset: Example of the exponential decay of the Green's function used to determine the localization length.(c) Weak disorder: Now, the $hc/2e$ oscillation period is also apparent and localization lengths are very large (note log scale here). For wires much shorter than the zero flux localization length, the $hc/e$ period will not be apparent. (d) Conductance Oscillation: Direct measure of conductance oscillation for a wire of length $l = 100$ and width $L = 9$ , with strong disorder $W = 2\Delta$ . Maximum conductance occurs at $\pi$ -flux. . . . .	46
5.1	Examples of determining physical system properties using parities. The boxes represent an eighth of the Brillouin Zone and the TRIMs are at the corners. The signs represent the parities of the occupied states at the TRIMs. In (a) the constraint of even number of odd parity states is violated, hence it cannot be an insulator. In (b) the parities require a non-vanishing Hall conductance, with odd Chern number in the $k_x k_y$ planes. In (c) a quantized magnetoelectric response $\theta = \pi$ is determined from number of odd parity states being 2 (modulo 4). In (d) A parity configuration corresponding to a frozen polarization is shown. . . . .	54
5.2	a) The parities at the TRIMs and b) the entanglement spectrum for a bipartition cut parallel to the $xy$ -plane of a hopping Hamiltonian. There are two zero-modes at the TRIM $(0, 0)$ and none at the other TRIMs, in consistency with the expectation from the parities. . . . .	58

5.3	Representation of $d$ -dimensional Hamiltonians by arcs and loops in the space of $d - 1$ -dimensional Hamiltonians. The grey region represents $\mathcal{H}_{d-1}$ : each point corresponds to a generic $d-1$ -dimensional Hamiltonian. The two ellipses on the side represent the components of $\mathcal{I}_{d-1}$ , the Hamiltonians with inversion symmetry. Inversion-symmetric $d$ -dimensional Hamiltonians are represented by arcs connecting points in $\mathcal{I}_{d-1}$ . Two of these Hamiltonians are equivalent if the end-points are in the same component of $\mathcal{I}_{d-1}$ and have the same winding numbers around holes in the space (represented by the white ellipse). For example, $\gamma_2$ and $\gamma_3$ are not equivalent because their final end-points are in different components; $\gamma_1$ and $\gamma_2$ are not equivalent because $\gamma_1\gamma_2^{-1}$ winds around the hole. . . . .	60
5.4	Examples of $\mathbf{n}_o$ vectors. Because they and the two rotations of $\mathbf{m}_{xy}$ form a complete basis for the unit cell of the eight-dimensional $\mathbf{n}_o$ vectors lattice for nontrivial band structures, the entire family of quantized behavior for inversion symmetric insulators can be found in these two examples and linear combinations of them. . . . .	62
5.5	Illustration of an evolution that changes the band parities at two TRIMs. The cubes represent the Brillouin zone of a system with two bands, the lower of which is filled. Initially, all the filled bands have +1 parity at TRIMs. A pair of Weyl points, monopoles in the Berry flux as in Appendix B.3, are created at one TRIM and they move to another TRIM where they annihilate. During such process, the parities of the states at both TRIMs are reversed. The open circles indicate where the monopoles are created and annihilated. . . . .	65
5.6	Inversion symmetric curves have to pass through an even number of TRIMs. Left, a curve that passes through one TRIM fails to be inversion symmetric; right, an inversion symmetric figure. If there is one curve through one of the TRIMs, it must go around the Brillouin zone and pass through another TRIM. . . . .	65
5.7	A comparison of the spectra of a nontrivial and a trivial system. Left: the entanglement spectrum, and right: surface spectrum, the two spectra can be continuously deformed into each other. Because time reversal symmetry requires Kramers' degeneracies at the TRIMs regardless of energy, the parity of the number of modes crossing the Fermi energy does not change. In the entanglement spectrum, the inversion symmetry protects the zero "energy" degeneracies at the TRIMs, allowing a determination of the quantum spin Hall index. . . . .	72
5.8	An example model with a single filled band and an odd quantum Hall effect parallel to $\mathbf{R}_z$ : a) The pattern of parities at the TRIMs, and b) The entanglement Fermi surface in the $xz$ surface Brillouin zone determined with $\Delta N_e(\kappa_\perp) = \frac{1}{2}(\Delta N(\kappa_1) + \Delta N(\kappa_2))$ . . . . .	73

5.9	Determining the polarization from the entanglement spectrum. a) Parities for an insulator with one filled band, with a half-filled Fermi sea in the entanglement spectrum. b) Possible entanglement Fermi arcs for a cut parallel to the $xz$ plane. The arcs surround half the surface Brillouin zone. If there are no nuclei on $y = 0$ , this crystal has a half-integer polarization in the $y$ -direction.	74
6.1	A cut that divides the physical system into two halves. . . . .	80
6.2	Entanglement edge states for the $\nu = 2$ integer quantum Hall state. . . . .	83
6.3	Brillouin zone of the (1,1,1) surface of the diamond lattice. The labelled points are time reversal invariant momenta. . . . .	84
6.4	Strong topological insulator: a) the dispersion of the physical surface states. Note that the node is not at zero energy, since particle-hole symmetry is broken; b) The entanglement spectrum, $\frac{1}{2} - p_i$ , which has the node at zero $\epsilon^e$ , in spite of broken particle-hole symmetry. . . . .	85
6.5	Weak topological insulator: a) The dispersion of the physical surface states; b) the entanglement spectrum. . . . .	86
6.6	Inversion symmetric insulators with broken time reversal symmetry. Note the physical surface states (a) are gapped, but the Dirac node remains in the entanglement spectrum (b). . . . .	87
6.7	Without inversion symmetry and time reversal symmetry, both the physical surface state (a) and the entanglement spectrum (b) are gapped. . . . .	87
6.8	(a) The transformation $\mathcal{I}_S$ of a single-body wave function. The image of a state $f^R$ under $\mathcal{I}_S$ is not defined on the merits of $f^R$ itself, but instead depends on the state of the system, the extended wave function $F_i = \sqrt{p_i}f_i^R + \sqrt{1-p_i}f_i^L$ , and $\mathcal{I}_S f^R$ is the right-hand part of this up to normalization, which can look completely different from the original $f^R$ . (b) The transformation $\mathcal{MI}$ of many-body states in a non-interacting system. Each term in the Schmidt decomposition is obtained by placing electrons on either the right or left of the $F_i$ 's indicated by the horizontal lines. Inversion applies to the system as a whole. Focusing on the half right-hand side of the system, inversion induces a particle-hole like transformation because levels $i$ that are occupied in $ \chi_R\rangle$ correspond to empty levels $\bar{i}$ in $\mathcal{MI} \chi_R\rangle$ . . . . .	90
7.1	Renyi entropy data for projected and unprojected Fermi sea state on the triangular lattice of size $18 \times 18$ with $L_A = 1\dots 8$ . Note, projection barely modifies the slope, pointing to a Fermi surface surviving in the spin wave function. We also separately plot $S_{2,sign}$ and $S_{2,mod}$ (as defined in the text) for the projected state, the former dominates at larger sizes. . . . .	102
7.2	Staggered spin-spin correlations for the projected $\pi$ -flux state on the square lattice for linear sizes $L$ upto 36 sites. The correlations show algebraic decay $\sim 1/r^{1+\eta}$ with $\eta \approx 0.96$ . . . . .	103

7.3	Renyi entropy for the projected Fermi sea state on the triangular lattice and square (with and without $\pi$ -flux) lattice as a function of the perimeter $P$ of the subsystem $A$ . Here $C$ is the constant part of the $S_2$ . We find $S_2 \sim P \log(P) + C$ for the projected triangular lattice state while $S_2 \sim P + C$ for the projected $\pi$ -flux square lattice state. For the square lattice state (no flux), the projection leads to a significant reduction in $S_2$ suggesting at most a very weak violation of the area-law. . . . .	103
7.4	Staggered spin-spin correlations for the projected Fermi sea state on the square lattice. $C(L/2, L/2)$ saturates at a finite value at large distances ( $L_{max} = 42$ ) indicating the presence of long range anti-ferromagnetic order. . . . .	104
8.1	Illustration of a square lattice hopping model connected with a $d + id$ superconductor. While the nearest neighbor hopping is along the square edges with amplitude $t$ ( $-t$ for hopping along dashed lines), the second nearest neighbor hopping is along the square diagonal (arrows in bold), with amplitude $+i\Delta$ ( $-i\Delta$ ) when hopping direction is along (against) the arrow. The two sublattices in the unit cell are marked as $A$ and $B$ . . . . .	112
8.2	The separation of the system into subsystem $A$ , $B$ , $C$ and environment, periodic boundary condition is employed in both $\hat{x}$ and $\hat{y}$ directions. . . . .	113
8.3	Illustration of finite size effect: chiral SL TEE $\gamma$ as a function of $2\Delta/t$ proportional to the relative gap size for characteristic system length $L_A = 3$ . The larger the gap, the closer the data approaches the ideal value. For comparison, TEE $\gamma$ for chiral SL at $L_A = 4$ and $2\Delta/t = 1.0$ is shown. On the same plot, TEE $\gamma$ of a lattice version of $\nu = 1/3$ Laughlin state at $L_A = 3$ , $2\Delta/t = 1.0$ is also shown. The dashed lines are the ideal TEE values of $\gamma = \log(\sqrt{2})$ for the chiral SL and $\log(\sqrt{3})$ for the $\nu = 1/3$ Laughlin state. . . . .	114
9.1	Two types of entanglement bipartitions on the torus: (a) A trivial bipartition with contractible boundaries for which the TEE $\gamma = \log D$ , and (b) A bipartition with non-contractible boundaries, where the TEE depends on ground state. . . . .	120
9.2	A torus (the top and bottom sides and left and right sides are identified). Subregions $A$ , $B$ , $C$ are defined as shown. Regions $A$ and $C$ are assumed to be well separated as compared to the correlation length. The regions $AB$ and $BC$ correspond to bipartitions of the torus into cylinders in orthogonal directions. . . . .	124
9.3	The separation of the system into subsystem $A$ , $B$ , $C$ and environment, periodic or antiperiodic boundary condition is employed in both $\hat{x}$ and $\hat{y}$ directions. a: The subsystem $ABC$ is an isolated square and the measured TEE has no ground-state dependence. b: The subsystem $ABC$ takes a non-trivial cylindrical geometry and wraps around the $\hat{y}$ direction, and TEE may possess ground-state dependence. . . . .	126

9.4	Numerically measured TEE $2\gamma - \gamma'$ for a CSL ground state from linear combination $ \Phi\rangle = \cos\phi 0, \pi\rangle + \sin\phi \pi, 0\rangle$ as a function of $\phi$ with VMC simulations using geometry in Figure 9.3b. The solid curve is the theoretical value from Eqn. 9.18. The periodicity is $\pi/2$ . . . . .	127
9.5	Illustration of a lattice of the toric code model, the links spanned by star and plaquette are highlighted in red and blue, respectively. . . . .	130
9.6	A snapshot of the ground state on the cylinder. Closed-loop strings (“ $Z_2$ electric fields”) can wrap around the cylinder. The ground states are doubly degenerate, corresponding to even and odd winding number sectors. The total number of string crossings the cut $\Delta$ equals the winding number, modulo 2. The number of string crossings at the boundary $\Gamma$ is even in the degenerate ground states. . . . .	131
9.7	The four minimum entropy states of the $Z_2$ topological phase corresponding to the bipartition shown in the figure expressed as linear combinations of the four magnetic flux states. The magnetic $\pi$ flux is represented by the thick blue and green lines. . . . .	134
C.1	Comparison of the exact result for Renyi entropy with that calculated using the Monte Carlo method described in the paper for free spinless fermions on a one-dimensional lattice consisting of 200 sites. . . . .	165
C.2	Comparison of the exact result for Renyi entropy with that calculated using the Monte Carlo method described in the paper for free spinless fermions on a two-dimensional square lattice of size $18 \times 18$ . . . . .	165

# List of Tables

8.1	Comparison between calculated TEE and expected value from field theory(second column) for topological phases. The * denotes that the calculated value is not divided by the expected value since the latter vanishes. . . . .	109
9.1	List of $Z_2$ magnetic flux $T_y$ , $Z_2$ electric flux $F_y$ and corresponding quasiparticle of Wilson loop operator for the four MESs $ \Xi_\alpha\rangle$ of the toric code with system geometry in Figure 9.1b. The definitions of $T_y$ and $F_y$ are in Appendix D.1. . .	134

## Acknowledgements

I am extremely thankful to my advisor Ashvin Vishwanath for supervision and support on my graduate studies and researches in all aspects during the past years.

It is also my great pleasure to have feedbacks from and interactions with numerous colleagues including Charles Kane, Joe Orenstein, T. Senthil, Dung-hai Lee, Harsh Mathur, David Carpentier, Joel E. Moore, Guillaume Paulin, Frank Pollmann, Erez Berg, Michael Levin, Andrew Essin, Sergery Savrasov, Xiangang Wang, Matthew Fisher, Ann B. Kallin, Roger G. Melko, Olexei I. Motrunich, Brian Swingle, Cenke Xu, Alexei Kitaev, Chetan Nayak, Shinsei Ryu, Itamar Kimchi and Pavan Hosur. Some portions of this dissertation have come out of completed publications with Ying Ran, Ari Turner, Tarun Grover, Masaki Oshikawa and Roger Mong. I am grateful to them for enlightening discussions, efforts and supports in literature preparation and permissions for using these materials within this dissertation.

I am obliged to the Department of Physics in University of California, Berkeley for its outstanding academic training, respectful work environment and diverse community as well as Lawrence Berkeley National Laboratory for its advanced computational facilities and accessible services. Part of the research included in this dissertation was performed at Kavli Institute for Theoretical Physics, University of California, Santa Barbara, and I greatly appreciate their hospitality.

I thank my dissertation and qualifying exam committee members Ashvin Vishwanath, Joel E. Moore, Feng Wang and K. Birgitta Whaley for their helpful comments and suggestions in this dissertation as well as my research career.

I also thank my wife Fangfei and my parents for their cheerful supports that made my research and dissertation preparation joyful and worthwhile.

# **Curriculum Vitæ**

**Yi Zhang**

## **Personal**

*Name:* Yi Zhang

*Address:* 521 Birge Hall, Department of Physics, University of California, Berkeley, CA, 94720

*Tel:* 510-642-7302

*Email:* zhangyi@berkeley.edu

## **Research Area**

Theoretical condensed matter physics with focus on strongly-correlated systems and topological phases

## **Education**

Ph. D. student: 2007 - present. University of California, Berkeley

Graduate fellow: 2010.01 - 2010.06. The Kavli Institute for Theoretical Physics, Santa Barbara

B. S.: 2003.09 - 2007.07 Fudan University, Shanghai

## **Teaching**

Graduate Student Instructor: Physics 111 Advanced Lab (2007-2008) at UC Berkekey.

Graduate Student Instructor: Physics 211 Advanced Statistical Mechanics(2008-2009) at UC Berkekey.

Graduate Student Instructor: Physics 250 Demystifying Quantum Field Theory(2012) at UC Berkekey.

## **Recognitions**

Jackson C. Koo Award in condensed matter physics (2011)

KITP graduate student fellowship (2010)

University outstanding GSI (2009)

Outstanding undergraduate thesis of Fudan University (2008)

Johnson Controls scholarship (2007)

## **Scientific Activities**

APS March Meeting 2012, Boston, MA (2012)

Princeton Summer School on Condensed Matter Physics on Ultra-cold Atoms and Magnetism, Princeton, NJ (2011)  
APS March Meeting 2011, Dallas, TX (2011)  
Boulder Summer School in Condensed Matter and Materials Physics on Computational and Conceptual Approaches to Quantum Many-Body Systems, Boulder, CO (2010)  
APS March Meeting 2010, Portland, OR (2010)  
Exotic Superconducting and Insulating Phases of Quantum Matter, Baltimore, MD (2010)  
KITP graduate fellow, Santa Barbara, CA (2010)  
Opportunity at the Nexus of Atomic and Condensed-matter Physics, Berkeley, CA (2009)  
California Condensed Matter Theory Meeting, Riverside, CA (2008)

## List of Publications

- 1. Quasi-particle Statistics and Braiding from Ground State Entanglement**  
Yi Zhang, Tarun Grover, Ari Turner, Masaki Oshikawa, and Ashvin Vishwanath  
*arXiv:1111.2342* and submitted to *Phys. Rev. X*.
- 2. Topological Entanglement Entropy of Z2 Spin Liquids and Lattice Laughlin States**  
Yi Zhang, Tarun Grover, and Ashvin Vishwanath  
*Phys. Rev. B* **84**, 075128 (2011).
- 3. Entanglement Entropy of Critical Spin Liquids**  
Yi Zhang, Tarun Grover, and Ashvin Vishwanath  
*Phys. Rev. Lett.* **107**, 067202 (2011).
- 4. Quantized Response and Topology of Magnetic Insulators with Inversion Symmetry**  
Ari M. Turner, Yi Zhang, Roger S. K. Mong, and Ashvin Vishwanath  
*Phys. Rev. B* **85**, 165120 (2012).
- 5. Probing Band Topology and Curvature Induced Berry Phase via Aharonov-Bohm Interference**  
Yi Zhang, and Ashvin Vishwanath  
*Phys. Rev. Lett.* **105**, 206601 (2010).
- 6. Entanglement and Inversion Symmetry in Topological Insulators**  
Ari M. Turner, Yi Zhang, and Ashvin Vishwanath  
*Phys. Rev. B* **82**, 241102R (2010).
- 7. Topological Insulators in Three Dimensions from Spontaneous Symmetry Breaking**  
Yi Zhang, Ying Ran, and Ashvin Vishwanath  
*Phys. Rev. B* **79**, 245331 (2009).

**8. One-dimensional Topologically Protected Modes in Topological Insulators with Lattice Dislocations**

Ying Ran, Yi Zhang, and Ashvin Vishwanath

*Nature Physics* **5**, 298 - 303 (2009).

**9. Design and Miniaturization of Split Ring Structures based on an Analytic Solution of Their Resonance**

S.T. Chui, Yi Zhang, and Lei Zhou

*J. Appl. Phys.* **104**, 035305 (2008).

**10. Electric and Magnetic Resonances in Broadside Coupled Split-ring Resonators: an Extended Mode-expansion Theory**

Xueqin Huang, Yi Zhang, S.T. Chui, and Lei Zhou

*Phys. Rev. B* **77**, 235105 (2008).



# Chapter 1

## Introduction

### 1.1 Motivation

Landau symmetry-breaking theory is a very successful theory once believed universal for all condensed matter systems. Yet in the last three decades, both experimental and theoretical condensed matter physics community has witnessed an explosion in the fields of topological phases, which lie beyond this paradigm. The two most active branches are: (1) the topological orders with degenerate ground states and quasiparticles with fractional statistics, examples including quantum spin liquids and fractional quantum Hall insulators; and (2) the more recently proposed topological insulators, with symmetry protected edge and surface states. The focus of this dissertation is the theoretical exploration of physical phenomena in topological phases and their realizations for experiments.

Condensed matter physics is mainly concerned with diverse phases of matters, their physical properties and transitions between them. The fascinating kaleidoscope of condensed matter systems lies in the exponentially large Hilbert space as the number of particles increases. This typical cause of difficulty in many-body physics seems intimidating, however, in many cases the physical properties only depend on the longest range physics and lowest energy excitations, while the rest degrees of freedom turns out to be irrelevant and invisible. Interestingly, at low energy, the collective modes - complex assemblies of particles - behave dramatically different from their constituents, and give rises to emergent quasiparticles such as phonons and spinons, whose appearance and properties determine a variety of different phases and their major characteristics. Without doubt, the concept of phase is at the center of condensed matter physics, and much emphasis is put upon how the phases and the corresponding quasiparticle properties depend on physical parameters.

Recent discoveries of quantum hall effects and topological insulators in different symmetry classes bring opportunities to study an additional family of phases - the topological phases,

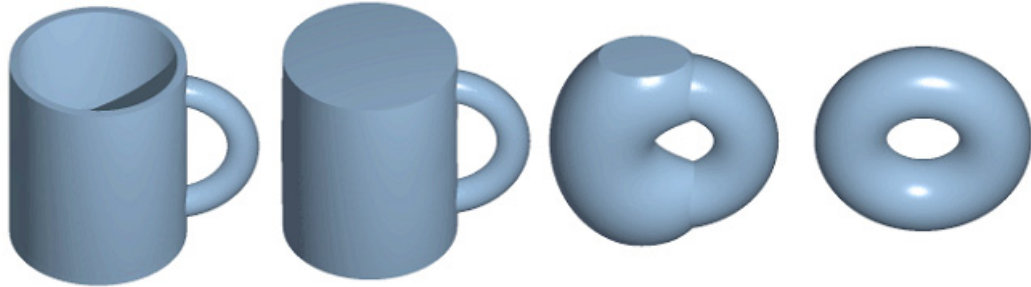


Figure 1.1. The continuous evolution from a cup into a torus suggests that they are topologically equivalent.

and diverse topological phenomena emerge. Instead of parameter dependence, here the major concentration is on “independence”, in connection to the term “topology”.

Topology is a major branch of mathematics concerned with properties that are preserved under continuous deformation without abrupt changes such as tearing or gluing. It provides information about the shapes and holes of an object. Figure 1.1 presents the idea how a torus is topologically identical to a cup. Quantitatively, these two objects have the same genus, a topological index defining the number of holes. Analogically, topological phenomena are physical properties protected by a bulk gap and insensitive to detailed short-range physics. For example, there are topological phases that host protected surface/edge states, quantized responses, extra Berry phases, fractional charges and statistics, nonlocal entanglement, etc. This suggests their potential for exciting and novel applications.

The topological phenomena are conceptually interesting because they come from a very different fundamental perspective. It points out a much richer ensemble of topological phases other than symmetry-breaking orders and also offers various implications and condensed matter realizations of important theoretical concepts in high energy physics. For example, the string-net condensation mechanism for topological order presents an explicit model that has a unified origin for gauge bosons and fermions[92, 94]; quantum spin liquids in frustrated magnets is an example for an emergent  $U(1)$  gauge theory and quantum number fractionalization[10], etc. They illustrate that the charge and statistics carried by quasi-particles - low energy elementary excitations of the strongly-correlated many-body ground state, can be fractional with respect to those of the original elementary particles.

The tolerance of topological phenomena to perturbations also suggest technological applications in electronic devices. In many cases, the non-trivial surface/edge states of topological phases become perfect conducting channels and allow dissipationless transport[41, 73, 113, 187]. These chiral edge states and helical surface modes prohibit backscattering, hence relatively stable against certain impurities. The complicated non-local quantum entanglement of topologically ordered phases also spurs proposition for fault tolerant quantum computation and memory media usage[25, 77, 80, 115]. The quantum information is distributed among distant particles and can not be destroyed by local perturbations, impurities and decoherence, therefore allows a much longer and safer encoding. On the other hand, braidings

of quasiparticles are nontrivial and generally do not commute in a non-Abelian topological order, providing a physical way to manipulate the encoded quantum information - a process of quantum computation. A recent experiment on Majorana fermions has shed light on the existence of non-Abelian quasiparticles[109], which is the first step towards the realization of a quantum computer. Such a quantum computer may be exponentially more powerful than a classical counterpart in certain cases.

## 1.2 Review of Topological Phases

### Topological classification of insulators

From a conventional point of view, noninteracting electrons in a periodic potential are characterized by the Bloch theorem:

$$\phi_{n\mathbf{k}}(\mathbf{r}) = e^{i\mathbf{k}\cdot\mathbf{r}} u_{n\mathbf{k}}(\mathbf{r}) \quad (1.1)$$

where  $n$  is the band index,  $\mathbf{k}$  is the wave vector defined in the Brillouin zone of the reciprocal lattice, and  $u_{n\mathbf{k}}(\mathbf{r})$  is the periodic Bloch function, the eigenstates of the single-particle Hamiltonian in the momentum space  $H(\mathbf{k})$  by Fourier transformation. The corresponding energy eigenvalues  $\epsilon_n(\mathbf{k})$  form the dispersion bands, which are filled upto the Fermi energy  $\epsilon_F$  according to the electron occupancy.

The Hamiltonian  $H(\mathbf{k})$  can be regarded as a mapping from the Brillouin zone to the Hamiltonian manifold defined by the symmetry of the system. For insulators with Fermi energy in a finite band gap, there are well-defined conducting ( $\epsilon_n(\mathbf{k}) < \epsilon_F$ ) and valence ( $\epsilon_n(\mathbf{k}) > \epsilon_F$ ) bands, thus equivalence classes may be established: the classification is based on adiabatic deformation without a closure of the band gap. In other words, there is a continuous route between two systems from the same class, so that the band structure is always gapped during the evolution from one system to the other one. These classes of topological phases are usually labeled by integer topological indices. The distinction between topological phases are protected by the bulk gap, thus stable against moderate amount of disorders and interactions.

What makes a topologically nontrivial insulator different? Commonly, a topologically nontrivial insulator will have exotic and stable edge or surface states, although in certain cases insulators without surface or edge states are also topologically nontrivial; a more generic definition is based upon macroscopic bulk properties such as quantized responses in close connections with the topological indices. These topological phases may host exotic low energy excitations completely different from their parent materials.

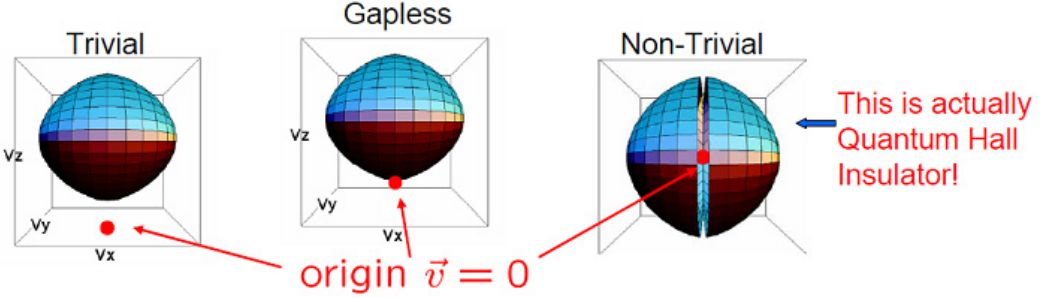


Figure 1.2. The  $\tilde{\mathbf{v}}$  parameter surface for a trivial insulator (left), a gapless model (center) and a nontrivial insulator with  $\nu = 1$  (right).

### Integer quantum Hall insulators

One well-known example is the integer Quantum Hall effect observed in two-dimensional electron systems in low temperatures and strong magnetic fields. A two-dimensional integer Quantum Hall insulator is known to have chiral edge states and carry quantized Hall conductance, even in the presence of moderate amount of disorders. Although there is a unique ground state and no symmetry difference between the quantum hall insulators and the trivial insulators, the topological distinction can manifest itself in different ways.

Here is a simple two-band model Hamiltonian for illustration:

$$H(\mathbf{k}) = \mathbf{v}_x(\mathbf{k})\sigma_x + \mathbf{v}_y(\mathbf{k})\sigma_y + \mathbf{v}_z(\mathbf{k})\sigma_z \quad (1.2)$$

where the  $\sigma_i$  matrices are Pauli matrices and the  $\mathbf{v}_i$ 's are analytical functions of momentum  $k_x$  and  $k_y$  in two dimensions, which may be visualized as two-dimensional surfaces in a three-dimensional space as in Figure 1.2. The dispersion relation  $\epsilon(\mathbf{k}) = \pm |\tilde{\mathbf{v}}(\mathbf{k})|$  suggests that the system is gapped only if the surface does not go through the origin of the  $\tilde{\mathbf{v}}$  parameter space.

As we stated before, under continuous evolution the surface has to avoid the origin, therefore the number of wrappings around the origin  $n$  is a constant integer stable against adiabatic deformation. That is actually the TKNN number or Chern number labeling different Integer Quantum Hall phases[173].

A more physical classification is based on quantized response fixed upon continuous evolution. Using the Kubo formula, the Hall conductivity of the filled band is:

$$\sigma_{xy} = \frac{e^2}{h} n \quad (1.3)$$

and:

$$n = \frac{i}{2\pi} \int_{BZ} dk_x dk_y \cdot [\nabla \times \langle u_{\mathbf{k}} | \nabla | u_{\mathbf{k}} \rangle]_z \quad (1.4)$$

where  $u_{\mathbf{k}}$  is the wave function of the occupied states in the filled band.  $n \in \mathbb{Z}$  is 0 for a trivial insulator and nonzero for a quantum Hall insulator; the insulator has  $n$  chiral edge

states along the boundaries, if any. On the other hand, according to Eqn. 1.2,  $u_{\mathbf{k}}$  is a spinor in the  $-\tilde{\mathbf{v}}(\mathbf{k})$  direction, hence Eqn. 1.4 gives exactly the  $\tilde{\mathbf{v}}$ 's winding numbers  $n$  around the origin, making a consistent connection between the topological index and the quantized Hall conductivity  $\sigma_{xy}$  as given by Eqn. 1.3.

## Topological insulators

There is no general symmetry requirement for an integer Quantum Hall insulator. More recently, however, more possibilities of topologically nontrivial insulators protected by symmetry have been raised into horizon, and the two-dimensional and three-dimensional topological insulators are interesting representatives with time reversal symmetry.

The two-dimensional topological insulator, or the quantum spin Hall insulator, is first discovered by Bernevig, Kane, Mele and others on a honeycomb lattice with spin-orbit interaction from neighboring nuclei as an effective magnetic field[14, 73, 74]. Importantly, the up-spin and down-spin moving electrons receive opposite effective magnetic fields, which preserves time reversal symmetry important for the definition of this category of topological insulators. Intuitively, the two-dimensional topological insulator may be described as two integer quantum Hall insulators with opposite spin and TKNN integer.

Two-dimensional topological insulator has exotic edge states. As stated before, the quantum Hall insulator with TKNN integer  $n$  has  $n$  chiral states on its edges stable against impurity. Similarly, a nontrivial two-dimensional topological insulator has a pairs of helical modes on each edge, which form a Kramers pair so they can't be lifted by backscattering from time reversal symmetric impurities. However, although backscattering is forbidden within each Kramers pair, it is allowed between different pairs, therefore continuous time reversal symmetric deformation may generate or eliminate an even number of Kramers pairs at a time, see Figure 1.3. For nontrivial two-dimensional topological insulator that starts with an odd number of pairs of edge states, there remains at least one pair of edge states. This also suggests that unlike quantum Hall insulator, two-dimensional topological insulator has a  $\mathbb{Z}_2$  classification denoted by the parity of  $n$ . Transport measurements on HgTe quantum wells have provided evidence for the existence of two-dimensional topological insulator[13, 84].

The topological insulator is extended to three dimensions by Fu, Joel, Roy and others[41, 105, 151]. The three-dimensional topological insulator has surface states with cone-shaped dispersion characterized by Dirac Hamiltonians. It is categorized by four  $\mathbb{Z}_2$  topological indices. The strong topological index  $\mu_0$  controls whether the number of surface Dirac nodes is even(odd), or whether it is a strong(weak) topological insulator; the other three weak indices  $\mu_i$  control the position of the Dirac nodes in the surface Brillouin zone.

The strong topological insulator is a new state of matter. It has an odd number of Dirac nodes on the surface and breaks the fermion-doubling theorem and has a quantized magnetoelectric effect[32, 138]. Since the surface modes are helical due to spin-momentum correlation, no intra-node backscattering is allowed. Though inter-node scattering is possible it always modify the number of Dirac nodes by an even number, see Figure 1.3. Therefore, the parity of the number of Dirac nodes is stable as long as time reversal symmetry is pre-

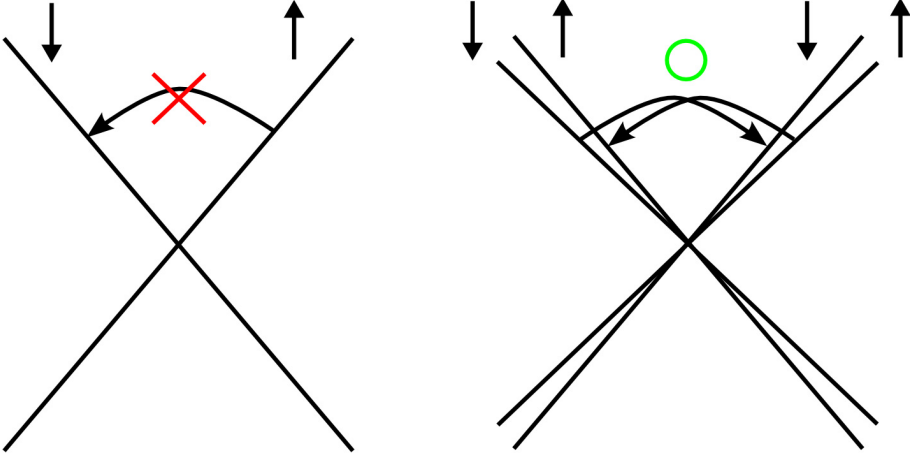


Figure 1.3. Illustrations of time reversal symmetric topological insulator surface dispersions: while the backscattering within a Kramers pair of a Dirac node is forbidden, it is possible between different Kramers pairs or Dirac nodes.

served, and nontrivial surface states exist in strong topological insulators. Surface sensitive experiments such as ARPES and STM have confirmed the existence of these exotic surface states in several materials believed to be strong topological insulators[63, 64, 197, 202]. More detailed reviews of time reversal symmetric topological insulators are in Ref. [57, 106, 140].

Yet that is far from the completion of the plethora of symmetry-defined topological insulators. Ref. [156] listed ten classes of noninteracting topological insulators and topological superconductors respecting certain discrete symmetries in general dimensions. This emerging field has becomes an ideal platform to explore novel topological phenomena.

## Topological orders

The topological order is motivated by the low energy effective theory of topological quantum field theory. They are not described by local order parameters, but rather by long-range quantum entanglement. Examples of topological order include fractional quantum hall insulators[86, 175] and gapped quantum spin liquids[4, 10, 88, 145, 146, 153, 188, 191]. Typical hallmarks and characterizations of topological order include ground states' topological degeneracy, nontrivial statistics and braiding of emergent quasiparticle excitations, and more recently a non-vanishing topological entanglement entropy.

In condensed matter physics cornerstone of Landau symmetry breaking theory, the ground-state degeneracy is determined by the pattern of the spontaneous symmetry breaking but not the topology of the system manifold, particles should have integer charges and either fermionic or bosonic statistics, and topological entanglement entropy vanishes. Here we briefly introduce the violation of the first and second rules in topological order and leave the third to the future chapters in the main text.

Bosons and fermions are consequences of quantum mechanics' major premise of identical

particles. Correspondingly, the overall phase of a state receives an additional  $+1$  or  $-1$  phase under exchange of a pair of particles. In two dimensions, however, due to the existence of non-contractible loops the state can acquire a nontrivial phase  $e^{i\theta}$  that is neither bosonic nor fermionic, where  $\theta$  is called the statistical angle. Such Abelian anyonic statistics has been realized in fractional quantum Hall insulators[175] and Laughlin wave functions[86]. If  $\psi_0(z_k) = e^{-|z_k|^2}$  is the single particle wave function in the lowest Landau level with  $z = (x + iy)/2l_B$  and  $l_B$  as the magnetic length, then Laughlin wave function is a trial wave function that captures many qualitative features[86]:

$$\psi_N(z_1, z_2, \dots, z_N) = \prod_{i>j} (z_i - z_j)^m \prod_{k=1}^N \psi_0(z_k) \quad (1.5)$$

where electrons bind an even number of magnetic fluxes to form composite fermions. A quasihole can be created at  $z_0$  when an extra magnetic flux with no associated electron is inserted:

$$\psi'(z_0) = \left[ \prod_{i=1}^N (z_i - z_0) \right] \psi_N(z_1, z_2, \dots, z_N) \quad (1.6)$$

such quasiparticles in collective state carry fractional elementary charge  $e^* = \nu e$  and fractional statistics  $\theta = \nu\pi$  where  $\nu = 1/m$  is the filling factor of the lowest Landau level[49, 51, 86]. Heuristically, by introducing  $m$  identical quasiholes and one additional electron in the lowest Landau level centered at  $z_0$ , the wave function becomes:

$$\psi^m(z_0) = \left[ \prod_{i=1}^N (z_i - z_0)^m \right] \psi_0(z_0) \psi_N(z_1, z_2, \dots, z_N) = \psi_{N+1}(z_0, z_1, z_2, \dots, z_N) \quad (1.7)$$

which is exactly the Laughlin wave function for  $N+1$  electrons in Eqn. 1.5, suggesting that  $m$  quasiholes' total charge cancels that of an electron. Therefore a quasiparticle or quasihole has charge:

$$e^* = \pm e/m \quad (1.8)$$

and similar for the statistical angle.

The fractional charge and statistics is also intimately related to the topological degeneracy of the ground states[124]. Let us consider a two-dimensional torus and define operators  $T_x$  and  $T_y$  for the processes that create a quasiparticle-quasihole pair, wrap them around the system along the  $\hat{x}$  and  $\hat{y}$  directions respectively, and return to a ground state by pair-annihilation. On the other hand, because the quasiparticles and quasiholes have associated fluxes,  $T_x$  introduce a phase shift of  $e^{2i\theta} = e^{i2\pi/m}$  in the  $\hat{y}$  direction, and vice versa. Thus  $T_x$  and  $T_y$  do not commute:

$$T_x T_y = T_y T_x e^{i2\pi/m} \quad (1.9)$$

which immediately suggests that the eigenvalues of  $T_y$  have to differ by factors of  $e^{i2\pi/m}$ . It follows that the ground states are at least  $m$ -fold degenerate. This argument may be generalized to two-dimensional surfaces with higher genus. Note that the details of the excited states such as quasiparticle energy and dispersion, have no impact on the final conclusion.

Anyonic statistics can be further generalized to the non-Abelian topological orders, where the degenerate ground states evolve into each other under the braiding of particles, other than just picking up a phase. Different braiding schemes generally do not commute, hence the name “non-Abelian”. Well-known examples include the Moore-Read Pfaffian state[104], the  $\sigma_{xy} = \frac{5e^2}{2h}$  fractional quantum Hall plateau observed in experiments[29, 30, 126, 193, 196] and the recent theory[1, 98, 123, 154] and experiment[109] on realization of Majorana fermion in strong spin-orbit interacting semiconductor-superconductor devices. This is beyond the scope of the content of this dissertation, though some of our conclusions do have utilities and implications for non-Abelian topological orders.

## 1.3 Summary of Contents

We first present here a brief summary of the following chapters in this dissertation to conclude the introduction:

Topological defects such as domain walls and vortices are ubiquitous in crystalline solids and exhibit fascinating physics. We study the theory and phenomena of topological defects in topological insulators. We begin in Chapter 2 with an exhibition that dislocation lines in three-dimensional time-reversal symmetric topological insulators are associated with one-dimensional fermionic excitations. Their appearance is controlled by the weak indices and provides a bulk characterization of the topological phase. In contrast to fermionic excitations in a regular quantum wire, these modes are topologically protected and not scattered by nonmagnetic disorder. These excitations could dominate spin and charge transport in topological insulators and provide a novel route to creating a potentially ideal quantum wire in a bulk solid.

Another parallel application is the line defects in a three-dimensional topological Mott insulator, where the spin-orbit correlations are spontaneously generated by strong electron-electron repulsive interaction. We show in Chapter 3 that these topological Mott insulators differ from their band insulator counterparts in that they possess an additional rotation matrix order parameter, which describes the spontaneous breaking of spin-rotation symmetry and the associated one-dimensional fermionic excitations are controlled by the strong index. An example microscopic model and possible physical realizations in cold atom systems are discussed. This offers alternative realizations to topologically nontrivial materials other than strong spin-orbit interaction.

We also present in Chapter 3 a generalized theory of one-dimensional excitations along line defects based on topological insulator’s surface curvature induced Berry phase, which may be generalized to the surface states as well. In connection, we study the transport properties of a topological insulator nanowire when a magnetic field is applied along its length in Chapter 4. We predict that with strong surface disorder, a characteristic signature of the band topology is revealed in Aharonov Bohm oscillations of the conductance. These oscillations have a component with anomalous period  $\Phi_0 = hc/e$ , and with conductance maxima at odd multiples of  $\frac{1}{2}\Phi_0$ , i.e. when the Aharonov Bohm phase for surface electrons

is  $\pi$ . We discuss similarities and differences from experiments on  $\text{Bi}_2\text{Se}_3$  nanoribbons, and optimal conditions for observing this effect.

Topological insulators are usually characterized by symmetry-protected surface modes; on the other hand, the discussions of one-dimensional modes along line defects in Chapter 2 and Chapter 3 help to clarify a foundational point of view of the topological insulators: they may be determined by the bulk and a surface is not required. From another perspective, we confirm in Chapter 5 that the three-dimensional inversion symmetric topological insulators are nontrivial despite the metallic surface states are absent, and prove with entanglement spectrum in Chapter 6 that the bulk ground-state wave function alone is fully indicative of the topological insulators.

In particular, in Chapter 5 we study the classification of three-dimensional insulators with inversion symmetry, in which other point group and time reversal symmetries are generically absent. We find that certain response properties of such materials are determined by just the eigenvalues of occupied states at time reversal invariant momenta under inversion symmetry: if the total number of -1 eigenvalues is odd, the material cannot be an insulator and will likely be a Weyl semimetal; if the material is an insulator and has vanishing Hall conductivity, a quantized magnetoelectric response can be defined upon the parity eigenvalues. We generalize the rule for time reversal symmetric materials and suggest that a nonzero quantized magnetoelectric response is protected if the total number of time reversal symmetric momenta points with -1 parities is twice an odd number. All inversion symmetric insulators can be classified by these inversion parities and three Chern numbers. Our theory open a broader area of possible magnetic insulators for large topologically protected responses.

An alternate geometrical derivation of these results is obtained by the entanglement spectrum of the ground-state wave function in the bulk, as described at the end of Chapter 5 and in Chapter 6. We prove that whenever protected surface states exist, a corresponding protected mode exists in the entanglement spectrum as well. Besides, the entanglement spectrum sometimes succeeds better in indicating topological phases than surface states, especially in cases when the surface break the defining symmetry of the topological insulator. We discuss the action of the inversion symmetry as an anti-unitary symmetry on the entanglement spectrum, hence a Kramers degeneracy arises even when time-reversal symmetry is absent. This degeneracy persists for interacting systems. The entanglement spectrum is therefore a promising tool to characterize topological insulators and superconductors beyond the free-particle approximation.

Indeed, quantum entanglement provides a powerful probe to the physical properties of many-body systems in addition to the conventional response properties such as conductivity, susceptibility, etc. We focus on more discussion on the relations of quantum entanglement and topological states of matter in Chapter 7, Chapter 8 and Chapter 9. For instance, topological order is an exotic quantum phase of matter beyond the Landau symmetry breaking theory and described not by order parameter from spontaneous symmetry breaking, but rather by long range quantum entanglement. We unite the theory of bipartite entanglement entropy and the computational variational Monte Carlo method to study the quantum structure of a variety of topological orders. Even for non-sign-positive wave functions, the Renyi entropy  $S_2$  can be calculated on relatively large systems ( $>324$  spins) to suppress finite size

effect. In Chapter 7, we construct critical spin liquid wave functions by Gutzwiller projecting electron Fermi sea states. These critical spin liquids are intriguing phases not captured by local order parameters and have strongly interacting low energy excitations. On the triangular lattice, we find that entanglement entropy of this bosonic spin wave function violates the Area Law with  $S_2$  enhanced by a logarithmic factor and reflects the presence of gapless emergent fermions. In contrast, for an algebraic spin liquid the entanglement entropy abides by the Area Law, and similarly for a well-nested spinon surface, which leads to a magnetic order.

Other examples of topological order include fractional quantum hall insulators and gapped quantum spin liquids. Typical hallmark of topological order includes ground-state degeneracy, non-zero topological entanglement entropy and nontrivial statistics and braiding of quasiparticle excitations. In Chapter 8, we construct the candidate ground-state wave functions for spin  $SU(2)$  symmetric gapped spin liquids and a lattice version of fractional quantum hall insulator phases obtained by the Gutzwiller projection technique, and verify that they are topologically nontrivial and carry nonzero topological entanglement entropy  $\gamma$ . Our variational Monte Carlo calculations on a  $12 \times 12$  lattice has small finite size effects and agree very well with either benchmarks or the field theoretic result  $\gamma = \log D$ , where  $D$  is the total quantum dimension of the phase. For a chiral spin liquid wave function, the calculated value is within 4% of the ideal theoretical value. We also find good agreement for a lattice version of the Laughlin  $\nu = 1/3$  phase with the expected  $\gamma = \log \sqrt{3}$ .

In addition, we contain in Chapter 9 a study of topologically ordered phases through their statistics and braiding properties and demonstrate a method to extract these information only with the set of ground-state wave functions on a torus. This is achieved by studying the topological entanglement entropy on partitioning the torus into two cylinders. In this setting, general considerations dictate that the topological entanglement entropy generally differs from that in trivial partitions and depends on the chosen ground state. Central to our scheme is the identification of ground states with minimum entanglement entropy, which reflect the quasiparticle excitations of the topological phase. The transformation of these states allows for a determination of the modular  $\mathcal{S}$  and  $\mathcal{U}$  matrices which encode quasiparticle properties. Through calculations within the variational Monte Carlo scheme, we verify the topological entanglement entropies' dependence and demonstrate our method by extracting the modular  $\mathcal{S}$  matrix of a chiral spin liquid phase. We prove that the quasiparticles obey semionic statistics. This method offers a route to a nearly complete determination of the topological order in certain cases.

# Chapter 2

## Helical Metal Inside a Topological Insulator

### 2.1 Introduction

Recent theoretical work on the effect of spin orbit interactions on the band structure of solids predicted the existence of novel topological insulators (TIs) in two[14, 73, 74] and three dimensions[41, 105, 151]. In two dimensions, these new insulators strongly resemble the quantum Hall states, although there are no applied magnetic fields, and time reversal symmetry is preserved. While there is an excitation gap in the bulk as in conventional band insulators, there are gapless modes at the edge, which appear in time reversed pairs with opposite spin and velocity. Transport measurements on HgCdTe quantum wells[13, 84] have provided evidence for the existence of these ‘helical’ edge states[73, 195, 198]. In three dimensions, topological insulators are classified as strong ( $\nu_0 = 1$ ) or weak ( $\nu_0 = 0$ ), the former has surface states with an odd number of Dirac points, which cannot be realized in two-dimensional band structures with time reversal symmetry. In addition, three-dimensional TIs are characterized by indices ( $\nu_1, \nu_2, \nu_3$ ) with respect to a basis of reciprocal lattice vectors ( $\vec{G}_1, \vec{G}_2, \vec{G}_3$ ). These essentially serve to define a time reversal invariant momentum (TRIM)  $\vec{M}_\nu = \frac{1}{2}(\nu_1\vec{G}_1 + \nu_2\vec{G}_2 + \nu_3\vec{G}_3)$ . The recent prediction[41] and evidence from angle resolved photoemission experiments[63] for a strong TI phase in the alloy Bi<sub>0.9</sub>Sb<sub>0.1</sub>, has led to heightened interest in these systems. Weak TIs are entirely characterized by  $\vec{M}_\nu \neq 0$ , and can be obtained by stacking layers of two-dimensional TIs along the  $\vec{M}_\nu$  direction. It is sometimes stated that even weak disorder will immediately wipe out the weak topological insulator. However, as argued at the end of this chapter, a more careful consideration

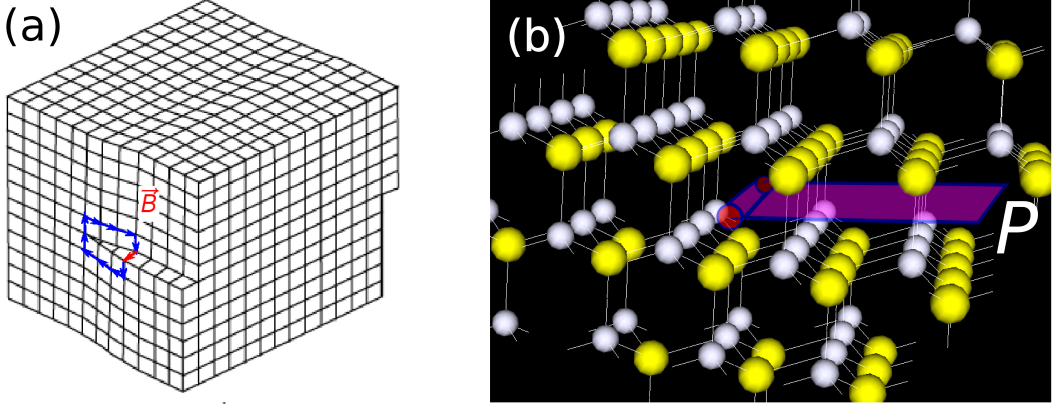


Figure 2.1. Screw Dislocations: [a] Cubic lattice screw dislocation with Burger's vector  $\vec{B}$ ; [b] Diamond lattice screw dislocation along  $\vec{B} = a(1, 1, 0)$  direction (shown as a cylinder with red ends), studied in the text. The two diamond sublattices are shown as yellow and white spheres. A cutting plane  $P$  plane that was used to generate the dislocation is shown, orthogonal to the strength  $t$  nearest neighbor bond along  $a/2(1, -1, -1)$ .

based on the results here points to a different conclusion. For the present, we will assume crystalline long range order.

Dislocations are line defects of the three-dimensional crystalline order, characterized by a vector  $\vec{B}$  (Burgers vector), which is a lattice vector. This is rather like the quantized vorticity of a superfluid vortex, and must remain constant over its entire length. The center of the dislocation is at  $\vec{R}(\sigma)$  where  $\sigma$  parameterizes the line defect. A convenient way to visualize a dislocation is via the Volterra process. One begins with the perfect crystal and chooses a plane  $P$  that terminates along the curve  $\vec{R}(\sigma)$  where the defect is to be produced. The crystal on one side of the plane  $P$  is then displaced by the lattice vector  $\vec{B}$ , and additional atoms are inserted or removed if required. At the end, crystalline order is restored everywhere except near the curve  $\vec{R}(\sigma)$ . A screw dislocation (see Figure 2.1a) is a straight line defect that runs parallel to its Burgers vector, i.e. the tangent vector  $\vec{t} = d\vec{R}(\sigma)/d\sigma$  is constant, and  $\vec{t} \parallel \vec{B}$ , while an edge dislocation is also a straight line defect that runs perpendicular to the Burgers vector  $\vec{t} \perp \vec{B}$ . In general, a dislocation varies between these two simple types along its length, depending on the orientation of its tangent vector relative to the Burgers vector.

With these preliminaries, our results are readily stated. Consider a three-dimensional topological insulator characterized by  $\nu_0$ ,  $\vec{M}_\nu$ , and insert a dislocation along  $\vec{R}(\sigma)$  with Burgers vector  $\vec{B}$ . Then, if:

$$\vec{B} \cdot \vec{M}_\nu = \pi \pmod{2\pi} \quad (2.1)$$

the dislocation induces a pair of one-dimensional modes bound to it, that propagate in opposite directions and traverse the bulk band gap. They closely resemble the helical modes at the edge of a two-dimensional quantum spin Hall insulator. Once established, they are

protected by time reversal symmetry and the bulk energy gap, and reflect the nontrivial topology of the band structure. While a trivial insulator could also develop one-dimensional propagating modes along a dislocation, the precise count obtained here - a single Kramers pair of propagating modes - cannot arise. The topological stability of a single pair of modes results from time reversal symmetry, which prohibits backscattering between the oppositely propagating one-dimensional modes[74]. From Eqn. 2.1 we note that some dislocations e.g. with  $\vec{B} \perp \vec{M}_\nu$  do not carry these helical modes. Also, there is the 'pristine' strong topological insulator  $\nu_0 = 1$ ,  $\vec{M}_\nu = 0$ , where none of the dislocations induce helical modes. Note that  $\text{Bi}_{0.9}\text{Sb}_{0.1}$ , which experiments indicate is a topological insulator, is characterized by  $\nu_0 = 1$  and a nontrivial  $\vec{M}_\nu$ , which connects the  $\Gamma$  and  $T$  points in the Brillouin zone. We will later comment on experimental consequences arising from the dislocation induced helical liquids in this material. In this chapter we focus on dislocations, the electronic properties of other defects (eg. domain walls, see [37] for an early discussion of these in PbTe semiconductors) are left to future work. This chapter is related to the previously published work of Ref. [144].

## 2.2 Dislocations in the Diamond Lattice Topological Insulator

Instead of plunging into a general proof of our results, we first present a numerical calculation of the electronic structure of a dislocation in a simple realization of a TI, which vividly displays our central result Eqn. 2.1. Following Ref. [41] we consider a tight binding model on the diamond lattice with nearest neighbor hopping, and spin orbit induced next neighbor hopping:

$$H = t \sum_{\langle ij \rangle} c_{i\sigma}^\dagger c_{j\sigma} + i \frac{8\lambda_{SO}}{(2a)^2} \sum_{\langle\langle ik \rangle\rangle} c_{i\sigma}^\dagger (\vec{d}_{ik}^1 \times \vec{d}_{ik}^2) \cdot \vec{\sigma}_{\sigma\sigma'} c_{k\sigma'} \quad (2.2)$$

where  $\vec{d}_{ik}^1$ ,  $\vec{d}_{ik}^2$  are the two nearest neighbor bond vectors leading from site  $i$  to  $k$ ,  $\vec{\sigma}$  are the spin Pauli matrices, and  $2a$  is the cubic cell size. The system is a Dirac metal at this point, and a full gap is opened upon distorting the lattice, by making the nearest neighbor hopping strengths  $t + \delta t$  along one of the directions e.g.  $\frac{a}{2}(1, 1, 1)$ . If  $\delta t > 0$  ( $\delta t < 0$ ), the system is a strong (weak) topological insulator with  $\nu = 1$  ( $\nu = 0$ ) and  $\vec{M}_\nu = \frac{\pi}{2a}(1, 1, 1)$ . We now introduce a dislocation. For numerical convenience we study a screw dislocation, which is simple to model, and use periodic boundary conditions - which requires us to consider a pair of (separated) dislocations. Translation symmetry is present along the dislocation axis, and we label states by the crystal momentum ( $k$ ) in this direction. The precise geometry we use is shown in the Figure 2.1b. If  $\vec{a}_1 = a(0, 1, 1)$ ,  $\vec{a}_2 = a(1, 0, 1)$ ,  $\vec{a}_3 = a(1, 1, 0)$  represent the diamond lattice basis vectors, the dislocations are along the  $\vec{a}_3$  axis. A screw dislocation is readily implemented in a tight binding model as follows. The bonds cut by the imaginary

plane shown in Figure 2.1b, which are moved to connect to the next layer of atoms, have their hopping amplitudes changed by  $t \rightarrow te^{\pm ik\hat{k} \cdot \vec{B}}$ .

For a pair of unit screw dislocations  $\vec{B} = a(1, 1, 0)$  in this direction, we find four one-dimensional modes, two down moving and two up moving modes, within the bulk gap (Figure 2.2a). The wave functions of these modes are peaked along the two dislocations (Figure 2.2c) - hence a pair of oppositely propagating modes is present for each dislocation line. The modes are time reversal (Kramers) conjugates of each other. Not all dislocations carry these gapless modes - if we double the Burgers vector of this dislocation (Figure 2.2b), or consider a different relative orientation when the unequal bond is orthogonal to the Burgers vector (Figure 2.2d), the one-dimensional modes do not appear. The sign of  $\delta t$  however is immaterial - both weak and strong topological insulators show this physics.

For an isolated dislocation, these time reversed one-dimensional modes are topologically protected, and can only be removed if the band gap in the bulk of the crystal closes, or if time reversal symmetry is broken. This allows us to immediately deduce the following result. The condition for a gapless line mode to exist on a dislocation cannot depend on its orientation, since it must propagate through the entire defect. Hence, it can only depend on the Burgers vector  $\vec{B}$  which remains constant through the entire length of the dislocation. Therefore, although we have explicitly considered the case of a screw dislocation, the result also holds for an edge or mixed dislocation with the same Burgers vector.

We now present an analytical rationalization for the existence of gapless modes along the dislocation line, in this model of the strong TI. We study the model in a limit that is analytically tractable, but nevertheless adiabatically connected to the parameter regime of interest. Consider the imaginary plane  $P$  (orthogonal to  $(1, -1, -1)$ ), used to construct the dislocation, which ends along the dislocation line. Extend this plane through the entire crystal, weakening all bonds that are cut by it. This plane cuts the strength  $t$  nearest neighbor bonds, which runs along the  $(1, -1, -1)$  direction. Now, the crystal is almost disconnected into two disjoint pieces. The disconnected crystal has gapless states on the two surfaces  $S_+$ ,  $S_-$  that are created, with a single Dirac node located at the surface momentum  $\vec{m}_D = \frac{\pi}{2a}(1, 1, 0)$ . Electronic states in the vicinity of the Dirac point can be expanded as  $\Psi(x_1, x_2) \sim e^{i\vec{m}_D \cdot \vec{x}} \psi(\vec{x})$ , where  $\psi(\vec{x})$  varies slowly over a lattice spacing. The effective Hamiltonian for such states on the two surfaces is  $\pm H_0$  [41], with:

$$H_0(p) = v_1 p_1 \hat{n}_1 \cdot \vec{\sigma} + v_2 p_2 \hat{n}_2 \cdot \vec{\sigma} \quad (2.3)$$

where  $p_1, p_2$  are surface momenta measured from the Dirac point, with  $p_1$  along the dislocation line (the  $(1, 1, 0)$  direction), and  $p_2$  orthogonal to it. The  $\vec{\sigma}$  are the spin Pauli matrices and  $\vec{n}_{1,2}$  are two linearly independent unit vectors. Thus if  $\mu_z = \pm 1$  represents the two surfaces, the effective Hamiltonian is  $H = H_+(p)\mu_z$ . Now, if we imagine reconnecting the surfaces without creating a dislocation, we add a hopping term ( $m$ ) between the two surfaces:  $H = H_+(p)\mu_z + m\mu_x$ , which leads to fully gapped dispersion, with gap  $2m$ , which can be adiabatically connected to the uniform bulk insulator.

Now consider introducing a screw dislocation, by displacing the surface to one side of the plane  $P$  by the lattice vector  $\vec{B} = a(1, 1, 0)$ . Reconnecting the bonds is now described as follows. In our surface coordinate system, the dislocation line is along the  $x_1$  axis, at  $x_2 = 0$ ,

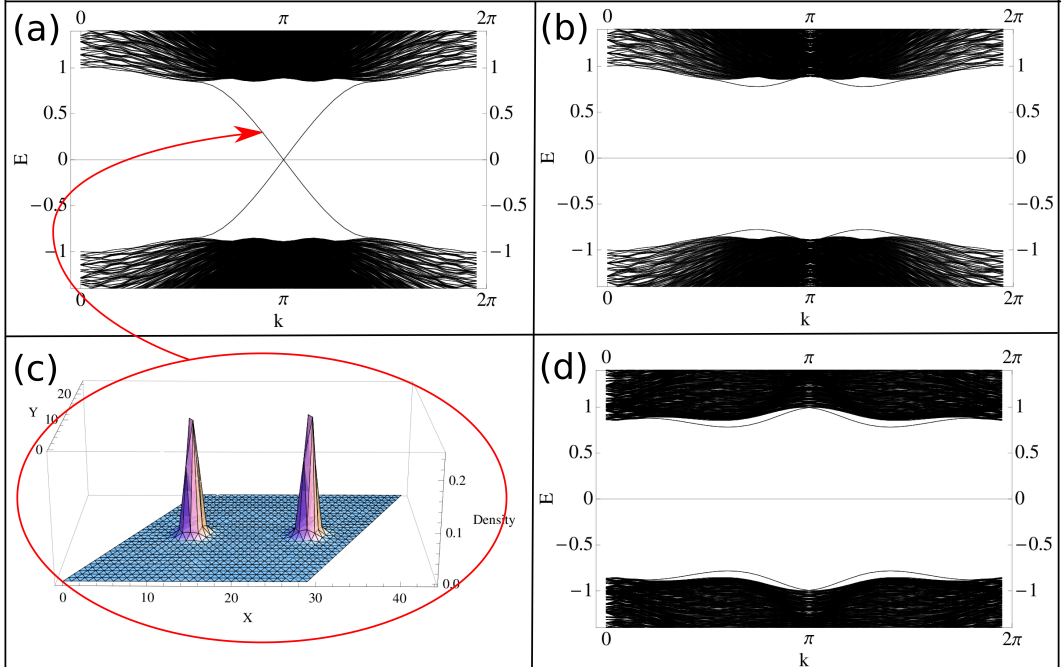


Figure 2.2. Dislocation Induced Electronic States: spectrum of the diamond lattice strong TI ( $\vec{M}_\nu = \frac{\pi}{2a}(1, 1, 1)$ ) in the presence of a pair of screw dislocations. Electronic states are shown as a function of  $k$ , the wavevector along the dislocation. For [a][b][c], the dislocations are oriented along the  $\vec{a}_3 = a(1, 1, 0)$  axis. [a] Spectrum, when the dislocation Burgers vector  $\vec{B} = \vec{a}_3$  and satisfies  $\vec{B} \cdot \vec{M}_\nu = \pi$ . A pair of counter-propagating modes per dislocation is found, that span the band gap (each midgap level happens to be doubly degenerate). [b] Spectrum when  $\vec{B} = 2\vec{a}_3$  and  $\vec{B} \cdot \vec{M}_\nu = 0 \pmod{2\pi}$ . No dislocation modes occur. [c] Probability distribution of a pair of midgap modes shown in the  $\vec{a}_1, \vec{a}_2$  plane that intersects the dislocations. The modes are bound near the dislocations. [d] The dislocations are oriented along  $\vec{B} = a(0, 1, -1)$  and  $\vec{B} \cdot \vec{M}_\nu = 0$ . No dislocation modes occur. Calculations were done on a 36x36x18 unit cell system with periodic boundary condition along  $\vec{a}_1, \vec{a}_2, \vec{B}$  directions, and dislocations separated by a half system size. The hopping parameters used in Eqn. 2.2 are  $t = 1$ ,  $t + \delta t = 2$ , and  $\lambda_{SO} = 0.125$ .

and the plane  $P$  is at  $x_2 > 0$ . The crucial observation is that when reconnecting the bonds across the plane  $P$ , the Dirac particles acquire a phase shift of  $e^{i\vec{m}_D \cdot \vec{B}} = -1$  as the Dirac node is located at the specific wavevector  $\vec{m}_D$  which when displaced by the Burgers vector  $\vec{B}$  leads to a  $\pi$  phase shift. The effective Hamiltonian in the presence of a dislocation is then:

$$H_{\text{dis}} = H_+(-i\hbar\nabla)\mu_z + m(x_2)\mu_x \quad (2.4)$$

where the Dirac mass term is now position dependent:  $m(x_2 < 0) = m$  but  $m(x_2 > 0) = -m$ . Such Dirac Hamiltonians are well known to lead to low energy modes that are protected by Index Theorems[114]. We explicitly demonstrate this below.

Since  $p_1$  is a good quantum number, consider first the Hamiltonian at  $p_1 = 0$ .  $H_{\text{dis}}(p_1 = 0) = v_2 \hat{n}_2 \cdot \vec{\sigma} \mu_z (-i\hbar\partial_{x_2}) + m(x_2)\mu_x$ . Such a one-dimensional Dirac equation is well known to have a zero energy state[67]:

$$\psi(x_2) = e^{\frac{1}{\hbar v_2} \int_0^{x_2} dx_2 m(x_2)} \psi_0 \quad (2.5)$$

where  $\psi_0$  satisfies:  $\mu_y \hat{n}_2 \cdot \vec{\sigma} \psi_0 = +\psi_0$ . Since  $m(x_2 \rightarrow +\infty) < 0$  and  $m(x_2 \rightarrow -\infty) > 0$ , the state is normalizable. In fact, there is a Kramers pair of degenerate states present. The dispersing one-dimensional modes are obtained by studying the splitting of this pair, on changing the momentum  $p_1$ . For small momenta, this leads to the effective Hamiltonian is  $H_{\text{eff}} = v_1 p_1 \vec{n}_{1\perp} \cdot \vec{\sigma} \mu_z$ , where  $\vec{n}_{1\perp} = \hat{n}_2 \times (\hat{n}_1 \times \hat{n}_2)$ , which leads to a pair of counter-propagating one-dimensional modes with linear dispersion  $\epsilon(p_1) = \pm v_1 p_1 \sqrt{1 - \hat{n}_1 \cdot \hat{n}_2}$  that are confined to the dislocation.

These one-dimensional modes span the band gap, connecting the filled and empty bands. As long as time reversal symmetry is present, a single pair of them cannot acquire a gap[74], which makes them a defining property of the phase. Note, the crucial step in the derivation of the one-dimensional modes above, was the fact that the low energy surface states on the cut surface were at the nontrivial surface momentum  $\vec{m}_D$  such that  $\phi = \vec{B} \cdot \vec{m}_D = \pi$ . More generally, if there are several such surface Dirac modes  $\vec{m}_D^i$ , what is required is that an odd number of them acquire a  $\pi$  phase shift on circling the dislocation  $\sum_i \vec{m}_D^i \cdot \vec{B} = \pi(\text{mod}2\pi)$ . This guarantees the existence of at least a pair of gapless one-dimensional modes on the dislocation. If on the other hand,  $\sum_i \vec{m}_D^i \cdot \vec{B} = 0(\text{mod}2\pi)$ , there are no protected modes on the dislocation. Indeed, this occurs in the model above if, for example, we choose the  $\vec{B}$  orthogonal to the  $(1, 1, 1)$  direction (the direction of the strong bond).

## 2.3 Dislocations in a General Topological Insulator

Armed with these insights for a specific model, one may discuss the general case of an arbitrary dislocation in a topological insulator, and when a protected one-dimensional gas is expected to occur. For a topological insulator characterized by  $\{\nu_0, \vec{M}_0\}$ , and a dislocation with Burgers vector  $\vec{B}$ , the condition for the existence of a protected 1 D mode is given by Eqn. 2.1, and derived in the general case in the Methods section.

For the weak TI case, however, a more intuitive derivation of this result is possible. The weak TI is adiabatically connected to a stack of decoupled two-dimensional TIs, stacked

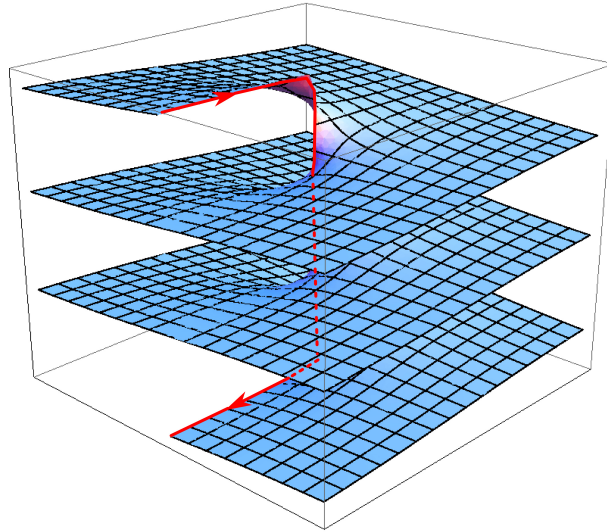


Figure 2.3. Screw dislocation in a weak topological insulator: the unpaired edge modes (one member of the edge mode pair is shown in red) of the top and bottom layer must propagate through the dislocation by continuity.

along the  $\vec{M}_\nu$  direction. The top and bottom surfaces of the stack are fully gapped. Consider creating a screw dislocation in such a stack, by cutting and regluing layers in the manner shown in Figure 2.3. Cutting a plane results in a pair of edge modes, which are gapped after the planes are glued back together. However, edge modes in the top and bottom layers are left out in this process - just one member of the counter-propagating edge mode pair is shown in the figure. Since a single pair of such modes cannot begin or end, they must propagate through the dislocation core to complete the circuit. Thus, helical dislocation modes must occur in this setup. Similarly, an edge dislocation created by inserting an additional half-plane in this layered setup will carry protected edge modes. Note, such a graphical derivation is not feasible for a strong TI, where no two-dimensional limit exists. For a three-dimensional Chern insulator[83], characterized by a reciprocal lattice vector  $\vec{G}_0$  a dislocation line should have  $\frac{\vec{G}_0 \cdot \vec{B}}{2\pi}$  chiral modes propagating along it.

It is sometimes stated that in the presence of disorder, only the  $\nu_0$  index is robust, while the  $\vec{M}_\nu$  index is irrelevant. Hence weak TIs, whose surface states can be localized, are believed to be unstable to disorder[41]. Since our results pertain to a distinct topological property controlled by the  $\vec{M}_\nu$  index, they shed light on the stability of weak TIs. For sufficiently weak disorder the system stays insulating and dislocations are expected to remain well defined (discussed in more detail below). Then, the helical edge modes accompanying the relevant dislocations continue to be protected, which means that the  $\vec{M}_\nu$  index, and weak TIs, remain well defined. When can dislocations be meaningfully defined in a disordered crystal? Crystalline long range order is a sufficient condition, since the local order parameter can

then be used to define dislocations. In some cases, even in the absence of long range order, dislocations may be well defined - for example the Bragg glass phase only has algebraic order, but dislocations are not proliferated[18]. Certainly, in real crystals which are inevitably disordered, dislocations are well defined objects, and hence the physics discussed in this chapter should apply. However, if disorder is so strong that the dislocations are no longer well defined, then the only remaining distinction is the  $\nu_0$  index. Similarly, an insulator with  $\vec{M}_\nu \neq 0$  can be converted to one with  $\vec{M}_\nu = 0$ , by introducing a potential modulation with period  $\vec{M}_\nu$ . Elementary dislocations that carry helical modes will then cost infinite energy per unit length.

## 2.4 Experimental Consequences

In real solids, dislocations are always present and the predicted helical modes should have important experimental consequences. Scanning tunneling microscopy (STM) of a topological insulator surface where dislocations terminate, is particularly well suited to verify these predictions. Since the precise atomic arrangement is visualized by STM, the nature of the dislocations involved can be characterized. At the same time, the finite density of states associated with the one-dimensional modes will lead to an enhanced tunneling density of states near the dislocation core. This will be particularly striking if one tunes to an energy where the surface modes contribute minimally (eg. at the Dirac node). Such experiments are immediately feasible on the putative topological insulator  $\text{Bi}_{0.9}\text{Sb}_{0.1}$  with A7 structure. Since the band structure of that material is complex and still debated[172], we demonstrate qualitatively what is expected, in the simpler diamond lattice strong TI model Eqn. 2.2. Moreover, since the crystal symmetry in the two cases share several features - such as a three fold axis parallel to the  $\vec{M}_\nu$  vector, some predictions for the diamond lattice model may be directly relevant to the A7 structure. First consider the surface orthogonal to the strong bond  $(1, 1, 1)$  direction. We choose this surface to cut three strength  $t$  bonds (rather than a single strong bond) in order to obtain a surface band structure similar in some respects to the  $(111)$  surface of  $\text{Bi}_{0.9}\text{Sb}_{0.1}$ . We call this the  $(111)'$  surface. This surface has a single Dirac node centered at the  $\Gamma$  point in the surface Brillouin zone. We consider a pair of separated screw dislocations with  $\vec{B} = a(1, 1, 0)$ , which carry one-dimensional helical modes, that terminate on the surface. STM measures the local density of states (LDOS) at a given energy and surface location  $\rho(\vec{r}, E) = \sum_\alpha |\psi_\alpha(\vec{r})|^2 \delta(E - E_\alpha)$ , where the  $\alpha$  sum runs over all eigenstates. The dislocations appear as peaks in the LDOS as shown in Figure 2.4a, due to these one-dimensional modes. Note, the ledge connecting the two screw dislocations on the surface also shows an enhanced DOS.

More striking evidence for the relation Eqn. 2.1 appears when we consider the edge dislocations on the  $(\bar{1}\bar{1}1)$  surface. If the Burgers vector of the dislocation is  $\vec{B} = a(1, 0, 1)$  the one-dimensional modes are present (Figure 2.4b), but if  $\vec{B} = a(1, -1, 0)$  then they are absent (Figure 2.4c). This is reflected in the LDOS maps in Figure 2.4b,2.4c. Here, there is no physical line connecting the two defects.

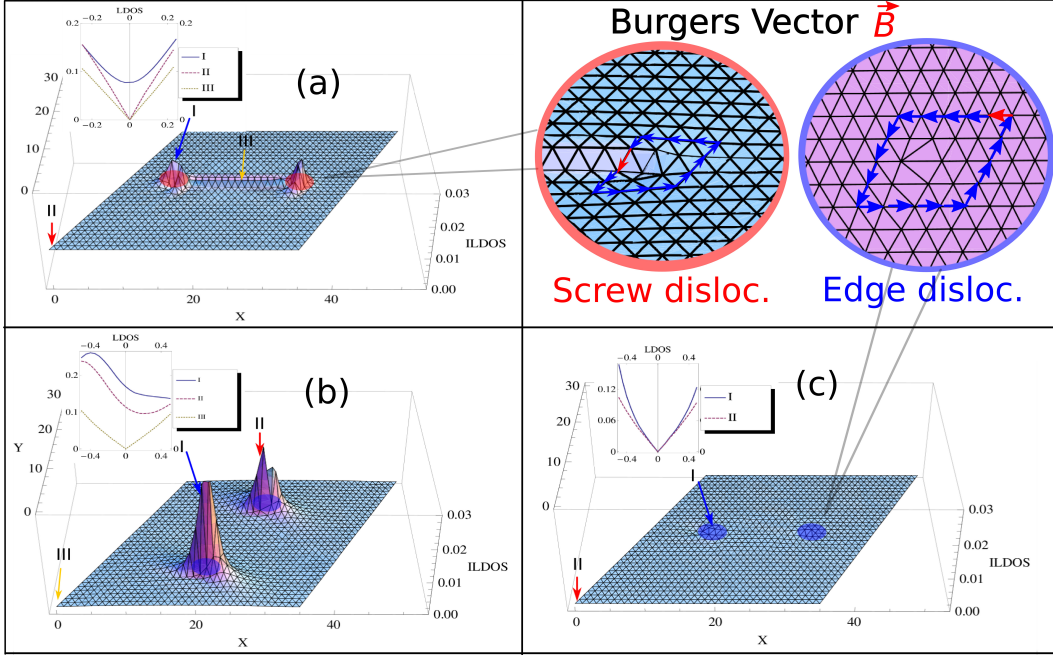


Figure 2.4. Surface density of states in the presence of dislocations: LDOS as measured by STM, for various dislocation configurations, in the diamond lattice strong TI with parameters as in Figure 2.2. In all cases dislocation pairs (and are directed along  $\vec{a}_3$ ) are separated by a half system size. Topography of the integrated LDOS in the energy window  $[-0.1, 0.1]$  is shown, with insets displaying energy dependent LDOS at special points on the surface. [a] The  $(111)'$  surface intersecting a pair of screw dislocations with  $\vec{B} = a(1, 1, 0)$ . These carry one-dimensional modes which give rise to a peak in the integrated LDOS. In [b] and [c], edge dislocations on the  $(\bar{1}\bar{1}1)$  surface. In [b], the dislocation satisfies  $\vec{B} \cdot \vec{M}_\nu = \pi$ , and has one-dimensional modes visible in the LDOS while in [c] the dislocation has  $\vec{B} \cdot \vec{M}_\nu = 0$ , hence no one-dimensional line mode and no enhanced LDOS. In [a][b][c] only the top layer of atoms is shown, and calculations are done on  $36 \times 36 \times 18$  unit cell system, with periodic boundary conditions in the  $\vec{a}_1$ ,  $\vec{a}_2$  directions.

Since elastic scattering by nonmagnetic impurities cannot scatter electrons between the counter-propagating helical modes of the dislocation, they behave as ideal quantum wires at low temperatures, when inelastic processes are frozen out. This will have obvious consequences for electrical transport, although the challenge will be to separate this conduction mechanism from protected surface mode conduction, which is also present. In conduction across the short direction of anisotropic samples (eg. disc shaped), dislocation induced direct conduction paths should dominate over surface conduction. If dislocations can be induced in a controlled fashion during the growth process, then the direction dependent condition for the existence of helical modes, and dislocation density dependence of conductivity can be used to isolate this contribution. Another possibility is to introduce magnetic impurities on the surface of the insulator, which could potentially localize surface modes but have little impact on dislocation helical modes deep in the bulk. A rough estimate of the excess conductivity induced by dislocation modes for a dislocation density  $n_d \sim 10^{12} \text{ m}^{-2}$  and a low temperature scattering length  $l \sim 1 \mu\text{m}$  along the dislocation[84] yields  $\rho = \frac{\hbar}{2e^2} \frac{1}{n_d l} \sim 10 \text{ m}\Omega\text{m}$ , which should be experimentally accessible. It is conceivable that such novel quantum wires appearing within an insulating bulk medium, may be potentially relevant for spin and charge transport applications. A more exotic application might be to topological quantum computing for which a remarkable new architecture has recently been proposed, utilizing vortex Majorana states confined at the interface between a conventional superconductor and a strong TI[40]. Analogs of this proposal involving dislocations, rather than vortices, are worth exploring.

## 2.5 Methods

For a general topological insulator characterized by  $\{\nu_0, \vec{M}_0\}$ , and a dislocation with Burgers vector  $\vec{B}$ , the condition for the existence of a protected one-dimensional mode is given by Eqn. 2.1 and derived below. First, let us briefly review the meaning of the topological insulator invariants  $(\nu_0; \vec{M}_\nu)$ . These are conveniently expressed in terms of quantities  $\delta_i$  defined at the  $i = 1 \dots 8$  TRIMs of the three-dimensional Brillouin zone, which can be computed for a given band structure[41]. However, these quantities depend in general on the gauge of the band wave functions, and are not directly meaningful. Certain products though are physically meaningful, such as  $\prod_{i=1}^8 \delta_i = (-1)^{\nu_0}$ . One can utilize the gauge dependence to bring the  $\delta_i$  into a simple form with the minimal number of TRIMs at which  $\delta_i = -1$ . For the strong TI, one can arrange for a single negative value at precisely the TRIM  $\vec{M}_\nu$ , i.e.  $\delta_{\vec{M}_\nu} = -1$ . For the weak TI, there are necessarily two negative values,  $\delta_{\vec{M}_\nu} = -1$  and  $\delta_\Gamma = -1$ , where  $\Gamma = (0, 0, 0)$ . Other physically meaningful combinations of the  $\delta_i$  control properties of surface states that will be crucial for our purposes. Consider a crystal surface orthogonal to the reciprocal lattice vector  $\vec{G}_3$ . An important characteristic of the surface bands is the number of times they cross a generic Fermi energy which lies within the bulk gap, along a line in the Brillouin zone. In particular, the parity of the number of such band crossings (even vs odd)  $N_{\text{cross}}$ , when connecting two surface TRIMs  $\vec{m}_1, \vec{m}_2$  is a topologically

protected quantity related to the product[41]:

$$(-1)^{N_{\text{cross}}} = \delta_{\vec{m}_1} \delta_{\vec{m}_2} \delta_{\vec{m}_1 + \frac{\vec{G}_3}{2}} \delta_{\vec{m}_2 + \frac{\vec{G}_3}{2}} \quad (2.6)$$

Consider now creating a screw dislocation in a general topological insulator with Burgers vector  $\vec{B}$ . This is created using a cutting surface containing the dislocation - the surface is perpendicular to a reciprocal lattice vector which we call  $\vec{G}_3$ . Atoms on one side of the surface are displaced by  $\vec{B}$  and reconnected.

To derive the general condition for the existence of protected helical modes along the dislocation, we replay the analytical justification given previously for a specific model, for this more general case. A crucial step in that derivation was the fact that the surface states on the cut surfaces were Dirac nodes located at TRIMs. If an odd number of these modes acquire a  $\pi$  phase shift on creating the dislocation, a protected one-dimensional mode results. Although in general, the surface band structure may be quite complicated, for the purpose of deriving robust topological properties one may adiabatically deform the crystal structure (during which the bulk gap remains open, and the Bravais lattice structure stays fixed). By this process, the surface modes can always be deformed into Dirac nodes that cross the band gap, centered at the surface TRIMs. First assume that the Burgers vector is a primitive lattice vector  $\vec{B} = \vec{b}$  i.e. it is the minimum length lattice vector in that direction. We take the surface reciprocal lattice vectors to be  $\vec{G}_1, \vec{G}_2$ , with  $\vec{G}_1 \cdot \vec{b} = 2\pi$  and  $\vec{G}_2 \cdot \vec{b} = 0$ . Also, for a screw dislocation  $\vec{b} \cdot \vec{G}_3 = 0$ . The surface TRIMs are located at  $\vec{m}_i \in \{\Gamma, \frac{\vec{G}_1}{2}, \frac{\vec{G}_2}{2}, \frac{\vec{G}_1 + \vec{G}_2}{2}\}$ . Then, there are two surface TRIMs  $\vec{m} = \{\frac{\vec{G}_1}{2}, \frac{\vec{G}_1 + \vec{G}_2}{2}\}$  for which  $\vec{B} \cdot \vec{m} = \pi(\text{mod}2\pi)$ . If the number of surface Dirac nodes present in total at these two TRIMs  $N_{\text{Dirac}}$  is odd, then the dislocation will host a protected helical mode. Clearly, the parity of  $N_{\text{Dirac}}$  is related to the number of band crossings between the two surface TRIMs given by Eqn. 2.6. Thus, the condition for the helical modes is

$$\delta_{\frac{\vec{G}_1}{2}} \delta_{\frac{\vec{G}_1 + \vec{G}_2}{2}} \delta_{\frac{\vec{G}_1 + \vec{G}_3}{2}} \delta_{\frac{\vec{G}_1 + \vec{G}_2 + \vec{G}_3}{2}} = -1 \quad (2.7)$$

The product above can be simplified by going to the convenient gauge where only a single non-zero momentum TRIM has a negative  $\delta$ , i.e.  $\delta_{\vec{M}_\nu} = -1$ . Note, the defining property of the four TRIMs appearing in the product above is that  $\vec{M} \cdot \vec{B} = \pi$ . Hence, if the momentum  $\vec{M}_\nu$  also satisfies this condition, then it appears in the product above, and the equation is satisfied. This leads us to the condition  $\vec{B} \cdot \vec{M}_\nu = \pi(\text{mod}2\pi)$  for the existence of helical dislocation modes. In general, the Burgers vector is a multiple of the primitive lattice vector. If it an odd multiple, the derivation above is unaffected. If, however, it is an even multiple, there are no dislocation modes since the phase shifts are always trivial. These more general cases are also captured by the formula above and hence we arrive at the general condition Eqn. 2.1, for the existence of protected helical modes along the dislocation. Note, this derivation holds for both weak and strong TI.

# Chapter 3

## Topological Insulators in Three Dimensions from Spontaneous Symmetry Breaking

### 3.1 Introduction

Seminal work by Thouless and coworkers[173] pointed out that band insulators are not identical, but can differ in fundamental respects, that are characterized by a topological property of the bands. The central example discussed was the integer quantum Hall state, whose topological properties are characterized by an integer which is essentially the Hall conductance. Realizing such a state naturally requires breaking of time reversal symmetry, typically by the application of a strong magnetic field on a two-dimensional system. The topological nature of the integer quantum Hall state is also revealed by studying the edge of a two-dimensional sample, where chiral (one way propagating) edge states occur at energies within the bulk energy gap.

Recently, it has been realized that band insulators with spin orbit interactions (SOIs) can also be characterized by their band topology. In two dimensions, the quantum spin hall (QSH) phase is closely analogous to the quantum Hall state. However, since it preserves time reversal symmetry, it has a pair of counter-propagating one-dimensional modes at the edge. Such a state can occur with SOIs that preserve spin rotation symmetry (SRS) about an axis[73, 74]. It was shown in Ref. [74], that even in the absence of such spin rotation invariance, the counter-propagating modes remain protected by time reversal symmetry. The topological property of these insulators are characterized, not by an integer, but by a

$Z_2$  number, so that all topologically non-trivial insulators of this kind fall within the same topological class. An experimental realization of this phase has been reported in HgTe heterostructures[13, 84].

Turing to three dimensions, an insulator with nontrivial band topology can be realized just by stacking such two-dimensional QSH states. These are called the weak topological insulators (WTI). However, a more surprising possibility, the strong topological insulator (STI), has been predicted theoretically[39, 41, 105]. Once again, the surface physics is exotic, which provides a physical characterization of this phase. STIs have an odd number of Dirac nodes on their surface, which are stable against moderate perturbations that preserve time reversal symmetry[41]. Such a band structure cannot be realized in any two-dimensional system with time reversal invariance. There have been experimental realizations of these predictions in bismuth antimony[63, 64, 120] and in bismuth selenium[197, 202], which have been verified by angle resolved photoemission spectroscopy. Note, in contrast to the QSH state, in order to realize the STI the SRS must be completely broken.

The topological insulator (TI) and QSH phases normally exist in systems with strong SOI that explicitly breaks SRS[41, 74, 112]. However, as pointed out in Ref. [142] an extended Hubbard model on a two-dimensional honeycomb lattice can have spontaneous SRS breaking and result in a QSH phase, with the right kind of repulsive interactions[142]. SRS is only preserved about an axis  $\hat{n}$ , which is spontaneously chosen, leading to gapless Goldstone modes. This was termed a topological Mott insulator (TMI) - the separation of energy scales between the low lying magnetic excitations and the gapped charge excitations being typical of Mott insulators. We will also adopt this nomenclature although it must be noted that local moment physics, often associated with Mott insulators, does not occur here. Subsequently, it was argued in Ref. [46] that skyrmions of  $\hat{n}$  carry charge  $2e$ .

Here, we consider the analogous problem of a three-dimensional system without bare spin orbit couplings, and full SRS, being driven into a TI state by strong interactions. The key difference from the two-dimensional case, is that in order to realize the STI, SRS must be completely broken. Hence the order parameter in this case is a rotation matrix  $\overleftrightarrow{\mathbf{R}} \in O(3)$ , similar to superfluid Helium-3 A and B-phases. Physically, this order parameter describes the orientation of the spin coordinate system, relative to the spatial coordinates. Spatial variations of the order parameter lead to a rich set of topological textures. We describe a microscopic model, an extended Hubbard model on the diamond lattice that, within a mean field treatment, leads to this phase. The order parameter supports a number of topological defects. In particular, a vortex like line defect occurs, but with a  $Z_2$  charge. This line defect in the STI is found to be associated with a pair of gapless fermionic excitations that travel along its length. These modes are topologically stable against moderate perturbations such as impurities and interactions as long as time reversal symmetry is intact. This is the main result of the chapter - an analytical derivation is provided which relies on the properties of the Dirac equation on a two-dimensional curved surface.

We now contrast our results with other recent work. In Chapter 2 we have shown similar exotic behavior also occurs in TIs, along crystal defects such as dislocations. Gapless fermionic excitations emerge there when a  $Z_2$  parameter formed by the product of the dislocation Burgers vector and three WTI indices[144] is nonzero - which in principle can occur in

both the weak and strong TI. In contrast, in the present chapter, the fermionic modes along the line defect are solely determined by the more elusive strong index. They are absent in the case of the WTI. Thus far, the characterization of the TI phase has relied on the surface behavior. This result provides a route to identifying the strong TMI via a bulk property.

Similar modes have been identified propagating along a solenoid of  $\pi$  flux, inserted into a STI[139, 143]. Here, the  $2\pi$  rotation of the electron spin around the line defect leads to a Berry's phase, providing a physical realization of the  $\pi$  flux. Analogous phenomena occur in the context of line defects in superfluid He<sub>3</sub>-B[137].

The order parameter  $\overleftrightarrow{\mathbf{R}}$  also admits a skyrmion like texture, which is a point object in three dimensions (Shankar monopole). We find that in contrast to the skyrmion of the QSH effect[46], these are uncharged.

In most solids where electron-electron interactions are important tend to have some degree of SOIs - which will confine the defects. Hence, we propose realizations of this physics in optical lattices of ultracold atoms, utilizing molecules with multipole moments to obtain the proposed extended Hubbard models. The two-dimensional version[142] is found to be naturally realized with electric dipoles. Realizing the three-dimensional case is more challenging, however molecules with electric quadrupole moments confined in optical lattice can realize some of the key ingredients required.

This chapter is organized as the following: In Section 3.2, we will present the order parameter manifold and the line modes'  $Z_2$  dependence on the winding number; in Section 3.3, we will justify our claim with numerical and analytical results; another texture Shankar monopole will be discussed in Section 3.4; in Section 3.5, we will establish our model Hamiltonian on a diamond lattice and show the mean field stability of TMI phases; we give two possible experimental realizations in cold atom systems in Section 3.6; we conclude the main result of this chapter in the Section 3.7. Hereafter we use  $\sigma$  and  $\tau$  for the spin and sublattice degree of freedom, respectively. This chapter incorporates materials previously published in Ref. [206].

## 3.2 Topological Mott Insulators and Order Parameter Textures in Three Dimensions

In order to describe the TMI phase, we consider a concrete example in the following. In a subsequent section, we address the question of how such a phase may be microscopically realized. To contrast the TMI phase with the regular TI, consider the model Hamiltonians of a TI introduced in Ref. [41]. We consider nearest neighbor hopping ( $t_{ij}$ ) on the sites of a

diamond lattice, and spin-orbit induced hopping on next-neighbor sites:

$$\begin{aligned}
H_{\text{TI}} &= H_{\text{hop}} + H_{\text{SO}} \\
H_{\text{hop}} &= \sum_{\langle ij \rangle} t_{ij} c_i^\dagger c_j \\
H_{\text{SO}} &= i(8\lambda_{SO}/a^2) \sum_{\langle\langle ij \rangle\rangle} c_i^\dagger \vec{\sigma} \cdot (\vec{d}_{ij}^1 \times \vec{d}_{ij}^2) c_j
\end{aligned} \tag{3.1}$$

where  $c^\dagger = (c_\uparrow^\dagger, c_\downarrow^\dagger)$  is the electron creation operator and  $\vec{\sigma}$  is the spin Pauli matrix. The SOI for a pair of second neighbor sites  $ij$ , depend on  $\vec{d}_{ij}^p$  ( $p = 1, 2$ ) the two nearest neighbor bond vectors connecting the second neighbor sites  $ij$ . The SOIs are thus determined by the crystal structure. Note, the SU(2) SRS is completely broken, which is required to realize the STI in three dimensions.

In contrast, in the TMI phase discussed here, the underlying Hamiltonian possesses full SU(2) SRS that is spontaneously broken. The order parameter  $\overleftrightarrow{\mathbf{R}}$  then is a rotation matrix that describes the relative orientation between the real space coordinate system and the spin axes. The spin orbit term then takes the form:

$$H_{\text{SO}}^{\text{TMI}} = i(8\lambda_{SO}/a^2) \sum_{\langle\langle ij \rangle\rangle} c_i^\dagger \vec{\sigma} \cdot \overleftrightarrow{\mathbf{R}_i} \cdot (\vec{d}_{ij}^1 \times \vec{d}_{ij}^2) c_j \tag{3.2}$$

There is one important difference between the TI and TMI: since in the latter  $\overleftrightarrow{\mathbf{R}}$  arises from symmetry breaking it can vary spatially to give rise to a topologically nontrivial texture. To identify the topologically stable defects, we first note that the order parameter manifold is a three-dimensional orthogonal matrix  $\overleftrightarrow{\mathbf{R}} \in O(3)$ . It can represent by  $\overleftrightarrow{\mathbf{R}} = (\hat{e}_1, \hat{e}_2, \hat{e}_3)$ , where  $\hat{e}_i$  are orthogonal unit vectors representing the basis vectors of the spin coordinate system. An example is shown in Figure 3.1.

The target manifold of this order parameter is  $O(3) = SO(3) \times Z_2$ , and  $Z_2$  determines the chirality  $\det(\overleftrightarrow{\mathbf{R}}) = \pm 1$ , or whether the rotation is proper or improper. Hereafter we mainly focus on the continuous  $SO(3)$  part of the order parameter, for it has nontrivial homotopy groups in two and three dimensions. Then, each proper rotation can be described by the parameters  $(\hat{n}, \theta)$ , where  $\hat{n}$  is the direction of the rotation axis and  $\theta \in [0, \pi]$  is the rotation angle around it. To visualize it we can map all proper rotation matrices to a solid ball with radius  $\pi$ , where  $\hat{n}$  maps to the radial direction and rotation angle maps to the radius of the image point. Note a rotation of  $\pi$  about  $\hat{n}$  is the same as that of  $\pi$  about  $-\hat{n}$ , so opposite points on the spherical surface are identified. The resulting geometry is a three-dimensional projective plane  $P^3$ [114].

We now discuss the topological defects of this order parameter space. The discrete  $Z_2$  symmetry breaking implied by the  $Z_2 \times SO(3)$  order parameter leads to domain walls in three dimensions. More interestingly, line defects also exist (we assume three spatial dimensions in the following). These can be captured by considering the order parameter along a closed curve in real space, which encircles the line defect. This defines a closed

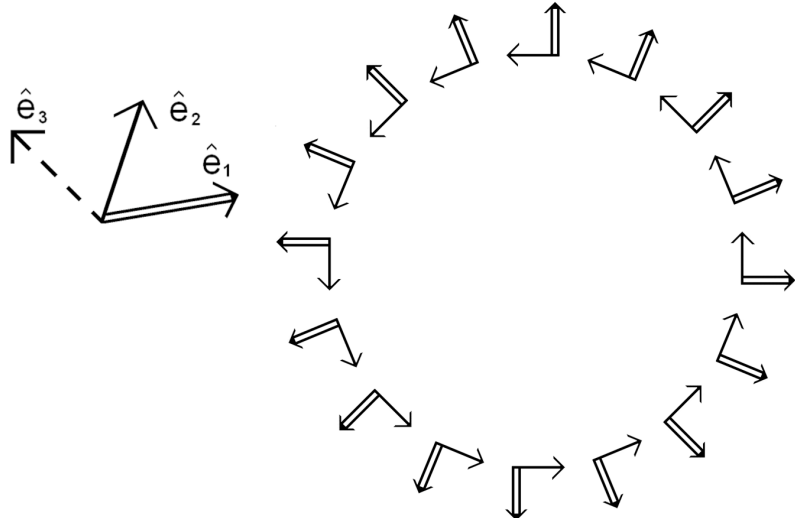


Figure 3.1. An illustration of order parameter  $\mathbf{R}$  of a nontrivial line defect in the  $x - y$  plane,  $\hat{z}$  direction is translation-invariant. The hollow and solid arrow are the  $\hat{x}$  and  $\hat{y}$  axes of local coordinate, the  $\hat{z}$  axis points out of the paper for proper rotation.

loop in the order parameter space and distinct classes of such closed loops correspond to the topological line defects. There are two classes of closed loops for the  $SO(3)$  space described above. In addition to the trivial closed loop, that can be shrunk continuously to a point, there exists a nontrivial loop that connects the antipodal points  $(\hat{n}, \pi)$  and  $(-\hat{n}, \pi)$ . Since these represent the same rotation, this is in fact a closed loop. Thus there is a nontrivial line defect characterized just by a  $Z_2$  topological charge. Technically  $\pi_1(SO(3)) = Z_2$  [114]. An example is shown in Figure 3.1 with translational invariance along  $z$  direction although generically, the line can be of arbitrary shape and direction. The electronic properties of such a line defect is studied in the following section - protected one-dimensional modes that propagate along the defect are found in the case of the strong TMI, but not in the case of the weak TMI. We also note that since  $\pi_2(SO(3)) = 0$ , no nontrivial point defects exist in three dimensions. However, since  $\pi_3(SO(3)) = Z$ , ‘skyrmion’ like textures (called Shankar monopoles[161]) exist in three dimensions. In contrast to topological defects, they are smooth textures without a singular core. We investigate the electronic structure of these objects and find that they are neutral in the large size limit, in contrast to skyrmions in the two-dimensional QSH state which carry charge  $2e$ [46].

### 3.3 Electronic Structure of a Line Defect: Numerical and Analytical Results

We study the electronic structure of the  $Z_2$  line defect in the diamond lattice model of a TMI discussed before. We choose the nearest neighbor hopping in three directions to be equal  $t_{ij} = t > 0$  while the fourth is different  $t_{ij} = t + \delta t$ . A strong (weak) TI phase occurs if  $\delta t > 0$  ( $\delta t < 0$ ) [41]. We choose an order parameter texture that incorporates line defects:

$$H = \sum_{\langle ij \rangle} t_{ij} c_i^\dagger c_j + i (8\lambda_{SO}/a^2) \sum_{\langle\langle ij \rangle\rangle} c_i^\dagger \vec{s} \cdot \overleftrightarrow{\mathbf{R}}_l \cdot (\vec{d}_{ij}^1 \times \vec{d}_{ij}^2) c_j \quad (3.3)$$

with:

$$\overleftrightarrow{\mathbf{R}}_l(\varphi) = \begin{pmatrix} \cos(l\varphi) & \sin(l\varphi) & 0 \\ -\sin(l\varphi) & \cos(l\varphi) & 0 \\ 0 & 0 & 1 \end{pmatrix} \quad (3.4)$$

where  $\overleftrightarrow{\mathbf{R}}_l$  depends only on the azimuthal angle of the atom connecting sites  $i$  and  $j$ . Note, only the parity of  $l$  is topologically stable. Here we study a system of  $24 \times 24$  with a maximally separated vortex ( $l = 1$ ) and anti-vortex ( $l = -1$ ), and with periodic boundary condition in  $x - y$  plane and translational invariance in  $z$  direction. Note, time reversal symmetry is preserved by this Hamiltonian.

For a  $\delta t > 0$  strong TMI system with  $l = \pm 1$ , two pairs of conducting line modes are found in the bulk gap. These states' density profiles are strongly localized at the cores or the two defects (Figure 3.2 top, shows only one of them for clarity). Therefore a Kramer pair of modes is localized along the thread of core. Given the particle hole symmetry that happens to be present in this model, they cross at zero energy (Figure 3.2 bottom). In contrast, these modes are absent in the cases of the weak TMI  $\delta t < 0$  or if  $l = 0, \pm 2$  in either type of TMI, and the bandstructure remains fully gapped. This is direct evidence that these  $Z_2$  dependent line modes within the bulk identify the strong TMI.

An analytical argument for these modes can be developed in several ways. We can derive these modes based on the three-dimensional Dirac continuum limit of the Hamiltonian Eqn. 3.3; however, below we consider deriving these modes using the known properties of surface states of STIs. Consider a bulk sample with a infinitely long cylindrical hole of radius  $R$  drilled through its center. We consider the low energy states on the cylindrical surface, both without and with a line defect inserted in the cylindrical hole (Figure 3.3). We show that in the limit of  $R \rightarrow 0$ , a propagating midgap mode survives only when the defect is present; otherwise a fully gapped insulator results. Interestingly, the key ingredient here is the property of the two-dimensional surface Dirac state on a curved manifold. In contrast to the states of a particle on a ring, where the zero angular momentum eigenstate remains at low energy even when the ring radius is shrunk to zero, here, the Dirac particle acquires a Berry's phase of  $\pi$  on rotating around the cylinder surface, which excludes the zero angular momentum state. Hence on shrinking the radius, no low energy states remain, and the bulk insulator is recovered. However, if a topological defect of the spin-orbit coupling matrix

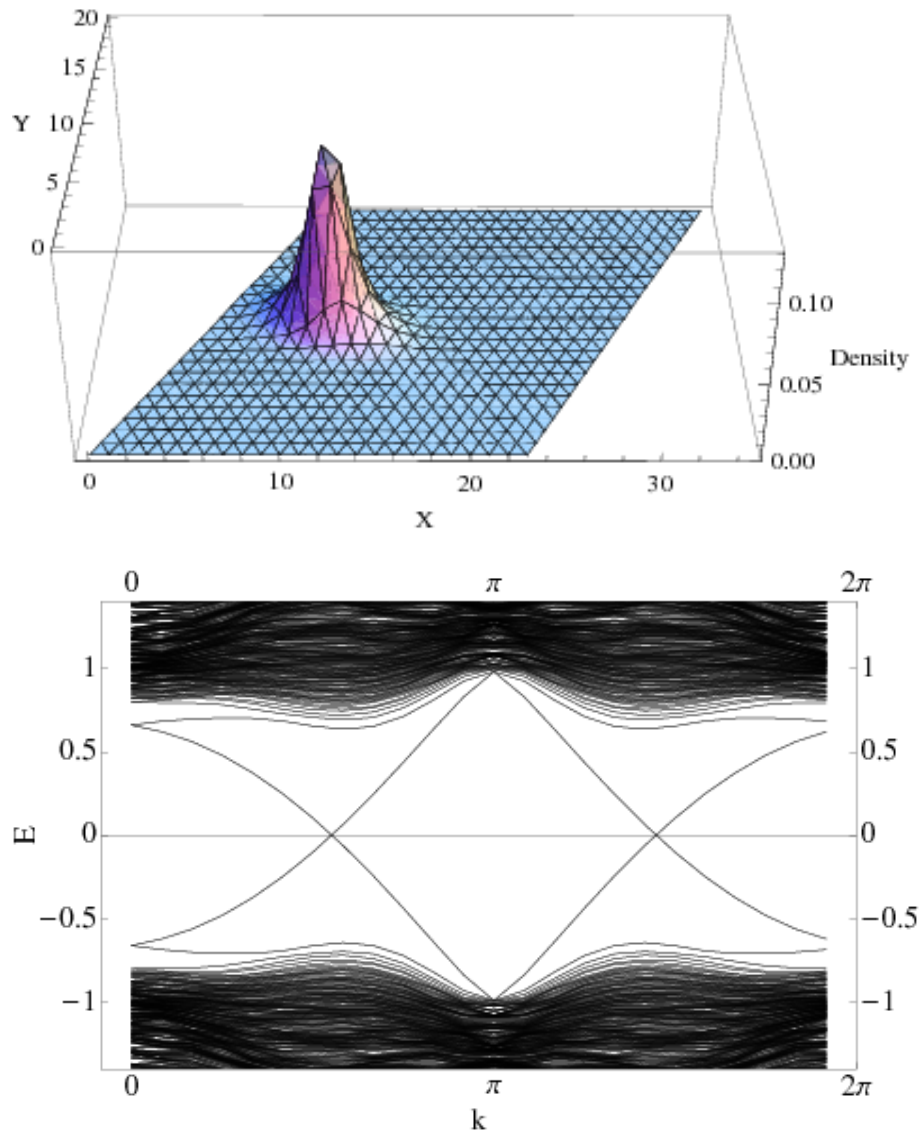


Figure 3.2. Up: The density distribution of a midgap mode ( $k = 1.05, E = 0.25$ ) in the  $\vec{a}_1, \vec{a}_2$  plane, the mode is well localized at the  $l = 1$  vortex, the other state ( $k = 1.05, E = -0.25$ ) is well localized at the  $l = -1$  antivortex; Down: Electronic spectrum of diamond lattice strong TMI along  $p_z$  in the presence of a pair of defects. The parameters used in the Hamiltonian are  $t = 1.0$ ,  $\delta t = 1.0$ , and  $\lambda_{SO} = 0.125$ .

is inserted through the cylinder, an additional Berry's phase of  $\pi$  is now acquired by the electrons. This ultimately results from the rotation of the electron's spin by  $2\pi$ , on following the texture. With this additional phase, the zero angular momentum mode is allowed, and a low energy propagating mode results when the cylinder radius is shrunk to zero. These are the topologically protected one-dimensional modes in the core of the defect. Note, since we are establishing the presence of a topologically protected excitations, it is sufficient to use a simple Dirac dispersion for the surface states of the STI, since a general surface state can always be adiabatically mapped to it. We first describe the surface Dirac hamiltonian in the presence of curvature, and apply this to the case of a cylinder with a defect inserted through it.

*Dirac Theory on a Curved Surface:* On a flat surface, spanned by the unit vectors  $\hat{n}_1, \hat{n}_2$ , the surface Dirac Hamiltonian for a strong TI can be taken as:

$$H_{\text{flat}} = \sigma_{\tilde{1}} \hat{n}_1 \cdot \vec{p} + \sigma_{\tilde{2}} \hat{n}_2 \cdot \vec{p} \quad (3.5)$$

where we assume for simplicity that the spin lies in the same plane, with a relative angle of  $\theta$  to the momentum, hence  $\sigma_{\tilde{1}} = (\hat{n}_1 \cos \theta + \hat{n}_2 \sin \theta) \cdot \vec{\sigma}$  and  $\sigma_{\tilde{2}} = (\hat{n}_2 \cos \theta - \hat{n}_1 \sin \theta) \cdot \vec{\sigma}$ . Note, for  $\theta = 0$  this reduces to  $H = \vec{p} \cdot \vec{\sigma}$ , as in Ref. [40]. In general, the  $\sigma$  matrices involve both spin and sublattice degrees of freedom, but the essential physics is captured by taking them to be simply spin matrices.

On a curved surface there should be additional terms due to the curvature. The effective Hamiltonian can be systematically derived[166], as described in Appendix A. Here we just present the result in the general case when the radii of curvature along the two tangent directions  $\hat{n}_1, \hat{n}_2$  are  $R_1, R_2$  respectively (which are defined via  $(\hat{n}_i \cdot \vec{p}) \hat{n}_j = i\hbar \delta_{ij} \hat{n}_1 \times \hat{n}_2 / R_i$  for  $i = 1, 2$ ):

$$\begin{aligned} H_{\text{curved}} &= \sigma_{\tilde{1}} \hat{n}_1 \cdot \vec{p} + \sigma_{\tilde{2}} \hat{n}_2 \cdot \vec{p} \\ &+ \frac{\hbar}{2} \left( \frac{1}{R_1} + \frac{1}{R_2} \right) [\sin \theta + i \cos \theta (\hat{n}_1 \times \hat{n}_2) \cdot \vec{\sigma}] \end{aligned} \quad (3.6)$$

We now apply this result to the problem of surface states on the cylindrical surface of radius  $R$  with axis along  $\hat{z}$  and radius  $R$  with strong TMI outside and vacuum inside (see Figure 3.3). We use cylindrical coordinates  $z, \phi$ , hence  $\hat{n}_z = (0, 0, 1)$  and  $\hat{n}_\phi = (-\sin \phi, \cos \phi, 0)$ ,  $\hat{n}_r = -\hat{n}_z \times \hat{n}_\phi$  the two radii of curvature  $R_1 = \infty, R_2 = R$ . For simplicity we consider  $\theta = 0$ . The effective Hamiltonian in the absence of a defect is:

$$H_0 = (\hat{n}_z \cdot \vec{\sigma}) p_z + (\hat{n}_\phi \cdot \vec{\sigma}) p_\phi + \frac{\hbar}{2R} i \vec{\sigma} \cdot \hat{n}_r \quad (3.7)$$

where  $p_z = -i\hbar \partial_z$  and  $p_\phi = -i\frac{\hbar}{R} \partial_\phi$ . We can solve for the energies  $H_0 \psi = E \psi$  by first performing the unitary transformation  $\psi = U_z(\phi) \psi'$  where  $U_z(\phi) = e^{-i\phi \sigma_z / 2}$ . Note, since  $U_z(\phi + 2\pi) = -U_z(\phi)$ , the new wave functions  $\psi'$  satisfy antiperiodic boundary conditions. The transformed Hamiltonian  $H'_0 = p_z \sigma_z + p_\phi \sigma_y$  has eigenvectors  $\psi' = e^{ikz} e^{in\phi} \chi$ , where  $\chi$  is a fixed spinor. The energy eigenvalue  $E$  then satisfies:

$$E_n^2(k) = \hbar^2 (k^2 + n^2 / R^2) \quad (3.8)$$

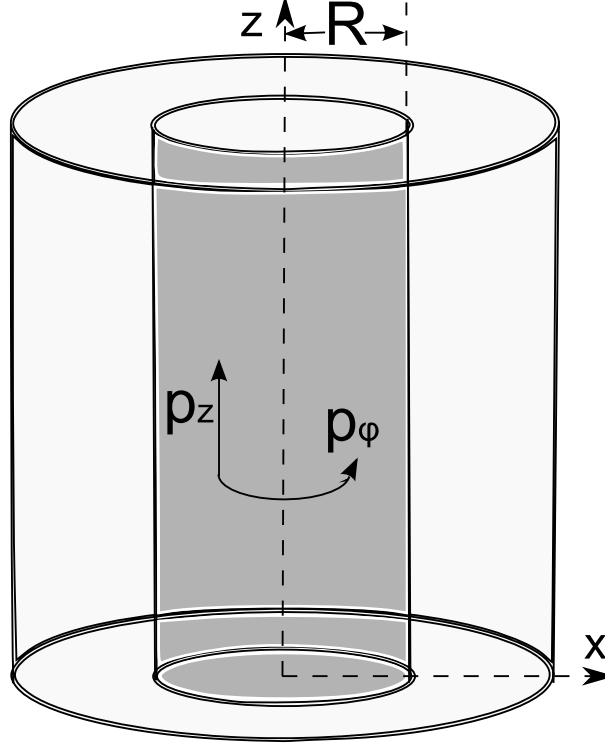


Figure 3.3. Illustration for the model on an effective Hamiltonian on a curved surface we study. The radius of the cylinder is  $R$  with strong TMI outside and vacuum inside.  $p_z$  and  $p_\phi$  are momentum along  $\hat{z}$  and the azimuthal direction, respectively.  $\theta$  is the angle between  $\vec{\sigma}'$  and  $\vec{p}$ .

now, due to the antiperiodicity of the  $\psi'$ , we require  $n + \frac{1}{2}$  to be integer. Hence,  $E_n(k)$  in Eqn. 3.8 above, all correspond to massive Dirac dispersions whose mass increases as  $R \rightarrow 0$ .

We now consider introducing a texture in the order parameter. A strength ‘l’ is readily introduced by the spin rotation  $U_z(l\phi)$ . The Hamiltonian then is:

$$H_l = U_z^\dagger(l\phi) H_0 U_z(l\phi) \quad (3.9)$$

The eigenstates  $\psi$  of  $H_l$  can be obtained by the unitary transformation  $\psi = U_z([l-1]\phi)\psi'$ , and the transformed Hamiltonian for the wave functions  $\psi'$  is identical to  $H'_0$  above. The energy eigenvalues are then given by Eqn. 3.8. However, the crucial difference is that the single valuedness property of the wave function now requires  $n + \frac{l-1}{2}$  to be an integer. Hence, for odd values of  $l$ , when the topologically nontrivial defect is present, an  $n = 0$  solution is allowed. The dispersion of this mode is  $E_0(k) = \pm k$ , hence there is a up and down moving mode, that survives at low energies even when  $R \rightarrow 0$ .

The physical picture is: on the surface of a cylinder the momentum  $p_\phi$  is quantized according to boundary condition and the inter-level spacing is proportional to  $R^{-1}$ . Also, because of the spin-momentum relation, when electron circles about the line defect it picks up a Berry phase of  $(l+1)\pi$  when the vortex winding number is  $l$ . When the total phase is an integer multiple of  $2\pi$  it enforces periodic boundary condition, otherwise anti-periodic

boundary condition is applied and the quantized  $p_\varphi$  will miss the origin. As we shrink the cylinder radius to zero, all quantized  $p_\varphi$  will diverge except  $p_\varphi = 0$ . Therefore, with time reversal symmetry a Kramers pair of line modes exist when  $l$  is odd and its dispersion only depends on  $p_z$ . Also, the distinction between the strong TMI and weak TMI can be made clear by the number of surface modes. For a weak TMI, there are an even number of surface modes, leading to an even number pairs of line modes with the above reasoning. However, they are unstable against inter-node scattering. In contrast, a strong TMI always has an odd number pairs of surface modes.

### 3.4 Shankar Monopole in Three Dimensions

The line vortex is not the only nontrivial texture in three dimensions. The other texture we study is the Shankar monopole, a mapping  $S_3 \rightarrow SO(3)$  characterized by the homotopy classification  $\pi_3(SO(3)) = \mathbb{Z}$  [161]. Imagine an identical phase faraway from the monopole, where matrix  $\overleftrightarrow{\mathbf{R}}(\hat{n}, \varphi)$  is independent of  $\hat{r}$ , we can identify the infinity of real space  $R_3$  thus obtain  $S_3$ . As an specific example here the  $\overleftrightarrow{\mathbf{R}}$  matrix connecting  $\vec{p}$  and  $\vec{\sigma}$  is  $\overleftrightarrow{\mathbf{R}}(\hat{r}, r) = \exp(i\theta(r)\hat{r} \cdot \hat{J})$ , where  $\hat{r}$  and  $r$  are the directional vector and distance from the origin to the site linking  $i$  and  $j$ , and  $\hat{J}$  are classical rotation generators in three dimensions. The rotation axis  $\hat{n} = \hat{r}$ , and the rotation angle is  $\theta(r)$ , a function 0 at the origin and smoothly increases to  $2l\pi$  ( $l \in \mathbb{Z}$ ) at infinity. The homotopy class  $\pi_3(SO(3))$  is described by integer  $l$ , suggesting the base manifold wraps the target manifold  $l$  times. It is protected against any continuous deformation. This is a zero dimensional defect so the localized states should be localized charge at the monopole, if any.

However, numerical results show this topological defect does not carry localized states even in the strong TMI phase. We studied a single monopole at the center of a  $32^3$  unit cell system. To treat the large system size we found a way to sidestep a complete diagonalization of the spectrum. Instead, we estimate the boundaries of the energy eigenstates using ARPACK (Arnoldi Package), and shift the spectrum so that all states below (above) the band gap are at negative (positive) energies. Then, we only need to look at the difference in the number of negative and positive energy eigenvalues, to determine the monopole charge. This can be done via an efficient  $LDL^T$  factorization, where the Hamiltonian is factorized into a lower triangular matrix  $L$  and a diagonal matrix  $D$ . The entries of the diagonal matrix preserves the sign of the eigenvalues, but not their magnitude. Counting the number of positive and negative eigenvalues is then readily accomplished. While smaller system sizes sometimes show charged monopoles, at the largest sizes, they are found to be neutral. We conclude that the Shankar monopole texture does not carry charge in the TMI phase.

### 3.5 Topological Mott Insulator in an Extended Hubbard Model on Diamond Lattice

We now discuss the question of realizing the three-dimensional TMI phase beginning with a microscopic model with full SRS. We consider an extended Hubbard model on the diamond lattice within mean field theory. As always, the results of such a mean field treatment should be treated with caution especially since strong interactions are involved. Nevertheless, we use this analytically tractable approach to obtain a range of parameters where the TMI phase is stabilized over the other obvious candidate phases - the disordered semi-metal, antiferromagnetic insulator or spin density wave (SDW) and the charge density wave (CDW). Realizing the three-dimensional TMI which completely breaks SRS spontaneously, requires, in mean field theory, further neighbor repulsion (between second than third nearest neighbors) as well as a small antiferromagnetic coupling between second neighbors, as shown in Figure 3.5.

We now discuss the details of this mean field treatment. The model Hamiltonian we study is an extended Hubbard model on a three-dimensional diamond lattice at half filling (Figure 3.4):

$$H = - \sum_{\langle ij \rangle, \sigma} t (c_{i\sigma}^\dagger c_{j\sigma} + h.c.) + U \sum_i n_{i\uparrow} n_{i\downarrow} + \sum_{ij} V_{ij} \rho_i \rho_j + J \sum_{\langle\langle ij \rangle\rangle} \vec{S}_i \cdot \vec{S}_j \quad (3.10)$$

where  $t$  is the nearest neighbor hopping strength,  $J$  is the second nearest-neighbor antiferromagnetic coupling strength between spins  $\vec{S}_i = c_i^\dagger \vec{\sigma} c_i$ , and  $V_{ij} = V_2$  for second nearest-neighbor repulsion,  $V_{ij} = V_3$  for third nearest-neighbor repulsion while  $U$  is the onsite repulsion strength. All of these operate within the same sublattice as can be seen from Figure 3.4. For simplicity, we assume no nearest neighbor interaction:  $V_1 = 0$ ; however, as long as  $V_1$  (or fourth-nearest neighbor repulsion  $V_4$ ) is not so large that a nearest-neighbor CDW becomes energetically favored, they can be included but will be irrelevant to our mean field results. We neglect further neighbor interactions.  $n_{i\sigma} = c_{i\sigma}^\dagger c_{i\sigma}$  is the number operator on site  $i$  for spin  $\sigma$ , and  $\rho_i = n_{i\uparrow} + n_{i\downarrow} - 1$ . Note the Hamiltonian has full  $SU(2)$  SRS.

Without repulsive interaction the system is in a semi-metal phase with gapless excitations along lines in the Brillouin zone ('Dirac lines') and a vanishing DOS at the Fermi level. We turn on interactions and investigate possible phases including the TMI, second and third nearest neighbor CDW insulators, and nearest-neighbor SDW insulator. Note, the diamond lattice is composed of a FCC Bravais lattice, plus a two site basis that forms the two sublattices. The natural SDW phase has alternating spin densities on two sublattices, resulting from the effective antiferromagnetic coupling from nearest neighbor hopping and  $U$ . Note, this is a  $q = 0$  order, i.e. preserves lattice translations. In contrast, the likely CDW orders resulting from second and third neighbor repulsion break translation symmetry within each sublattice. The phases can be mapped to a three-dimensional Ising model on an FCC lattice[134], and both the second and the third nearest neighbor CDWs has the same

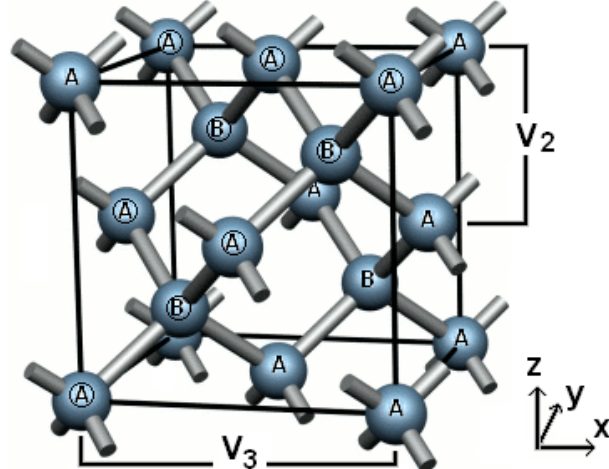


Figure 3.4. A three-dimensional plot of diamond lattice. Each unit cell contains two sublattices, denoted by  $A$  and  $B$  respectively, which each forms an FCC crystal. The repulsive interactions  $V_2$  and  $V_3$  between the second neighbor and third neighbor are shown. They are both between the atoms of the same sublattice.

charge density distribution for two sublattices but nonuniform distribution from unit cell to unit cell. Finally, in the TMI phase one develops second nearest-neighbor correlations  $\langle c_{i\sigma}^\dagger c_{j\sigma'} \rangle \sim i\vec{\sigma}_{\sigma\sigma'} \cdot (\vec{d}_i \times \vec{d}_j)$  that mimic the SOI and breaks the  $SU(2)$  symmetry completely. Within the mean field approximation we solve the ground state energy for each phases in the following, and the resulting phase diagram with fixed  $J = 0.3t$  is shown in Figure 3.5. Note there is a TMI phase in the center.

We now discuss the mean field energetics of these phases in more detail.

(i) *Semimetal*: For relatively weak interactions, the semimetal phase arising from the nearest neighbor hopping model on the diamond lattice remains stable due to the vanishing density of states at the Fermi energy. This phase retains all symmetries of the Hamiltonian.

(ii) *Spin Density Wave* In the limit of large onsite repulsion  $U$  the SDW phase with opposite spin on the two sublattices is stabilized. More precisely, if  $U - 24J \gg V_2$ , the SDW phase becomes energetically favorable. Define the order parameter  $\theta$ :

$$\langle c_{i\uparrow}^\dagger c_{i\uparrow} \rangle = \langle c_{j\downarrow}^\dagger c_{j\downarrow} \rangle = \cos^2 \theta, \langle c_{i\downarrow}^\dagger c_{i\downarrow} \rangle = \langle c_{j\uparrow}^\dagger c_{j\uparrow} \rangle = \sin^2 \theta$$

The ground state energy per unit cell is calculated using mean field approximation:

$$E_{SDW} = \frac{U}{2} + \left( \frac{U}{2} - 12J \right) \chi - \frac{1}{L^3} \sum_k \sqrt{(U - 24J)^2 \chi + 4|t(k)|^2}$$

here  $\chi = \cos^2 2\theta$ .  $\chi = 0$  denotes the semimetal phase.  $t(k) = t \sum_{n=1}^4 e^{i\vec{k} \cdot \vec{t}_n}$ ,  $t_n = 1, 2, 3, 4$  are the vector from one atom to its nearest neighbor.  $L$  is the number of points along each direction within the first Brillouin Zone.

(iii) *Charge Density Wave* In the limit of strong further neighbor repulsion  $V_2, V_3$ , a CDW is expected. The problem with just the density repulsion can be mapped to the FCC lattice Ising model. In that context it is known that  $V_2$  will favor a what is called a Type III CDW phase, while  $V_3$  will favor a type II CDW phase[134], described below. The type III CDW phase has Neel state in the (100) plane and frustrated arrangement between neighboring planes which leads to a  $Z_2$  degeneracy per plane; the type II CDW phase can be described as a combination of four independent simple cubic CDWs. The CDW phase is important despite the frustration. As a matter of fact, in Ref. [142] the second nearest neighbor CDW phase, which the authors neglected, will dominate the large  $V_2$  region and the Quantum Anomalous Hall phase can be realized only with inclusion of  $U$ . To suppress the CDW phases, we choose the ratio of  $V_3/V_2$  to be 1/2 so the system is close to the transition between type II and type III CDW phases[134]. Hereafter we fix  $V_3 = V_2/2$ , and point out that the phase diagram is similar without  $V_3$  but the TMI phase will generally occur at a larger  $U$  region.

Assuming inversion symmetry and SRS are intact, we define order parameter  $\rho$  for type III CDW phase:

$$\langle c_{1\sigma}^\dagger c_{1\sigma} \rangle = \langle c_{2\sigma}^\dagger c_{2\sigma} \rangle = \frac{1+\rho}{2}, \langle c_{3\sigma}^\dagger c_{3\sigma} \rangle = \langle c_{4\sigma}^\dagger c_{4\sigma} \rangle = \frac{1-\rho}{2}$$

where footnote 1 and 3 are on the first sublattice of two neighboring unit cells and footnote 2 and 4 are on the second sublattice and  $\sigma$  is the spin index. The energy per original unit cell is:

$$E_{CDW} = 3V_2\rho^2 + U(1 - \rho^2)/2 - \frac{2}{L^3} \sum_k \sqrt{g_1^2 + |g_2|^2 + |g_3|^2 \pm \sqrt{4g_1^2|g_2|^2 + (g_2g_3^* + g_2^*g_3)^2}}$$

where  $g_1 = (3V_2 - U/2)\rho$ ,  $g_2 = t(1 + e^{i\vec{k}\cdot\vec{a}_1})$ ,  $g_3 = t(e^{i\vec{k}\cdot\vec{a}_2} + e^{i\vec{k}\cdot\vec{a}_3})$ , and  $\vec{a}_i$  are the lattice vectors for the FCC lattice. The momentum summation is over  $L^2/2$  points of the unit cell doubles. The CDW instability is signalled by a non-zero  $\rho$ .

(iv) *Topological Mott Insulator* More importantly, similar to the QSH phase in two dimensions[142], at intermediate couplings the TMI phase is favored, with order parameters:

$$\langle c_{is}^\dagger c_{js'} \rangle = i(\vec{\chi}_{ij} \cdot \vec{\sigma})_{ss'} = i|\chi| \begin{pmatrix} \cos \theta_{ij} & \sin \theta_{ij} e^{-i\varphi_{ij}} \\ \sin \theta_{ij} e^{i\varphi_{ij}} & -\cos \theta_{ij} \end{pmatrix}$$

where  $i, j$  are second nearest neighbors. Our mean field ansatz assumes for simplicity that all  $\vec{\chi}_{ij}$  have the same magnitude but their directions are arbitrary and described by the angles  $\theta_{ij}$  and  $\varphi_{ij}$ . Note  $\vec{\chi}_{ij} = -\vec{\chi}_{ji}$  for Hermiticity. Lattice translation, rotation and inversion symmetries are also considered to be intact. This implies that the order parameters on the

other sublattice are the negative of these. We decouple the Hamiltonian:

$$H = \frac{UL^3}{2} + 24L^3(V_2 - J)|\chi|^2 - \sum_k \left( t(k) c_k^\dagger I_\sigma \otimes \tau^- c_k \right. \\ \left. + h.c. \right) - \sum_{k, \vec{d}_{ij}} 2(V_2 - J)|\chi| \sin \left( \vec{k} \cdot \vec{d}_{ij} \right) \\ \left[ \cos \theta_{ij} \left( c_k^\dagger \sigma^z \otimes \tau_z c_k \right) + \sin \theta_{ij} \left( e^{i\phi_{ij}} c_k^\dagger \sigma^+ \otimes \tau_z c_k + h.c. \right) \right]$$

where the summation is over the two occupied bands.  $\vec{d}_{ij}$  are the vector from on site to its six second nearest neighbors(one for each opposite pair). We then obtain the ground state energy per unit cell:

$$E_{TMI} = \frac{U}{2} + 24(V_2 - J)|\chi|^2 \\ - \frac{2}{L^3} \sum_k \sqrt{\left| t(k) \right|^2 + 4(V_2 - J)^2 |\chi|^2 \left| \sum_{\langle\langle ij \rangle\rangle} \sin \left( \vec{k} \cdot \vec{d}_{ij} \right) \hat{\chi}_{ij} \right|^2}$$

where  $\hat{\chi}_{ij} = (\sin \theta_{ij} \cos \phi_{ij}, \sin \theta_{ij} \sin \phi_{ij}, \cos \theta_{ij})$ .

It is straightforward to see that the energy only depends on  $|\chi|$  and the relative angles between  $\vec{\chi}_{ij}$ . Under global rotation to all  $\vec{\chi}_{ij}$  the energy remains invariant and directly leads to an  $SU(2)$  degeneracy.

This is not a TMI phase in the strict sense, since there are dirac nodes at the Fermi level. However, an arbitrarily small distortion of the lattice will introduce anisotropy of nearest neighbor hopping strengths  $t_{dist}(k) = \sum_{n=1}^4 t_n e^{ik \cdot \vec{t}_n}$  and an effective mass that leads to a gap of size  $\delta t$  [41]. In the simplest case that one nearest neighbor hopping strength is different from the other three  $t_{dist}(k) = t(k) + \delta t$ , a stronger bond  $\delta t > 0$  will lead to a strong TMI phase while a weaker bond  $\delta t < 0$  will lead to a weak TMI phase.

*Phase Diagram:* For each phase, we search for the global minimum with respect to its order parameters and compare different phases. Numerical evaluation of energies was done on a Brillouin zone with  $40 \times 40 \times 40$   $k$  space points. For simplicity we present the phase diagram with a fixed next nearest antiferromagnetic coupling strength  $J = 0.3t$ , and  $V_3 = 0.5V_2$  (Figure 3.5). The semimetal phase exists at small  $U$  and  $V_2$  region; the CDW phase occurs at large  $V_2$ ; the SDW phase occurs at large  $U$ . Most importantly, there is a TMI phase in the center of the phase diagram.

This TMI phase has second nearest neighbor correlation similar to that arising from SOIs in the Fu-Kane-Mele model on the same lattice[41], except for an arbitrary  $SU(2)$  spin rotation,  $\hat{\chi}_{ij} \sim \overleftrightarrow{\mathbf{R}} \cdot (\vec{d}_i \times \vec{d}_j)$  for each second nearest neighbor pair  $i$  and  $j$ , where  $\vec{d}_i$  and  $\vec{d}_j$  are nearest neighbor bond vectors connecting this pair of sites, and  $\overleftrightarrow{\mathbf{R}}$  is an arbitrary constant three-dimensional rotation matrix.

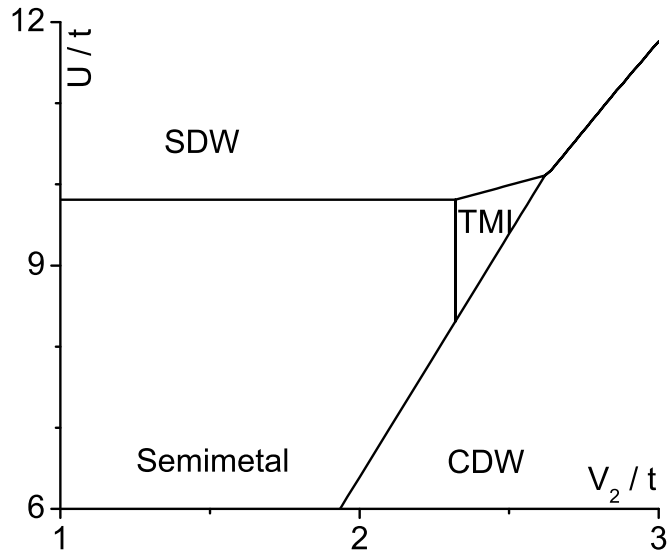


Figure 3.5. Phase diagram for an extended Hubbard model on three-dimensional diamond lattice. The phase transitions from semimetal to SDW, CDW and TMI are all second order transitions. Other parameters are  $V_3 = V_2/2$  and  $J = 0.3t$ . The system size is  $L = 40$  for calculation.

If we further increase  $J$  the stability of the TMI phase is enhanced and it now a wider parameter range. However, at still larger values, a different TMI phase, that breaks lattice symmetries is realized via a continuous transition. However, since this occurs in the very large  $U$  regime, where mean field theory may not be accurate, we do not present further details of this phase.

## 3.6 Towards Experimental Realizations

An experimental realization of the TMI phase must contend with two challenges. First, the system should have weak intrinsic spin-orbit coupling, but strong interactions. Next, the further neighbour repulsion should be substantial compared to the nearest neighbor interactions. We believe these difficulties can be overcome in cold atom system, where intrinsic spin orbit couplings are irrelevant, if particles with electric multipole moments are confined to optical lattice sites. We first discuss a two-dimensional example involving electric dipoles, for which a fairly definite experimental setup can be constructed. Although the phase realized here is two-dimensional and does not break SRS completely (a  $U(1)$  spin rotation remains unbroken), it illustrates how the necessary ingredients can be assembled.

Subsequently we discuss ideas for realizing the three-dimensional TMI, the main subject of this chapter, using electric quadrupole moments.

*Two-dimensional Case: Electric Dipoles on a diamond lattice layer* Dipole-dipole interactions between hetero-nuclear polar molecules, such as Rb<sub>87</sub> and K<sub>40</sub> have already been shown to be strong[118, 125]. Consider a fermionic spin 1/2 molecule, with an electric dipole moment (which is independent of the spin) confined to the sites of an optical lattice. We note here that the diamond lattice has a special property that if the dipole-moment is along the [100] directions, then the nearest neighbor interaction  $V_1$  vanishes. Thus, the second nearest neighbor interaction  $V_2$  becomes dominant. However, the difficulty is that within the twelve second nearest neighbors, only interactions between neighbors within a plane perpendicular to the dipole moment are repulsive. This problem can be solved if we restrict the molecules within a two-dimensional (111) layer of the diamond lattice (still contain both sublattices and essentially two layers of triangular lattices), as the sites circled in Figure 3.4. Then if the dipole moment is perpendicular to the plane all possible nearest neighbor interactions are repulsive.

We solve for the mean field phase diagram of this model, as was done previously for the three-dimensional case. Note, since the lattice is essentially the honeycomb lattice, this is essentially the model studied in Ref. [142]. There exists a two-dimensional TMI phase at the center of the  $U - V_2$  phase diagram (Figure 3.6). Note this phase diagram differs from the same model in Ref. [142] which has an extended two-dimensional TMI phase. This is because we also allow for the second nearest neighbor CDW that the authors neglected. Though frustrated, this order will dominate at large  $V_2$ .

The resulting TMI phase in our case has a second nearest neighbor correlation resembling that of a QSH state and SU(2) SRS is only broken down to U(1). The resulting order parameter will be  $SU(2)/U(1) = S_2$  instead of  $SU(2)$ . Since  $\pi_1(S_2) = 0$  there are no point topological defects - however skyrmions acquire a charge  $2e$  in this phase. Note, the parameters in the phase diagram seem rather accessible for dipolar molecular systems in this setup, assuming that the onsite  $U$ , which results from a combination of dipolar and microscopic interactions, is not too large.

*three-dimensional TMI: Electric quadrupoles on a distorted diamond lattice.* We now discuss some ideas for realizing the three-dimensional TMI. While these are not as straightforward as the ones discussed earlier, we nevertheless offer them as one avenue that presents itself at the current time. Another possible origin of repulsive interaction is the quadrupole-quadrupole interaction. One can show that for two parallel uniaxial quadrupoles (quadrupole tensors are identical and diagonal), the interaction is:

$$E = \frac{3Q^2}{r^5} (3 - 30 \cos^2 \theta + 35 \cos^4 \theta) \quad (3.11)$$

where  $Q$  is the electric quadrupole moment,  $r$  is the distance between two quadrupoles and  $\theta$  is the angle between the quadrupole symmetry axis and the direction between the quadrupoles.

From this expression if  $\cos^2 \theta \simeq 0.742$  the quadrupole -quadrupole interaction will vanish. Therefore, assume the quadrupole moment is along the crystal unit cell  $\hat{z}$  axis to retain

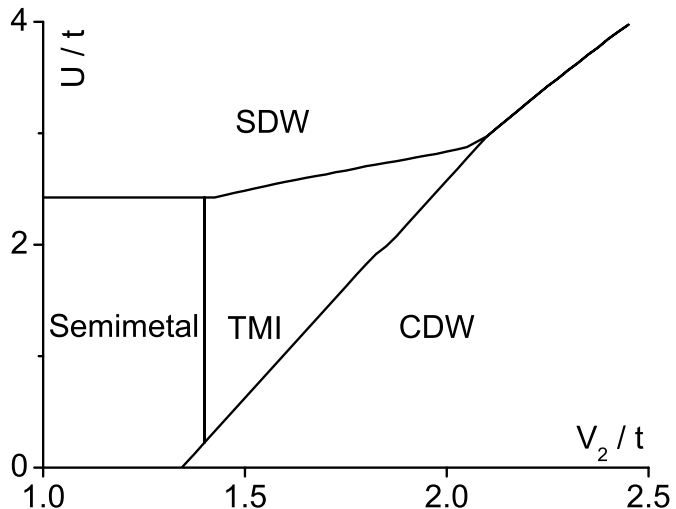


Figure 3.6. Phase diagram for an extended Hubbard model on two-dimensional diamond lattice layer including both sublattices (essentially honeycomb lattice). Note its difference from Ref. [142]. The TMI is limited to the center of the phase diagram and only partially breaks the  $SU(2)$  SRS. The system size is  $L = 40$  for calculation.

as many symmetries as possible, if we elongate the lattice along one direction to make the nearest neighbor satisfy this condition, we will obtain a system where second nearest neighbor interaction dominates. This gives  $c/a \simeq 2.40$ . Note the distortion brings no change to the Hamiltonian we started with. Within this lattice, the ratio between the repulsive interaction from the second nearest neighbor out of the quadrupole perpendicular plane and that from those in plane is  $E_{\perp}/E_{\angle} = 0.945$ . The  $V_2$  anisotropy is reasonably small, thus we believe the physics we discussed with an isotropic  $V_2$  is unchanged. However, in this arrangement,  $V_3$  is rather small.

To give an reasonable estimate of the quadrupole strength necessary to drive the system into a TMI phase, we notice the typical nearest neighbor hopping strength in an cold atom system is of order  $10^{-8} \sim 10^{-6} K$  limited by the cooling temperature and the typical lattice dimension is about the laser wavelength  $0.5 \times 10^{-6} m$ . This leads to a quadrupole of  $10^{-18} \sim 10^{-17} e \cdot m^2$ ,  $e$  is unit charge. This is rather large but maybe realizable in multi-electron molecules. Also, the critical quadrupole moment can be further reduced by lowering the temperature or using lasers with shorter wavelength. Finally, a moderate second nearest neighbor antiferromagnetic coupling may result from second nearest neighbor hopping super-exchange effect. We leave for future work construction of a more realistic setting that can realize the three-dimensional TMI phase.

### 3.7 Conclusion

We have argued that appropriate repulsive interactions can induce a spontaneous SRS breaking state, the TMI, where spin orbit couplings are induced by interactions.

In addition to exotic surface states, line defects of the order parameter are found to carry protected one-dimensional modes along their length in the strong TMI, which provides a bulk signature of this phase.

Also, potential experimental directions towards creating these phases in cold atom system are discussed. An interesting open question is whether the form of the SOIs near a line defect, and hence these protected line modes, can be realized by suitably modifying the atomic structure in a strong topological band insulator.

# Chapter 4

## Anomalous Aharonov-Bohm Conductance Oscillations from Topological Insulator Surface States

### 4.1 Introduction

There has been much recent interest in topological insulators (TIs), three-dimensional solids which are insulating in the bulk but display protected metallic surface states (see Ref. [57, 106, 140] for reviews), in the presence of time reversal ( $\mathcal{T}$ ) invariance. Surface sensitive experiments such as ARPES and STM [57, 106, 140], have confirmed the existence of this exotic surface metal. However, so far there have been no transport experiments verifying the topological nature of the surface states. Besides the fact that bulk impurity bands may contribute significantly to conductivity, the key transport property is the absence of localization when  $\mathcal{T}$  invariance is present. This has been hard to convert into a clear-cut experimental test. Here we discuss a topological feature of TI surface states that can lead to a transport signature.

Consider a wire of topological insulator, with magnetic flux applied along its length. The surface states can be considered a collection of one-dimensional modes, that come in pairs moving up and down the wire. Time reversal symmetry is present at zero flux, and also, approximately for the surface states, when the surface encloses an integer multiple of  $\frac{1}{2}\Phi_0$  ( $= hc/2e$ ) flux quanta. However, there is an important difference between even and odd multiples of  $\frac{1}{2}\Phi_0$ -flux. Odd multiples of  $\frac{1}{2}\Phi_0$ -flux leads to a  $\pi$  Aharonov-Bohm phase for surface electrons, resulting in an odd number of pairs of modes. This one-dimensional state

is topologically protected and cannot be localized with  $\mathcal{T}$  symmetry[73]. In contrast, even multiples of  $\frac{1}{2}\Phi_0$ -flux leads to an even number of modes which are not protected. Thus, with sufficiently strong disorder, even flux leads to a fully localized state for a long wire while odd flux leads to a metallic state whose conductance approaches  $2e^2/h$ , under ideal conditions. Interestingly, as discussed below, a crucial component of this even-odd effect is a surface curvature induced  $\pi$  Berry's phase. Throughout we assume low temperatures so the thermal dephasing length exceeds the sample dimensions.

Note, this oscillatory dependence has a flux  $hc/e$  period, in contrast to Aharonov-Altshuler-Spivak (AAS) oscillations which have period  $hc/2e$ . There has been much discussion on the question of  $hc/e$  vs  $hc/2e$  oscillations, in mesoscopic rings[21, 167, 186] and cylinders[2, 6, 43, 117, 162]. For rings, both periods are observed, the first period is attributed to AB interference of single electrons, and the second to AAS oscillation arising from weak localization effects. However in metallic cylinders, only the  $hc/2e$  period has been experimentally reported [2, 43, 162]. The  $hc/e$  period has been theoretically predicted[6, 117, 167], but always occurs with random sign, i.e. they can peak at either even or odd multiples of  $\frac{1}{2}\Phi_0$ . Therefore an ensemble average tends to wash out this effect, which, according to Ref. [21, 167, 186], is why the  $hc/2e$  effect is more commonly observed.

In contrast, the  $hc/e$  oscillation described here are unique in having maxima always at odd-integer multiples of  $\frac{1}{2}\Phi_0$ , and only occur in strong topological insulators.

A recent experiment on topological insulator  $\text{Bi}_2\text{Se}_3$  nanowires has indeed reported such an anomalous  $hc/e$  flux period[130]. However, there is a crucial difference from the effect described above - the conductivity is found to be minimum at the locations of the predicted maxima. Hence Ref. [130] is presumably observing different physics, explaining which is an interesting open question. The regime described in this chapter is best accessed by going to strong disorder on the surface, or by enhancing the one-dimensional nature of the system, eg. by considering narrower wires. We believe this regime could well be accessed by future experiments of a similar nature.

We first describe the physical ingredients that give rise to this anomalous AB effect, such as curvature induced Berry phase, in clean systems. Subsequently we report the result of numerical experiments on disordered cylinders of topological insulators, realized in a three-dimensional lattice model. Strong disorder is confirmed to expose this anomalous AB effect. The contents contained in this chapter is covered in Ref. [207], and similar results are obtained using an ideal Dirac dispersion with twisted boundary conditions as a simple model of TI surface states experiencing magnetic flux in an independent work[11].

## 4.2 Surface Dirac Theory and Curvature Induced Berry Phase

A single Dirac cone is the simplest model of TI surface states, which naturally invites comparison with graphene, with a pair of Dirac nodes centered at momenta  $\pm K$ , for each spin projection. If scattering between the graphene's nodes are neglected, one might conclude that the topological insulator surface is simply '1/4th' of graphene. Here we point out a topological effect that is special to TI surfaces, connected to the fact that the surface Dirac fermions are sensitive to spatial topology, in the same way as Dirac particles in a curved two-dimensional space. There is no analog of this for graphene, even when it is rolled up into curved structures such as nanotubes and buckyballs.

The root of this difference can be traced back to the physical interpretation of the Dirac matrices. While in graphene, Dirac matrices act on an internal psuedospin space, in topological insulators they act on physical spin, which are locked to the surface orientation. Hence surface curvature introduces new effects in TIs as described in Ref. [206] and Appendix A. In particular, consider an electron circling the cylindrical surface of a topological insulator. Due to the locking of spin to the surface orientation, an additional Berry's phase of  $\pi$  is acquired during such a revolution. The surface modes of a cylinder appear in pairs moving up and down the axis. A consequence of the Berry phase is that there are an even number of these pairs. If modes are labeled by angular momenta  $k_\theta$ , these are quantized to half integers because of the Berry phase. Thus there is no unpaired low energy Dirac mode at  $k_\theta = 0$ . In contrast, in carbon nanotubes, the  $k_\theta = 0$  mode is present and responsible for the metallicity of eg. armchair nanotubes. Now, if an additional Aharonov-Bohm flux of  $\pi$  threads the cylinder of topological insulator, canceling the curvature Berry's phase, one reverts to the regular quantization i.e.  $k_\theta = 0$  is allowed, and hence an odd number of one-dimensional mode pairs are present (see Figure 4.1a,b).

To construct the surface Dirac theory, we first consider generalizing the Dirac Hamiltonian for a flat surface perpendicular to the  $z$  direction  $H = -iv_F\hbar(p_x\sigma_x + p_y\sigma_y)$ , to the case when the surface is curved. We utilize the fact that the surface is embedded in three-dimensional space, so  $\mathbf{r}(x^1, x^2)$  is the three vector defining the surface location, as the coordinates  $x^i$  ( $i = 1, 2$ ) are varied. Then,  $\mathbf{e}_i = \partial\mathbf{r}/\partial x^i$  are tangent vectors. Define conjugate tangent vectors  $\mathbf{e}^i$ , via  $\mathbf{e}^i \cdot \mathbf{e}_j = \delta_{ij}$ , the Kronecker Delta function. Naively, one might guess that the Dirac equation on this curved surface is just:  $H_1 = -iv_F\hbar(\alpha^1\partial_1 + \alpha^2\partial_2)$ , where  $\partial_i = \partial_{x^i}$  and  $\alpha^i = \mathbf{e}^i \cdot \boldsymbol{\sigma}$  are the Pauli matrices along the tangent vectors. However, the actual form is a little more involved, and is most compactly written if we assume  $x^i$  are normal (also called geodesic) coordinates. In these coordinates, (i) the  $\mathbf{e}^i$  are orthonormal  $\mathbf{e}^i \cdot \mathbf{e}^j = \delta_{ij}$ ; and (ii) the derivatives:  $\partial\mathbf{e}^i/\partial x^i$ , are along the surface normal  $\mathbf{e}^3 (= \mathbf{e}^1 \times \mathbf{e}^2 / |\mathbf{e}^1 \times \mathbf{e}^2|)$ . The coefficients of proportionality are the principal curvatures  $\partial\mathbf{e}^i/\partial x^j = -\frac{\delta_{ij}}{R_i}\mathbf{e}^3$ . Such a set of coordinates can always be found locally. In these coordinates it is readily established that there is an additional term:

$$H_D = -iv_F\hbar(\alpha^1\partial_1 + \alpha^2\partial_2) + i\frac{\hbar v_F}{2}\left(\frac{1}{R_1} + \frac{1}{R_2}\right)\beta \quad (4.1)$$

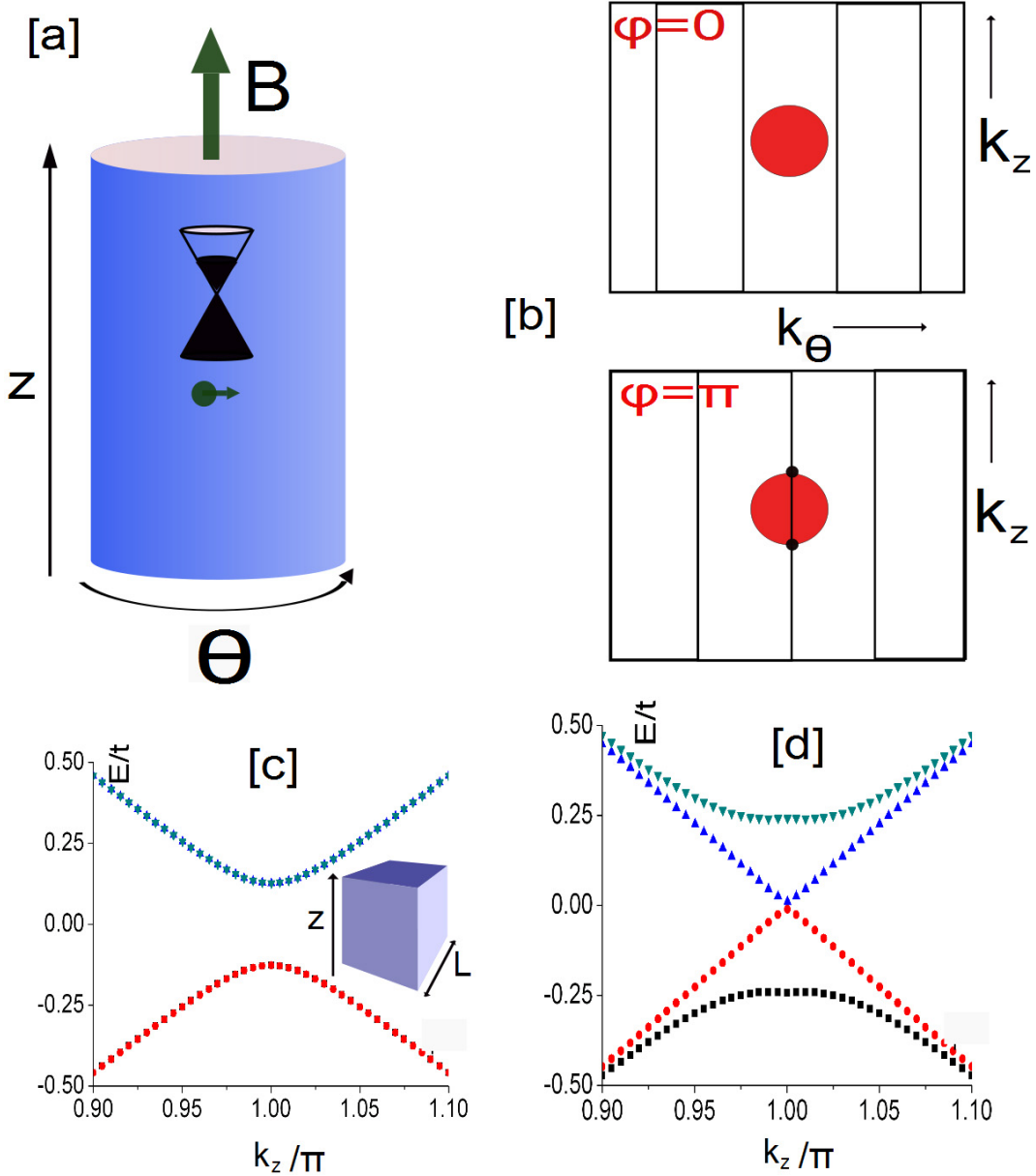


Figure 4.1. (a) proposed geometry, with (weak) magnetic field applied along the wire axis, with flux  $\varphi = 2\pi\Phi/\Phi_0$  enclosed. (b) Quantization of transverse momenta  $k_\theta$  for a cylinder, as a function of applied flux. The shaded area boundary in the Fermi surface. For  $\varphi = 0$ , an even number of one-dimensional mode pairs occurs; but with  $\varphi = \pi$  flux, an odd number of pairs, protected by time reversal symmetry, is expected. Demonstration in a microscopic model: spectrum of a cuboid of clean topological insulator, with cross section 10x10 unit cells (geometry shown in inset), as a function of momentum  $k_z$  along its length. (c) Spectrum for  $\varphi = 0$ , each band shown is doubly degenerate (d) For flux  $\varphi = \pi$ , all modes except the linear one are doubly degenerate; hence an odd number of one-dimensional mode pairs is present.

where  $\beta = \mathbf{e}^3 \cdot \sigma$ . A shortcut to obtaining it is requiring that the Hamiltonian  $H_D$  be Hermitian and also anticommute with the local  $\beta$  matrix (note, the matrices  $\alpha^i$ ,  $\beta$  are space dependent).

A more formal derivation of the same result proceeds from the general form for a Dirac equation in curved space:  $H_D = -i\hbar v_F(\alpha^1 D_1 + \alpha^2 D_2)$ , where  $D_i$  is the covariant derivative along a pair of general coordinates  $x^i$ , defined as  $D_i = \partial_i + \Gamma_i$ , and  $\Gamma_i$  is the spin connection, which here is given by the equation:

$$[\Gamma_i, \alpha^j] = \partial_i \alpha^j + \Gamma_{ik}^j \alpha^k \quad (4.2)$$

where  $\alpha^k = \mathbf{e}^k \cdot \sigma$ , and summation over repeated indices is assumed. The  $\Gamma_{ik}^j$  are the Christoffel symbols. This can be solved explicitly to give the following simple expression:

$$\Gamma_i = -\frac{1}{2}\beta \partial_i \beta \quad (4.3)$$

The Christoffel symbols are defined from the derivatives of the tangent vectors, projected into the tangent plane:  $[\partial_i \mathbf{e}^j]_{\parallel} = -\Gamma_{ik}^j \mathbf{e}^k$  (indices take on values  $\in \{1, 2\}$ ), see Appendix A. Now, we switch to normal coordinates. Clearly, the Christoffel symbols vanish since the derivatives of the tangent vector are now normal to the surface. Thus from Eqn. 4.2 the spin connection is given by  $\Gamma_{1,2} = \pm \frac{i}{2R_{1,2}} \alpha^{2,1}$ , which leads back to Eqn. 4.1. An alternate elegant formalism is developed in Ref. [87], for quantized Hall states.

Now, let us specialize to a cylindrical surface such that  $x^1 = z$  along the cylinder axis and  $x^2 = R\theta$ , where  $R$  is the radius and  $\theta$  is the angle around the cylinder. Now,  $R_1 = \infty$  and  $R_2 = R$ , in Eqn. 4.1. The unitary transformation  $U = e^{i\sigma_z \theta/2}$ , transforms that into the canonical form  $H'_D = -i\hbar v_F(\sigma_z \partial_z + \sigma_y \partial_\theta/R)$ . However, since the unitary transformation changes sign  $\theta \rightarrow \theta + 2\pi$ , the wave functions for the new Hamiltonian satisfy antiperiodic boundary conditions on circling the cylinder. Therefore, only angular momenta  $\hbar(m + 1/2)$  are allowed, where  $m$  is integer. Hence, the zero angular momentum is absent, and there are an even number of one-dimensional modes pairs. Now threading an additional  $\pi$  flux, the periodic boundary conditions are restored, and the parity of the mode pairs is reversed; see Appendix A for a more general argument. Although the cylinder has vanishing Gaussian curvature, a nonzero spin connection leads to the Berry's phase of  $\pi$ . This topological property is also ultimately responsible for metallic dislocation lines[144, 206].

## 4.3 Numerical Experiments on Disordered Topological Insulator Cylinders

We now demonstrate this effect for a lattice model of a strong topological insulator (which is more general than the Dirac approximation). We use the model of Fu-Kane-Mele on the

diamond lattice[41]:

$$H = \sum_{\langle aij \rangle} t_{ij} c_{i\sigma}^\dagger c_{j\sigma} + 8i\lambda_{SO} \sum_{\langle ik \rangle} c_{i\sigma}^\dagger (\hat{\mathbf{d}}_{ik}^1 \times \hat{\mathbf{d}}_{ik}^2) \cdot \sigma s_{\sigma\sigma'} c_{k\sigma'} \quad (4.4)$$

where the  $\hat{\mathbf{d}}_{ik}^{1,2}$  are nearest neighbor unit vectors connecting a pair of second neighbor sites  $ik$ . We choose nearest neighbor hooping to be strong along direction (111) with strength  $t_1 = 2t$  and the remaining three bonds to be of equal strength  $t$  and the spin orbit interaction is taken to be  $\lambda_{SO} = 0.25t$ . These parameters give a strong topological insulator with bulk gap  $\Delta = 2t$ . The 'cylinder' used for the computations is actually parallelepiped, with the long axis  $z$  being along (110), and the cross section axes being along (011) and (101). Symmetry of the diamond lattice relates the surface Dirac nodes along the two distinct surfaces, hence they are at the same energy. A more general situation is when there is no particular relation between the two - however, the topological properties should however remain unchanged, including the anomalous Aharonov-Bohm oscillations.

A long cuboid with cross section  $L \times L$  is taken along the weak index direction of this model, and surface states are labeled by momenta  $k_z$  along the long axis. Note, the single Dirac node at the surface of the long faces is located at  $k_z = \pi$ . This does not affect any of the results since this wavevector is along the propagation direction, and can be ignored. A uniform magnetic flux  $\Phi$  is introduced uniformly through the cross section, denoted in units of the flux quantum:  $\varphi = 2\pi\Phi/\Phi_0$ . The surface spectrum is shown in Figure 4.1. All modes are doubly degenerate except the linearly dispersing mode in Figure 4.1d. Thus, even for small sizes  $L = 10$ , the even-odd mode effect and the gap closing at flux  $\varphi = \pi$  is apparent. While the breaking of time reversal symmetry at this flux implies there is always a gap, this is seen to be very small, and the curves appear  $2\pi$  periodic, so time reversal is approximately a good symmetry at these flux values. Thus, even in the clean limit, metallic behavior appears at odd multiples of  $\pi$  flux, for a carefully tuned chemical potential near the node. However, on raising the Fermi energy, the flux strength with the larger number of modes oscillates between flux zero and  $\pi$ . A robust response however is exposed by the presence of strong disorder, which we discuss next.

We now consider adding disorder only on the surfaces of the model above, via a random onsite potential  $V_i n_i$ , ( $\mathcal{T}$  invariant disorder), where  $n_i$  is the charge density onsite, and  $V_i$  a random variable picked from a box distribution  $[-W, W]$ . We calculate the Greens function for a system composed of  $N$  layers in the  $z$  direction, and transverse size  $L \times L$ , at energy  $E$ :  $G_N(r, r'; E)$ . The position and spin coordinates are lumped into  $r$ . The transport properties of the surface states are characterized by extracting the localization length of the system in the quasi-one-dimensional limit. Subsequently, we will directly calculate the conductivity.

The technical simplification for localization length  $\lambda$  is that it is self averaging and one only needs the Greens function between the first and last layers of the system as the system length is increased:

$$\lambda^{-1} = \lim_{N \rightarrow \infty} \frac{-2}{N} \log(|\mathbf{G}_{1,N+1}^{(N+1)}|^2) \quad (4.5)$$

which is extracted by a linear fit (an example is shown in Figure 4.2a inset) to the logarithm of the Greens function between the first and last layers of a system with  $N+1$  layer denote by

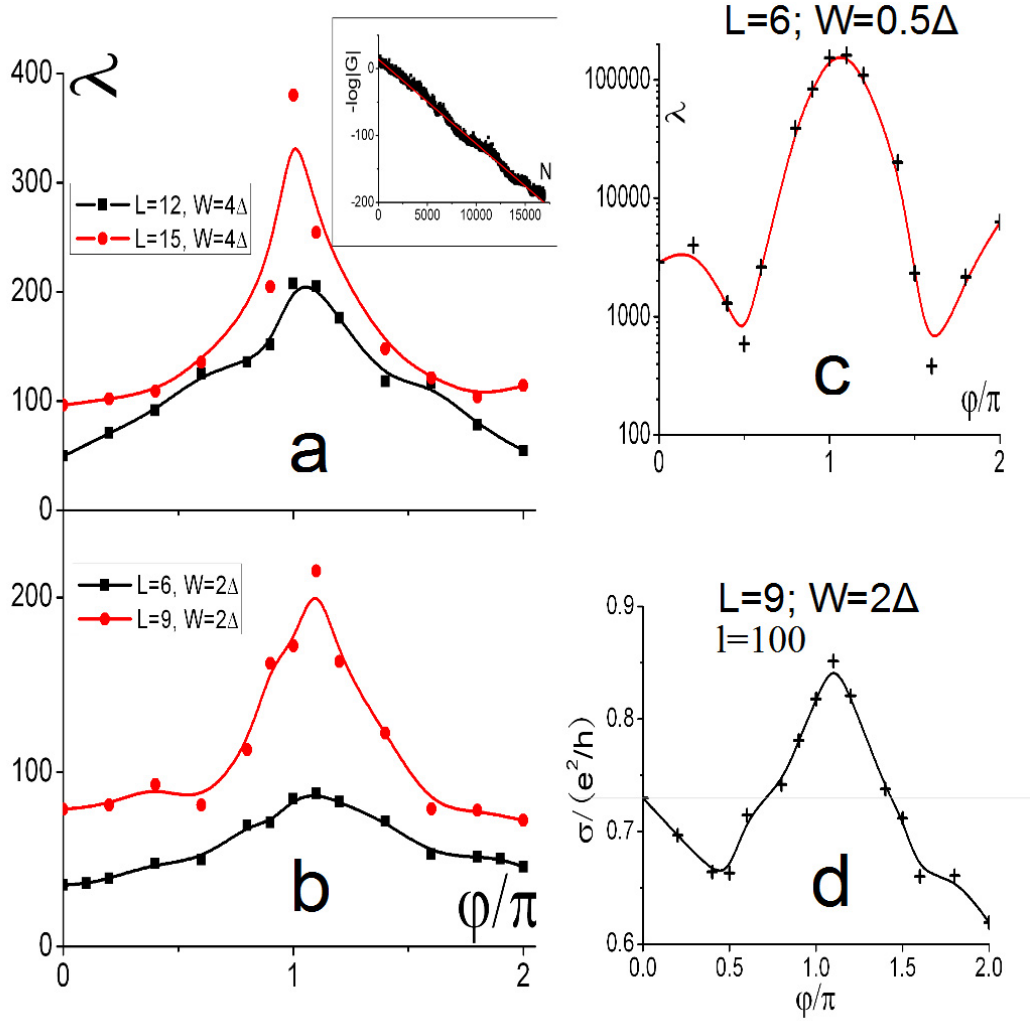


Figure 4.2. (a), (b) and (c): Localization length  $\lambda$  in the quasi-one-dimensional geometry, for different widths  $L$  (measured in unit cells) and disorder strengths  $W$  (in units of the bulk gap  $\Delta$ ). Error bars are smaller than the symbol size. (a) and (b) Strong disorder: variation has flux-period  $hc/e$  and  $\lambda$  is maximum at flux  $\varphi = \pi$ . Inset: Example of the exponential decay of the Green's function used to determine the localization length. (c) Weak disorder: Now, the  $hc/2e$  oscillation period is also apparent and localization lengths are very large (note log scale here). For wires much shorter than the zero flux localization length, the  $hc/e$  period will not be apparent. (d) Conductance Oscillation: Direct measure of conductance oscillation for a wire of length  $l = 100$  and width  $L = 9$ , with strong disorder  $W = 2\Delta$ . Maximum conductance occurs at  $\pi$ -flux.

the matrix  $\mathbf{G}_{1,N+1}^{(N+1)}$ , where the matrix indices refer to sites in the layer, and the energy label is suppressed. It can be efficiently and recursively calculated, assuming only nearest neighbor hopping between layers denoted by the matrix  $\mathbf{t}$  and  $\mathbf{t}^\dagger$ . If the single layer Hamiltonian is  $\mathbf{H}_{N+1}$ , then the Greens function within this layer when attached to the remaining  $N$  layers is[24, 61]:

$$\begin{aligned}\mathbf{G}_{N+1,N+1}^{(N+1)} &= \left[ (E + i\eta) - \mathbf{H}_{N+1} - \mathbf{t}^\dagger \mathbf{G}_{N,N}^{(N)} \mathbf{t} \right]^{-1} \\ \mathbf{G}_{1,N+1}^{(N+1)} &= \mathbf{G}_{1,N}^{(N)} \mathbf{t} \mathbf{G}_{N+1,N+1}^{(N+1)}\end{aligned}\quad (4.6)$$

where the energy label is suppressed. The last equation gives us the desired Greens function.

Results are shown in Figure 4.2, where parameters were chosen to obtain a bulk gap  $\Delta = 2t$ , the hopping strength. System sizes with perimeter  $4L$ , with  $L = 6, 9, 12, 15$  were studied and the quasi-one-dimensional localization length  $\lambda(\varphi)$  was extracted as a function of flux. We consider strong disorder, to obtain a localization length short enough to be measured:  $W = 2\Delta$  for the first two and  $W = 4\Delta$  for the last two sizes. The chemical potential was taken to be near the middle of the gap ( $E = 0$ ), where the Dirac node appears in the clean limit. For these strong disorder strengths, results are nearly independent of chemical potential location inside the bulk gap. As seen in Figure 4.2a,b a clear maximum in localization length is seen near  $\varphi = \pi$ . Note, time reversal is already an approximate symmetry even for the smallest sizes, given the location of the maximum near  $\varphi = \pi$  and the  $\varphi \rightarrow 2\pi - \varphi$  approximate symmetry. However at  $\varphi = \pi$ , localization length is finite, so time reversal symmetry breaking enters here. Clearly, for larger widths the symmetry is more accurate, given the weaker fields prevailing on the surface states. If we denote:

$$g_\varphi = \lambda(\varphi)/4L$$

this ranges from  $g_0 = 1.6$  to  $g_\pi = 6.3$ , as the flux is varied, for  $L = 15$ . Hence, for these parameters, wires with aspect ratios roughly within this range should exhibit conductance oscillations as a function of flux with a maximum at flux  $\pi$ . This is explicitly checked below. We have also checked that the Zeeman splitting induced by the field for these sizes do not affect results qualitatively, if their energy scale  $E_z \leq 0.025\Delta$ , which should be readily satisfied in experiments.

In Figure 4.2c, we plot a system with weak disorder, where  $W = 0.5\Delta$ , and the chemical potential is tuned to  $E = 0.15\Delta$ , where there is a large density of states. The localization lengths are now significantly longer (note the log scale for  $\lambda$ ), and a prominent anti-localization feature is present near flux  $\varphi = \pi/2, 3\pi/2$ . The latter will contribute to an AAS  $hc/2e$  period in conductance oscillations. Since  $g_0 = 125$ , at smaller aspect ratios the system is unaware that there is an even longer localization length at  $\pi$  flux, and the most visible feature is likely to be the  $hc/2e$  AAS oscillations. This illustrates the important role of strong disorder in observing the effect of interest.

Finally, in Figure 4.2d, we present the conductance of a wire with length  $l = 100$ , cross section  $9 \times 9$  and strong disorder strength  $W = 2\Delta$ . The conductance is extracted from the Greens function using the Kubo formula,  $\sigma = \frac{e^2 h}{\pi l^2} \text{Tr} [v_z \text{Im} \mathbf{G} v_z \text{Im} \mathbf{G}]$  with  $v_z = \frac{i}{\hbar} [H, z]$ . The effect of leads is modeled by sandwiching the disordered system between  $4 \times 10^3$  layers

of clean wire on either side. We take  $\mu = 0.15\Delta$ , to obtain a finite density of states in the leads. The localization length for these parameters is close to that in Figure 4.2b, so  $l$  is intermediate between the localization lengths obtained there. A small imaginary part  $\epsilon \sim 5 \times 10^{-4}\Delta$  is inserted in the energy to obtain finite results; results are insensitive to its precise value. Each data point is obtained by averaging log of conductance over 500 samples. Clearly, a conductance maximum at flux  $\pi$  is observed. Note however, the  $hc/2e$  oscillations are more prominent here than in the localization length plots, and the overall contrast in conductance is of order  $0.1e^2/h$ . This will increase for longer wires and wider cross sections, where the effects of  $T$  breaking at  $\pi$  flux are less important, and localization of states away from this flux will set in. While a more extensive conductance analysis is left to the future, these results corroborate the basic picture.

## 4.4 Experimental Realizations

How do these results scale to experimentally relevant system sizes, and in particular will the effects described here survive? As a reference, we note that a  $\text{Bi}_2\text{Se}_3$  nanowires studied in Ref. [130], was 350nm in circumference, and about  $2\mu\text{m}$  in length. While a direct conversion into unit cell lengths is difficult due to the extreme anisotropy of the material, we estimate aspect ratios (length to circumference) between 5-10. The circumferences themselves are about 5-10 times larger in unit cell lengths, than those considered here. While in the truly two-dimensional limit a metallic (symplectic metal) phase is expected, hence  $g(L \rightarrow \infty) \rightarrow \infty$ , this growth is slow. The scaling to larger widths is captured by the beta function  $\beta(g) = d \log g / d \log L$ , similar to the well known beta function for conductance. This function is known for spin-orbit metals in two dimensions[5]. For large  $g$ , the topological insulator surface displays identical behavior[12, 121]; i.e.  $\beta(g) \sim 0.64/g$ . We estimate this to be reasonably accurate for  $g \geq 2$  for TI surfaces, then  $g(\tau L) \approx g(L) + 0.64 \log \tau$ . The localization length ratio for  $\tau = 10$  times wider system compared to the  $L = 15$  case, will be  $g(L = 150) \approx 3.2$  at zero flux , an aspect ratio that is easily exceeded. Note, the localization length at  $\pi$  flux diverges more rapidly, since the effects of  $T$  breaking are weaker at larger widths. It is readily seen that this scales asymptotically as  $\lambda(\varphi = \pi) \sim L^4$  (since the time reversal symmetry breaking strength scales as  $\delta \sim 1/L^2$ , and the localization length for weak  $T$  breaking disorder scales as  $\lambda \sim 1/\delta^2$ ). Thus the oscillatory effects should remain visible at these longer scales, with strong disorder.

In Ref. [130], nanowires of  $\text{Bi}_2\text{Se}_3$  were subjected to a field along their length and an oscillatory dependence of conductance  $O(e^2/h)$  with applied flux was reported. The oscillation period was consistent with surface states sensing a  $hc/e$  flux. However, the conductivity maxima were generally located at integer multiples of the flux quantum, rather than half integer multiples as predicted here. Therefore we believe a different effect is at play there. The main ingredients required to access the  $\pi$  flux effect discussed here is quasi-one-dimensionality and strong disorder. The former can be achieved by studying narrower wires; eg. wires with half the width of those studied were produced in Ref. [130]. For the latter, one is aiming to reduce the metallicity of the surface layer, which in a Drude model is just  $(e^2/h)k_F l$ . This

can be achieved either by decreasing the scattering length  $l$ , via greater surface disorder, or tuning the chemical potential to an energy with smaller carrier density.

## 4.5 Conclusion

We described a topological property of the surface states of TIs. An Aharonov-Bohm phase of  $\pi$  strengthens the metallic nature of surface states, leading to a clear-cut transport signature. Conductance oscillations with flux are expected in nanowires of topological insulator, with maxima at odd-integer multiple of  $\frac{1}{2}\Phi_0$ . The key requirements for observing this effect are quasi-one-dimensionality and strong disorder, which we believe are achievable given current experimental capabilities.

# Chapter 5

## Quantized Response and Topology of Magnetic Insulators with Inversion Symmetry

### 5.1 Introduction

Certain electromagnetic phenomena in insulators are insensitive to details about the material. They result from a) symmetry or b) topology of the bands (or the indecomposability of the insulator into separate atoms). The Quantum Hall effect is a striking example - in a strong magnetic field, a two-dimensional gas of electrons becomes insulating but has a Hall current when an electric field is applied:  $J_H = \sigma_H E$  with  $\sigma_H = Ne^2/h$  quantized. The Hall coefficient is usually connected to the filling fraction of Landau levels, but the more general explanation is that it is related to the topology of the band structure of the electrons. Thus it is unchanged by continuous changes in the crystal lattice. The same effect can occur in a two-dimensional material where the applied magnetic field is replaced by electromagnetic interactions of the electrons and nuclei.

A real class of materials with time-reversal symmetry known as topological insulators exhibit similar topological phenomena[57, 106, 141]. They have “protected” surface states and a “magnetoelectric response”[32, 138], in which an applied electric field induces a magnetization  $M = \theta \frac{e^2}{2\pi h} E$ . The magnetoelectric response may be observed only if there is a gap on the surface as well as in the bulk, so the “chiral” surface states must be eliminated by coating a magnetic material or doping the bulk to move the Fermi energy into the band gap[22].

If the material were spontaneously magnetically ordered, one would also be able to observe the magnetoelectric effect. However, materials that break time reversal symmetry in the bulk tend to have a small value of  $\theta$ [59]. The origin of the large  $\theta$  in a topological insulator is related to the time reversal symmetry: the allowed values of  $\theta$  are quantized because time-reversal takes  $\theta \rightarrow -\theta$ ; this seems to rule out a nonzero  $\theta$ , but since  $\theta$  is only defined modulo  $2\pi$ , 0 and  $\pi$  are both compatible with the symmetry.

In this chapter, we will focus on magnetically ordered materials with spatial symmetries that keep  $\theta$  large, especially the inversion ( $\mathbf{r} \rightarrow -\mathbf{r}$ ) symmetry common in magnetic insulators. For example, all Bravais lattices are inversion symmetric. Inversion transforms  $\theta$  the same way as time reversal does, so  $\theta$  will have two possible values 0 and  $\pi$  as well. Since  $\theta$  is quantized, there should be a simple rule for determining its value, and we show that the formula of Fu and Kane[39] generalizes to the case with magnetic order, where time reversal symmetry is absent. Antiferromagnetic phases with magnetic symmetry groups can also be classified using a similar approach[103].

Rather than focussing solely on the magnetoelectric effect, we study a more general question: “Which phenomena in topological insulators can be determined by studying just the symmetry properties of Bloch states at special momenta?” When inversion is the only symmetry, Bloch states at time-reversal invariant momenta (TRIMs) can be classified by their inversion parities, which generalize the notion of the sign  $\pm 1$  picked up by an orbital wave function of a molecule when it is inverted. In an infinite insulator, inversion parities are defined for the Bloch states at TRIMs, which are invariant under the inversion  $\kappa \rightarrow -\kappa$ . In molecules, parity eigenvalues lead mainly to microscopic effects, such as selection rules for transitions. In bulk, however, phenomena on a larger scale can be determined by just these parities[39].

When only inversion symmetry is present, which patterns of the number of odd parity states at the eight TRIMs are permitted after time reversal symmetry breaking and what are the phenomena associated with these parity patterns? We find the following phenomena: first, if the total number of odd parity states at all TRIMs is an odd integer, then the material is not an insulator. Second, if the material is insulating and the number of odd parity states at some individual TRIMs is odd, then the material has either electrostatic polarization or bulk quantized Hall conductivity. Third, if the material is insulating, and the total number of odd parity states is twice an odd integer, then the material must have a magnetoelectric effect of  $\theta = \pi$ .

Here we would like to emphasize the first and the third phenomena, about the non-insulating behavior and the magnetoelectric effect, which may have some interesting experimental implications. If the product of all the TRIM parities is  $-1$ , as the parity assignment in Figure 5.1a, then the material cannot be an insulator. Such a material is likely to be a “Weyl semimetal” and the dispersions for the filled and empty bands have at least two touching points called Weyl points. It may have characteristic thermodynamic and conductivity properties related to its vanishing density of states. Furthermore, it should have interesting quantized responses corresponding to the “chiral anomalies” of field theory[27]. Weyl points cannot occur in a material with both time reversal and inversion symmetry, where the states come in Kramers pairs and the product of the parities is always  $+1$ .

Besides, the formula for  $\theta$  may help the search for materials with a large magnetoelectric effect. It shows that a magnetic material may have a magnetoelectric response but no protected surface states. Furthermore, the formula for  $\theta$  suggests that the magnetoelectric effect can occur in materials with essentially no spin-orbit coupling, but instead with non-planar magnetic order. In these materials, nontrivial band topology is induced by Berry's phases in the hopping amplitudes due to the magnetic order, rather than spin-orbit coupling. Ref. [181] studies whether the magnetoelectric effect and Weyl semimetal behavior may be present in magnetically ordered iridates.

The content of the chapter is the following. We begin with a brief summary of our results in Section 5.2, and explain the various conductivity and response properties constrained by the inversion symmetry of a band structure.

Then in Section 5.3 we systematically present the derivation and look for all response properties that are determined by inversion symmetry. We classify all the phases with inversion symmetry in a similar way to the classification of phases with different Altland and Zirnbauer symmetry groups[78, 156] and identify the phases with interesting quantized dynamical responses with a process of elimination. The outcome of the classification is that all insulators in three dimensions are parameterized by three Chern numbers and a set of inversion parities. Chern numbers are three integers in three dimensions describing topological properties of the Bloch states as a function of momentum, and are present even in the absence of inversion symmetry. The inversion parities can be encapsulated in the eight numbers of odd parity states at each of the TRIMs.

Next, we determine these responses and their relation to the inversion parities in Section 5.4. We derive the criterions that ensure a material non-insulating and an insulator magnetoelectric, as well as relations between parities, Hall conductivity and polarization. Our procedure also implies that these are the only response properties. Although there are infinitely many ways of assigning inversion parities, most of them have no response and can be realized in ionic crystals, where each electron is tightly bound to a single atom. After the ionic portions of the band structures are separated out, only a finite number of phases remain.

In Section 5.5 we give an alternative approach based on entanglement and explain why the relationships between inversion parities and responses usually depend on the numbers of odd parity states modulo 2 or 4. The entanglement spectrum can be derived from the ground-state wave function without perturbing the system into an excited state and consists of a set of modes that behave like physical surface modes. They can give a signature for a topological phase[17, 34, 75, 149, 177]. We give a formula for the number of entanglement modes in an inversion symmetric insulator in terms of the inversion parities and then re-derive some of the electromagnetic properties in a simple fashion. The magnetoelectric effect formula depends on the inversion parities in the same way as Ref. [39], but applies to a wider class of materials, including those that cannot be adiabatically connected to one with time reversal symmetry.

We briefly conclude the chapter in the last section. This chapter is rebuilt from a previously published work in Ref. [176]. Ref. [177] discusses the entanglement spectrum of

inversion symmetric insulators without presenting the relation to TRIM parities. The discussion in this chapter also provides the basis for Ref. [181], where the electronic structure of yttrium iridates is studied using the constraint on the total number of odd parity states and expressions of  $\theta$  in terms of the TRIM parities. The prediction that a material with an odd number of states is metallic also has an interesting corollary, as mentioned in Ref. [111]: if time-reversal symmetry is broken, no general continuous transitions between  $\theta = 0$  and  $\theta = \pi$  insulators can be found, without going through a Weyl semimetal phase.

## 5.2 Summary of Results

Let us first define some crystal lattice conventions. For simplicity, we assume cubic lattice with unit lattice spacing. All quantities will be written with respect to a coordinate system aligned with the crystal axes. The primitive lattice vectors are  $\mathbf{R}_i$  and the reciprocal lattice vectors are  $\mathbf{g}^i$  where  $\mathbf{g}^i \cdot \mathbf{R}_j = 2\pi\delta_j^i$ . It is convenient to translate the results to any lattice by re-interpreting the coordinate system expressions.

As in the study of spectra of small molecules, it is useful to look at inversion parities to study insulators with inversion symmetry. In a bulk material, such parities can determine how electrons move in response to a field and used to be classify the phases, to understand such relationships is the main objective of this chapter. The main technical distinction between solids and molecules is that, the occupied states can be labeled by momentum in solids, given by:  $\psi_{ik}(\mathbf{r}) = u_{ik}(\mathbf{r})e^{i\mathbf{k}\cdot\mathbf{r}}$ . Only states at the TRIMs can be classified by parity under inversion. The TRIMs are the momenta given by

$$\kappa = \frac{n_1}{2}\mathbf{g}_1 + \frac{n_2}{2}\mathbf{g}_2 + \frac{n_3}{2}\mathbf{g}_3 \quad (5.1)$$

where  $n_1, n_2, n_3$  are integers. Such a momentum maps to itself modulo the reciprocal lattice under inversion,  $-\kappa \equiv \kappa$ . Hence the wave functions at  $\kappa$  must be invariant, and their parities can be defined:

$$\mathcal{I}\psi_{a\kappa}(\mathbf{r}) = \eta_a(\kappa)\psi_{a\kappa}(\mathbf{r}) \quad (5.2)$$

Appendix B.1 explains how to determine these parities within a tight-binding model.

We now introduce a key quantity  $n_o(\kappa)$  at every TRIM  $\kappa$ . It is defined as the number of states with odd parities at TRIM  $\kappa$ . They cannot change without a phase transition, at least in a non-interacting system. Besides these eight integers, the quantum Hall conductance gives three more invariant integers:  $\mathbf{G}_H = \frac{e^2}{2\pi\hbar}\tilde{\mathbf{G}}_H$  where  $\frac{\tilde{\mathbf{G}}_H}{2\pi}$  has integer components

For inversion symmetric insulators, the Chern numbers and the  $n_o$ 's can be used to distinguish phases. Furthermore, these 11 integers, together with the total number of occupied bands  $n$ , give a complete description of the set of phases. Any two band structures with the same integers can be tuned into each other a phase transition. This is derived in Section 5.3. Certain physical properties of each phase can be predicted in terms of these integers. We will find all the basic observable quantities that can be expressed in terms of the  $n_o$ 's.

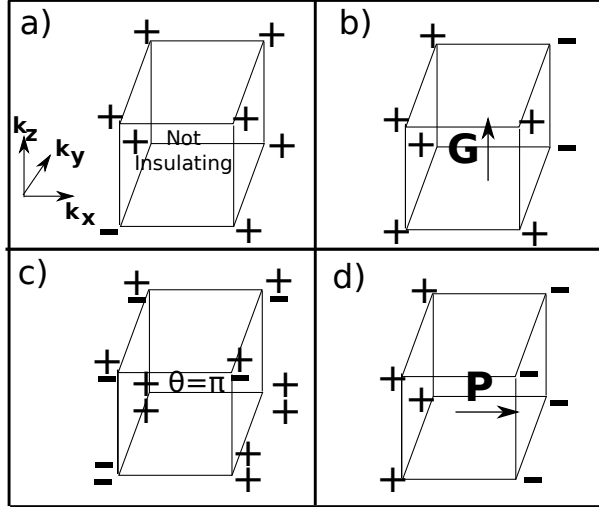


Figure 5.1. Examples of determining physical system properties using parities. The boxes represent an eighth of the Brillouin Zone and the TRIMs are at the corners. The signs represent the parities of the occupied states at the TRIMs. In (a) the constraint of even number of odd parity states is violated, hence it cannot be an insulator. In (b) the parities require a non-vanishing Hall conductance, with odd Chern number in the  $k_x k_y$  planes. In (c) a quantized magnetoelectric response  $\theta = \pi$  is determined from number of odd parity states being 2 (modulo 4). In (d) A parity configuration corresponding to a frozen polarization is shown.

### Total parity constraint and metallic behavior

The first two relationships between physical properties and inversion parities can be written in terms of net parities:

$$\eta_\kappa = (-1)^{n_o(\kappa)} = \prod_a \eta_a(\kappa). \quad (5.3)$$

For any insulator, one can show:

$$\prod_\kappa \eta_\kappa = 1. \quad (5.4)$$

that is, the total number of filled states with odd parity must be even.

In contrary, if  $\prod_\kappa \eta_\kappa = -1$  for some band structure, then the system must be gapless. For example, if a system has the parities in Figure 5.1a, it must be metallic, because there are an odd total number of occupied states with odd parity. The gap must close at some Weyl points in the Brillouin zone, three-dimensional points where the valence and conduction bands meet with a dispersion shaped like a cone. Under certain circumstances the Fermi energy pass through the Weyl points, the material is a semimetal with density of states equals zero.

Note that the index  $(-1)^{\delta_0}$  in Eqn. 5.4 differs from Ref. [39], where it is only the product of the parities of “half” the occupied states for systems with both time reversal and inversion symmetry. Because when these symmetries are present, the states always come in pairs due to Kramers’ theorem, the product in Eqn. 5.4 always equal 1. Besides, the result below in Eqn. 5.6 generalizes the strong index.

## Quantum Hall effect

The net parities also determine the quantum Hall integers modulo 2. For example, The  $\hat{z}$ -component of  $\tilde{\mathbf{G}}_{\mathbf{H}}$  satisfies:

$$e^{\frac{i}{2}\tilde{G}_{Hz}} = \prod_{\kappa: \mathbf{R}_z=0} \eta_\kappa \quad (5.5)$$

that is, whether the Hall conductivity along the  $\hat{z}$  is an even or odd multiple of  $2\pi$  can be determined by multiplying the  $\eta$ ’s around either of the squares parallel to the  $xy$ -plane. If a system has the parities shown in Figure 5.1b, the Hall conductivity cannot vanish. The component along the  $z$ -direction,  $G_{Hz}$ , must be an odd multiple of  $\frac{e^2}{h}$  per layer of the crystal.

Eqn. 5.4 and 5.5 also have an interpretation as constraints between the invariants of insulating phases. The 11 integers  $\tilde{\mathbf{G}}_{\mathbf{H}}$  and  $n_o(\kappa)$  are not completely independent and have to satisfy these four relationships. In addition, these are the only constraints; if these relationships are satisfied, the invariants can be realized in principle in certain band structure.

## Magnetoelectric effect

The magnetoelectric effect is related to the magnetoelectric polarizability  $\alpha_j^i$ , where an applied magnetic field induces a polarization,  $P^i = \alpha_j^i B^j$ . In the absence of the quantum Hall effect,  $\alpha_j^i$  is well-defined; otherwise the polarization can be neutralized by a charge flow in the surface states. The polarizability  $\alpha_j^i$  is odd under inversion:  $\mathbf{P}$  changes sign while  $\mathbf{B}$  does not. Note that  $\alpha$  is defined modulo  $(\frac{e^2}{h})\delta_{ij}$  due to possible integer quantum hall effect on the surface. Therefore, if the system is inversion symmetric,  $\alpha_j^i$  is isotropic and quantized  $\alpha_j^i = \frac{e^2}{2\pi h}\theta\delta_j^i$ , where  $\theta$  is a multiple of  $\pi$ .

Earlier work has considered  $\theta$  for the case of materials with time reversal symmetry, where the magnetoelectric effect  $\theta = \pi$  is related to a nonzero strong index[32, 138]. The criterion was also constructed if the system also has inversion symmetry[39]. When the time reversal symmetry is not present, we find that essentially the same formula can be used to determine  $\theta = \pi$ . Instead, it depends on  $n_o$ ’s:

$$\frac{\theta}{\pi} \equiv \frac{1}{2} \sum_{\kappa} n_o(\kappa) \pmod{2} \quad (5.6)$$

which is an integer according to Eqn. 5.4.

This result is more general because the details of the band structure can be quite different in the presence of magnetism: there may be an odd number of occupied states at the TRIMs

when time reversal is broken. Because of Kramers' theorem, such band structures cannot be adiabatically connected to a material with time reversal symmetry, yet the magnetoelectric effect is still determined by Eqn. 5.6. One such band structure is illustrated in Figure 5.1c; it is not adiabatically connected to any time reversal symmetric insulator because of the unpaired odd parity state at the TRIMs. The total number of odd parity states is even in accord with Eqn. 5.4 and is twice an odd number, hence  $\theta = \pi$ .

## Frozen polarization

Let us complete the discussion of physical properties that are constrained by the “net parities”  $\eta_\kappa = \pm 1$ . Eqn. 5.5 determine the Chern numbers modulo 2 and fix three of the eight degrees of freedom contained in the parities. Note also that any pattern of parities satisfying the constraint Eqn. 5.4 can be factored into 7 seven parts:

$$\eta(\kappa) = \pm (-1)^{\frac{1}{\pi^2} \tilde{g}_x \kappa_y \kappa_z} (-1)^{\frac{1}{\pi^2} \tilde{g}_y \kappa_x \kappa_z} (-1)^{\frac{1}{\pi^2} \tilde{g}_z \kappa_x \kappa_y} (-1)^{\frac{2}{\pi} \tilde{\mathbf{P}}_e \cdot \kappa} \quad (5.7)$$

three factors depending on integers  $\tilde{g}_i$ , three depending on half-integers  $\tilde{\mathbf{P}}_e$  and an overall sign in the front.  $\tilde{\mathbf{g}}$  is the Hall conductivity modulo 2. The pattern  $\tilde{g}_z = 1$  and all other  $\tilde{\mathbf{g}}$  and  $\tilde{\mathbf{P}}_e$  set to 0, is shown in Figure 5.1b. With  $\tilde{\mathbf{g}}$  set to zero, the patterns of  $\eta_\kappa$  corresponds to a plane wave, and the wave-number  $\tilde{\mathbf{P}}_e$  turns out to determine the intrinsic polarization.

Intrinsic electrical polarization is a ferroelectric phenomenon with an ambiguity similar to  $\theta$  [148]: it is determined modulo a lattice vector times  $e$ . This is because while the total polarization can be altered by surface charges, the intrinsic part of it is determined by the bulk properties. Inversion symmetry constrains the components to be integers or half-integers times  $e$ . Hence the polarization is determined by three degrees of freedom revealed in Eqn. 5.7.  $\mathbf{P}_e$  only describes the polarization of the electrons relative to the Bravais lattice, for the total polarization charges of the nuclei need to be included:

$$\mathbf{P} = e\tilde{\mathbf{P}}_e - \sum_i Z_i e \mathbf{r}_{Ni}, \quad (5.8)$$

where  $\mathbf{r}_{Ni}$  and  $-Z_i e$  are the position vector and charge of the  $i^{\text{th}}$  nucleus, respectively. For example, consider the polarization of a crystal with the band structure illustrated in Figure 5.1d, it is  $\mathbf{P} = e\mathbf{R}_1/2$  if the nuclei are all on the Bravais lattice.

When the intrinsic polarization is nonzero, it may lead to a ferroelectric moment, so that the crystal would have a surface charge of  $\frac{1}{2}e$  per unit cell and a large electric field. But it does not always appear as a polarization. Alternatively, it is also possible that the translational symmetry of the surface may be spontaneously broken through a spontaneous charge density wave reconstruction or the surface may be metallic[178].

## Possibility of other effects

Many insulators have parity patterns that does not display any of the phenomena described above and cannot be characterized in any macroscopic way either. They belong

to distinct phases, but these phases all behave the same. For example, if there are 4 odd parity states at  $\kappa = 0$ , and 4 even parity states at all other TRIMs, this phase is definitely a distinct phase separated by a phase transition from the one where all states are even, so it may seem that some property would distinguish the two phases. However, Eqn. 5.5, 5.6, and 5.7 give trivial Hall conductivity,  $\theta$  and polarization. Actually, in Section 5.3 we show that no response property distinguishes this phase from any insulating phase where  $\theta$ , the Hall coefficients and the polarization vanish.

One may construct examples of Hamiltonians with certain parity patterns. One example is a hopping model where the local orbitals are labeled even ( $s, d, \dots$ ) or odd ( $p, f, \dots$ ) and electrons can hop between them. The hopping matrix elements must respect inversion symmetry, which constrains the relative signs of hopping in opposite directions. If orbital  $a$  is centered around a point of inversion symmetry,  $t_{a \rightarrow b} = \pm t_{a \rightarrow b'}$  where the orbitals  $b$  and  $b'$  are orbitals in opposite directions from orbital  $a$  and the sign depends on whether  $a$  and  $b$  have the same or opposite parities. A detailed example Hamiltonian with the parities in Figure 5.2a is given in Appendix B.1.

## The entanglement spectrum

The entanglement spectrum[131] produces an alternative explanation for these results, each is connected to a certain type of “entanglement surface state”. An insulator with inversion symmetry has a special particle-hole symmetry  $\mathcal{I}_e$  in its entanglement spectrum  $\epsilon_a(\mathbf{k})$  when the entanglement bipartition plane goes through an inversion center. This makes it possible to determine qualitative properties of the Fermi arcs and count the number of zero modes at the surface TRIMs  $\kappa_\perp$  in the entanglement spectrum[177].

Let  $\Delta N_e(\kappa_\perp) = \text{tr}_{\epsilon=0} \mathcal{I}_e$  be the number of even modes minus the number of odd modes with zero entanglement-energy at  $\kappa_\perp$ , then they can be expressed in terms of parities of the bulk states  $n_o(\kappa)$ :

$$\Delta N_e(\kappa_\perp) = \frac{1}{2}(\Delta N(\kappa_1) + \Delta N(\kappa_2)), \quad (5.9)$$

where  $\Delta N(\kappa) = \text{tr}_{E<0} \mathcal{I} = n - 2n_o(\kappa)$  and  $\kappa_1$  and  $\kappa_2$  are the two TRIMs that project to  $\kappa_\perp$ . In other words, the difference between the number of even and odd parity states on the entanglement “Fermi surface” at a surface TRIM is half the difference between the even and odd parity states at the corresponding bulk TRIMs.

For illustration, we calculate the entanglement spectrum of a Hamiltonian whose inversion parities suggest that  $\theta = \pi$  and  $\tilde{G}_{Hi} \equiv 0 \pmod{2}$ , see Figure 5.2a. The Hamiltonian has a cubic unit cell and is detailed in Appendix B.1. The entanglement bipartition is along the  $xy$ -plane. As expected, there is a Dirac point at  $(0, 0)$ , see Figure 5.2b, despite the absence of physical surface states. It reflects a nonzero  $\theta$ .

From the relation between the entanglement spectrum and the parities, one can give an alternative derivation of the connections between electromagnetic properties and inversion parities. This formula also leads to an alternative derivation of the formula for the indices of topological insulators that count the physical surface states in Ref. [39]. Here, the

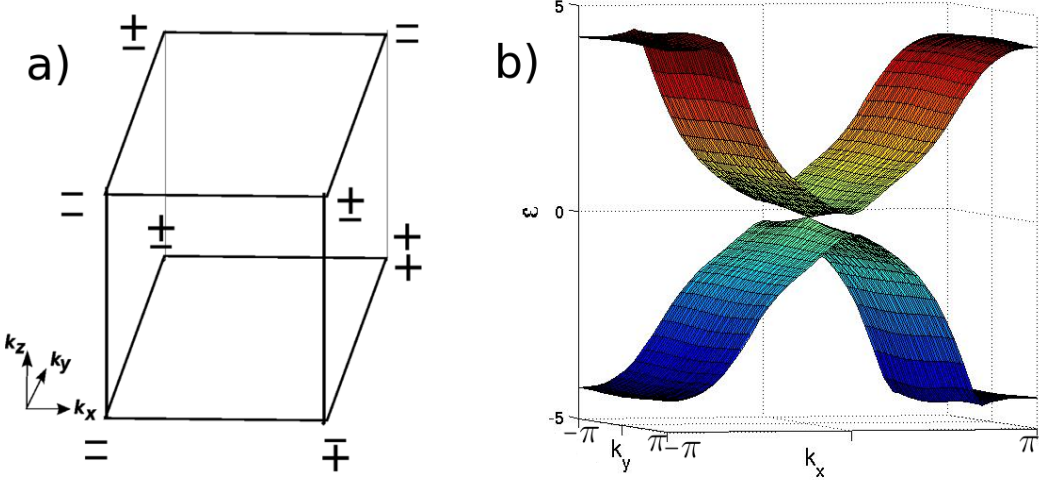


Figure 5.2. a) The parities at the TRIMs and b) the entanglement spectrum for a bipartition cut parallel to the  $xy$ -plane of a hopping Hamiltonian. There are two zero-modes at the TRIM  $(0, 0)$  and none at the other TRIMs, in consistency with the expectation from the parities.

entanglement states are easy to count with the help of symmetry, and can be deformed continuously into the physical spectrum.

### 5.3 Classifying Inversion Symmetric Insulators

In this section we show why the inversion parities and the Chern numbers give the full classification of noninteracting insulators with inversion symmetry. The result follows from the classification of Hamiltonians without any symmetry, because the space of inversion symmetric Hamiltonians and the space of all Hamiltonians are related. The Hamiltonians without symmetry are classified by Chern numbers for two-dimensional cross sections of the Brillouin zone. The only additional parameters that appear when the Hamiltonians are inversion symmetric come from the classification of "zero-dimensional insulators" associated with the TRIMs. Like finite molecules, these states can be classified by inversion parities.

Let's consider the Hamiltonian  $H(\mathbf{k})$  and the corresponding wave functions  $\psi_{n\mathbf{k}}$ . By using a tight-binding model with  $n$  filled bands out of  $N$  bands, the Hamiltonian is an  $M \times M$  matrix. Since it is inversion symmetric:

$$I_0 H(\mathbf{k}) I_0 = H(-\mathbf{k}) \quad (5.10)$$

where  $I_0$  is the matrix describing how the orbitals within the unit cell transform under inversion. The only points in the Brillouin zones where the inversion symmetry constrains the Hamiltonian are the TRIMs  $\kappa$ . Each of these points can be interpreted as a zero-dimensional system with  $H(\kappa)$  invariant under  $I_0$ , since Eqn. 5.10 implies  $I_0 H(\kappa) I_0 = H(\kappa)$ .

Let  $n_o(\kappa)$  be the number of negative energy eigenvalues odd under  $I_0$ . As the Hamiltonian evolves adiabatically, the states at this TRIM can mix but only between the same parity classes, so the value of  $n_o(\kappa)$  stays invariant.

The second set of characteristic integers of the Hamiltonian are the Chern numbers, invariant topological winding numbers describing the Hall conductivity[7, 173].

We will show that these integers give a complete classification of Hamiltonians with inversion symmetry. For non-interacting insulators, a phase transition occurs when the gap closes and states cross the Fermi energy  $\mu = 0$ . Two Hamiltonians are in the same phase can be connected without a phase transition. Topologically, we can define an equivalence relationship for the matrix fields  $H(\mathbf{k})$ :

$$\begin{aligned} H(\mathbf{k}) \sim H'(\mathbf{k}) &\text{if } H(\mathbf{k}) \text{ can be deformed to } H'(\mathbf{k}) \\ &\text{without any eigenvalues vanishing} \\ &\text{while maintaining inversion symmetry} \end{aligned} \quad (5.11)$$

If  $H(\mathbf{k})$  and  $H'(\mathbf{k})$  are two Hamiltonians both with  $n$  occupied states and  $N_o$  odd parity states out of  $N$  total states, they can be deformed into one another while preserving inversion symmetry, i.e.  $H(\mathbf{k}) \sim H'(\mathbf{k})$  if:

$$\begin{aligned} n_o(\kappa) &= n'_o(\kappa) \text{ (for all TRIMs } \kappa) \\ \tilde{\mathbf{G}}_H &= \tilde{\mathbf{G}}'_H \end{aligned} \quad (5.12)$$

at least for  $N - n, n \geq 2$ , because when there are too few bands some Hamiltonians cannot be deformed into one another just because there are not enough degrees of freedom[107]. Our classification theorem does not capture these distinctions, which are not related to any generic properties. If one adds sufficiently many trivial occupied and unoccupied bands to an insulator, any two insulators with the same invariants can be deformed into one another. Similarly, we do not usually consider the integers  $N$  and  $N_o$  to be important invariants, since their values can be changed without modifying the physics by adding even or odd parity states with a very high or very low energy. In a continuous space, there are infinitely many available orbitals.

Here we present the proof of the classification of inversion symmetric insulators with  $n_o(\kappa)$  and  $\mathbf{G}_H$ .

The derivation is based on dimension reduction - the relation of Hamiltonian in  $d$  dimensions with one in a smaller number of dimensions. For generality we take  $d$  to be arbitrary and we will focus on the  $d = 3$  case later. Let  $\mathcal{H}_d$  be the space of general Hamiltonians in  $d$  dimensions, while  $\mathcal{I}_d$  is the subspace of Hamiltonians that have inversion symmetry. A generic Hamiltonian in  $\mathcal{H}_d$  can be regarded as a closed loop in  $\mathcal{H}_{d-1}$ : when the  $d^{\text{th}}$  component of  $\mathbf{k}$  have a value  $k_d$ , one obtains a  $(d-1)$ -dimensional Hamiltonian  $H_{k_d}(k_1, k_2, \dots, k_{d-1}) \equiv H(k_1, k_2, \dots, k_d)$ . As  $k_d$  varies,  $H_{k_d}$  traces out a closed loop in  $\mathcal{H}_{d-1}$  because the Brillouin zone is periodic.

A Hamiltonian in  $\mathcal{I}_d$  has a different interpretation as an arc in  $\mathcal{H}_{d-1}$  from  $k_d = 0$  to  $\pi$ , which is half of the previous loop. The rest of the loop is determined by inversion symmetry.

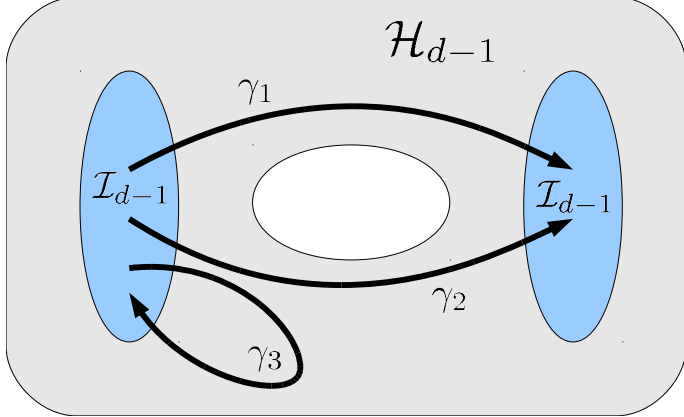


Figure 5.3. Representation of  $d$ -dimensional Hamiltonians by arcs and loops in the space of  $d - 1$ -dimensional Hamiltonians. The grey region represents  $\mathcal{H}_{d-1}$ : each point corresponds to a generic  $d-1$ -dimensional Hamiltonian. The two ellipses on the side represent the components of  $\mathcal{I}_{d-1}$ , the Hamiltonians with inversion symmetry. Inversion-symmetric  $d$ -dimensional Hamiltonians are represented by arcs connecting points in  $\mathcal{I}_{d-1}$ . Two of these Hamiltonians are equivalent if the end-points are in the same component of  $\mathcal{I}_{d-1}$  and have the same winding numbers around holes in the space (represented by the white ellipse). For example,  $\gamma_2$  and  $\gamma_3$  are not equivalent because their final end-points are in different components;  $\gamma_1$  and  $\gamma_2$  are not equivalent because  $\gamma_1\gamma_2^{-1}$  winds around the hole.

The end-points of the arc have to be on  $\mathcal{I}_{d-1}$  because the inversion takes the  $k_d = 0, \pi$  cross-sections to themselves.

Thus, classifying inversion symmetric Hamiltonians is equivalent to the problem of classifying the arcs can be deformed into one another. That is, consider arcs  $\gamma_1, \gamma_2$  in  $H_{d-1}$  connecting two points in the subspace  $I_{d-1}$  as illustrated in Figure 5.3, what conditions ensure that it is possible to move  $\gamma_1$  to  $\gamma_2$ ? This deformation is possible if we can first slide the end-points of  $\gamma_1$  within  $\mathcal{I}_{d-1}$  onto the end-points of  $\gamma_2$  and then smoothly deform the curves connecting them. Therefore, two arcs are equivalent if their end-points are in the same component of  $\mathcal{I}_{d-1}$  and do not have any hole in between them. We can thus classify  $d$ -dimensional Hamiltonians by solving two problems: describing the different components of  $\mathcal{I}_{d-1}$ , and classifying the arcs connecting a pair of points in  $\mathcal{H}_{d-1}$  up to homotopy.

Let us now consider  $d = 3$ . The connected components of  $\mathcal{I}_2$  are the different classes of two-dimensional inversion-symmetric Hamiltonians as defined in Eqn. 5.11. First we slide the interior of arc  $\gamma_1$  onto arc  $\gamma_2$ . Classifying arcs with fixed end-points in a given space is closely related to classifying closed loops, which can be classified by two winding numbers  $\oint d\alpha(k_z)$  and  $\oint d\beta(k_z)$ , where  $\alpha$  and  $\beta$  are angular variables around holes in  $\mathcal{H}_2$ . Note the two winding numbers  $\oint_{-\pi}^{\pi} d\alpha(k_z), \oint_{-\pi}^{\pi} d\beta(k_z)$  are given by the Chern numbers  $\tilde{G}_{Hx}$  and  $\tilde{G}_{Hy}$  of the full Hamiltonian for the following reason: the closed loops in  $\mathcal{H}_2$  corresponds to a three-dimensional Hamiltonian in  $\mathcal{H}_3$  without any special symmetry, which is classified by their Chern numbers  $\tilde{G}_{Hx}$  and  $\tilde{G}_{Hy}$ .

Therefore, the inversion symmetric Hamiltonians corresponding to arcs connecting two fixed points in the space  $\mathcal{H}_2$  can be classified by the change in  $\alpha$  and  $\beta$ :  $\Delta\alpha = \int_0^\pi d\alpha(k_z)$  and  $\Delta\beta = \int_0^\pi d\beta(k_z)$ , the “winding numbers” of the open arcs, which are half as big as the Chern numbers due to the inversion symmetry. If the Chern numbers of the Hamiltonians are equal, the arcs  $\gamma_1, \gamma_2$  have the same values of  $\Delta\alpha$  and  $\Delta\beta$  so they are equivalent.

Now we return to the problem of sliding the end-points to one another. This is the same as classifying inversion symmetric Hamiltonians in two dimensions. This problem may be solved by studying arcs and loops in  $\mathcal{H}_1$  by reducing one more dimension. For two equivalent Hamiltonians in  $k_x - k_y$  space, the winding number  $\tilde{G}_{Hz}$  needs to be the same, and the one-dimensional Hamiltonians in  $\mathcal{I}_1$  on the boundary must be equivalent.

Then we classify inversion-symmetric Hamiltonians in one dimension, i.e. arcs in  $\mathcal{H}_0$ . There are no winding numbers in  $\mathcal{H}_0$ , so the problem reduces directly to classifying the zero-dimensional end-points. Two zero-dimensional Hamiltonians are equivalent if the numbers of even and odd occupied states are the same. Hence the eight integers  $n_o(\kappa)$  and the total number of occupied states  $n$  must match. The original Hamiltonian has bifurcated into eight zero-dimensional Hamiltonians since each step of passing from arcs to end-points doubles the number of Hamiltonians.

Hence, three-dimensional Hamiltonians are classified by  $\tilde{G}_{Hx}, \tilde{G}_{Hy}$  and  $\tilde{G}_{Hz}$  together with the parities at the TRIMs  $n_o(\kappa)$ .

Next we show a classification scheme from a different perspective and look for physical interpretations of the parities. Some parity patterns imply a non-vanishing physical quantity, we would like to determine all such relationships.

We search for nontrivial parities  $n_o(\kappa)$ ’s by eliminating all the “frozen” insulators where the electrons cannot move and do not have any response. Most  $n_o(\kappa)$ ’s combinations can occur in frozen insulators, hence only finite number of phases have distinctive behavior. We will determine the behavior for each of these phases.

To picture the different types of insulators, we represent the  $n_o(\kappa)$  quantum numbers geometrically as a vector in an imaginary eight-dimensional lattice. Combining the orbitals of two materials in the same space corresponds to adding their  $n_o$  vectors. The  $n_o$  vectors for “frozen” phases form a Bravais lattice because the sum of two frozen vectors is also frozen. Then the frozen  $n_o$  Bravais lattice is described as the following: define  $w_{xyz} = \sum_\kappa n_o(\kappa) \bmod 4$  and  $u_z = \sum_{\kappa \perp \mathbf{R}_z} n_o(\kappa) \bmod 2$  and similarly for  $u_x, u_y$ , a frozen site suggests all of these quantities are zeros, see Appendix B.2. For example, consider an insulator with four odd parity states at  $\kappa = 0$  and all other states’ parity even. It satisfies the conditions  $w_{xyz} = u_x = u_y = u_z = 0$ , hence it is a “frozen” phase.

Since there are four possible values for  $w_{xyz}$  and  $2^3$  possible values for  $u$ ’s, this  $n_o$  crystal has a unit cell of 32 sites; one is frozen, and the other 31 can be represented in terms of four vectors, see Figure 5.4:

$$n_o = u_{xy}m_{xy} + u_{xz}m_{xz} + u_{yz}m_{yz} + w_{xyz}m_{xyz} \quad (5.13)$$

where the  $u$ ’s are each 0 or 1 and  $w_{xyz}$  is 0, 1, 2 or 3.

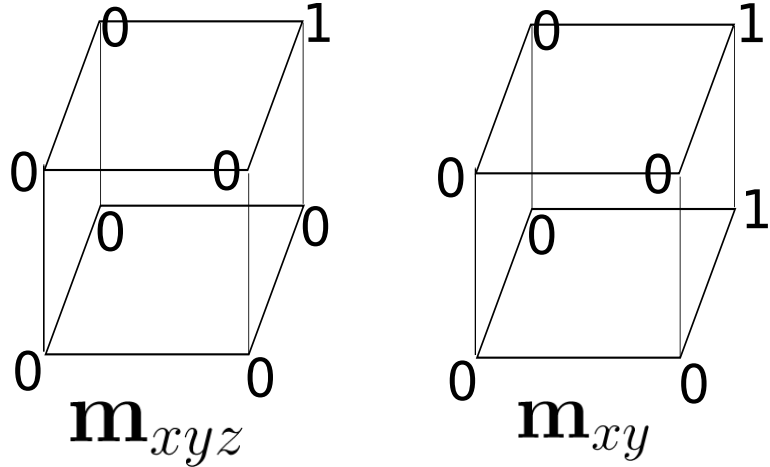


Figure 5.4. Examples of  $\mathbf{n}_o$  vectors. Because they and the two rotations of  $\mathbf{m}_{xy}$  form a complete basis for the unit cell of the eight-dimensional  $\mathbf{n}_o$  vectors lattice for nontrivial band structures, the entire family of quantized behavior for inversion symmetric insulators can be found in these two examples and linear combinations of them.

Compounds with equal Chern numbers and equivalent positions in the  $n_o$  unit cell given by Eqn. 5.13 have equivalent quantized response properties as they differ by a “frozen” state. Since the  $u$ ’s and  $w_{xyz}$  distinguish the 32 sites in a unit cell, it will be these parameters that determine all the quantized response properties. In Section 5.4, we will determine the properties of each types in Eqn. 5.13.

Note that materials corresponding to equivalent sites in this classifying crystal could have different static properties, since “frozen” insulators can have intrinsic electric polarization. Since polarization is defined modulo one-half of a lattice vector, there are still only a few combinations of the  $n_o$ ’s that are nontrivial.

The key step in the argument is the identification of the “frozen” crystals and the corresponding  $n_o$  vectors. Consider an ionic or “frozen” insulator with positive nuclei on the Bravais lattice and electrons fixed on certain sites, and zero hopping amplitudes. The simplest inversion symmetric example has a single electron per unit cell located at half of a Bravais lattice vector  $\mathbf{d} = \frac{\mathbf{R}}{2}$  and its translates. When there are two electrons per unit cell, they may be located at any point and its inversion image. Indeed, all other “frozen” insulators may be constructed from these two cases.

The parities of the former insulator depend on  $\kappa$ , and are found by transforming from the localized  $\mathbf{R}$  basis to the plane wave  $\mathbf{k}$  basis:  $|\mathbf{k}\rangle_{\mathbf{d}} = \sum_{\mathbf{R}} e^{i\mathbf{k}\cdot(\mathbf{R}+\mathbf{d})} |\mathbf{R}+\mathbf{d}\rangle$ . Then at a TRIM, the inversion eigenvalue is given by:

$$\mathcal{I}|\kappa\rangle_{\mathbf{d}} = \pm e^{2i\mathbf{d}\cdot\kappa} |\kappa\rangle_{\mathbf{d}} \quad (5.14)$$

where the sign depend on the parity of the electron orbital. For each  $\kappa$ , we may have  $n_o(\kappa) = 1$  if  $\frac{2\mathbf{d}\cdot\kappa}{\pi}$  is even(odd) and electron orbital is odd(even). They give eight primitive vectors

$\mathbf{f}_d$ , which generate the  $n_o$  Bravais lattice of “frozen” insulators. Appendix B.2 illustrates a method to determine the unit cell starting from these primitive vectors.

In general, two materials with the same Chern numbers and  $n_o$  vectors differ by a vector in the “frozen” lattice have the same response whether the vector has negative or positive coefficients  $\mathbf{n}_{o1} - \mathbf{n}_{o2} = \sum_{\mathbf{p}} n_{\mathbf{p}} \mathbf{f}_{\mathbf{p}}$ . Define  $\mathbf{f}_+$  as the sum of the terms with positive coefficients, and similarly  $\mathbf{f}_-$  as the sum of the terms with negative coefficients, both  $\mathbf{f}_{\pm}$  are realized for ionic crystals. Then,  $\mathbf{n}_{o1} + \mathbf{f}_- = \mathbf{n}_{o2} + \mathbf{f}_+$ , so the materials belong to the same phase after combining the ionic crystals  $\mathbf{f}_-$  and  $\mathbf{f}_+$  respectively, hence they all have the same quantized response properties.

As an example of a state that can be decomposed into “frozen” insulators, consider again the Hamiltonian  $H$  with four odd parity states at  $\kappa = 0$  and no where else. Its  $\mathbf{n}_o$  vector may be expressed as  $\sum_{d \neq 0} \mathbf{f}_d - 3\mathbf{f}_0$ : it is a superposition of the eight basic “frozen” insulators. Because of the minus sign, this argument is not quite straightforward, and there is no actual “frozen” insulator with the same parities as  $H$ . Nevertheless,  $H$  does not have any special response properties, since if one combines  $H$  with 3 copies of the  $d = 0$  “frozen” insulator, one gets a material that is in the same phase as a “frozen” insulator.

## 5.4 Physical Properties and Inversion Parities

Now we study the properties of all the sites in the unit cell of the  $n_o$  crystal in three stages: sixteen of the sites can occur only in non-insulators; 14 of the remaining insulators have a nonzero Hall conductivity; and the rest two insulators can be distinguished by magnetoelectric susceptibility.

### Constraints on parities in gapped materials

We start by showing Eqn. 5.4, that if  $\sum_{\kappa} n_o(\kappa)$  is odd for a certain band structure, then this band structure is not an insulator. This determines the basic behavior of a crystal with the  $\mathbf{n}_o$  vector  $\mathbf{m}_{xyz}$  in Figure 5.4a and Eqn. 5.13, since  $\sum_{\kappa} n_o(\kappa) \equiv w_{xyz} \bmod 4$ .

We show two arguments that  $\sum_{\kappa} n_o(\kappa)$  must be even in an insulator. First, let us understand a more general question: what happens when the parities of the occupied states at the TRIMs change? These parities change if an even parity state below the Fermi energy and an odd parity state above the Fermi energy pass through one another at the TRIM, or vice versa. Appendix B.3 shows that, each time  $n_o(\kappa)$  changes 1 by such an interchange, a inversion symmetric pair of Weyl points appears or disappears. These Weyl points are points in the Brillouin zone when the conduction and valence bands touch, hence when they are present, the material is not an insulator. Therefore, if the insulator starts out as a “frozen” insulator with all  $n_o(\kappa) = 0$ , then the first change of  $n_o(\kappa)$  makes the material non-insulating.

Furthermore, the Weyl points cannot become gapped out unless more  $n_o(\kappa)$ ’s change.

A Weyl point is stable in isolation because it has a “chirality”  $\pm 1$  and the total chirality of Weyl points is conserved, see Appendix B.3. Also, these Weyl points are Berry-flux monopoles in momentum space, so they have a conserved charge as well[180]. A pair of inversion-symmetric Weyl points can either annihilate with a second pair or with each other. However, the latter cannot occur when the parities at the TRIMs are fixed, because they have to meet each other at a TRIM due to inversion symmetry, where a change in the parity would happen.

Start from a trivial Hamiltonian with all electrons on the Bravais lattice and all the states at TRIMs are parity even, after an odd number of unit changes in  $n_o(\kappa)$ , there are an odd number of pairs of Weyl points, because only two pairs of Weyl points may annihilate, the material can not be insulating. In general, the number of pairs of Weyl points equals the sum of the  $n_o(\kappa)$ ’s modulo 2.

A material with a single pair of Weyl points is a Weyl semimetal and has unusual conductivity behaviors. Due to the Luttinger theorem, the area of electron-like Fermi surfaces has to match the area of the hole-like Fermi surfaces for an undoped material. Thus, if there is only one pair of Weyl points, the Fermi energy cannot move away from zero, or it would lead to Fermi spheres containing the same type of carrier. The Fermi energy would be pinned at the Weyl points, resulting a zero density of states. This phenomenon does not occur if time reversal and inversion symmetry are both present, since a Weyl point is not invariant under the product of the symmetries. Weyl points can also occur when  $n_o(\kappa)$  is even[181], but more symmetry would be necessary to pinpoint the Fermi energy.

Any set of parities  $n_o(\kappa)$  satisfying  $\prod_{\kappa} \eta_{\kappa} = 1$  can be realized in an insulator and there is no direct phase transition between two phases when two or more  $\eta_{\kappa}$ ’s are different. When two states exchange in order to change the value of  $n_o$  at one TRIM, Weyl points will be created, and the system will be a semimetal. The Weyl points must then move to a second TRIM and annihilate, so that the system returns to an insulator again, as illustrated in Figure 5.5. There can be direct transitions where the value of  $n_o$  at a single TRIM changes by 2. However, such transitions are fine-tuned, because two states above and below the Fermi energy have to switch places simultaneously.

The alternative argument for the presence of Weyl points when Eqn. 5.4 is violated is based on the Bloch states as a function of  $\mathbf{k}$ . Let us first suppose there is a single occupied band  $|\psi_{1\mathbf{k}}\rangle$ . To determine whether the wave function is parity even or odd, let us take its overlap with an even parity  $|s\rangle$  centered at the origin,  $s_1(\mathbf{k}) = \langle s|\psi_{1\mathbf{k}}\rangle$ . Consider the equation in the Brillouin zone:

$$s_1(\mathbf{k}) = 0 \tag{5.15}$$

which is a complex equation with two equations for three variables, so its solutions are curves. At a TRIM,  $\psi_{1\kappa}(\mathbf{r})$  is either even or odd under inversion: if it is odd, its overlap with  $|s\rangle$  vanishes; if it is even, the overlap generally does not vanish. Hence, there is a curve through each TRIM where  $|\psi_{1\kappa}\rangle$  has odd parity. But since the curves are inversion symmetric, they have to pass through an even number of TRIMs, see Figure 5.6. Hence, the total number of TRIMs where  $\mathcal{I}\psi_{1\kappa} = -\psi_{1\kappa}$  is even.

When there are several isolated filled bands,  $\prod_{\kappa} \eta_a(\kappa) = 1, 1 \leq a \leq n$  holds for each

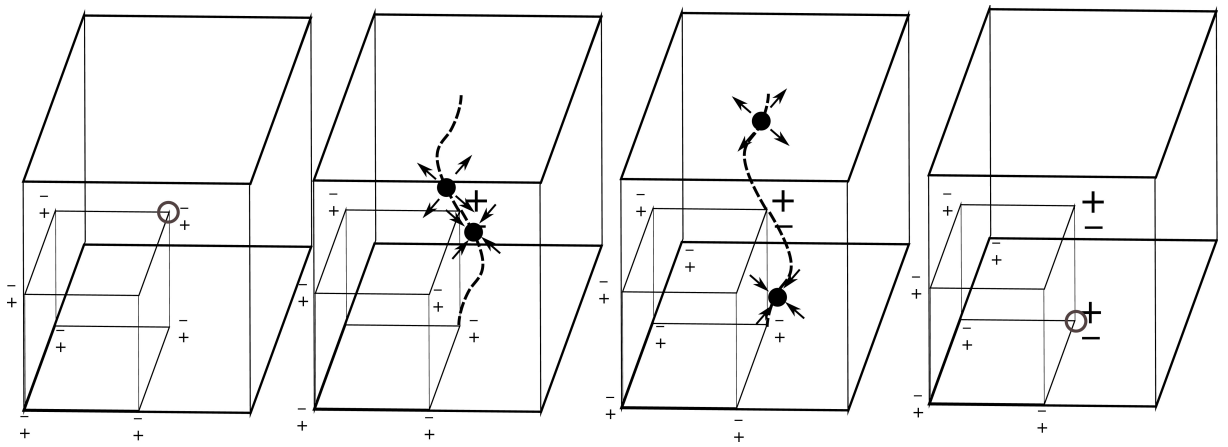


Figure 5.5. Illustration of an evolution that changes the band parities at two TRIMs. The cubes represent the Brillouin zone of a system with two bands, the lower of which is filled. Initially, all the filled bands have +1 parity at TRIMs. A pair of Weyl points, monopoles in the Berry flux as in Appendix B.3, are created at one TRIM and they move to another TRIM where they annihilate. During such process, the parities of the states at both TRIMs are reversed. The open circles indicate where the monopoles are created and annihilated.

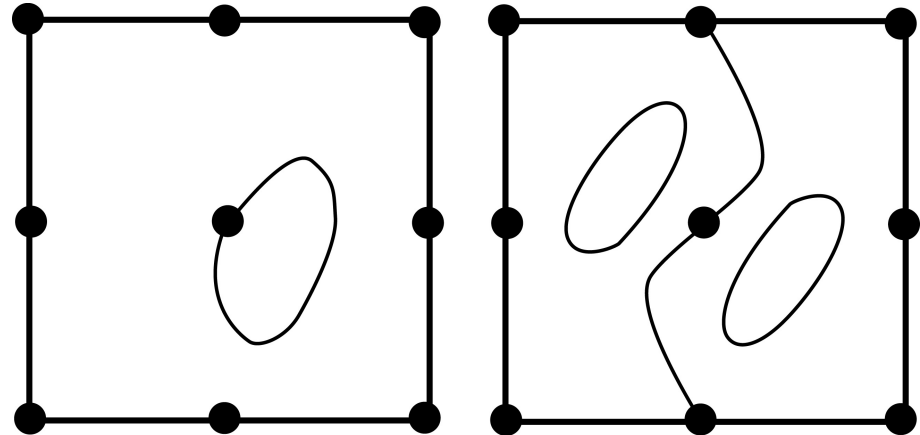


Figure 5.6. Inversion symmetric curves have to pass through an even number of TRIMs. Left, a curve that passes through one TRIM fails to be inversion symmetric; right, an inversion symmetric figure. If there is one curve through one of the TRIMs, it must go around the Brillouin zone and pass through another TRIM.

occupied band separately, therefore their product  $\prod_{\kappa} \eta_{\kappa} = 1$ . If bands touch, the product for a single band may be  $-1$ , but the product for all bands is still  $1$ . To see this, consider the curves given by  $s_a(\mathbf{k}) = \langle s | \psi_{a\mathbf{k}} \rangle = 0$  for all the occupied bands  $1 \leq a \leq n$ . Some of these curves may be open arcs and end at a point where band  $a$  and band  $a+1$  meet and  $s_a(\mathbf{k})$  becomes discontinuous. Then there is always an arc starting from the point in the  $(a+1)^{\text{th}}$  band, see more details in Appendix B.3. All the arcs and curves of the occupied states therefore again produces a set of closed curves. Hence we can still tell that they pass through the TRIMs an even number of times in total, i.e.  $\sum_{\kappa} n_o(\kappa)$  is even.

## Polarization and Hall conductivity

Next, we interpret the  $u$  indices and show that  $u_{xy} \equiv \frac{\tilde{G}_{Hz}}{2\pi} (\text{mod } 2)$ . This result is equivalent to Eqn. 5.5 and applies to the remaining insulating phase.

We first derive the expression for the electrostatic polarization in one dimension, which is not captured by the eight-dimensional lattice  $n_o$  crystal because it is not a response property. Both polarization and the Hall coefficient can be expressed in terms of the Berry connection, a vector function in momentum space. For a single band, the Berry connection is defined as:

$$\mathbf{A}_a(\mathbf{k}) = i \langle u_{a\mathbf{k}} | \nabla_{\mathbf{k}} | u_{a\mathbf{k}} \rangle \quad (5.16)$$

and the total Berry connection  $\mathbf{A}(\mathbf{k})$  is the sum of the Berry connections over the occupied bands.

Consider a one-dimensional crystal, to prove that the intrinsic polarization is given by Eqn. 5.7 and 5.8 modulo  $e$  times a lattice vector, we start from intrinsic polarization of an arbitrary crystal[148]:

$$P = e\tilde{P}_e - \sum_i Z_i e(x_i - x_0). \quad (5.17)$$

where the second term is the polarization of the nuclei in the unit cell relative to an origin  $x_0$ , and the first term is the polarization of the electrons relative to  $x_0$ . Since the electrons are delocalized, calculating its contribution is subtle and given by:

$$\tilde{P}_e = \frac{1}{2\pi} \sum_a \int dk A_a(k). \quad (5.18)$$

This expression for the polarization is defined up to multiples of  $e$  to account for the surface charges. If the Bloch wave functions are redefined by  $u_{ak} \rightarrow e^{i\theta(k)} u_{ak}$ , then the polarization shifts by  $\frac{e}{2\pi}(\theta(2\pi) - \theta(0))$ , an integer multiple of  $e$  and essentially the winding number of  $e^{i\theta(k)}$  around the unit circle.

To evaluate the polarization of an insulator with inversion symmetry, Let us set the inversion center as  $x_0 = 0$ . The wave functions at  $k$  and  $-k$  must be the same up to a phase  $\psi_{-k} = e^{i\theta(k)} \psi_k$ , therefore  $A(k) + A(-k) = \theta'(-k)$ . Combining  $k$  and  $-k$  in Eqn. 5.18,  $\tilde{P}_e = \frac{1}{2\pi} \int_0^\pi \theta'(-k) dk = \frac{1}{2\pi}(\theta(-\pi) - \theta(0))$ . Note that  $e^{i\theta(k)}$  is the parity of the wave function

at TRIMs  $k = 0, \pi$ , hence if they are different,  $\tilde{P}_e \equiv \frac{1}{2} \pmod{1}$ . If there are multiple bands, we need to sum over them. In general, the polarization satisfies:

$$(-1)^{2\tilde{P}_e} = \eta_0 \eta_\pi. \quad (5.19)$$

The polarization in three dimensions can be deduced from this as detailed below.

Let us show that the Chern number for a two-dimensional inversion symmetric system  $H(k_x, k_y)$  obeys  $(-1)^{\tilde{G}_{Hz}} = \prod_\kappa \eta_\kappa$ , which is the two-dimensional version of Eqn. 5.5. When  $k_y$  is fixed, the Hamiltonian leads to a one-dimensional Hamiltonian  $H_{k_y}$ . As  $k_y$  changes, the polarization  $P(k_y)$  of the one-dimensional system changes, which means current flows from one end to the other. According to Thouless's pumping argument, the Hall conductivity  $\tilde{G}_{Hz}$  equal the total charge pumped through the one-dimensional material when  $k_y$  changes by  $2\pi$ , thus  $\tilde{G}_{Hz} = -\frac{1}{e} \int_{-\pi}^{\pi} dP(k_y)$ . Now if  $\prod_\kappa \eta(\kappa) = -1$  the polarizations at  $k_y = 0$  and  $k_y = \pi$  differ by a half integer  $\int_0^\pi dP = (k + \frac{1}{2})e$ . Due to inversion symmetry,  $dP(k_y) = dP(-k_y)$ , so the change in the polarization between 0 and  $2\pi$  is  $2(k + \frac{1}{2})e$  and the Hall coefficient is odd,  $\tilde{G}_{Hz} = -(2k + 1)2\pi$ .

Eqn. 5.5 for the Hall coefficient in three dimensions is a restatement and generalizations of the two-dimensional result. Each of the three components of  $\mathbf{G}_H$  is equal to the two-dimensional Hall coefficient for the corresponding cross-section of the Brillouin zone:

$$G_{Hz} = \int \frac{dk_z}{2\pi} G_{Hz}^{2d}(k_z) = G_{Hz}^{2d}(k_{z0}) \quad (5.20)$$

because varying  $k_z$  is like taking a two-dimensional system and deforming it continuously, the Chern number for any cross-section  $k_z = k_{z0}$  is the same. The Hall coefficient can be obtained modulo 2 by focusing on an inversion symmetric plane at either  $k_z = 0$  or  $k_z = \pi$ , which leads to Eqn. 5.5. Note that this gives another reason for the constraint  $\prod_\kappa \eta_\kappa = 1$ : the two planes have to agree on  $\tilde{G}_{Hz}$ 's parity.

The expression for Hall coefficient can also be understood from the evolution from a frozen Hamiltonian into one with the parities  $\mathbf{m}_{xy}$  and the corresponding monopoles in the interim semimetal phase in Figure 5.5. When the monopoles move through the Brillouin zone from  $(\pi, \pi, 0)$  to  $(\pi, \pi, \pi)$ , they leave behind a magnetic flux so the Chern number is 1, and also flip the parities at the two TRIMs, hence the product of  $\eta_\kappa$  on either of the perpendicular faces is  $-1$ .

On the other hand, for a well-defined three-dimensional polarization  $\mathbf{P}_e = e \iiint \frac{d^3\mathbf{k}}{(2\pi)^3} \sum_a \mathbf{A}_a(\mathbf{k})$ ,  $\mathbf{G}_H$  must be 0 so that there are no surface modes. Then according to Eqn. 5.7, the pattern of  $\eta_\kappa$  is a plane wave; in this situation, all the one-dimensional polarizations at TRIMs  $P_{1d}^x(\kappa_y, \kappa_z)$  are the same and coincide with the three-dimensional polarization. In detail, the three-dimensional polarization is the integral over one-dimensional polarizations,  $P^x = \iint \frac{dk_y dk_z}{(2\pi)^2} P_{1d}^x(k_y, k_z)$  for  $G_{Hy} = G_{Hz} = 0$ . The integrand is not a constant, but by inversion symmetry  $P_{1d}^x(k_y, k_z) - P_{1d}^x(0, 0) = -(P_{1d}^x(-k_y, -k_z) - P_{1d}^x(0, 0))$ . Hence  $P^x = P_{1d}^x(0, 0)$ . For example, in Figure 5.1d each of the four vertical lines through TRIMs looks like a one-dimensional insulator with half-integer polarization, so the net polarization per unit cell of the three-dimensional crystal is also  $\frac{e}{2}\mathbf{R}_3$ .

Also note that even if  $\mathbf{G}_H$  is nonzero, then part of the polarization is still well-defined. If  $\mathbf{G}_H$  is parallel to  $\hat{x}$ , the surface chiral modes circle around in the  $y - z$  plane and do not provide a short circuit between the two ends in  $\hat{x}$  which would allow the  $\hat{x}$  polarization to leak out. This component of the polarization is still given by Eqn. 5.7 and 5.8.

The relationships we have proved so far give the physical interpretation of  $u$  and  $w$  modulo 2. They also complete the list of all the phases in insulating materials and show which combinations of the 11 integers  $\mathbf{G}_H$  and  $n_o(\kappa)$  occur: they must satisfy Eqn. 5.4 and Eqn. 5.5.

## Magnetoelectric response

Now we prove Eqn. 5.6:  $\theta = \frac{\pi}{2} \sum_{\kappa} n_o(\kappa)$  for insulators with  $\mathbf{G}_H = 0$ , and show  $\theta = \pi$  for the case  $n_o(\kappa) = 2m_{xyz}$ . This is the only nontrivial point consistent with the conditions that the material is insulating and has no Hall conductivity in the unit cell of the eight-dimensional classifying crystal, so other case can be related to this one by adding and subtracting “frozen” insulators. Note that it is not possible to define  $\theta$  for materials with Hall conductivity, because the surface states smear out the definition of  $P$ .

To calculate  $\theta$  for  $n_o(\kappa) = 2m_{xyz}$ , it is enough to consider systems with two filled bands with appropriate parities. Any additional bands can be obtained by adding frozen bands. The expression for  $\theta$  in terms of the Berry connection can be evaluated for the two bands insulator using symmetry arguments[32, 33, 138]. The argument for the time-reversal symmetric case[185] applies to systems with inversion symmetry as well:

$$\frac{\theta}{\pi} = \frac{1}{24\pi^2} \iiint d^3\mathbf{k} \epsilon^{ijk} (B^\dagger \partial_i B B^\dagger \partial_j B B^\dagger \partial_k B) \quad (5.21)$$

where  $B_{a_1 a_2}(\mathbf{k}) = \langle u_{a_1}(-\mathbf{k}) | I | u_{a_2}(\mathbf{k}) \rangle$  and  $u_a(\mathbf{k})$  are the wave functions for the two occupied states. The spaces of occupied states are symmetric under inversion.  $B(\mathbf{k})$  measures how far the basis wave functions are from being inversion-symmetric. In a nontrivial phase, it is not possible to choose the basis functions in a continuous way without breaking the symmetry.

$B(\mathbf{k})$  gives a map from a three-dimensional toric Brillouin zone to  $SU_2$ .  $\theta/\pi$  in Eqn. 5.21 equals the degree of this map, i.e. the number of times the torus covers  $SU_2$ , which is the number of solutions to  $B(\mathbf{k}) = -1$  modulo 2. We may count only the satisfied TRIMs because all other solutions come in pairs at  $\mathbf{k}$  and  $-\mathbf{k}$  due to inversion symmetry. The number of TRIMs where  $B = -1$  is determined by the sum of  $n_o(\kappa)$ .

We have found that only certain combinations of the  $n_o(\kappa)$ ’s modulo 2 and 4 have physical interpretations. In the next section, we will give another perspective on why only values of the  $n_o(\kappa)$  modulo 4 are important: all the  $n_o(\kappa)$ ’s have interpretations in the entanglement spectrum, although the entanglement modes cannot be observed directly, but numbers of entanglement modes modulo 2 are related to various observable properties.

## 5.5 Parities and the Entanglement Spectra

The relations between the properties of the insulator and the parities can be derived geometrically using the entanglement spectrum and its counting rules for the number of states based on the parities.

The entanglement spectrum measures quantum correlations in the ground state of a system[131]. When the physical system is partitioned by an imaginary plane through a center of inversion symmetry, the many-body ground-state wave function can be Schmidt decomposed,

$$|\Psi\rangle = \frac{1}{\sqrt{Z}} \sum_{\alpha} e^{-\frac{E_{\alpha}^e}{2}} |\alpha\rangle_L |\alpha\rangle_R. \quad (5.22)$$

where  $Z$  is a normalization constant and  $|\alpha\rangle_L$  and  $|\alpha\rangle_R$  are the entanglement states. The weight of a given product state is described by the entanglement “energy”  $E_{\alpha}^e$ .

When the wave function of the entire non-interacting system described by a Slater determinant, the entanglement states  $|\alpha\rangle_L$  are also Slater determinants[131]. They are just like the excited states of a system of free electrons, by selecting wave functions from a certain orthonormal family of single-particle wave functions  $f_{i\mathbf{k}_{\perp}}^L(\mathbf{r})$  labeled by  $\mathbf{k}_{\perp}$  the momentum along the surface. Each of these wave functions has an associated “energy”  $\epsilon_{Li}(\mathbf{k}_{\perp})$  as if they were eigenfunctions of a single-particle Hamiltonian. The entanglement “energy”  $E_{\alpha}^e$  is the sum of all the “energies” of the occupied states. The state in the Schmidt decomposition with the smallest “energy” and largest overall weight is obtained by filling up all states with  $\epsilon_{Li} < 0$ , suggesting the Fermi “energy” is 0.

The entanglement spectra  $\epsilon_{Li}(\mathbf{k}_{\perp})$  can be used to determine “topological” properties of a system. When a material is insulating in the bulk, it may still have a gapless entanglement spectrum implying that “topologically nontrivial” states are delocalized across the cut, unlike the electrons in a “frozen insulator”. Physical topological surface states can be deduced from such entanglement spectrum states: the entanglement spectrum can be continuously deformed into the physical spectrum, so topologically protected states are present in both spectrum[34, 177].

Determining basic properties of the entanglement spectrum is simple in the presence of inversion symmetry[177]. We will see that a special inversion  $\mathcal{I}_e$  takes each state to another state whose momentum  $\mathbf{k}_{\perp}$  and “energy”  $\epsilon_{Li}(\mathbf{k}_{\perp})$  have the opposite sign. Thus the entanglement spectrum has a particle-hole symmetry  $\mathcal{I}_e$  that leads to a rule for the number of entanglement states at each surface TRIM.

At surface TRIMs  $\mathcal{I}_e$  ensures that states appear in pairs with “energies”  $\pm\epsilon$  when  $\epsilon \neq 0$ . However, there can be a single state at  $\epsilon = 0$ . If present, this zero-“energy” state will stay at zero “energy” protected by the inversion symmetry. In addition, the space of zero-“energy” states is invariant under  $\mathcal{I}_e$ , so they can be classified by their parities. Let us define an invariant index  $\Delta N_e(\kappa_{\perp})$  as the difference between the number of states of even and odd parity at a TRIM. While even and odd zero-“energy” states can split and move to nonzero “energies”  $\pm\epsilon$ , two states of the same parity cannot. Thus, there must be at least  $\Delta N_e(\kappa_{\perp})$

states at TRIM  $\kappa_\perp$ . This imbalance index can be determined from the bulk band structure:

$$\Delta N_e(\kappa_\perp) = 1/2(\Delta N(\kappa_1) + \Delta N(\kappa_2)) \quad (5.23)$$

where  $\kappa_1$  and  $\kappa_2$  are the two bulk inversion-symmetric momenta that project to  $\kappa_\perp$  and  $\Delta N(\kappa_i) = n - 2n_o(\kappa_i)$  is the difference between the number of even and odd occupied states at  $\kappa_i$ ,  $i = 1, 2$ . This result applies to any dimensions.

We now briefly define the particle-hole symmetry and derive Eqn. 5.23 for  $\Delta N_e$ , more details are included in Section 6.5, Appendix B.4 and Ref. [16, 82, 131, 177]. As the entanglement states are built up from the single-particle states, the entanglement modes are actually eigenfunctions of a “Hamiltonian”  $H_L$  defined on the left part of the cutting plane. The eigenvalues of  $H_L$  are related to the entanglement “energy”  $\epsilon_{Li}$ :

$$H_L |f_{i\mathbf{k}_\perp}^L\rangle = \frac{1}{2} \tanh \frac{1}{2} \epsilon_{Li}(\mathbf{k}_\perp) |f_{i\mathbf{k}_\perp}^L\rangle \quad (5.24)$$

The Hamiltonian  $H_L$  is the “flat-band Hamiltonian”  $H_{\text{flat}}$  confined to the left half of space.  $H_{\text{flat}}$  is defined to have the same eigenfunctions as the true Hamiltonian but eigenvalues  $-\frac{1}{2}$  for the occupied states and  $+\frac{1}{2}$  for the empty ones. The spectrum of  $H_L$  ranges from  $-\frac{1}{2}$  to  $\frac{1}{2}$ . Each bulk state has an “energy” exactly equal to  $\pm\frac{1}{2}$  so any state with a finite  $\epsilon_{Li}$  is a surface state.

While  $H_L$  is obtained from  $H_{\text{flat}}$  by cutting off the right half of space, cutting away the left half of the space leads to a partner Hamiltonian  $H_R$ . The eigenstates of these three Hamiltonians have unusual connections that the eigenstates of  $H_L$  and  $H_R$  are in one-one correspondence via a map  $\mathcal{M}$ , which reverses the sign of the “energy”[177]. Furthermore, it is possible to build up a complete set of occupied states of  $H_{\text{flat}}$  from these pairs:

$$F_{i\mathbf{k}_\perp}(\mathbf{r}) = \sqrt{\frac{1}{2} \operatorname{sech} \frac{\epsilon_{Li}(\mathbf{k}_\perp)}{2}} \times \left[ e^{-\frac{1}{4}\epsilon_{Li}(\mathbf{k}_\perp)} f_{i\mathbf{k}_\perp}^L(\mathbf{r}) + e^{\frac{1}{4}\epsilon_{Li}(\mathbf{k}_\perp)} \mathcal{M} f_{i\mathbf{k}_\perp}^L(\mathbf{r}) \right] \quad (5.25)$$

which is an occupied state since applying  $H_{\text{flat}}$  to it gives an eigenvalue of  $-\frac{1}{2}$ . As  $f_i^L$  spans all eigenstates of  $H_L$ ,  $F$  spans the occupied states in the bulk ground state.

When the bulk system is inversion symmetric,  $\mathcal{M}$  and  $\mathcal{I}$  can be combined together to give a symmetry  $\mathcal{I}_e = \mathcal{I}\mathcal{M}$  for the left half of the space and a transformation for  $f_i^L$ . Note that  $\mathcal{I}$  preserves  $\epsilon$  while  $\mathcal{M}$  reverses its sign, therefore  $\mathcal{I}_e$  acts as a particle-hole symmetry; similarly  $\mathcal{M}$  preserves  $\mathbf{k}_\perp$  while  $\mathcal{I}$  reverses its sign, so  $\mathcal{I}_e$  also reverses the sign of  $\mathbf{k}_\perp$  [177].

Now we can count the zero entanglement “energy” states at TRIMs and derive Eqn. 5.23. Eqn. 5.25 extends a state  $f_{i\kappa_\perp}^L$  with parity  $\eta_{i\kappa_\perp}^e$  under  $\mathcal{I}_e$  to an occupied state:

$$F_{i\kappa_\perp} = \frac{1}{\sqrt{2}} \left[ (f_{i\kappa_\perp}^L(\mathbf{r}) + \eta_{i\kappa_\perp}^e f_{i\kappa_\perp}^L(-\mathbf{r})) \right]. \quad (5.26)$$

where we have used  $\mathcal{I}\mathcal{M}f_{i\kappa_\perp}^L = \eta_{i\kappa_\perp}^e f_{i\kappa_\perp}^L$  to relate  $f^R$  to  $f^L$ . This state  $F_{i\kappa_\perp}$  is invariant under ordinary inversion  $\mathcal{I}$  and the parity is also  $\eta_{i\kappa_\perp}^e$ . The number of occupied even parity states  $W_e$  minus the number of occupied odd parity states  $W_o$  is given by  $W_e - W_o = \operatorname{tr} \mathcal{I}$

for a periodic one-dimensional system. The result in higher dimensions will follows since we can fix  $\mathbf{k}_\perp$  to obtain a one-dimensional system.

One orthonormal basis is obtained by a bipartition of the system along a diameter and the two cutting points are 0 and  $\frac{L}{2}$ . The corresponding  $F$  states in Eqn. 5.25 form a full basis for the wave functions on the ring. According to Eqn. 5.26, the zero-“energy” states give parity eigenstates centered on each of the two cuts, and contribute  $2\Delta N_e$  to  $W_e - W_o$ . The remaining states do not contribute because they can be organized into inversion-related pairs,  $F_i(x)$  and  $F_i(-x)$ , which are all mutually orthonormal because their left and right halves correspond to different eigenvalues of  $H_L, H_R$ . Then the inversion matrix  $\mathcal{I}$  has only off-diagonal matrix elements between  $F_i(x)$  and  $F_i(-x)$ .

On the other hand, instead of the real space wave functions, we can use the extended Bloch functions  $\psi_a(k_x)$ . While the wave functions at momentum  $\pm k_x$  do not contribute to the trace of  $\mathcal{I}$  due to similar reason of the last paragraph, the wave functions at the TRIMs contribute  $\Delta N(\pi) + \Delta N(0)$  to  $W_e - W_o$ . Matching the two expressions gives Eqn. 5.23.

To understand the physical surface properties of a two-dimensional insulator, we focus on a inversion symmetric two-dimensional quantum spin Hall index, which may be generalized to three-dimensional indices. The dispersions form continuous loops or zigzags because of the double-degeneracies protected by Kramers’ theorem, see Figure 5.7 and the quantum spin-Hall index  $\nu$  is the number of physical edge modes between 0 and  $\pi$  modulo 2. Counting states in the entanglement spectrum is easy due to the particle-hole symmetry, see Figure 5.7. Once they are established in the entanglement spectrum, they may be adiabatically deformed into the physical spectrum and  $\nu$  remains the same even though the surface states no longer have particle-hole symmetry.

For example, for an entanglement spectrum of decomposing the system at axis  $y = 0$ , the spin Hall index is the parity of the number of times the dispersion  $\epsilon(k_x)$  crosses  $\epsilon = 0$  between  $k_x = 0$  and  $\pi$ . Between 0 and  $\pi$  the number of crossings is even since the crossings come in pairs due to  $\mathcal{T}\mathcal{I}_e$  symmetry at  $\epsilon = 0$ , so only the modes at the ends of the interval are important.

All the  $\epsilon = 0$  modes at one TRIM have the same parity or they may be gapped out, then by Eqn. 5.23 the number of modes at  $k_x = 0, \pi$  is:

$$|\Delta N_e(k_x)| = |n - n_o(k_x, 0) - n_o(k_x, \pi)| \quad (5.27)$$

so the number of crossings between  $k_x = 0$  and  $\pi$  is:

$$\begin{aligned} \nu &\equiv \frac{1}{2} \sum_{k_x=0}^{\pi} |\Delta N_e(k_x)| \\ &\equiv \frac{1}{2} \sum_{\kappa} n_o(\kappa) \end{aligned} \quad (5.28)$$

modulo 2, in agreement with Eqn. 5.6. Applying this result to an insulator with both time reversal and inversion symmetry reproduces the result from Ref. [39].

The effects of polarization and Hall coefficient discussed in Section 5.4 may be determined by sketching the arcs of the entanglement Fermi surface according to the number of zero

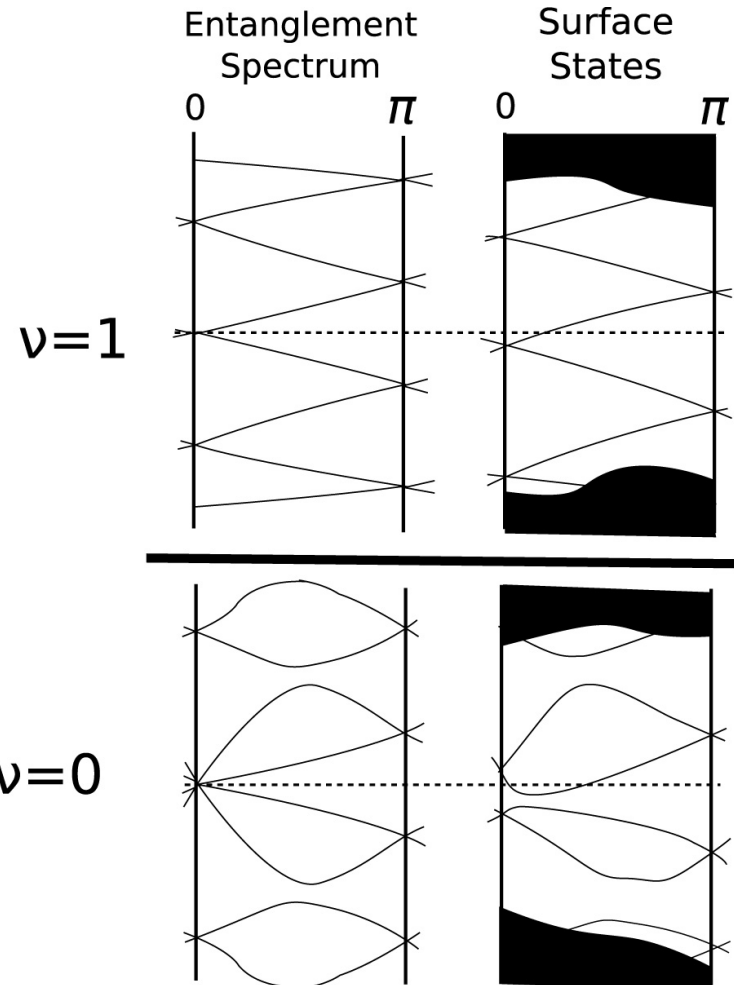


Figure 5.7. A comparison of the spectra of a nontrivial and a trivial system. Left: the entanglement spectrum, and right: surface spectrum, the two spectra can be continuously deformed into each other. Because time reversal symmetry requires Kramers' degeneracies at the TRIMs regardless of energy, the parity of the number of modes crossing the Fermi energy does not change. In the entanglement spectrum, the inversion symmetry protects the zero “energy” degeneracies at the TRIMs, allowing a determination of the quantum spin Hall index.

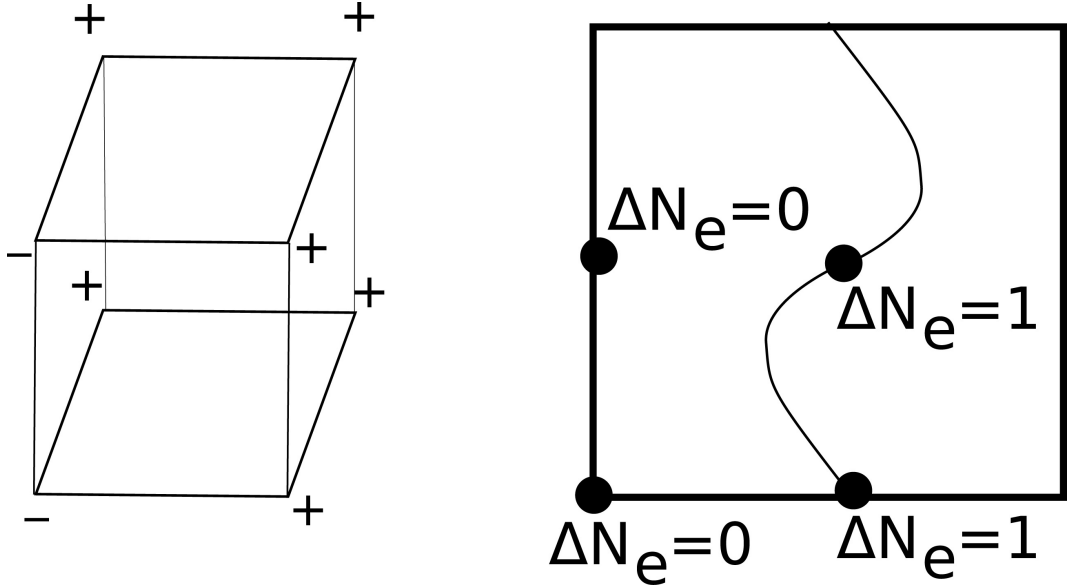


Figure 5.8. An example model with a single filled band and an odd quantum Hall effect parallel to  $\mathbf{R}_z$ : a) The pattern of parities at the TRIMs, and b) The entanglement Fermi surface in the  $xz$  surface Brillouin zone determined with  $\Delta N_e(\kappa_{\perp}) = \frac{1}{2}(\Delta N(\kappa_1) + \Delta N(\kappa_2))$ .

entanglement “energy” states at the TRIMs. However, while each zero “energy” state at a TRIM gives at least a Fermi point, not all of these points extend to Fermi arcs. Still, it is proved in Appendix B.4 that the parity of the number of Fermi arcs is the same as  $\Delta N_e$ ’s.

For Hall coefficient, again take the parity pattern in Figure 5.1b discussed in Section 5.2 as an example and consider the  $xz$ -plane entanglement spectrum of this insulator. According to Eqn. 5.23 there must be an odd number of arcs through  $(\pi, 0)$  and  $(\pi, \pi)$  and an even number through the other two TRIMs. Minimally, there is only one Fermi arc, as illustrated in Figure 5.8. Hence as one travels along  $k_x$  across the Brillouin zone, one the Fermi arc will be crossed. Since the  $z$ -component of the Hall conductivity  $\tilde{G}_z$  is the number of arcs,  $\frac{1}{2\pi}\tilde{G}_{Hz} = \pm 1$  where the sign depends on the sign of the group velocity. In general, only the parity of  $\frac{1}{2\pi}\tilde{G}_{Hz}$  is determined because there may be additional pairs of inversion symmetric Fermi arcs that do not pass through TRIMs and are thus not controlled by the  $n_o(\kappa)$  parameters.

The polarization is the surface charge per unit cell, this definition may be applied also to the entanglement spectrum as well. Again take the parity pattern in Figure 5.1d discussed in Section 5.2 as an example and consider the  $xz$ -plane entanglement spectrum of this insulator. The surface Brillouin zone is separated into filled and empty states, but exactly half the Brillouin zone is filled because of the the inversion symmetry, as illustrated in Figure 5.9. This implies that  $P_e^y = \frac{e}{2}$  in agreement with Eqn. 5.8.

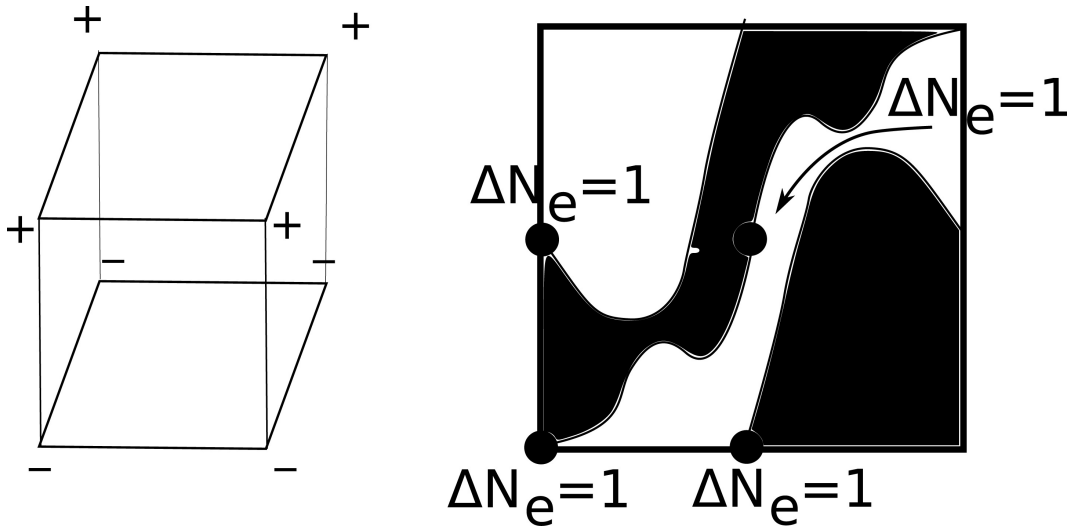


Figure 5.9. Determining the polarization from the entanglement spectrum. a) Parities for an insulator with one filled band, with a half-filled Fermi sea in the entanglement spectrum. b) Possible entanglement Fermi arcs for a cut parallel to the  $xz$  plane. The arcs surround half the surface Brillouin zone. If there are no nuclei on  $y = 0$ , this crystal has a half-integer polarization in the  $y$ -direction.

## 5.6 Conclusion

We have shown in this chapter that beyond the Chern numbers, the only protected quantities for inversion symmetric insulators are the parities of the occupied states at the TRIMs.

For bulk materials, certain values of the parities imply non-vanishing electrostatic properties. In particular, if the number of occupied odd parity states is odd, the material cannot be an insulator.

The parities also provide a simple criterion for determining when a crystalline compound has a non-vanishing magnetoelectric response, a generalization of the result on an insulator with time-reversal as well as inversion symmetry. Hence, the magnetoelectric effect could occur in magnetic materials. There are two consequences: The magnetoelectric effect could be generated by the magnetic ordering, rather than spin-orbit coupling, thus there are more possible materials besides the ones with heavy elements where the electrons spin-orbit coupling are stronger. It would be interesting to search for such materials. Second, in a magnetic material with  $\theta = \pi$  the observation of magnetoelectric effect would be easier, because it does not have gapless surface states in a topological insulator that would interfere the observation.

Beyond these properties, the static polarization and the Hall conductivities, there are no independent response properties that are related to the inversion parities, since any two insulators which have these equivalent response properties can be deformed into each other by combining certain trivial frozen insulators.

The properties of inversion symmetric insulators can also be derived with the entanglement spectrum, illustrating an example where entanglement modes can be indirectly observed: a magnetoelectric response of  $\theta = \pi$  corresponds to a material with an odd number of Dirac points in the entanglement spectrum.

Understanding the stability of the parity invariants to interactions will be an interesting subject for future study. Ref. [35] shows that phases in one dimension can merge when interactions are present. Also, more complicated point groups may lead to further classifications and more interesting phases in non-interacting systems, raising the possibilities of new types of quantized responses.

# Chapter 6

## Entanglement And Inversion

## Symmetry in Topological Insulators

### 6.1 Introduction

According to the Landau paradigm, phases of matter are classified by their pattern of symmetry breaking. While this accounts well for a number of experimentally observed phenomena, several exceptions have also cropped up. These include the fractional quantum Hall states and models of gapped spin liquids, which are characterized by a topological order: for these phases, the ground-state degeneracy depends on the spatial topology of the sample. Perhaps the simplest phases for which a topological distinction is present are topological insulators and superconductors, composed of noninteracting particles. Experimental manifestations include the integer quantum Hall effect, spin-orbit induced  $Z_2$  topological insulators in two[13, 73, 74, 84] and three dimensions[41, 63, 64, 105, 120, 151, 197, 202], as well as superfluid  $He^3 - B$ . Here, although there is a unique ground state and no symmetry difference from the trivial state, the topological distinction can manifest itself in different ways. These include a quantized response function[173] (such as the Hall effect), or protected surface states. Given the subtleties associated with identifying topological phases, a new tool in this respect would be welcome.

Recently, it has been shown that studying the entanglement spectrum is a promising direction to identifying topological phases. Given the ground-state wave function, and a partition of the system into a left and right half, one can perform a Schmidt decomposition:

$$|G\rangle = \sum_{\alpha} \frac{1}{\sqrt{Z}} e^{-\frac{E_{\alpha}^e}{2}} |\alpha L\rangle |\alpha R\rangle \quad (6.1)$$

Measuring the right half of the system shows it to be in state  $|\alpha R\rangle$  (called a Schmidt state) with probability  $e^{-E_\alpha^e}/Z$ . The quantities  $E_\alpha^e$  comprise the entanglement spectrum, and are somewhat like “energies” characterizing how unlikely a given fluctuation is to occur. Note that we use the superscript “e” when describing the entanglement. The entropy associated with this probability distribution is the entanglement entropy, which captures the same features of a phase as ground-state degeneracy of topological order[93]. However, the entire spectrum can be expected to contain more information, allowing one to capture a wider class of distinctions. Even though entanglement related quantities are hard to measure directly, they can be conceptually very useful in identifying phases.

It has been shown for fractional quantum Hall states that although their bulk is gapped, the entanglement spectrum contains information about the edge modes. Numerical studies[95] reveal that the largest entanglement eigenvalues (smallest  $E_\alpha^e$ ) mimic the low-energy spectrum of surface modes. A relationship of this type is very interesting because the entanglement spectrum can be calculated entirely from the ground-state wave function. In contrast, the edge modes are excited states of the Hamiltonian in a sample with boundaries. In a classical system, one would not be able to look at the ground state and determine its dynamics. But a quantum mechanical system, even in its ground state, has some zero-point motion that can give one a sense of its excited state properties. A direct classification of phases from their ground-state wave functions is highly desirable and could be applied to cases where a candidate ground state such as a Gutzwiller projected state is available.

Here we study the entanglement spectrum in the context of the simplest class of topological phases - noninteracting topological band insulators. We show that whenever topological surface states are present, the entanglement spectrum, as a function of the momentum parallel to the cut, also has protected entanglement modes. Essentially, the entanglement spectrum is known to result from diagonalizing an operator, and this operator can be viewed as a band insulator Hamiltonian which retains the topology of the physical insulator. Explicit examples of the entanglement spectrum are worked out, including an analytical calculation for Landau levels (similar to the work of Ref. [149]) and a numerical study of three-dimensional topological insulators. Similar reasoning can be applied to topological superconductors. Such a relation has also been noticed in isolated examples, like the quantum Hall[149] and the  $p_x + ip_y$  superconductor edge[17]. Independent studies have appeared[34], pointing to a similar connection.

Next, we consider the converse, i.e. do protected modes in the entanglement spectrum necessarily imply protected surface excitations? We show explicitly that this is not true, by studying an example of a insulator with only inversion symmetry. Here no protected surface excitations exist, but the entanglement spectrum features protected states, which points to a more subtle distinction between phases. The entanglement spectrum remains gapless because inversion symmetry is retained when dividing the system for the purposes of calculating entanglement entropy, but is implemented in a strange way, as a particle-hole symmetry of the single particle entanglement states. This leads to protected modes. Thus studying systems with inversion symmetry (or another symmetry that maps the left and right halves to one another) is a good way to break the close correspondence between edge states and entanglement, a point noticed earlier for one-dimensional interacting states

in Ref. [135, 136]. When this correspondence breaks down, the protected entanglement degeneracies still indicate a distinct phase, although there are no physical surface states. Understanding the consequences of this hidden degeneracy should be interesting. Although disorder breaks inversion symmetry, and is hence not normally studied while classifying topological insulators[78, 156], clean physical systems with inversion symmetric bulk states can certainly be realized.

Finally, we recast the theory given here in a form that is suitable for studying interacting systems: the action of inversion  $I$  is defined on the many-body Schmidt states. It is shown to act as an anti-unitary operator  $IM$ , which must satisfy  $(IM)^2 = +1$  or  $(IM)^2 = -1$ . The latter corresponds to the topologically nontrivial case, and leads to a two fold degeneracy of all states in the entanglement spectrum. This degeneracy remains on introducing weak interactions. Part of the topological distinction implied by this observation is contained in the quantized magnetoelectric polarizability of insulators, which remains quantized in inversion-symmetric systems. We also discuss finer distinctions between inversion-symmetric insulators, see details from the previous chapter 5 and Ref. [176]. A shorter version of this chapter is previously published[177].

## 6.2 Topological Band Insulators

A band insulator is described by the single particle Hamiltonian:

$$H = \sum_{\gamma, \mathbf{k}} \epsilon_\gamma(\mathbf{k}) d_{\gamma\mathbf{k}}^\dagger d_{\gamma\mathbf{k}} \quad (6.2)$$

where  $\mathbf{k}$  is crystal momentum, and  $\gamma = 1, \dots, N$  is a band index, of which  $n$  bands are filled, i.e.  $\epsilon_\gamma(\mathbf{k}) < 0$  if  $1 \leq \gamma \leq n$  and  $\epsilon_\gamma(\mathbf{k}) > 0$  if  $n < \gamma \leq N$ . The band wave functions are:

$$d_{\gamma\mathbf{k}}^\dagger = \sum_{\mathbf{r}} \phi_{\gamma\mathbf{k}}(\mathbf{r}) \psi^\dagger(\mathbf{r}), \quad (6.3)$$

where we have suppressed spin and orbital indices (These variables can be included in  $\mathbf{r}$  with the spatial coordinates).

Topological phases of band insulators may be defined by their band topology. Two insulators differ topologically if they cannot be connected by smooth changes of the Hamiltonian while the band gap remains finite. It is possible to define a topological invariant to distinguish between different phases that depends only on the wave functions of the filled bands[173].

Given a general band insulator Eqn. 6.2, a topologically equivalent insulator can be constructed by setting the energy of all occupied bands to be equal and negative, and all unoccupied bands to be equal and positive, e.g.:

$$\begin{aligned} \epsilon_{F\gamma}(\mathbf{k}) &= -\frac{1}{2} \text{ if } \gamma \leq n \\ \epsilon_{F\gamma}(\mathbf{k}) &= +\frac{1}{2} \text{ if } \gamma > n. \end{aligned} \quad (6.4)$$

Let us call the corresponding operator  $\hat{Q}$ . Note, this is related to the projection operator  $\hat{P}$  on the filled bands via  $\hat{Q} = \frac{1}{2}\mathbf{1} - \hat{P}$ . This “flat band” limit has been found to be useful in the classification of topological insulators[156], and will be used here as well. An important connection is with the correlation function  $C(\mathbf{r}, \mathbf{r}') = \langle \psi_{\mathbf{r}}^\dagger \psi_{\mathbf{r}'} \rangle$ , evaluated in the ground state. Now  $\hat{P} = \hat{C}$ , i.e. the correlation function of the band insulator, viewed as a matrix, is simply the projection operator onto the filled bands. Hence:

$$\hat{Q} = \sum_{\mathbf{r}} \frac{1}{2} \psi_{\mathbf{r}}^\dagger \psi_{\mathbf{r}} - \sum_{\mathbf{r}, \mathbf{r}'} C(\mathbf{r}, \mathbf{r}') \psi_{\mathbf{r}}^\dagger \psi_{\mathbf{r}'} . \quad (6.5)$$

describes the flat-band insulator. Since correlations in a gapped state like a band insulator fall off exponentially rapidly with separation, the effective “flat band” Hamiltonian (6.5) has essentially short ranged matrix elements, as for a physical operator. Hence, it can be viewed also as a bona fide Hamiltonian, with the same band topology as the starting Hamiltonian in Eqn. 6.2.

Most band insulators with nontrivial band topology are characterized by edge states. Consider representing the Hamiltonian of a band insulator in real space:

$$\begin{aligned} H &= \sum_{\mathbf{r}, \mathbf{r}'} \mathcal{H}(\mathbf{r}, \mathbf{r}') \psi^\dagger(\mathbf{r}) \psi(\mathbf{r}') \\ \mathcal{H}(\mathbf{r}, \mathbf{r}') &= \sum_{\gamma \mathbf{k}} \epsilon_\gamma(\mathbf{k}) \phi_{\gamma \mathbf{k}}^*(\mathbf{r}) \phi_{\gamma \mathbf{k}}(\mathbf{r}') \end{aligned} \quad (6.6)$$

A boundary along the plane  $x = 0$ , with the physical system to the right ( $x > 0$ ), is obtained by truncating the Hamiltonian:

$$\begin{aligned} \mathcal{H}^R(\mathbf{r}, \mathbf{r}') &= 0 \text{ if } x < 0 \text{ or } x' < 0 \\ \mathcal{H}^R(\mathbf{r}, \mathbf{r}') &= \mathcal{H}(\mathbf{r}, \mathbf{r}') \text{ otherwise} \end{aligned} \quad (6.7)$$

The spectrum of states localized deep in the bulk is unaffected by the cut, due to the presence of a finite gap. However, as one approaches the edge, it is possible that states appear within the bulk gap. Most topologically nontrivial insulators have protected edge states throughout the bulk gap; they cannot be removed by smooth changes of the Hamiltonian. Thus, if the Hamiltonian Eqn. 6.2 has protected edge modes, so must its “flat band” version Eqn. 6.5 when restricted to a half space.

## 6.3 The Entanglement Spectrum

Now we will review what the entanglement spectrum is, and show that the edge modes of the flat band Hamiltonian are in fact edge modes of the entanglement spectrum.

Consider the ground-state wave function of a general Hamiltonian  $H$ ,  $\Psi_G(\{a_i^R\}, \{a_i^L\})$ , where  $\{a_i^R\}$  ( $\{a_i^L\}$ ) specifies the configuration of the system to the right (left) of an imaginary

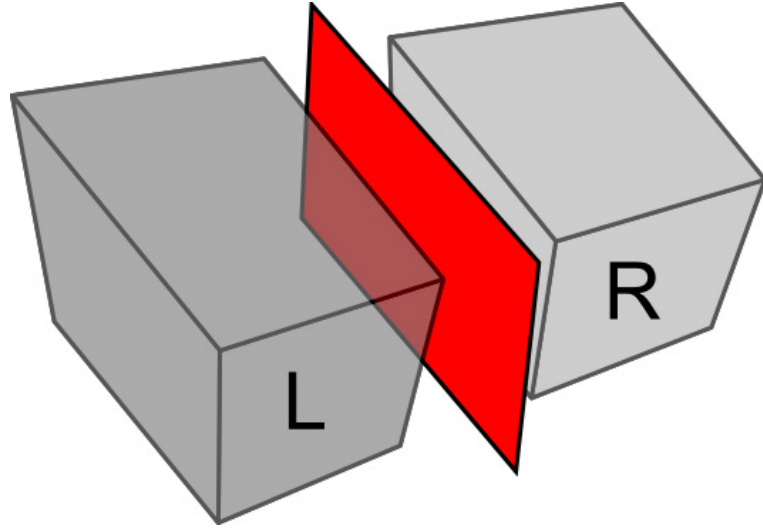


Figure 6.1. A cut that divides the physical system into two halves.

cut. Tracing out the degrees of freedom on the left, one obtains the density matrix:

$$\rho_R(\{a_i^R\}, \{\tilde{a}_i^R\}) = \sum_{\{a_i^L\}} \Psi_G(\{a_i^R\}, \{a_i^L\}) \Psi_G^*(\{\tilde{a}_i^R\}, \{a_i^L\}) \quad (6.8)$$

For a normalized wave function,  $\text{Tr}[\rho_R] = 1$ , and the eigenvalues of  $\rho_R$  lie in the range  $[0, 1]$ . Thus we can write:

$$\rho_R = Z^{-1} e^{-H_R^e}; \quad Z = \text{Tr} e^{-H_R^e}. \quad (6.9)$$

We will call  $H_R^e$  the entanglement “Hamiltonian”. The eigenvalues of the density matrix are denoted by  $\rho_\alpha = Z^{-1} e^{-E_\alpha^e}$ , where the set  $E_\alpha^e$  is termed the “entanglement spectrum”. Note, these “energies” have nothing to do with the physical energies of the system - they refer entirely to properties of the ground state, and  $Z$  is introduced in order to allow us to set the zero of “energy” conveniently.

If both the system and the cut preserve translation symmetry, one can simultaneously diagonalize the density matrix and the translation operators parallel to the cut  $T_x, T_y$ . The entanglement spectrum is then obtained as a function of momentum  $\mathbf{K}_\perp$  along the cut:  $E_\alpha^e(\mathbf{K}_\perp)$ . This object can capture fairly detailed properties of the ground-state wave function that are discussed in what follows.

For the case of single particle Hamiltonians, such as Eqn. 6.2, Ingo Peschel has shown how to determine the entanglement Hamiltonian and its eigenvalues[131]. The first step is to realize that the entanglement Hamiltonian must be quadratic in the Fermionic operators:

$$H_R^e = \sum_{r,r'} \psi_r^\dagger H_{rr'}^R \psi_{r'} \quad (6.10)$$

This can be seen, and the single particle ‘‘entanglement Hamiltonian’’  $H^R$  determined, by noting that any correlation function of operators that only involve degrees of freedom on the right is unaffected by tracing out the left half of the system. For example, consider the correlation function  $C(\mathbf{r}, \mathbf{r}') = \langle \psi_{\mathbf{r}}^\dagger \psi_{\mathbf{r}'} \rangle$ , in the ground state, before the system is cut. Now, if both coordinates  $\mathbf{r}, \mathbf{r}'$  belong to the right half of the system, then they are unaffected on tracing over the left half. Therefore, the same result should be obtained by using the density matrix for the right half:

$$\text{Tr}[\rho^{\mathbf{R}} \psi_{\mathbf{r}'}^\dagger \psi_{\mathbf{r}}] = C_R(\mathbf{r}, \mathbf{r}') \quad (6.11)$$

where  $C_R$  is the correlation function restricted to this half, namely  $C_R(\mathbf{r}, \mathbf{r}') = C(\mathbf{r}, \mathbf{r}')$  if both coordinates are on the right, and zero otherwise. A similar argument applies to multiparticle correlations. Thus, since Wick’s theorem is obeyed by correlation functions in the original uncut system, it will continue to hold for just the right half of the system in the mixed state  $\rho^{\mathbf{R}}$ . Consequently,  $\rho^{\mathbf{R}}$  must be Gaussian, i.e. the exponential of a quadratic form of Fermion operators. Requiring also conservation of particle number leads to the general form in Eqn. 6.10. An expression for  $H^R$  may be obtained by returning to two-point correlations, and requiring that the ‘‘Boltzmann’’ distribution, Eqn. 6.9, gives the expression Eqn. 6.11. One expands the Fermion operators in a basis which diagonalizes  $H^R$ ; in this basis,  $C$  becomes a diagonal matrix recording the mean occupation numbers of the states, given by the Fermi distribution. Thus  $\hat{C}_R = [1 + e^{H^R}]^{-1}$ , or:

$$H^R = \log \left[ \frac{\mathbf{1} - \hat{C}_R}{\hat{C}_R} \right] \quad (6.12)$$

Equivalently, the operator  $\hat{Q}_R = \frac{1}{2}\mathbf{1} - \hat{C}_R$ , satisfies the relation:  $\hat{Q}_R = \frac{1}{2} \tanh[\frac{1}{2}H^R]$ . Thus if  $p_i$  are the eigenvalues of  $\hat{C}_R$ , which are readily seen to satisfy  $0 \leq p_i \leq 1$ , then the eigenvalues  $\epsilon_i^e$  of the ‘single particle’ entanglement Hamiltonian  $H^R$  are obtained from Eqn. 6.12:

$$\epsilon_i^e = \log \left[ \frac{1 - p_i}{p_i} \right] \quad (6.13)$$

The many body entanglement spectrum  $E_\alpha^e$  is obtained by deciding the occupancy of the single Fermion modes, so that mode  $i$  has  $n_i^\alpha = 0, 1$ . Then  $E_\alpha^e = \sum_i n_i^\alpha \epsilon_i^e$ . The density matrix eigenstate with the largest eigenvalue is like the Fermi sea of a physical system; it corresponds to the lowest ‘‘energy’’  $E_\alpha^e$  obtained by filling all  $\epsilon_i^e < 0$ .

For a translational symmetric cut the entanglement ‘‘energy’’ can be resolved as a function of the total transverse momentum  $\mathbf{K}_\perp$  following Ref. [95]. These ‘‘energies’’ can again be built from the single particle ‘‘energies’’ of the occupied states,  $\epsilon_i^e(\mathbf{k}_\perp)$ , which are functions of the momentum parallel to the cut. The total momentum  $\mathbf{K}_\perp$  is also just the sum of the momenta of the filled single particle states. Thus, the fundamental object we will focus on is the single particle ‘‘spectrum’’ as a function of transverse momentum  $\epsilon_i^e(\mathbf{k}_\perp)$ .

## 6.4 From the Entanglement Spectrum to the Edge Modes

The previous discussion clarifies the precise connection between the entanglement spectrum and the edge spectrum of an insulator. The single particle entanglement spectrum  $\epsilon_i^e(\mathbf{k}_\perp)$  is related to the spectrum for a flat band version of a physical Hamiltonian in the presence of an edge. The eigenvalues of the flat band Hamiltonian  $\hat{Q}$  are  $\frac{1}{2} - p_i(\mathbf{k}_\perp)$  and related to the entanglement spectrum  $\epsilon_i^e(\mathbf{k}_\perp)$  via Eqn. 6.13, or:

$$\frac{1}{2} - p_i(\mathbf{k}_\perp) = \frac{1}{2} \tanh[\frac{1}{2}\epsilon_i^e(\mathbf{k}_\perp)] \quad (6.14)$$

Most states have eigenvalues  $\epsilon_i \rightarrow \pm\infty$ , because of the nonlinear relationship; the eigenvalues of  $\hat{C}$  in the bulk are 1 and 0. Very negative eigenvalues represent bulk states that are occupied, and large positive eigenvalues represent unoccupied states. In cases where topologically protected surface states of the physical Hamiltonian are expected, the flat band deformation which is topologically equivalent is also expected to have surface states, filling the whole gap between the bulk states at  $+\infty$  and  $-\infty$ .

Note however, the converse is not necessarily true. We will show in the Section 6.5 that for inversion symmetry, the edge of the flat band Hamiltonian has structure which signifies protected features of a phase, although such structure is not present in the physical surface states of a generic Hamiltonian in the same topological class.

Next we illustrate our reasoning with various examples. Let us summarize the procedure for obtaining the entanglement spectrum. The following prescription takes advantage of  $\mathbf{k}_\perp$  conservation to reduce the problem to a one-dimensional problem:

1. obtain the correlation function restricted to the right half, by summing over occupied bands. If the wave function of the filled orbitals at momentum  $\mathbf{k} = (k_x, \mathbf{k}_\perp)$  is  $\phi_{i\mathbf{k}} e^{i\mathbf{k}\cdot\mathbf{r}}$ , then:

$$C_{\mathbf{k}_\perp}^R(x, a; x', a') = \sum_{i, k_x} e^{ik_x(x-x')} \phi_{i\mathbf{k}}^*(a') \phi_{i\mathbf{k}}(a) \quad (6.15)$$

where  $\mathbf{r}$  is the unit cell position,  $i$  is the band index, and  $a$  refers to other indices such as sublattice and spin.

2. find  $C$ 's eigenvalues  $p_i(\mathbf{k}_\perp)$ , by solving the eigenvalue equation:

$$\sum_{x' a'} C_{\mathbf{k}_\perp}^R(x, a; x', a') f_{i\mathbf{k}_\perp}^R(x', a') = p_i(\mathbf{k}_\perp) f_{i\mathbf{k}_\perp}^R(x, a) \quad (6.16)$$

3. then the single particle entanglement spectrum  $\epsilon_i^e(\mathbf{k}_\perp)$  can be read off from Eqn. 6.14 and the eigenfunctions are  $f_{i\mathbf{k}_\perp}(x) e^{i\mathbf{k}_\perp \cdot \mathbf{r}_\perp}$ . We will graph our results for  $\frac{1}{2} - p_i(\mathbf{k}_\perp)$  instead of  $\epsilon_i^e(\mathbf{k}_\perp)$ , since they are monotonically related.

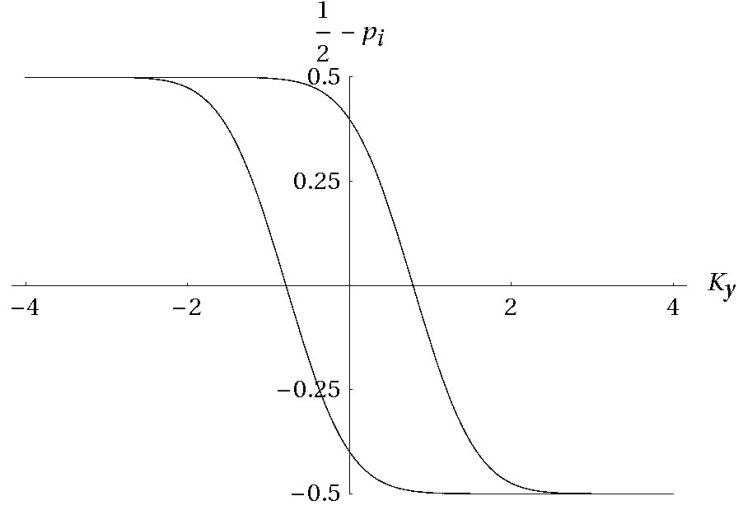


Figure 6.2. Entanglement edge states for the  $\nu = 2$  integer quantum Hall state.

### Integer quantum Hall state

The first example is based on the work of Ref. [149] on the integer quantum Hall effect. This is an especially clear illustration of the general relationship between the correlation function and the entanglement Hamiltonian. Consider electrons confined to a plane and in a strong magnetic field and exactly  $\nu$  Landau levels are fully occupied and assume there is no crystal potential. We show that the entanglement spectrum contains the expected  $\nu$  chiral edge modes. Using the Landau gauge,  $A_y = Bx$ , and labeling the states by the momentum along the cut  $k_\perp = k_y$ , the restricted correlation function is given by:  $C_{k_y}^R(x, x') = \sum_{n=1}^\nu \phi_{nk_y}^*(x')\phi_{nk_y}(x)$  where the normalized eigenstates are:

$$\phi_{nk_y}(x) = H_n(X - K_y)e^{-(X - K_y)^2/2} \quad (6.17)$$

here  $X = x/l$  and  $K_y = k_y l$  are dimensionless variables scaled by the magnetic length  $l = \sqrt{\hbar/eB}$ , and  $H_n$  are appropriately normalized Hermite polynomials.

Now, an eigenfunction of  $C_{k_y}^R$  must be constructed from linear combinations of the Landau level states  $f^a = \sum_{m=1}^\nu c_m^a \phi_m$  ( $k_y$  has been suppressed). The coefficients  $c_m^a$  are easily seen to be eigenvectors of the  $\nu \times \nu$  matrix  $F_{nm}(k_y) = \int_0^\infty dx \phi_{nk_y}^*(x)\phi_{mk_y}(x)$ . For  $\nu = 1$ , this is a number, which is the eigenvalue itself. Thus:

$$1/2 - p_0(k_y) = -\frac{1}{2}\text{erf}(K_y) \quad (6.18)$$

which interpolates between  $-1/2$  (when  $k_y = -\infty$ ) and  $+1/2$  (when  $k_y = +\infty$ ). This is the expected single chiral mode. Similarly, the  $\nu = 2$  case can be solved analytically, the result for the two eigenvalues is:

$$\frac{1}{2} - p_{1,2} = -\frac{1}{2}[\text{erf}(K_y) - e^{-K_y^2} \left( \frac{K_y}{2\sqrt{\pi}} \pm \sqrt{\frac{2 + K_y^2}{\pi}} \right)] \quad (6.19)$$

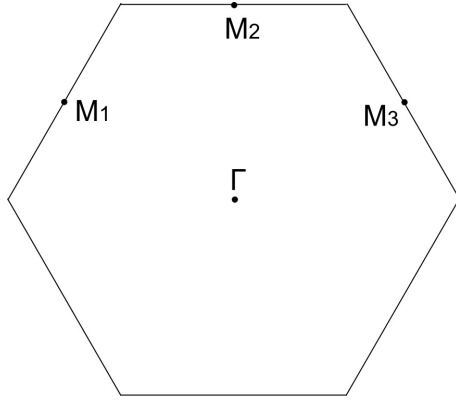


Figure 6.3. Brillouin zone of the (1,1,1) surface of the diamond lattice. The labelled points are time reversal invariant momenta.

leading to two modes as shown in Figure 6.2. These two modes are like the dispersion of two chiral particles in a one-dimensional system. In general, the entanglement Hamiltonian of a gapped system behaves like the Hamiltonian of a system with one dimension fewer. There may be infinitely many bands besides those near  $\epsilon^e = 0$ , but their “energies” rapidly approach  $\pm\infty$ .

### Three-dimensional topological insulator with time reversal symmetry

We now calculate the entanglement spectrum for a three-dimensional topological band insulator, an insulator with surface modes protected by time reversal symmetry. By explicit calculation we confirm the expectation that these modes are also captured by the entanglement spectrum, both in the case of strong and weak topological insulators.

We consider the model Hamiltonian of a topological insulator on the diamond lattice introduced in Ref. [41]:

$$H = \sum_{ij} t_{ij} c_{i\sigma}^\dagger c_{j\sigma} + 8it_{SO} \sum_{\langle\langle ik \rangle\rangle} c_{i\sigma}^\dagger (\mathbf{d}_{ik}^1 \times \mathbf{d}_{ik}^2) \cdot \sigma_{\sigma\sigma'} c_{k\sigma'} \quad (6.20)$$

where the first term contains the four nearest neighbor hopping elements which are taken as  $t$  for three of the bonds, and  $t + \delta t$  for the fourth bond oriented along the (-1,1,-1) direction. The spin orbit interaction  $t_{SO}$  appears in the second term, inducing hopping between second neighbor sites. In this term,  $\mathbf{d}_{ik}^1$ ,  $\mathbf{d}_{ik}^2$  are the two nearest neighbor bond vectors leading from site  $i$  to  $k$ , and  $\sigma$  are the spin Pauli matrices. This model respects time reversal symmetry, and also inversion symmetry, i.e.  $\mathbf{r} - \mathbf{r}_0 \rightarrow \mathbf{r}_0 - \mathbf{r}$  about a bond center  $\mathbf{r}_0$ . Without the second-neighbor hopping, the model’s bulk and surface spectra display the non-generic feature that all energy levels come in  $\pm E$  pairs at each momentum. To access a generic Hamiltonian we also include regular second-neighbor hopping  $t_2$  in all directions (not shown in Eqn. 6.20).

We now compare the physical surface states that appear in this model and the entangle-

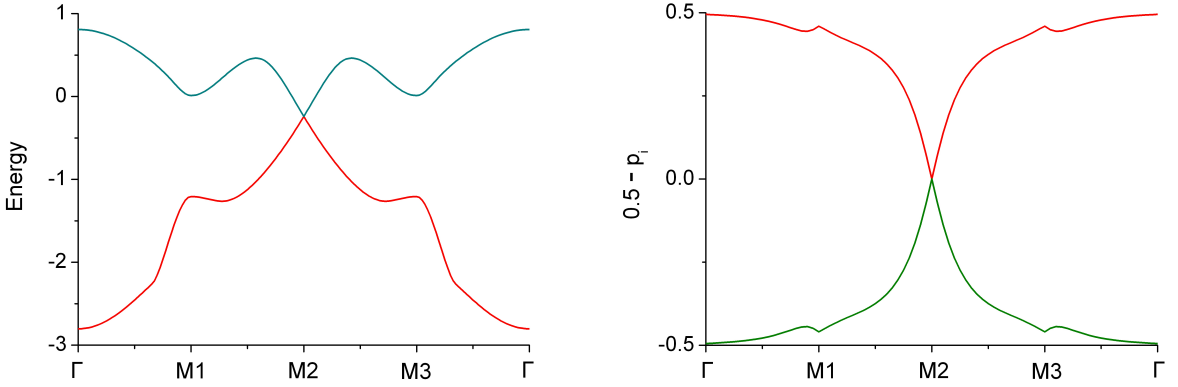


Figure 6.4. Strong topological insulator: a) the dispersion of the physical surface states. Note that the node is not at zero energy, since particle-hole symmetry is broken; b) The entanglement spectrum,  $\frac{1}{2} - p_i$ , which has the node at zero  $\epsilon^e$ , in spite of broken particle-hole symmetry.

ment spectrum of a cut with the same orientation. We choose a surface normal to the (1,1,1) direction so as to cut bonds with strength  $t$ . One obtains a strong topological insulator, with an odd number of surface Dirac nodes if  $\delta t > 0$  (assuming  $t > 0$ ). The surface states computed for a single surface are shown in Figure 6.4a, and a single Dirac node characteristic of the strong topological insulator is obtained. The node is centered at the time reversal invariant  $M2$  point of the surface Brillouin Zone (BZ) (see Figure 6.3). This is selected by the direction of the strong bond  $t + \delta t$ . Note that the surface spectrum is not symmetric between positive and negative energies, as it would be if the model were particle-hole symmetric.

We briefly describe the computation that gives us the entanglement spectrum in the figures. Essentially, we follow the three step procedure outlined in the beginning of Section 6.4, where  $\mathbf{k}_\perp$  is a momentum on the surface BZ. Instead of dealing with a pair of semi-infinite systems  $R, L$ , it is more convenient to divide a periodic system into two parts, one part whose reduced density matrix is computed, and another part that is traced over. This gives us two entanglement surfaces, but since they are well separated by a gapped region, the spectra are essentially independent, and we only plot those whose wave functions are concentrated near one of the cuts. For the numerics we have taken the separation to be 80 unit cells thick, and we have taken the following parameters in the Hamiltonian Eqn. 6.20:  $t = 1.0$ ,  $t_{SO} = 0.125$ ,  $\delta t = 1$  ( $-0.9$ ),  $t_2 = 0.1$  for the strong (weak) topological insulator. The bulk energy bands as well as the entanglement spectrum eigenvalues near  $1/2 - p = \pm 1/2$  are not shown for clarity.

In Figure 6.4b, we display the two surface eigenvalues of the single particle entanglement spectrum  $\epsilon_i^e(\mathbf{k}_\perp)$ , obtained from the ground state of the Hamiltonian in Eqn. 6.20 by dividing the system into two halves. The plane that divides the system is oriented in the same way as the physical boundary previously discussed. It is more convenient to display  $\frac{1}{2} \tanh(\frac{\epsilon_i^e(\mathbf{k}_\perp)}{2})$  which is related to the eigenvalues  $p_i(\mathbf{k}_\perp)$  of the correlation function  $C_R$  via  $\frac{1}{2} \tanh(\frac{\epsilon_i^e(\mathbf{k}_\perp)}{2}) =$

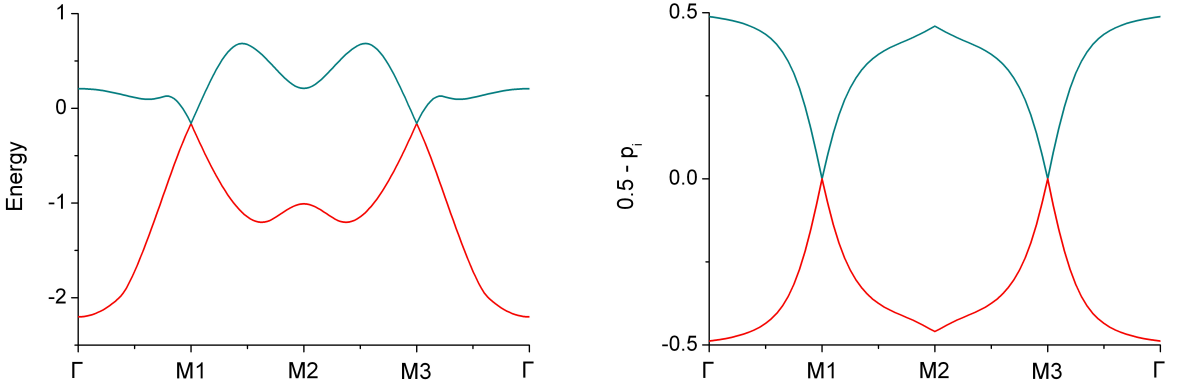


Figure 6.5. Weak topological insulator: a) The dispersion of the physical surface states; b) the entanglement spectrum.

$\frac{1}{2} - p_i(\mathbf{k}_\perp)$ . Note zero ‘‘energy’’,  $\epsilon_i^e(\mathbf{k}_\perp) = 0$ , also corresponds to the zero of  $\frac{1}{2} - p_i$ . Clearly, we see that the entanglement spectrum also displays the same characteristics as the protected surface modes. There is a single Dirac cone which is centered at the same point in the surface BZ as the surface state itself. The ‘‘energy’’ of this Dirac cone is curiously zero and we will discuss more about this in Section 6.5.

Similarly, if we choose  $\delta t < 0$ , we obtain a weak topological insulator, whose physical surface states for the same surface as above and entanglement spectrum are compared in Figure 6.5. Again, the Dirac nodes of the physical surface states and their location in the BZ fixed by band topology, are captured by the entanglement spectrum.

This has demonstrated that when a protected physical surface state is present, this is reflected in the entanglement spectrum. That the Dirac nodes in the entanglement spectrum are centered at zero, in contrast to the physical surface spectrum in the same model, is an important observation. Moreover, the entire entanglement spectrum remains symmetric under  $\epsilon^e \rightarrow -\epsilon^e$ ,  $\mathbf{k}_\perp \rightarrow -\mathbf{k}_\perp$ . We will see that this is a consequence of inversion symmetry, and the Dirac node in the entanglement spectrum remains secure even when time reversal invariance is broken. This is shown in Figure 6.6. The physical spectrum of the surface states Figure 6.6a is gapped because of a uniform Zeeman field  $H_T = h \sum_i c_i^\dagger \sigma_z c_i$  applied to every site, with  $h = 0.9$ . However, the entanglement spectrum Dirac node remains intact in Figure 6.6b, despite the loss of time reversal symmetry. When both time reversal symmetry and inversion symmetry are destroyed via an additional staggered potential  $H_I = V \sum_i (-1)^i c_i^\dagger c_i$  with  $V = 0.1$ , the entanglement spectrum is also gapped as in Figure 6.7b.

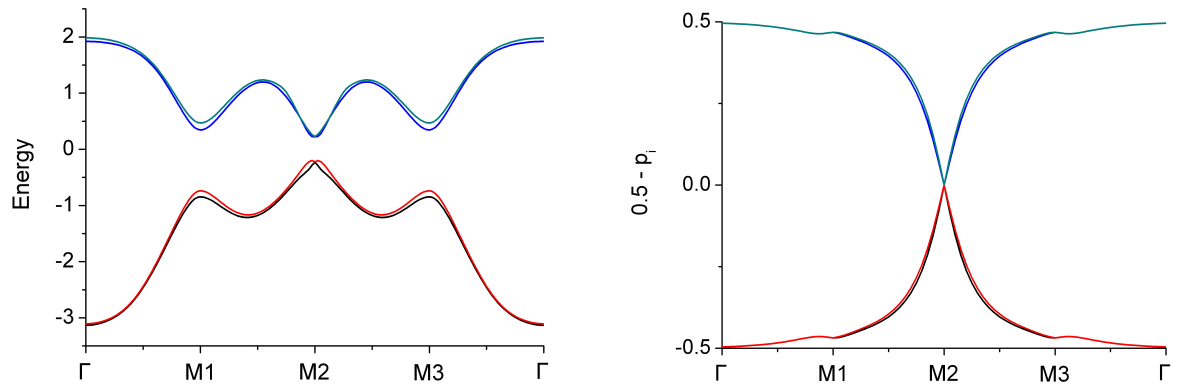


Figure 6.6. Inversion symmetric insulators with broken time reversal symmetry. Note the physical surface states (a) are gapped, but the Dirac node remains in the entanglement spectrum (b).

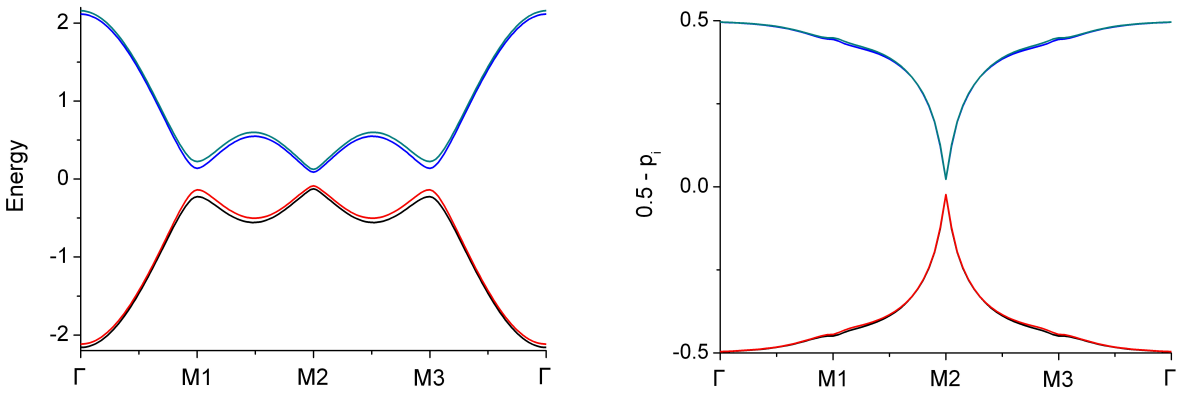


Figure 6.7. Without inversion symmetry and time reversal symmetry, both the physical surface state (a) and the entanglement spectrum (b) are gapped.

## 6.5 Topological Insulator with only Inversion Symmetry

We now discuss the origin of Figure 6.6, where the entanglement spectrum still has a Dirac node at zero entanglement “energy”, although the surface states are gapped after a perturbation breaking time-reversal symmetry has been added. Therefore, while a system with topologically protected surface states also has topologically protected entanglement states, the converse may not be true. The Dirac node is a feature in the entanglement spectrum of inversion symmetric insulators, which defines a distinct phase, although there are no generical topological surface states for the physical Hamiltonian. The entanglement spectrum is an especially useful tool for identifying insulators of this type. In this section, we describe how this symmetry constrains the entanglement states, and use this to prove the stability of the entanglement Dirac node. Then we discuss what physical difference could be embodied in this topologically distinct entanglement spectrum.

Why the entanglement spectrum works for identifying phases with inversion symmetry, while physical surface states fail? A physical boundary necessarily breaks inversion, since inversion maps the insulator to its exterior. But now consider a cut that passes through a center of inversion. The inversion  $\mathcal{I}$  through this point relates the left and right sides of an entanglement cut. This inversion symmetry leads to a symmetry of the entanglement Hamiltonian, and realized as a sort of particle-hole symmetry for the two-dimensional entanglement spectrum, also see Ref. [135, 136].

To see why inversion symmetry acts as a particle-hole symmetry, we give an additional interpretation of the entanglement eigenstates  $f_{i\mathbf{k}_\perp}^R$ . The entanglement spectrum can be understood intuitively by showing that a set of wave functions for the full system[16, 82]:

$$F_{i\mathbf{k}_\perp}(x, \mathbf{r}_\perp) = \left[ \sqrt{\mathbf{p}_i(\mathbf{k}_\perp)} \mathbf{f}_{i\mathbf{k}_\perp}^R(\mathbf{x}) + \sqrt{1 - \mathbf{p}_i(\mathbf{k}_\perp)} \mathbf{f}_{i\mathbf{k}_\perp}^L(\mathbf{x}) \right] e^{i\mathbf{k}_\perp \cdot \mathbf{r}_\perp} \quad (6.21)$$

can be constructed with two properties: first, the  $f^R$ 's and  $f^L$ 's form an orthonormal family of wave functions in the two halves. Second, filling all the states  $F_{i\mathbf{k}_\perp}$  gives the band insulator, i.e. they can be obtained from the filled band wave functions Eqn. 6.6 by a unitary transformation.

Eqn. 6.21 leads to an intuitive way of understanding the entanglement spectrum, reviewed in Appendix B.4. The eigenvalues  $p_i(\mathbf{k}_\perp)$  have a simple interpretation in light of Eqn. (6.21). Each state  $F_{i\mathbf{k}_\perp}$  is certainly occupied by an electron in the band insulator, and the eigenvalue  $p_i(\mathbf{k}_\perp)$  represents the probability that the electron in this state is found on the right half. For example, when  $p_i \approx 1$ , the electron in  $F_i$  is almost certainly on the right half. This fits with the previous definition of the  $f^R$ 's, since the corresponding  $\epsilon_i \rightarrow -\infty$  is far below the “Fermi energy”, so the  $i^{\text{th}}$  state is almost occupied in the “Fermi sea” of the entanglement Hamiltonian.

Because of the inversion symmetry, there is a map  $\mathcal{I}_S$  on the single-particle states that takes a state  $f_{i\mathbf{k}_\perp}^R$  to another state  $f_{i-\mathbf{k}_\perp}^R$  and flips the sign of the entanglement “energy”,  $\epsilon_i^e(-\mathbf{k}_\perp) = -\epsilon_i^e(\mathbf{k}_\perp)$ . The mapping arises directly from inversion symmetry acting on the  $F$ 's

(see Figure 6.8a), which produces from any occupied state  $F_i$  with momentum  $\mathbf{k}_\perp$  a second state,  $F_{\bar{i}}$ , with the opposite momentum:

$$F_{\bar{i}-\mathbf{k}_\perp}(x, \mathbf{r}_\perp) = F_{i\mathbf{k}_\perp}(-x, -\mathbf{r}_\perp) \quad (6.22)$$

Expanding this equation gives:

$$\begin{aligned} & \left[ \sqrt{p_{\bar{i}}(-\mathbf{k}_\perp)} f_{\bar{i}-\mathbf{k}_\perp}^R(x) + \sqrt{1-p_{\bar{i}}(-\mathbf{k}_\perp)} f_{\bar{i}-\mathbf{k}_\perp}^L(x) \right] e^{-i\mathbf{k}_\perp \cdot \mathbf{r}_\perp} \\ &= \left[ \sqrt{p_i(\mathbf{k}_\perp)} f_{i\mathbf{k}_\perp}^R(-x) + \sqrt{1-p_i(\mathbf{k}_\perp)} f_{i\mathbf{k}_\perp}^L(-x) \right] e^{-i\mathbf{k}_\perp \cdot \mathbf{r}_\perp} \end{aligned} \quad (6.23)$$

Since inversion maps the left-hand side to the right-hand side, these equations imply that  $p_{\bar{i}}(-\mathbf{k}_\perp) = 1 - p_i(\mathbf{k}_\perp)$  and that  $f_{\bar{i}}^R$  is obtained from a state on the other side of the partition, namely  $f_{\bar{i}-\mathbf{k}_\perp}^R(x) = f_{i\mathbf{k}_\perp}^L(-x)$ . Using the relation between  $p$  and  $\epsilon$ , it follows that a mode with “energy”  $\epsilon^e$  and momentum  $\mathbf{k}_\perp$ , is mapped by inversion to one with  $-\epsilon^e$  and  $-\mathbf{k}_\perp$ .

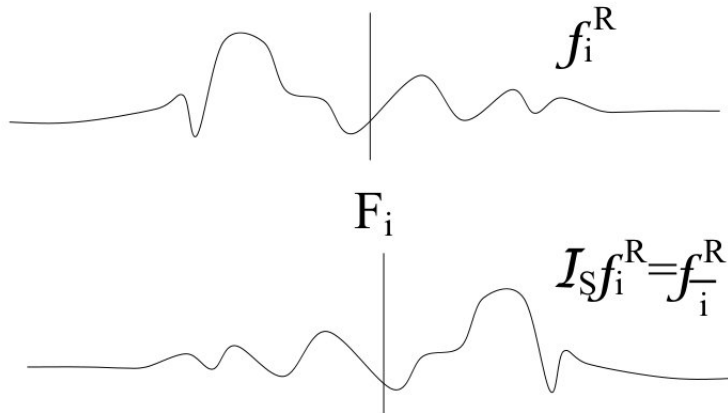
Having established the action of inversion, we now turn to the stability of Dirac modes in the entanglement spectrum in the presence of inversion. A Dirac mode in the entanglement spectrum (or physical surface spectrum) occurs at a time reversal invariant momentum (TRIM)  $\kappa_\perp$ , half of a reciprocal lattice vector, i.e.,  $\kappa_\perp \in \{\Gamma, M1, M2, M3\}$ , so that  $\kappa_\perp \equiv -\kappa_\perp$  modulo the reciprocal lattice.

First consider the modes in the unperturbed crystal, that is both time-reversal and inversion symmetric. There are two degenerate states at the Dirac points  $f_{a\kappa_\perp}^R, f_{b\kappa_\perp}^R$ . They must have  $\epsilon^e = 0$ , otherwise applying  $\mathcal{I}_S$  would produce a second Dirac point. Then, the symmetry  $\mathcal{I}_S$  ensures that these Dirac modes have to remain at zero “energy” when time-reversal symmetry is broken by a small perturbation. The inversion parities of these two states must be the same because the states formed a Kramers doublet under time-reversal symmetry before it was broken, so they transform into themselves under  $\mathcal{I}_S$  and linear combinations of them are inversion eigenstates. Therefore the states  $f_{a\kappa_\perp}^R$  and  $f_{b\kappa_\perp}^R$  cannot evolve into a pair  $f_{+,\kappa_\perp}^R, f_{-,\kappa_\perp}^R$  with “energies”  $\pm\epsilon^e$ , without a discontinuous change in the inversion parities. A more algebraic proof of this result is in Appendix B.4.

Note, in general, the spectrum consists of equal numbers of states that are even under inversion and odd under inversion. All the pairs of states at nonzero entanglement “energy” can be combined into pairs of states of opposite parity, since  $f_{\epsilon,\mathbf{k}_\perp} \rightarrow f_{-\epsilon,-\mathbf{k}_\perp}$ , and one can take symmetric and antisymmetric combinations of these. The only exceptions are states at zero “energy” located at a TRIM Dirac nodes. Thus, the number of ungappable states is given by  $\Delta\nu_{\kappa_\perp}$ , the difference between the number of even and odd states at the TRIM  $\kappa_\perp$ .

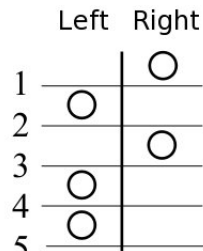
$\Delta\nu_{\kappa_\perp}$  cannot change except at a phase transition of the bulk crystal, where the entanglement spectrum becomes ill-defined or changes discontinuously. At a second order transition, in particular, this topological invariance breaks down because the entanglement Hamiltonian, Eqn. 6.5, has long-range hopping and infinitely many bulk bands collapse to zero “energy”, in analogy with the observations of Ref. [132]. The states may then all mix together.

The parity argument shows that there is a distinct phase of inversion symmetric insulators defined by having a protected Dirac dispersion in the entanglement spectrum. What

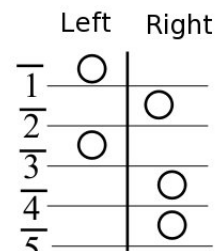


$\mathcal{I}F_i$

(a)



$|\chi_R\rangle$



$\mathcal{I}|\chi_R\rangle \quad \mathcal{M}\mathcal{I}|\chi_R\rangle$

(b)

Figure 6.8. (a) The transformation  $\mathcal{I}_S$  of a single-body wave function. The image of a state  $f^R$  under  $\mathcal{I}_S$  is not defined on the merits of  $f^R$  itself, but instead depends on the state of the system, the extended wave function  $F_i = \sqrt{p_i}f_i^R + \sqrt{1-p_i}f_i^L$ , and  $\mathcal{I}_S f^R$  is the right-hand part of this up to normalization, which can look completely different from the original  $f^R$ . (b) The transformation  $\mathcal{MI}$  of many-body states in a non-interacting system. Each term in the Schmidt decomposition is obtained by placing electrons on either the right or left of the  $F_i$ 's indicated by the horizontal lines. Inversion applies to the system as a whole. Focusing on the half right-hand side of the system, inversion induces a particle-hole like transformation because levels  $i$  that are occupied in  $|\chi_R\rangle$  correspond to empty levels  $\bar{i}$  in  $\mathcal{MI}|\chi_R\rangle$ .

physical property distinguishes this phase? Clearly, surface states are not the answer since all physical surface states are gapped. At least one distinction is captured by the electromagnetic response of the system[32, 138]. Consider integrating out the fermions in the presence of weak external electromagnetic fields, the effective action contains:

$$S_\theta = i\theta \left[ \frac{e^2}{2\pi h} \int d\tau d^3x \mathbf{E} \cdot \mathbf{B} \right]. \quad (6.24)$$

Inversion symmetry and time reversal symmetry each imply that  $\theta$  is quantized in units of  $\pi$ . Under time reversal, the sign of this term is changed since  $\mathbf{B} \rightarrow -\mathbf{B}$ . However, this does not rule out nonzero  $S_\theta$ , since it contributes a factor of  $e^{-S_\theta}$  to the weight of a field configuration in the path integral, so  $\theta$  and  $\theta + 2\pi$  are physically equivalent, given the term in square brackets is an integer for periodic boundary conditions in space and imaginary time. Hence  $S_\theta$  is effectively time reversal invariant as long as  $\theta$  is 0 or  $\pi$ . Furthermore, if the system only possesses inversion symmetry in the bulk, then one can argue  $\mathbf{E} \rightarrow -\mathbf{E}$  under inversion instead for the quantization of  $\theta$ .

The nonzero value  $\theta = \pi$ , is realized in strong topological insulators, time-reversal symmetric systems with an odd number of surface Dirac nodes[32, 138]. It is therefore natural also to suppose that an insulator with an odd number of entanglement nodes, but with only inversion symmetry, has an electromagnetic response of  $\theta = \pi$ . Indeed, this remains true even for inversion symmetric insulators that cannot be obtained by perturbing time-reversal symmetric insulators[176], see chapter 5. The entanglement spectrum gives us a very simple way to predict how the insulator responds to an electromagnetic field based solely on ground-state properties.

The physical meaning of  $S_\theta$  is that applying a magnetic field induces a parallel polarization of charge of magnitude  $\theta \frac{e^2}{2\pi h} \mathbf{B}$ . It is challenging to measure this, but still in principle a physical consequence of the entanglement nodes. The locations and numbers of nodes are also invariant, at least without interactions, but we do not know the physical consequences of these properties.

## 6.6 Inversion Symmetry and Many-body Spectrum

Thus far, we have discussed topological properties of systems without interactions. An interesting question is how many of the topological distinctions remain when the interactions between electrons are taken into account. When surface states exist, one can determine whether interactions affect their properties by studying whether the interactions are “relevant perturbations” to the field theory of the Dirac modes[41]. Furthermore, the bulk magnetoelectric polarizability remains quantized even when interactions are included. But the entanglement spectrum remains gapless even when there are no surface states and captures quantum numbers not accounted for by  $\theta$ : at the very least, we believe the values of  $\frac{1}{2}\Delta\nu_{\kappa\perp}$  are conserved modulo 2 at each transverse TRIM.

To describe inversion symmetry in an interacting state, one must understand how it acts on the many body states appearing in the Schmidt decomposition. Inversion turns out to be related to an anti-unitary operator,  $|\chi^R\rangle \rightarrow \mathcal{MI}|\chi^R\rangle$ , where the operators are defined below. The action of this symmetry is most interesting when restricted to the even-split Schmidt states, where half the  $N$  particles are on each side of the divider. Here, it satisfies  $(\mathcal{MI})^2 = -1$  when there are an odd number of Dirac nodes. Thus, inversion behaves exactly like the Kramers transformation, and each Schmidt state is doubly degenerate even with interactions included. Interestingly, fermion anticommutation is a key ingredient in establishing this fact. It has been shown recently that inversion acts on one-dimensional Haldane chains in a similar way[135, 136].

Consider the action of inversion symmetry  $\mathcal{I}$  on the many body Schmidt states

$$|\Psi_G\rangle = \sum_a e^{-E_a^e/2} |\Phi_a^R\rangle |\Phi_a^L\rangle. \quad (6.25)$$

Inversion maps a right-hand state to a left-hand one. Since this is a symmetry, the two must have the same entanglement eigenvalue  $E_a^e$ . Thus, if each eigenvalue has a non-degenerate eigenstate, the inversion transformation is simple: each state maps to its partner up to a phase. Things get more interesting when degenerate states are present in the entanglement spectrum.

Consider a multiplet of even-split states  $|\Phi_a^R\rangle$ , where we use the label  $a = 1, \dots, d$  to label the  $d$  degenerate states in the Schmidt basis above, Eqn. 6.25. Its image under inversion is a linear combination of states on the left:

$$|\Phi_a^R\rangle \rightarrow \sum_{b=1}^N I_{ba} |\Phi_b^L\rangle \quad (6.26)$$

If inversion is to be viewed as a symmetry to make statements about the entanglement eigenstates of a single subsystems, we need to return to the right portion of the system, see Figure 6.8b. Indeed, inversion can be converted to a symmetry of just one side using the pairing of left and right states in the Schmidt decomposition in Eqn. 6.25. This pairing is described by a transformation  $\mathcal{M}$  which maps  $|\Phi_a^L\rangle \rightarrow |\Phi_a^R\rangle$ . This rule can be extended consistently to an antilinear transformation on the rest of the Hilbert space for the left side of the system.

To see this, let us describe the partner of a general state  $|\chi^L\rangle$  on the left in a basis-independent way:

$$\mathcal{M}|\chi^L\rangle = \langle \chi^L | \rho_R^{-\frac{1}{2}} |\Psi_G\rangle. \quad (6.27)$$

The right-hand side is a partial inner product. It is not a number but a wave function for the right half of the system since only the degrees of freedom on the left half are summed over:

$$\mathcal{M}|\chi_L\rangle = \sum_{\{a_i^L\}} \Psi_G(\{a_i^R\}, \{a_i^L\}) \chi^{L*}(\{a_i^L\}) |\{a_i^R\}\rangle \quad (6.28)$$

where  $\{a_i^L\}, \{a_i^R\}$  are the variables describing the two halves.

Note that this is antilinear in  $|\chi^L\rangle$  because of the complex conjugation. Now,  $|\chi^L\rangle = \sum_a c_a |\Phi_a^L\rangle$  is mapped by this transformation to  $\sum_i c_a^* |\Phi_a^R\rangle$ . In particular, each Schmidt state maps to its partner. Eqn. 6.27 utilizes the ground state to connect the left and right halves, and the operator  $\rho_R^{-\frac{1}{2}}$  is there to strip off the different Schmidt weights.

Now the combination of  $\mathcal{M}$  and  $\mathcal{I}$  is a stand-in for inversion symmetry that returns states on the right-hand side of the cut back to the right-hand side; in the basis of Schmidt states, this transformation is represented by  $KI$  where  $K$  is complex conjugation and  $I$  is the matrix in Eqn. 6.26.

When  $\mathcal{MI}$  is performed twice, the state must return to itself, modulo a phase, hence:

$$II^* = \mathbf{1} e^{i\phi}. \quad (6.29)$$

This phase factor can be only  $\pm 1$  because it has to be real. More precisely, the operator  $(\mathcal{MI})^2$  has to have the same value  $(-1)^\delta$  for each Schmidt state which has half the electrons on each side, since the wave function Eqn. 6.1 is a parity eigenstate, see a more detailed proof in Appendix B.4.

The case  $I \cdot I^* = -\mathbf{1}$  is specially interesting. Time reversal symmetry of spin  $1/2 + n$  particles has the same property, which can be used to prove Kramers' degeneracy. This algebra has no one-dimensional representation. A two-dimensional representation is exemplified by:

$$I = \begin{pmatrix} 0 & -1 \\ 1 & 0 \end{pmatrix} \quad (6.30)$$

the antisymmetric matrix. Whenever the inversion operator in a particular system obeys this algebra, all levels must be at least doubly degenerate.

This is indeed how the inversion operator acts in the even-split states when there is an odd number of Dirac nodes. For an explicit example, we determine the value  $II^* = \pm 1$  for topological insulators in the noninteracting limit. This also allows us to make statements about the interacting case, since the value cannot jump when small interactions are introduced.

The ground state of the noninteracting system can be built up by creating particles in all the modes  $F_i$  in Eqn. 6.21. Suppose there is just one Dirac node. Then:

$$\begin{aligned} |\Psi_G\rangle &= \frac{1}{2}(r_a^\dagger + l_a^\dagger)(r_b^\dagger + l_b^\dagger) \\ &\times \prod_{\substack{i\mathbf{k}_\perp \\ p_i(\mathbf{k}_\perp) > \frac{1}{2}}} (\sqrt{p_i(\mathbf{k}_\perp)} r_{i\mathbf{k}_\perp}^\dagger + \sqrt{1-p_i(\mathbf{k}_\perp)} l_{i\mathbf{k}_\perp}^\dagger) \\ &\times \prod_{\substack{i\mathbf{k}_\perp \\ p_i(\mathbf{k}_\perp) < \frac{1}{2}}} (\sqrt{p_i(\mathbf{k}_\perp)} r_{i\mathbf{k}_\perp}^\dagger + \sqrt{1-p_i(\mathbf{k}_\perp)} l_{i\mathbf{k}_\perp}^\dagger) |0\rangle \end{aligned} \quad (6.31)$$

where:

$$\begin{aligned} r_{i\mathbf{k}_\perp}^\dagger &= \sum_{\mathbf{r}} e^{i\mathbf{k}_\perp \cdot \mathbf{r}_\perp} f_{i\mathbf{k}_\perp}^R(\mathbf{r}) \psi(\mathbf{r})^\dagger \\ l_{i\mathbf{k}_\perp}^\dagger &= \sum_{\mathbf{r}} e^{i\mathbf{k}_\perp \cdot \mathbf{r}_\perp} f_{i\mathbf{k}_\perp}^L(\mathbf{r}) \psi(\mathbf{r})^\dagger \end{aligned} \quad (6.32)$$

are the Dirac node states. Expanding Eqn. (6.31) gives the Schmidt decomposition. One should convince oneself of the following relation between the many-body transformations  $\mathcal{MI}$  and the one body implementation of inversion,  $\mathcal{I}_S$ : if  $|\chi_R\rangle$  is one of the Schmidt states, and  $f_i^R$  is occupied in this state, then  $\mathcal{I}_S f_i^R$  is empty in  $\mathcal{MI}|\chi_R\rangle$ , see Figure 6.8b.

Note that the second line of Eqn. 6.31 contains the states that are mostly on the right, and the third contains those mostly on the left. Inversion maps these states to one another. The two states at the Dirac node are inversion eigenstates, and they also have the same parity, so they map to themselves  $r_{a,b} \leftrightarrow l_{a,b}$ .

The highest weight states in the Schmidt decomposition of the wave function involve acting with  $r_i^\dagger$ 's when  $p_i > 1/2$  and with  $l_i^\dagger$ 's when  $p_i < 1/2$ , so these states are contained in

$$\frac{1}{2}(r_a^\dagger + l_a^\dagger)(r_b^\dagger + l_b^\dagger)|S_R\rangle|S_L\rangle \quad (6.33)$$

where  $|S_R\rangle$  and  $|S_L\rangle$  are the filled Fermi seas for the two sides, which are exchanged by  $\mathcal{I}$ .

Among the highest weight states, consider the two states:

$$|pair\rangle = r_a^\dagger l_b^\dagger |S_R\rangle|S_L\rangle + l_a^\dagger r_b^\dagger |S_R\rangle|S_L\rangle \quad (6.34)$$

with an equal number of fermions in the two sides. While these are converted into each other under inversion, it seems possible that they could mix and split, and give rise to one-dimensional representations of the inversion operation. We will show that the inversion matrix  $I$  satisfies  $II^* = -\mathbf{1}$ .

We can get  $|pair\rangle$  into the form of the Schmidt decomposition if we define the states:

$$\begin{aligned} |\Phi_1^R\rangle &= r_a^\dagger |S_R\rangle & |\Phi_1^L\rangle &= l_b^\dagger |S_L\rangle \\ |\Phi_2^R\rangle &= -r_b^\dagger |S_R\rangle & |\Phi_2^L\rangle &= l_a^\dagger |S_L\rangle \end{aligned} \quad (6.35)$$

The ground state can be written as the Schmidt sum:

$$|\Psi_0\rangle = s \frac{1}{2}(|\Phi_1^R\rangle|\Phi_1^L\rangle + |\Phi_2^R\rangle|\Phi_2^L\rangle) + \dots \quad (6.36)$$

$s$  is an unimportant sign due to Fermi statistics, see Appendix B.4.

Inversion maps:

$$\begin{aligned} |\Phi_1^R\rangle &\mapsto |\Phi_2^L\rangle \\ |\Phi_2^R\rangle &\mapsto -|\Phi_1^L\rangle \end{aligned} \quad (6.37)$$

while  $\mathcal{M}$  simply maps  $|\Phi_{1,2}^L\rangle$  to  $s|\Phi_{1,2}^R\rangle$ , so the inversion matrix is  $I^* = \begin{pmatrix} 0 & -s \\ s & 0 \end{pmatrix}$ . The crucial minus sign has arisen because of anticommutation of fermion operators.

The inversion matrix satisfies  $I \cdot I^* = -\mathbf{1}$ , and the states remain two fold degenerate. As mentioned above, this result persists for any state with equal numbers of fermions on the two sides. When interactions are included, the even-split states all mix together, but  $I$  can

be enlarged to describe the action of inversion on the whole space.  $I \cdot I^*$  remains  $-\mathbf{1}$ , so the degeneracies survive. Unlike the usual Kramers degeneracy for time-reversal, this result does not require an odd number of fermions.

For a more general topological insulator, one can show that  $I \cdot I^* = (-1)^\delta \mathbf{1}$  where  $\delta$  is the number of pairs of equal-parity single-body states with  $\epsilon^e = 0$ , i.e. the number of Dirac nodes.

## 6.7 Preserved Distinctions against Interactions

We suggest that some distinctions among insulators survive the introduction of interactions. While this will the quantized electromagnetic response of inversion symmetric insulators[138], which remains well defined in the interacting case as a response function, other more mysterious distinctions are also found.

Without interactions,  $\frac{1}{2}\Delta\nu_{\kappa\perp}$  is a fixed integer for each TRIM. With interactions, we give an argument that suggests that at least the number of Dirac nodes at each  $\kappa$ ,  $\frac{1}{2}\Delta\nu_{\kappa\perp}$ , is well-defined modulo 2 in an inversion symmetric insulator. In particular, the location of a single surface Dirac node in the Brillouin zone survives the introduction of interactions. The analogous quantity in the time reversal invariant insulator is the “weak” indices[41, 105, 151], which can be determined from the surface states[41] or metallic topological defects in the crystal[144]. Yet no analogous physical consequence seems available when time reversal symmetry is broken but inversion symmetry is retained.

These distinctions can be found by looking at a sample with  $2N_y + 1 \times 2N_z + 1$  unit cells in the  $y - z$  cross-section but infinite in the  $x$ -direction perpendicular to the cut. We have seen that, in a noninteracting insulator, the parities of the zero-“energy” single-body states determine whether there are many-body degeneracies. When only the Dirac nodes at certain TRIMs will satisfy the boundary conditions, the value of  $(\mathcal{MI})^2$  count the number of nodes at these TRIMs.

For periodic boundary conditions, the allowed transverse momenta will be  $(\frac{2\pi n_y}{2N_y+1}, \frac{2\pi n_z}{2N_z+1})$ . The only allowed TRIM is  $(0, 0)$ , thus all states come in pairs related by inversion symmetry except for unpaired states  $\frac{1}{\sqrt{2}}(l_{a,b}^\dagger + r_{a,b}^\dagger)$  at zero momentum. Therefore  $\delta = \frac{1}{2}\Delta\nu_{(0,0)}$  and there is a double degeneracy only if this is odd.

To isolate TRIMs, introduce antiperiodic boundary conditions along one or both of the directions. Then double degeneracy occurs when the number of modes at the newly allowed TRIM is odd.

It is possible that the actual integer values of the  $\Delta\nu$ ’s are conserved also when interactions are introduced, but there might be a more surprising classification of interacting phases. Refs. [35, 78] gave an example that an integer property of topological phases can be changed for one-dimensional topological insulators when interactions are included.

## 6.8 Conclusion

We have studied the entanglement spectrum of insulators with non-trivial band topology. Whenever a physical edge or surface state is present, the entanglement spectrum is also characterized by protected modes. Although this is purely bulk property of ground-state wave function, we showed that it can be mapped to the edge spectrum of a “flat band” version of the physical Hamiltonian.

Entanglement spectrum may succeed better and provide a unique perspective on characterizing topological phases. Protected modes in entanglement spectrum may occur in systems that do not possess physical surface states, in cases when a physical surface necessarily breaks an underlying symmetry of the bulk - for example the inversion symmetry. We illustrated this with three-dimensional insulators with inversion symmetry.

Another advantage of entanglement spectrum is that it allows to deduce properties that remain stable when interactions are present. For the case of inversion symmetric insulators, characteristic properties protected against interactions are discussed beyond the quantized magnetoelectric polarizability. The corresponding physical consequences remain to be identified.

# Chapter 7

## Entanglement Entropy of Critical Spin Liquids

### 7.1 Introduction

Entanglement properties of a ground-state wave function can serve as a diagnostic for characterizing a phase of matter[31]. Such a characterization is especially useful when a phase does not break any symmetry and consequently does not offer a local order parameter. Two examples of this observation are the presence of a non-zero topological entanglement entropy in a fully gapped topological ordered state[53, 55, 79, 93] and the relation between the edge state spectrum and the entanglement spectrum for the quantum Hall states[95]. Entanglement thus encodes fundamental properties of a quantum phase, and intersects diverse fields including quantum information, many body physics and high energy theory[31].

Critical spin-liquids are a distinct class of states that also do not have a local order parameter. These gapless states are less well understood compared to the gapped spin-liquids which have topological order. Interestingly though, a large class of experiments suggest that they may well have been already realized in certain organic materials[60, 122, 165, 199], which are quantum antiferromagnets on the triangular lattice. To gain a deeper understanding of these phases, in this chapter we investigate the quantum structure of a class of critical spin-liquids from an information theoretic point of view. We demonstrate that entanglement properties of model ground states can be calculated, even on fairly large systems involving  $> 324$  spins. In contrast to quantum Monte Carlo[58], we deal with non-positive wave functions that potentially describe ground states of frustrated quantum magnets.

Both gapped as well as gapless spin-liquids may be obtained within a slave-particle approach[190], where one expresses the spin operator in terms of a product of operators

( $f$ ), denoting emergent particles:  $\vec{S} = f_\sigma^\dagger \frac{\vec{\sigma}_{\sigma\sigma'}}{2} f_{\sigma'}$ . In a spin liquid phases, these emergent particles are the appropriate low energy excitations. Inevitably, they appear coupled to gauge fields. Gapped spin liquids are described by topological quantum field theories and are relatively well understood. In contrast, spin-liquids with gapless, strongly interacting excitations (critical spin liquids), are described by matter-gauge theories which are harder to analyze[3, 52, 89, 110].

A critical spin liquid, the spinon fermi sea (SFS) state, has been invoked[47, 90, 108] to account for the intriguing phenomenology of aforementioned triangular lattice organic compounds [60, 122, 165, 199]. In the SFS state, the  $f$  particles hop on the triangular lattice sites giving rise to a Fermi sea, while strongly interacting with an emergent ‘electromagnetic’  $U(1)$  gauge field. The metal like specific heat and thermal conductivity seen in these materials is potentially an indication of the spinon Fermi surface. A candidate ground-state spin wave function for the SFS state suggested by the slave-particle formalism, is obtained by projecting out all doubly occupied states from the Fermi sea wave function. This Gutzwiller projection technique works well in one dimension. There, the projected Fermi sea spin wave function captures long distance properties of the Heisenberg chain, and is even the exact ground state of the Haldane-Shastry Hamiltonian[50, 163]. Similar rigorous results are not available in two dimensions. However, the Gutzwiller projected Fermi sea is known to have excellent variational energy for the  $J_2 - J_4$  spin model on the triangular lattice, which is believed to be appropriate for the forementioned triangular lattice compounds[108]. Detailed comparisons between the projected wave function and exact numerics have also been made[15].

Using the Variational Monte-Carlo technique, we calculate the bipartite entanglement entropy, in particular Renyi entropy  $S_2$  of a critical spin liquid - the conjectured spinon Fermi sea state on the triangular lattice. We find a violation of the boundary law, with  $S_2$  enhanced by a logarithmic factor, an unusual result for a bosonic wave function strongly suggesting the presence of emergent fermions with a Fermi surface. This is also consistent with the recent exact numerical studies on multi-leg ladder spin-1/2 ring exchange models where the central charge is found to increase in proportion to the number of legs[15]. We also calculate Renyi entropy for an algebraic spin liquid state[190, 192] obtained by Gutzwiller projecting the wave function of free Fermions on a  $\pi$  flux square lattice. This state is found to obey the area law, consistent with the presence of emergent Dirac fermions in the system. Finally, we calculate Renyi entropy for projected Fermi sea state on the square lattice. Here a nested Fermi sea is present before projection. In this case the projection is found to result in long range magnetic order (see also Ref. [96]) and a significant reduction in entanglement entropy, especially of the area law violating term, compared to the unprojected Fermi gas. These different trends are found to set in even at relatively small system sizes, suggesting that this probe may be applied in the context of exact diagonalization and DMRG.

## 7.2 Renyi Entanglement Entropy and Monte Carlo Evaluation

Given a normalized wave function,  $|\phi\rangle$ , and a partition of the system into subsystems  $A$  and  $B$ , one can trace out the subsystem  $B$  to give a density matrix on  $A$ :  $\rho_A = \text{Tr}_B |\phi\rangle\langle\phi|$ . The Renyi entropies are defined by:

$$S_n = \frac{1}{1-n} \log(\text{Tr}\rho_A^n) \quad (7.1)$$

It is common to pay special attention to the von Neumann entropy,  $S_1 = -\text{Tr}[\rho_A \log \rho_A]$  (obtained by taking the limit  $n \rightarrow 1$ ). However, the Renyi entropies seem equally good measures of entanglement as they share many properties with von Neumann entropy  $S_1$ . Here we will focus on  $S_2 = -\log(\text{Tr}\rho_A^2)$ . For ground states of local Hamiltonians, both  $S_1$  and  $S_2$  are expected to follow a boundary law, i.e. they only grow as the surface area of the boundary of region  $A$  [31]. A well known violation occurs for critical phases in one dimension, where in contrast to a constant as expected from the area law,  $S_1, S_2 \sim \log L_A$ , where  $L_A$  is the size of system  $A$  embedded inside an infinite line[62, 169]. In higher dimensions,  $D = 2, 3$  an area law is believed to hold for  $S_1, S_2$  even for gapless states such as ordered phases with goldstone modes, and quantum critical points[19, 58, 100, 152]. Both  $S_1, S_2$  violate the area law in higher dimensions for free fermions with a Fermi surface[44, 194] and also share identical topological entanglement entropies for gapped phases[36]. Therefore  $S_2$  seems as good a measure of physical properties as the von Neumann entropy, and is often easier to calculate[58] as we detail now for our problem. Furthermore we note the inequality  $S_1 \geq S_2$ . This will be important when we find violation of area law for  $S_2$  as this would imply area law violation for the von Neumann entropy  $S_1$  as well.

Consider the wave function  $\phi(a, b)$ , where  $a$  ( $b$ ) be the configuration of subsystem A (B). The Renyi entropy  $S_2$  is conveniently expressed by imagining two copies of the system. Construct the product wave function:  $|\Phi\rangle = \sum_{a,b,a',b'} \phi(a, b)\phi(a', b')|a, b\rangle|a', b'\rangle$ , and define the Swap <sub>$A$</sub>  operator[58], which swaps the configurations of the  $A$  subsystem in the two copies: Swap <sub>$A$</sub>  $|a, b\rangle|a', b'\rangle = |a', b\rangle|a, b'\rangle$  then it is easily shown:

$$e^{-S_2} = \frac{\langle\Phi|\text{Swap}_A|\Phi\rangle}{\langle\Phi|\Phi\rangle} \quad (7.2)$$

This can be rewritten in a form suitable for Monte Carlo evaluation. Defining configurations  $\alpha_1 = a, b$ ,  $\alpha_2 = a', b'$  and  $\beta_1 = a', b$ ,  $\beta_2 = a, b'$ :

$$\langle\text{Swap}_A\rangle = \sum_{\alpha_1\alpha_2} \rho_{\alpha_1} \rho_{\alpha_2} f(\alpha_1, \alpha_2) \quad (7.3)$$

Here  $f(\alpha_1, \alpha_2) = \frac{\phi_{\beta_1}\phi_{\beta_2}}{\phi_{\alpha_1}\phi_{\alpha_2}}$  is averaged by sampling with the normalized weights:

$$\rho_{\alpha_i} = |\phi_{\alpha_i}|^2 / \sum_{\alpha_i} |\phi_{\alpha_i}|^2 \quad (7.4)$$

The Gutzwiller projected wave functions we will consider can be written as products of determinants. Such wave functions can be efficiently evaluated, which forms the basis for Variational Monte Carlo technique[45]. Since the entanglement entropy is at the very least expected to scale as the length of the boundary of subsystem  $A$ ,  $\sim L_A$ ,  $\langle \text{Swap}_A \rangle$  is at least exponentially small in  $L_A$ . Evaluating this small quantity may pose a problem - one solution called the ‘ratio trick’ discussed in Ref. [58] in the valence bond basis unfortunately does not work in our case, since the relevant states do not always have non-vanishing overlap unlike in that basis.

A more serious problem arises from the fact that  $f(\alpha_1, \alpha_2)$  is not necessarily positive, for the wave functions we will study. This is in contrast to Quantum Monte Carlo studies with positive ground-state wave functions[58]. With time reversal symmetry,  $f(\alpha_1, \alpha_2)$  is real but can fluctuate in sign. The calculational effort for  $\langle \text{Swap}_A \rangle$  is then found to scale exponentially with  $L_A$ . Although Variational Monte Carlo schemes are generally free of the fermionic sign problem, we encounter a mild variant here. Below we partially mitigate this by introducing a ‘sign trick’ algorithm that separates  $\text{Swap}_A$  into a product of two factors, both calculable within Variational Monte Carlo. This renders the calculation doable within few percent error for boundary sizes  $L_A \lesssim 10$ . For positive wave functions (i.e. ones that obey Marshall sign) we find an immense simplification, and the calculational cost only scales polynomially with  $L_A$  as in conventional Variational Monte Carlo. For a fixed value of boundary  $L_A$ , the cost of computation always scales polynomially with the total system size  $L$  irrespective of the wave function.

*Sign Trick:* After some algebra (see Chapter 8.2 and Appendix C.3 for detail), Eqn. 7.2 can in general be rewritten as a product of two averages:

$$\begin{aligned} \langle \text{Swap}_A \rangle &= \sum_{\alpha_1 \alpha_2} \rho_{\alpha_1} \rho_{\alpha_2} |f(\alpha_1, \alpha_2)| \left[ \sum_{\alpha_1 \alpha_2} \tilde{\rho}_{\alpha_1, \alpha_2} e^{i\phi(\alpha_1, \alpha_2)} \right] \\ &= \langle \text{Swap}_{A, \text{mod}} \rangle \langle \text{Swap}_{A, \text{sign}} \rangle \end{aligned} \quad (7.5)$$

For real wave functions, the phase factor reduces to a sign. Empirically, we find this leads to significant gains, the advantages are detailed in Appendix C.3.

We benchmarked our algorithm for three free fermion tight binding problems on: 1) A one-dimensional chain of  $L = 200$  sites with  $L_A$  up to 100 sites, 2) An  $18 \times 18$  square lattice with the linear size  $L_A$  up to 7 sites. 3) A honeycomb (graphene) lattice with Dirac dispersion. We find very good agreement with the exact results (see Appendix C.3) that were calculated using the correlation matrix technique[133].

## 7.3 Entanglement Entropy of Gutzwiller Projected Wave Functions

Next we calculate Renyi entropy for the problems of our actual interest namely projected Fermi liquid wave functions which are considered good ansatz for ground states of critical spin-liquids. We analyze two different classes of critical spin-liquids: states that at the slave-particle mean-field level have a full Fermi surface of spinons and those with only nodal fermions. For a triangular lattice with uniform hopping  $t_{rr'} = t$  one obtains a Fermi surface of spinons at the mean-field level while for a square-lattice with  $\pi$  flux through every plaquette (i.e.  $\Pi_{\square} t_{rr'} = -1$ ) one obtains nodal Dirac fermions. We also study the projected wave function on square lattice with uniform hopping (and no flux).

The wave functions for these spin-liquids are constructed by starting with a system of spin-1/2 fermionic spinons  $f_{r\alpha}$  hopping on a finite lattice of size  $L_1 \times L_2$  at half-filling with a mean field Hamiltonian:  $H_{MF} = \sum_{rr'} [-t_{rr'} f_{r\sigma}^\dagger f_{r'\sigma} + h.c.]$ . The spin wave function is given by  $|\phi\rangle = P_G |\phi\rangle_{MF}$  where  $|\phi\rangle_{MF}$  is the ground state of  $H_{MF}$  and the Gutzwiller projector  $P_G = \prod_i (1 - n_{i\uparrow} n_{i\downarrow})$  ensures exactly one fermion per site. The sign-structure of the projected wave function depends markedly on the underlying lattice. For a bipartite lattice with  $t_{rr'}$  non-zero and real only for the opposite sublattices, one can prove that the wave function satisfies the Marshall sign rule (see Appendix C.2). Thus, for a bipartite lattice, one only needs to calculate  $\langle \text{Swap}_{A,\text{mod}} \rangle$  since  $\langle \text{Swap}_{A,\text{sign}} \rangle$  trivially equals unity. The projected wave function for the square lattice with and without  $\pi$ -flux (as well as that for the one-dimensional Haldane-Shastry state) satisfies the Marshall's sign rule while that for the triangular lattice doesn't. We discuss these three cases separately. The one-dimensional case was previously discussed in Ref. [23].

*Triangular lattice:* As mentioned above the mean-field ansatz describes a spin-liquid with spinons hopping on a triangular lattice. We consider a lattice with total size  $18 \times 18$  on a torus and the region  $A$  of square geometry with linear size  $L_A$  upto 8 sites. We find a clear signature of  $L_A \log L_A$  scaling in Renyi entropy (Figure 7.1). This is rather striking since the wave function is a spin wave function and therefore could also be written in terms of hard-core bosons. This result strongly suggests the presence of an underlying spinon Fermi surface. In fact the coefficient of the  $L_A \log L_A$  term is rather similar before and after projection. This observation may be rationalized by picturing a two-dimensional Fermi surface as a collection of many independent one-dimensional systems in momentum space, each giving rise to a  $\log L$  contribution. Gutzwiller projection then just removes a single charge degree of freedom.

It is interesting to compare the contribution to  $S_2$  from  $S_{2,\text{sign}} \equiv -\log(\langle \text{Swap}_{A,\text{sign}} \rangle)$  and  $S_{2,\text{mod}} \equiv -\log(\langle \text{Swap}_{A,\text{mod}} \rangle)$  separately. Numerically,  $S_{2,\text{sign}}$  appears to be responsible for the logarithmic violation of the area law (Figure 7.1). This suggests that the sign structure of the wave function is crucial at least in this case. The area-law violation of the Renyi entropy for Gutzwiller projected wave functions substantiates the theoretical expectation that an underlying Fermi surface is present in the spin wave function.

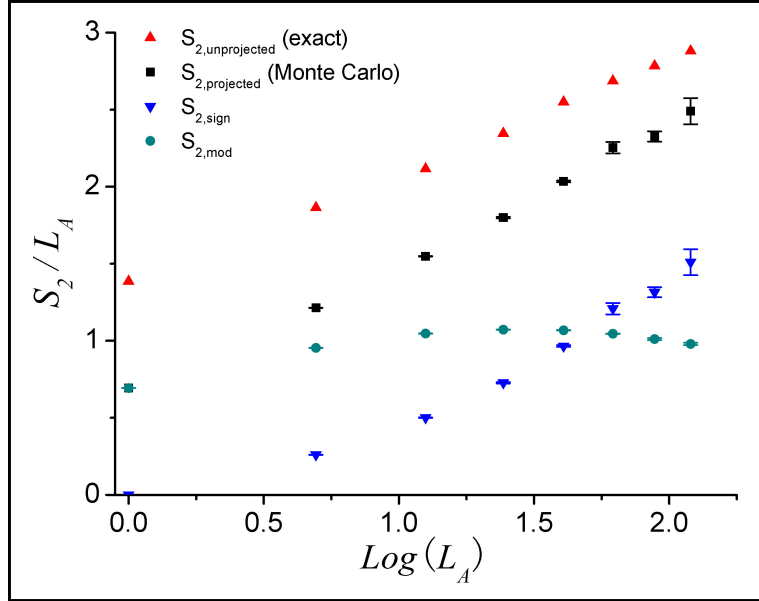


Figure 7.1. Renyi entropy data for projected and unprojected Fermi sea state on the triangular lattice of size  $18 \times 18$  with  $L_A = 1 \dots 8$ . Note, projection barely modifies the slope, pointing to a Fermi surface surviving in the spin wave function. We also separately plot  $S_{2,\text{sign}}$  and  $S_{2,\text{mod}}$  (as defined in the text) for the projected state, the former dominates at larger sizes.

*Square lattice with  $\pi$  flux:* The mean-field ansatz consists of spinons with Dirac dispersion around two nodes, say,  $(\pi/2, \pi/2)$  and  $(\pi/2, -\pi/2)$  (the locations of the nodes depend on the gauge one uses to enforce the  $\pi$  flux). The projected wave function has been proposed in the past as the ground state of an algebraic spin liquid. The algebraic spin-liquid is believed to be describable by a strongly coupled conformal field theory of Dirac spinons coupled to a non-compact  $SU(2)$  gauge field[190, 192]. Because of this the algebraic spin-liquid has algebraically decaying spin-spin correlations. We verify this explicitly for the projected wave function on a  $36 \times 36$  lattice (see Figure 7.2) using Variational Monte Carlo method as well as the technique explained in Ref. [128]. This state is different from that in Ref. [201], where Majorana fermions are coupled to a discrete  $Z_2$  gauge field making them effectively free at low energies, in contrast to our critical state.

Square lattice being bipartite, the projected wave function satisfies Marshall's sign rule and hence we were able to perform Monte Carlo calculation of Renyi entropy on bigger lattice sizes compared to the triangular lattice case. We chose the overall geometry as a torus of size  $L_A \times 4L_A$  with both region  $A$  and its complement of sizes  $L_A \times 2L_A$  (the total boundary size being  $L_A + L_A = 2L_A$ ). We considered  $L_A$  upto 14 sites. We found that the projected wave function follows an area law akin to its unprojected counterpart (Figure 7.3) and has the scaling  $S_2 \approx 0.30L_A + g$  where  $g \approx 1.13$  is a universal constant that depends only on the aspect ratio of the geometry[19, 152]. This is consistent with the presence of Dirac fermions at low energies.

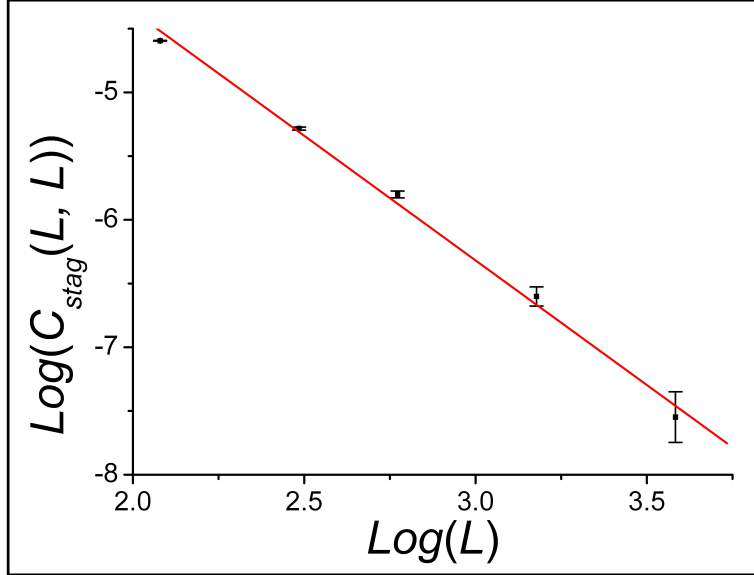


Figure 7.2. Staggered spin-spin correlations for the projected  $\pi$ -flux state on the square lattice for linear sizes  $L$  upto 36 sites. The correlations show algebraic decay  $\sim 1/r^{1+\eta}$  with  $\eta \approx 0.96$ .

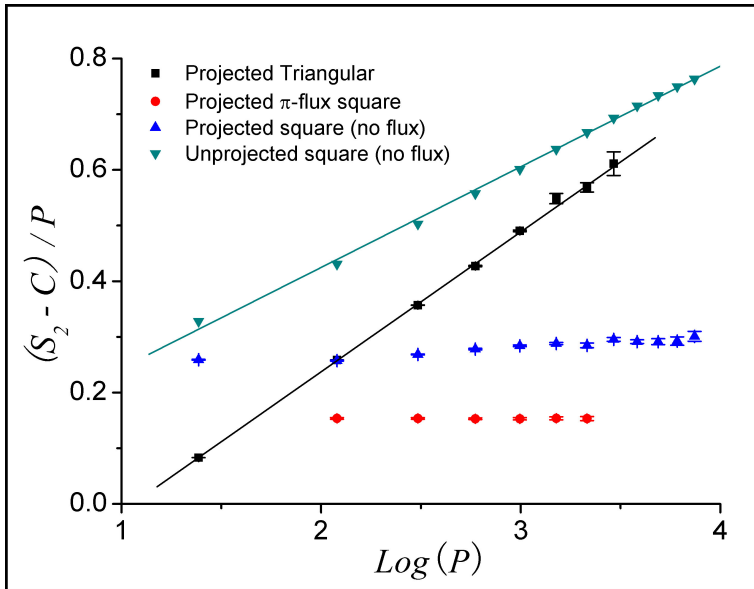


Figure 7.3. Renyi entropy for the projected Fermi sea state on the triangular lattice and square (with and without  $\pi$ -flux) lattice as a function of the perimeter  $P$  of the subsystem  $A$ . Here  $C$  is the constant part of the  $S_2$ . We find  $S_2 \sim P \log(P) + C$  for the projected triangular lattice state while  $S_2 \sim P + C$  for the projected  $\pi$ -flux square lattice state. For the square lattice state (no flux), the projection leads to a significant reduction in  $S_2$  suggesting at most a very weak violation of the area-law.

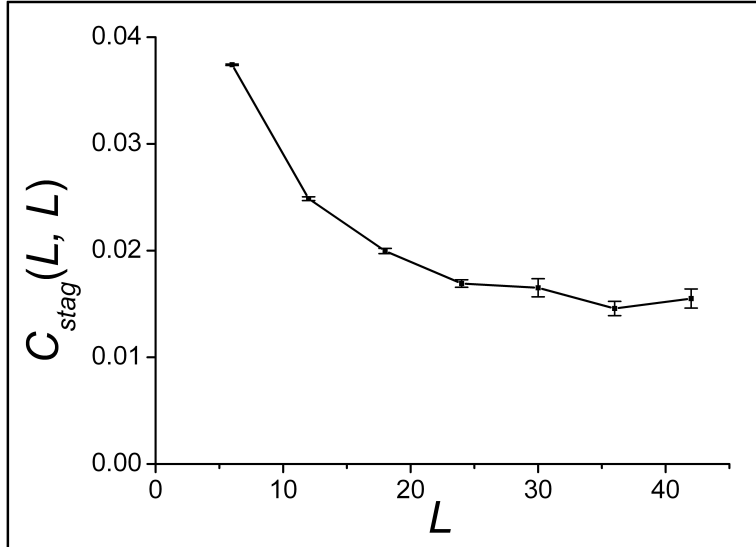


Figure 7.4. Staggered spin-spin correlations for the projected Fermi sea state on the square lattice.  $C(L/2, L/2)$  saturates at a finite value at large distances ( $L_{\max} = 42$ ) indicating the presence of long range anti-ferromagnetic order.

*Square lattice without any flux:* The unprojected Fermi surface is nested. Since projection amounts to taking correlations into account, one might wonder whether the Fermi surface undergoes a magnetic instability after the projection. Indeed, we found non-zero magnetic order in the projected wave function, consistent with an independent recent study Ref. [96]. This was verified by calculating staggered spin-spin correlations on a  $42 \times 42$  lattice (see Figure 7.4). Renyi entropy calculations were done on a lattice of total size  $24 \times 24$  with region  $A$  being a square upto size  $12 \times 12$ . The results are shown in the Figure 7.3. Though it is difficult to rule out presence of a partial Fermi surface from Renyi entropy, there is a significant reduction in the Renyi entropy as well as the coefficient of  $L_A \log L_A$  term as compared to the unprojected Fermi sea.

## 7.4 Conclusion

In this chapter we described a route to calculating the Renyi entropy  $S_2$  for a wide variety of wave functions that can handled by the Variational Monte Carlo method. Our starting point is the ground-state wave function rather than the Hamiltonian. This allows us to study interesting states on relatively large systems, that may not be obtainable from sign problem free Hamiltonians. We calculated  $S_2$  for Gutzwiller projected states that have been conjectured as the ground-state wave functions for gapless spin-liquids. We found that the projected Fermi sea on the triangular lattice violates the area law strongly indicating the presence of an emergent Fermi surface of neutral fermions. The sign structure of the wave function makes a dominant contribution to the entropy. We note our algorithm is readily

generalizable to calculate the higher Renyi entropies  $S_n$  ( $n > 2$ ). Also, it can be applied to study partially projected Fermi sea wave function which model correlated Fermi liquids. This opens a window to study the entanglement entropy of fermions away from the free limit. A very interesting direction that we leave for the future, is testing the Widom conjecture, proposed currently for free fermions[44], to interacting states with Fermi surfaces.

# Chapter 8

## Topological Entanglement Entropy of Spin Liquids and Lattice Laughlin States

### 8.1 Introduction

Quantum Spin Liquids(SLs) are states that arise from the collective behavior of spins, but are not characterized by a Landau order parameter. They are associated with remarkable phenomena such as fractional quantum numbers[4], transmutation of statistics (eg. fermions appearing in a purely bosonic model)[81, 145], and enabling otherwise impossible quantum phase transitions[160], to name a few. SLs may be gapless or gapped. While current experimental candidates for SLs appear to have gapless excitations[60, 122, 165, 199], gapped SLs are indicated in numerical studies on the Kagome[200] and honeycomb lattice[99]. Gapped SLs are characterized by topological order - i.e. ground-state degeneracy that depends on the topology of the underlying space[190].

Recently, a novel characterization of gapped SLs has emerged using quantum entanglement in terms of the Topological Entanglement Entropy (TEE)[53, 55, 79, 93]. This quantity takes a fixed value  $\gamma$  in a topologically ordered phase and remarkably can be calculated just knowing the ground-state wave function. The entanglement entropy of a two-dimensional disc shaped region  $A$  in a gapped phase obeys  $S_2 = al_A - \gamma$ , where a smooth boundary of length  $l_A$  is assumed to surround the region. By carefully subtracting off the leading dependence, the constant  $\gamma$  can be isolated. It is argued to be a characteristic of the phase,

$\gamma = \log D$ , where  $D$  is the quantum dimension of the phase[79, 93]. For the Abelian states discussed here,  $D^2$  is identical to the ground-state degeneracy on the torus.

Gapped SLs can be viewed as a state where each spin forms a singlet with a near neighbor, but the arrangement of singlets fluctuates quantum mechanically so it is a liquid of singlets. Theoretical models of this singlet liquid fall roughly into two categories. In the first, the singlets are represented as microscopic variables as in quantum dimer and related models[9, 101, 102, 150, 159], and are suggested by large N calculations[146, 153]. Topological order can then be established by a variety of techniques including exact solution and most recently quantum entanglement[20, 42, 54, 65, 127]. In contrast there has been less progress establishing topological order in the second category, which are  $SU(2)$  symmetric spin systems where valence bonds are emergent degrees of freedom. Anderson proposed constructing an  $SU(2)$  symmetric SL wave function by starting with a BCS state[4], derived from the mean field Hamiltonian:

$$H = - \sum_{rr'} \{ t_{rr'} f_{\sigma,r}^\dagger f_{\sigma,r'} + \Delta_{rr'} f_{\uparrow,r}^\dagger f_{\downarrow,r'}^\dagger \} + h.c. \quad (8.1)$$

and Gutzwiller projecting it so that there is exactly one fermion per site, hence a spin wave function. Variants of these are known to be good variational ground states for local spin Hamiltonians (see e.g. [47, 108, 174]) and are more viable descriptions of most experimental and  $SU(2)$  symmetric liquids. Approximate analytical treatments of projection, that include small fluctuations about the above mean field state, indicate that at least two kinds of gapped SLs can arise: chiral SLs[71, 72, 189] and  $Z_2$  SLs [146, 153, 158, 188]. However, given the drastic nature of projection, it is unclear if the actual wave functions obtained from this procedure are in the same phases. In this chapter we use TEE to establish topological order for of  $SU(2)$  symmetric chiral and  $Z_2$  SL wave functions. We show that the recently developed Monte Carlo technique used to study entanglement properties of gapless SLs[204] can be applied here as well to extract TEE for system sizes large enough (144 spins) so that it approaches its quantized value. Instead of using the more standard Von Neumann entropy, we focus on the Renyi entropy, which carries the same contribution from the TEE for both non-chiral[36] and chiral[26] states for a topologically trivial bipartition. The fact that the wave function is a determinant or product of determinants in these cases allows for its efficient evaluation. For a model of the chiral SL, the calculated TEE are remarkably accurate, within few percent of the expected  $\log \sqrt{2}$  value. To our knowledge, this is the first clear demonstration of topological order via TEE in  $SU(2)$  symmetric spin wave functions.

We also study lattice versions of the Laughlin  $\nu = 1/3$  state, which are obtained by a similar projective construction, although these are fermionic, not spin wave functions. Again we can extract TEE which is within 7% of the expected value to confirm these are in the same phase as the Laughlin state, although they differ significantly in microscopic structure.

We note earlier numerical work extracting TEE include exact digitalization studies on small systems, looking at quantum Hall Laughlin states[56, 85, 208] and perturbed Kitaev toric code models[54]. Recently, a quantum Monte Carlo study used TEE to detect  $Z_2$  topological order[65]. In contrast to the states studied here, this was a positive definite wave function, with  $U(1)$  rather than  $SU(2)$  spin symmetry. Our wave-function-only approach is ready-made for searching for topological order when one has a good variational ansatz

for a ground state, irrespective of whether the state is positive definite or not. Finally, we note that Ref. [66, 129] studied topological order in ‘nodal’  $Z_2$  SLs by constructing four orthogonal low energy states on the torus, and Ref. [201] studied TEE for the Kitaev model. This chapter has its major contribution from a previously published work in Ref. [205].

The format of this chapter and main results are summarized in the section below.

In Section 8.2 the TEE  $\gamma$  is defined, and an algorithm to calculate it numerically utilizing the Renyi entanglement entropy  $S_2$  is outlined. This is then applied to a series of topological phases, the results of which are summarized in Table 8.1.

(i) The first is a Chern insulator, built out of a square lattice tight binding model at half filling, in which the filled band has unit Chern number. For a lattice with  $2N$  sites, this is an  $N$  body Slater determinant  $\Phi(r_1, \dots, r_N)$ . Since this is an integer quantum Hall state, it is not expected to possess topological order. Indeed, calculation is consistent with a vanishing TEE, see Table 8.1 first row.

(ii) The chiral SL wave function is obtained from the wave function of  $2N$  spinful electrons with this tight binding band structure, by projecting out all double occupancies, and studied in Section 8.3. The chiral SL wave function can be written as a product of two Slater determinants, i.e.  $\Psi(r_1, r_2, \dots, r_N) = \mathcal{M}\Phi^2(r_1, \dots, r_N)$ , where  $\mathcal{M}$  an unimportant Marshall sign factor. If we view up spin as a hardcore boson, then this is the wave function analogous to half filled Landau level  $\nu = 1/2$  of bosons. It is therefore expected to have  $\gamma = \log \sqrt{2}$ . Indeed, for a particular choice of parameters with a large gap, numerical calculation (second and third rows of Table 8.1, with different linear dimensions  $L_A$  of the smallest subregions involved) yields a value very close to this. Detailed finite size analysis obtained by varying the correlation length of the chiral SL is presented in Section 8.3, providing further evidence for convergence to the expected value. We note that this wave function is  $SU(2)$  symmetric, and non-positive-definite, since the ground state is not time reversal symmetric.

(iii) Note, the construction of the chiral SL above is similar to the Laughlin construction of fractional quantum Hall states by taking products of the integer quantum Hall states. Extending the construction above, one can write wave functions for  $N$  fermions  $\Psi_{1/3}(r_1, r_2, \dots, r_N) = \Phi^3(r_1, \dots, r_N)$ , a lattice version of the Laughlin  $\nu = 1/3$  state. The entanglement entropy calculation for  $\Psi_{1/3}$  agrees well with what is expected for the topological order for  $\nu = 1/3$  Laughlin state, indicating it is in the same phase, despite not being constructed from lowest Landau level states. Note, since they differ significantly in microscopic detail from the Laughlin state, wave-function overlap is not an option in establishing that they are in the same phase. Also, calculating entanglement spectra[95] is currently not feasible for these wave functions, thus TEE appears to be the ideal characterization. Similarly, the lattice analog of Laughlin  $\nu = 1/4$  state for bosons, obtained via  $\Psi_{1/4}(r_1, r_2, \dots, r_N) = \Phi^4(r_1, \dots, r_N)$ , is found to have a TEE close to the expected  $\gamma = \log \sqrt{4}$ , as discussed in Section 8.4.

(iv) Finally, we construct a fully gapped  $Z_2$  SL wave function on the square lattice. For the largest system sizes we considered, the calculated  $\gamma$  is only 42% of the expected  $\log 2$  value(last row in Table 8.1). The difference is ascribed to larger finite size effects, as discussed in Section 8.5.

State	Expected $\gamma$	$\gamma_{\text{calculated}}/\gamma_{\text{expected}}$
Unprojected ( $\nu = 1$ )	0	-0.0008 $\pm$ 0.0059 *
Chiral SL $L_A=3$	$\log \sqrt{2}$	$0.99 \pm 0.03$
Chiral SL $L_A=4$	$\log \sqrt{2}$	$0.99 \pm 0.12$
Lattice $\nu = 1/3$	$\log \sqrt{3}$	$1.07 \pm 0.05$
Lattice $\nu = 1/4$	$\log \sqrt{4}$	$1.06 \pm 0.11$
$Z_2$ SL $L_A=4$	$\log 2$	$0.42 \pm 0.15$

Table 8.1. Comparison between calculated TEE and expected value from field theory(second column) for topological phases. The \* denotes that the calculated value is not divided by the expected value since the latter vanishes.

## 8.2 Topological Entanglement Entropy and Variational Monte Carlo Method

Given a normalized wave function  $|\Phi\rangle$  and a partition of the system into subsystems  $A$  and  $B$ , one can trace out the subsystem  $B$  to obtain the reduced density matrix on  $A$ :  $\rho_A = Tr_B |\Phi\rangle \langle \Phi|$ . The Renyi entropies are defined as:

$$S_n = \frac{1}{1-n} \log (Tr \rho_A^n) \quad (8.2)$$

Taking the limit  $n \rightarrow 1$ , this recovers the definition of the usual von Neumann entropy. In this chapter we will focus on the Renyi entropy with index  $n = 2$ :  $S_2 = -\log (Tr (\rho_A^2))$ , which is easier to calculate with our Variational Monte Carlo(VMC) method[204], see also Appendix C.

For a gapped phase in two dimensions with topological order, a contractible region  $A$  with smooth boundary of length  $l_A$ , the Area Law of the Renyi entropy becomes:

$$S_2 = al_A - \gamma \quad (8.3)$$

where we have omitted the sub-leading terms. Although the coefficient  $a$  of the leading boundary law' term is non-universal, the sub-leading constant  $\gamma$  is universal, and this TEE is a robust property of the phase of matter for which  $|\Phi\rangle$  is the ground state. It is given by  $\gamma = \log D$ , where  $D$  is the total quantum dimension of the model[79, 93], and offers a partial characterization of the underlying topological order. When region  $A$  has a disc geometry, it has been shown that  $\gamma$  for different Renyi indices  $n$  are identical for both chiral and non-chiral states[26, 36]. A simple limit where this is readily observed[53, 55, 93] is in a model wave function of a  $Z_2$  SL, which is an equal superposition of loops ( $Z_2$  electric field). This is achieved as a ground state in Kitaev's toric code model[80]. The Schmidt decomposition into wave functions in regions  $A$  and  $B$  can be indexed by the configuration of electric field lines piercing the boundary of the disc. If  $i = 1, 2, \dots, l$  are  $l$  bonds going through the boundary between region  $A$  and  $B$ , the presence (absence) of electric field lines

on bond  $i$  is denoted by  $q_i = 1$  ( $q_i = 0$ ). Since the loops are closed, we require  $\sum_i q_i = \text{even}$ . It can be shown that the wave function is simply an equal weight decomposition indexed by all possible configurations of  $q_i$ . There are  $C = 2^{l-1}$  of them, the global constraint of closed loops accounting for the missing factor of 2. Then:

$$|\Psi\rangle = \frac{1}{\sqrt{C}} \sum_{q_1 + \dots + q_l \text{ even}} |\Psi_{q_1 \dots q_l}^A\rangle |\Psi_{q_1 \dots q_l}^B\rangle \quad (8.4)$$

This implies there are  $C$  equal eigenvalues of the region A density matrix, each equal to  $1/C$  [93]. The Renyi entropy from Eqn. 8.2 is:  $S_n = \frac{1}{1-n} \log C^{-(n-1)} = (l-1) \log 2$ . Thus  $\gamma = \log 2$  from the definition above, if we identify  $l$  with the length of the boundary. Note, this follows independent of the Renyi index  $n$ , and is the expected value for a  $Z_2$  gauge theory with quantum dimension  $D = 2$ .

Practically, it is not convenient to extract the subleading constant by fitting the expression above, particularly on the lattice where edges frequently occur. Instead, one may use a construction due to Levin and Wen[93] or Kitaev and Preskill[79], that effectively cancels out the leading term and exposes the topological contribution. We use the latter, which requires calculating entanglement entropy for a triad of non overlapping regions A, B, C, and their various unions, and then constructing:

$$-\gamma = S_A + S_B + S_C - S_{AB} - S_{AC} - S_{BC} + S_{ABC} \quad (8.5)$$

here, any  $S_n$  can be used, and we choose to use  $S_2$  since it can be easily calculated. This guarantees that the contributions of boundaries and corners cancel when the dimensions of individual regions  $A, B, C$  is much larger than the correlation length.

Next we briefly review the VMC algorithm for calculating Renyi entropy  $S_2$  [58, 204]. Consider the configurations  $|\alpha_1\rangle = |a\rangle|b\rangle$ ,  $|\alpha_2\rangle = |a'\rangle|b'\rangle$ ,  $|\beta_1\rangle = |a'\rangle|b\rangle$ ,  $|\beta_2\rangle = |a\rangle|b'\rangle$ , where  $|a\rangle$  and  $|a'\rangle$  have their support only in the subsystem A while  $|b\rangle$  and  $|b'\rangle$  are in subsystem B. Following Ref. [58], we define an operator  $\text{Swap}_A$  that acts on the tensor product of two copies of the system and swaps the configurations of the spins belonging to the A subsystem in the two copies, i.e.  $\text{Swap}_A |\alpha_1\rangle \otimes |\alpha_2\rangle = |\beta_1\rangle \otimes |\beta_2\rangle$ . The Renyi entropy  $S_2$  for the bipartition A and B can be expressed in terms of the expectation value of  $\text{Swap}_A$  with respect to the wave function  $|\Phi\rangle \otimes |\Phi\rangle$ :

$$S_A = -\log (\text{tr} \rho_A^2) = -\log \langle \text{Swap}_A \rangle \quad (8.6)$$

$\langle \text{Swap}_A \rangle$  may be re-expressed as a Monte Carlo average:

$$\langle \text{Swap}_A \rangle = \sum_{\alpha_1, \alpha_2} \rho_{\alpha_1} \rho_{\alpha_2} f(\alpha_1, \alpha_2) \quad (8.7)$$

where the weights  $\rho_{\alpha_i} = |\langle \alpha_i | \Phi \rangle|^2 / \sum_{\alpha_i} |\langle \alpha_i | \Phi \rangle|^2$  are normalized and non-negative while the quantity to be averaged over the probability distribution  $\rho_{\alpha_1} \rho_{\alpha_2}$  is:

$$f(\alpha_1, \alpha_2) = \frac{\langle \beta_1 | \Phi \rangle \langle \beta_2 | \Phi \rangle}{\langle \alpha_1 | \Phi \rangle \langle \alpha_2 | \Phi \rangle} \quad (8.8)$$

Therefore, one can calculate the Renyi entropy using VMC method. This technique is particularly suited for projected wave functions since the projection is rather easy to implement in a VMC algorithm[45]. As shown in Ref. [204] and Appendix C.1, VMC algorithm correctly reproduces the exact results for free fermions with an error of less than a few percent.

We further facilitate our calculation with an algorithm that we referred to as the sign trick[204]. It offers simplification and reduces computational cost, see Appendix C.3. Basically, we separate  $\langle \text{Swap}_A \rangle$  as a product of two factors, which may be independently calculated within VMC method:

$$\begin{aligned} \langle \text{Swap}_A \rangle &= \langle \text{Swap}_{A,\text{mod}} \rangle \langle \text{Swap}_{A,\text{sign}} \rangle \\ &= \sum_{\alpha_1 \alpha_2} \rho_{\alpha_1} \rho_{\alpha_2} |f(\alpha_1, \alpha_2)| \left[ \sum_{\alpha_1 \alpha_2} \tilde{\rho}_{\alpha_1, \alpha_2} e^{i\phi(\alpha_1, \alpha_2)} \right] \end{aligned} \quad (8.9)$$

The first factor is the Renyi entropy of a sign problem free wave function  $|\phi_{\alpha_i}|$ . The second term is the expectation value of the phase factor  $e^{i\phi(\alpha_1, \alpha_2)} = \phi_{\alpha_1}^* \phi_{\alpha_2}^* \phi_{\beta_1} \phi_{\beta_2} / |\phi_{\alpha_1}^* \phi_{\alpha_2}^* \phi_{\beta_1} \phi_{\beta_2}|$  with probability distribution  $\tilde{\rho}_{\alpha_1, \alpha_2} = |\phi_{\alpha_1}^* \phi_{\alpha_2}^* \phi_{\beta_1} \phi_{\beta_2}| / \sum_{\alpha_1 \alpha_2} |\phi_{\alpha_1}^* \phi_{\alpha_2}^* \phi_{\beta_1} \phi_{\beta_2}|$ . Both factors can be calculated in a more efficient manner and most importantly, have much smaller errors than the direct calculation of  $\langle \text{Swap}_A \rangle$ .

### 8.3 Topological Entanglement Entropy for a Chiral Spin Liquid

In this section we calculate the Renyi entropy  $S_2$  and TEE  $\gamma$  for a chiral SL[71, 72, 189].

The chiral SL is a spin SU(2) singlet ground state, which breaks time reversal and parity symmetry[71, 72, 157, 189]. A wave function in this phase wave function may be obtained using the slave-particle formalism by Gutzwiller projecting a  $d + id$  BCS state [71, 72, 157, 189]. Alternately, it can be obtained by Gutzwiller projection of a hopping model on the square lattice. This model has fermions hopping on the square lattice with a  $\pi$  flux through every plaquette and imaginary hoppings across the square lattice diagonals:

$$H = \sum_{\langle ij \rangle} t_{ij} f_i^\dagger f_j + \sum_{\langle\langle ik \rangle\rangle} \Delta_{ik} f_i^\dagger f_k \quad (8.10)$$

Here  $i$  and  $j$  are nearest neighbors and the hopping amplitude  $t_{ij}$  is  $t$  along the  $\hat{y}$  direction and alternating between  $t$  and  $-t$  in the  $\hat{x}$  direction from row to row; and  $i$  and  $k$  are second nearest neighbors connected by hoppings along the square lattice diagonals, with amplitude  $\Delta_{ik} = i\Delta$  along the arrows and  $\Delta_{ik} = -i\Delta$  against the arrows, see Figure 8.1. The unit cell contains two sublattices  $A$  and  $B$ . This model leads to a gapped state at half filling and the

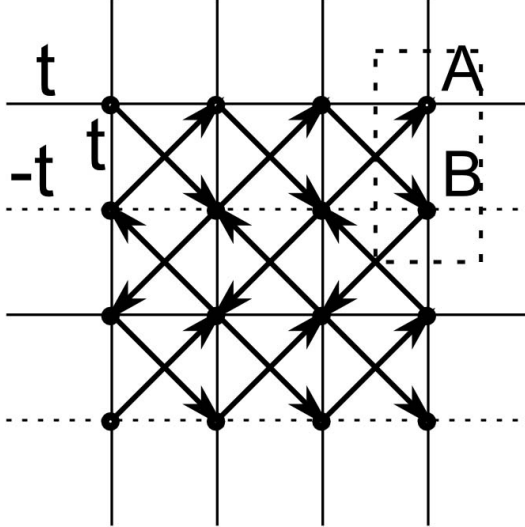


Figure 8.1. Illustration of a square lattice hopping model connected with a  $d + id$  superconductor. While the nearest neighbor hopping is along the square edges with amplitude  $t$  ( $-t$  for hopping along dashed lines), the second nearest neighbor hopping is along the square diagonal (arrows in bold), with amplitude  $+i\Delta$  ( $-i\Delta$ ) when hopping direction is along (against) the arrow. The two sublattices in the unit cell are marked as  $A$  and  $B$ .

resulting valence band has unit Chern number. This hopping model is equivalent to a  $d + id$  BCS state by an  $SU(2)$  Gauge transformation[97]. We use periodic boundary conditions throughout this section.

The unprojected ground-state wave function  $|\phi\rangle$  is obtained by filling all the states in the valence band ( $\epsilon_k < 0$ ) i.e.  $|\phi\rangle = \left[ \prod_{k,s} \gamma_{sk}^\dagger \right] |0\rangle$  where  $\gamma_{k,s}^\dagger = \psi_A(k) \sum_{r_A} f_{r_A,s}^\dagger e^{ik \cdot r_A} + \psi_B(k) \sum_{r_B} f_{r_B,s}^\dagger e^{ik \cdot r_B}$  is the creation operator for a valence electron with spin  $s$  and momentum  $k$ , and  $\psi_A(k)(\psi_B(k))$  is the wave function on sublattice A(B). The projected wave function that corresponds to the chiral SL is obtained as  $|\Phi\rangle = P|\phi\rangle$ , where  $P$  is the Gutzwiller projection operator that projects the wave function to the Hilbert space of one electron per site. This is implemented by restricting  $|\alpha\rangle$  to the Hilbert space of spins, i.e. one particle per site. Due to the fact that this Hamiltonian contains only real bipartite hoppings and imaginary hoppings between the same sublattices and preserves the particle-hole symmetry, this wave function  $\langle \alpha | \Phi \rangle$  can be written as a product of two Slater determinants  $\mathcal{M} \text{Det}(M_{ij})^2$ , where  $\mathcal{M}$  is just an unimportant Marshall sign factor, and:

$$M_{ij} = \{ [\psi_A(k_i) + \psi_B(k_i)] + (-1)^{y_j} [\psi_A(k_i) - \psi_B(k_i)] \} e^{ik_i \cdot r_j} \quad (8.11)$$

$r_j$  is the coordinates of the up spins in configuration  $\alpha$ , and  $k_i$  is the momentums in the momentum space. The Renyi entropy  $S_2$  of this wave function can be calculated by VMC method detailed above.

For an accurate calculation of TEE  $\gamma$ , it is important that the subleading terms in

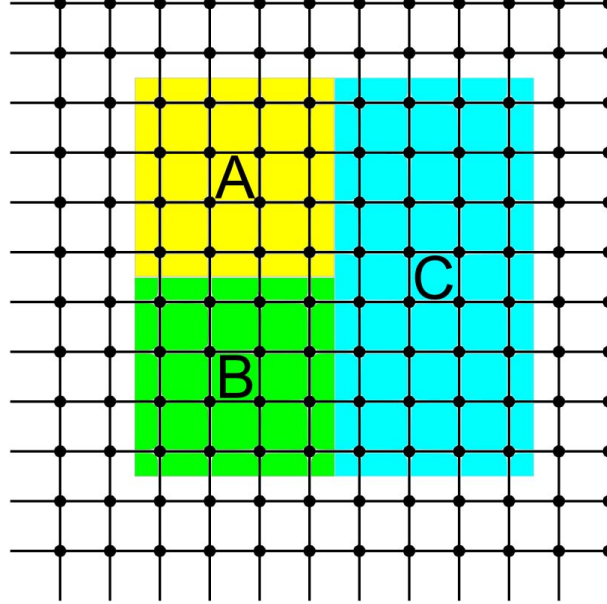


Figure 8.2. The separation of the system into subsystem  $A$ ,  $B$ ,  $C$  and environment, periodic boundary condition is employed in both  $\hat{x}$  and  $\hat{y}$  directions.

the Eqn. 8.3 be much smaller than the universal constant  $\gamma$  itself. This finite size error is suppressed when the excitation gap is large and correlation length is shorter than the system typical length scale. Note that the mean field gap is given by  $8\Delta$  for  $|\Delta| \leq 0.5t$  and  $2t\sqrt{8 - (t/\Delta)^2}$  for  $|\Delta| > 0.5t$ . To minimize the finite size effect, we take  $\Delta = 0.5t$  unless otherwise specified, so that the gap is large in both units of  $t$  and  $2\Delta$ , and our calculation estimates a correlation length of  $\xi \sim 0.45$ .

To calculate the TEE  $\gamma$  using the Kitaev-Preskill scheme[79], we study system with total dimensions  $12 \times 12$  lattice spacings in both directions with periodic boundary conditions. We separate the system into  $L_A \times L_A$  squares  $A$  and  $B$  and an  $L_A \times 2L_A$  rectangle  $C$ , see Figure 8.2. For this particular geometry, TEE is simply given by:

$$-\gamma = 2S_{2,A} - 2S_{2,AC} + S_{2,ABC} \quad (8.12)$$

where we have used the fact that  $S_{2,A} = S_{2,B}$ ,  $S_{2,AB} = S_{2,C}$  and  $S_{2,AC} = S_{2,BC}$  owing to the reflection and translation symmetry of the wave function. This simplifies the measurement of TEE into the measurement of  $S_2$  for only three subsystems  $A$ ,  $AC$  and  $ABC$ .

We use the unprojected wave function as a benchmark for extraction of TEE, which is non-interacting and hence exactly solvable. For an  $L_A = 3$  system, the VMC calculation gives  $\gamma = -0.0008 \pm 0.0059$ , in agreement with the absence of topological order and correspondingly vanishing TEE (Table 8.1 first row).

The Gutzwiller projected wave function is believed to be a chiral SL which can be thought of as a Laughlin liquid at filling  $\nu = 1/2$ . Using VMC method, we find  $\gamma = 0.343 \pm 0.012$  for an  $L_A = 3$  system and  $\gamma = 0.344 \pm 0.043$  for an  $L_A = 4$  system, both are in excellent

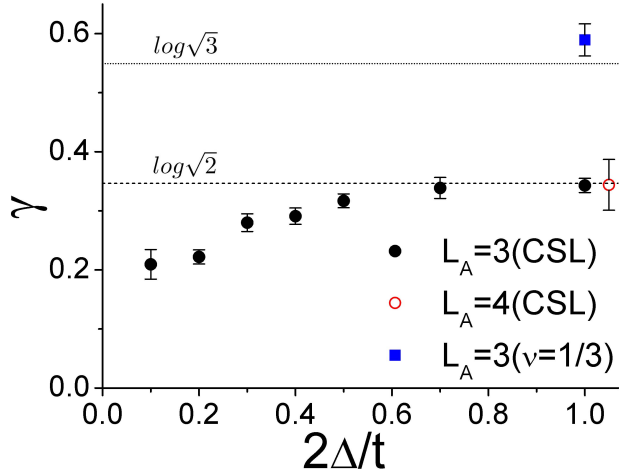


Figure 8.3. Illustration of finite size effect: chiral SL TEE  $\gamma$  as a function of  $2\Delta/t$  proportional to the relative gap size for characteristic system length  $L_A = 3$ . The larger the gap, the closer the data approaches the ideal value. For comparison, TEE  $\gamma$  for chiral SL at  $L_A = 4$  and  $2\Delta/t = 1.0$  is shown. On the same plot, TEE  $\gamma$  of a lattice version of  $\nu = 1/3$  Laughlin state at  $L_A = 3$ ,  $2\Delta/t = 1.0$  is also shown. The dashed lines are the ideal TEE values of  $\gamma = \log(\sqrt{2})$  for the chiral SL and  $\log(\sqrt{3})$  for the  $\nu = 1/3$  Laughlin state.

consistency with the expectation of  $\gamma = \log(\sqrt{2}) = 0.347$  for its ground states' two fold degeneracy, see Table 8.1 second and third rows and also Figure 8.3.

We also want to point out that Gutzwiller projection qualitatively changes the system ground state's topological and quantum behavior from the mean field result.

On the other hand, by lowering the ratio of  $2\Delta/t$  and correspondingly the gap size the correlation length increases and the finite size effects from subleading terms become more important. See Figure 8.3 for the approach of the extracted TEE  $\gamma$  to its universal value of  $\gamma = \log(\sqrt{2})$  as we lift the gap size controlled by  $2\Delta/t$  for a system with typical length scale  $L_A = 3$ . The finite size analysis and the above consistency between  $L_A = 3, 4$  confirm that finite size effect is small for our chosen sets of parameters for the system sizes we study.

## 8.4 Lattice Version of the Laughlin State

Using VMC method, we further study the situations where the wave function is the cube or the fourth power of the Slater determinant of the Chern insulator. For example, consider the wave function:

$$\Psi_{1/3}(r_1, r_2 \dots, r_N) = \Phi^3(r_1, \dots, r_N) \quad (8.13)$$

where  $\Phi$  is the Chern insulator Slater determinant defined above. Clearly, the product is a fermionic wave function, since exchanging a pair of particles leads to a sign change. This is similar in spirit to constructing the corresponding Laughlin liquid of  $m = 3$  of fermions, by taking the cube of the Slater determinant wave function in the lowest Landau level  $\psi(z_1, \dots, z_N) = \prod_{i < j} (z_i - z_j) e^{-\sum_i \frac{|z_i|^2}{4v_B^2}}$ . However, unlike the canonical Laughlin state, composed of lowest Landau level states, these are rather different lattice wave functions. An interesting question is whether the lowest Landau level structure is important in constructing states with the topological order of the Laughlin state, or whether bands with identical Chern number is sufficient, as suggested by field theoretic arguments.

To address this we calculate TEE and compare with expectation for the Laughlin phase. Again we choose  $L_A = 3$  in our VMC simulation, and obtain:  $\gamma = 0.5894 \pm 0.0272$  for the  $m = 3$  wave function, in reasonable agreement with the ideal value  $\gamma = \log(\sqrt{3}) = 0.549$  (Table 8.1 fourth row).

We also considered the fourth power of the Chern insulator Slater determinant:

$$\Psi_{1/4}(r_1, r_2, \dots, r_N) = \Phi^4(r_1, \dots, r_N) \quad (8.14)$$

this is a bosonic wave function, that is expected to be in the same phase as  $\nu = 1/4$  bosons. Indeed we find with  $L_A = 3$  in our VMC simulation,  $\gamma = 0.732 \pm 0.076$ , consistent with ideal value that must be realized in the thermodynamic limit of this phase:  $\gamma = \log(\sqrt{4}) = 0.693$  (Table 8.1 fifth row).

These results offered direct support for the TEE formula  $\gamma = \log D$  as well as their validity as topological ground-state wave functions carrying fractional charge and statistics. The lattice fractional Quantum Hall wave functions discussed here may be relevant to the recent studies of flat band Hamiltonians with fractional quantum Hall states[116, 147, 164, 168, 170, 183].

## 8.5 Topological Entanglement Entropy of a $Z_2$ Spin Liquid

With the projected wave function ansatz, we may also construct a topological  $Z_2$  SL by projecting another mean-field BCS state, given by the specific BdG Hamiltonian on a square lattice as the following[190]:

$$H = -\sum_{\langle ij \rangle} \left( \psi_i^\dagger \mu_{ij} \psi_j + h.c. \right) + \sum_i \psi_i^\dagger a_0^l \tau^l \psi_i \quad (8.15)$$

where  $\psi_i = (f_\uparrow, f_\downarrow)^T$ .  $\tau^{1,2,3}$  are Pauli matrices. The second term is related to chemical potentials, we set  $a_0^{2,3} = 0$ , with  $a_0^1$  fixed by the conditions  $\langle \psi^\dagger \tau^{1,2,3} \psi \rangle = 0$ . Matrices  $\mu_{ij}$

connecting nearest and next nearest neighbors:

$$\begin{aligned}\mu_{i,i+x} &= \mu_{i,i+y} = -\tau^3 \\ \mu_{i,i+x+y} &= \eta\tau^1 + \lambda\tau^2 \\ \mu_{i,i-x+y} &= \eta\tau^1 - \lambda\tau^2\end{aligned}\tag{8.16}$$

This mean field model is readily solvable, with dispersion:

$$\begin{aligned}E_k &= \sqrt{\epsilon_k^2 + |\Delta_k^2|} \\ \epsilon_k &= 2(\cos(k_x) + \cos(k_y)) \\ \Delta_k &= 2\eta[\cos(k_x + k_y) + \cos(k_x - k_y)] + a_0^1 \\ &\quad - 2i\lambda[\cos(k_x + k_y) - \cos(k_x - k_y)]\end{aligned}\tag{8.17}$$

We choose  $\eta = \lambda = 1.5$  for a large gap and our calculation estimates that the correlation length is  $\xi \sim 1.4$  lattice spacings.

The VMC algorithm need little change[45], except that instead of Slater determinants product, the wave function for spin product configuration  $|\alpha\rangle$  is given by:

$$\phi_\alpha = \langle \alpha | \Phi \rangle = \det(a_{ij})\tag{8.18}$$

here  $a_{ij} = a(r_{i,\uparrow} - r_{j,\downarrow})$  is the Fourier transform of the superconducting pairing function  $f_k$ ,  $r_{i,\uparrow}$  and  $r_{j,\downarrow}$  are the coordinates of the up-spins and down-spins, respectively:

$$f_k = \frac{\Delta_k}{|E_k + \epsilon_k|}\tag{8.19}$$

For numerical simulations we again study  $12 \times 12$  lattice spacing systems and separate the system into subsystems including  $L_A \times L_A$  squares  $A$  and  $B$  and  $L_A \times 2L_A$  rectangle  $C$ , again see Figure 8.2. The TEE  $\gamma$  is given by Eqn. 8.12 as before. First, we use the unprojected BCS state as a benchmark, for which we expect a result of  $\gamma = 0.003$  from an exact solution (since the unprojected state is a free particle ground state, one may use the correlation matrix method[133]) and consistent with its absence of topological order. Indeed, we obtain  $\gamma = 0.012 \pm 0.062$  using VMC method, the almost vanishing value of  $\gamma$  is consistent with the expected value, which also serves as a check on our Monte Carlo calculations.

On the other hand, the projection qualitatively alters the topological properties of the system, and for simulation accuracy and efficiency, we employ the 'sign trick'. For an  $L_A = 4$  system, the VMC calculation gives  $\gamma = 0.288 \pm 0.107$ . This is considerably lower than the  $Z_2$  SL which has  $D^2 = 4$  sectors and  $\gamma = \log(D) = \log(2) \simeq 0.693$ . The TEE is found to be only 42% of the expected value(Table 8.1 last row). Other studies on  $Z_2$  phases eg. the quantum Monte Carlo on a Bose Hubbard model in Ref. [65] have also found values that underestimate the topological entropy (75% of the expected zero temperature value in that case). The smaller than expected value is probably due to spinon excitations with a finite gap, causing breaking of  $Z_2$  electric field lines over the finite system size  $L_A = 4$  we consider. Indeed, spin correlations decay more slowly for the  $Z_2$  state, as compared to the chiral SL, which also arrives closer to its expected  $\gamma$  value.

## 8.6 Conclusion

In this chapter we studied entanglement properties of candidate wave functions for  $SU(2)$  symmetric gapped SLs and Laughlin states, and established their topological order using the notion of TEE. We studied two classes of SLs: 1) wave functions that describe quantum Hall states and are obtained from the wave function of a Chern insulator by taking multiple copies of it 2) A  $Z_2$  SL state that is obtained by Gutzwiller projecting a fully-gapped BCS superconductor. These wave functions have long been used as ansatz for exploring SLs states and it is reassuring that topologically ordered states can be good variational ground states for realistic Hamiltonians. Our method is directly applicable to any wave function that can be dealt within VMC method and would be especially useful in cases where one is dealing with a Hamiltonian that has Monte Carlo sign-problem and only has a variational ansatz for the corresponding ground state. We also note that since the quantum Hall wave functions we study are not constructed from the lowest Landau level but rather from the band structures that have non-zero Chern number, our results are also relevant to the recently discovered quantum Hall physics in flat band Hamiltonians [116, 147, 164, 168, 170, 183].

Let us consider a few problems where our method may find immediate application. Firstly, it would be interesting to apply our method to  $Z_2$  SLs that have gapless nodal spinons. These SLs are obtained by Gutzwiller projecting a nodal BCS state. We note that in this case one would find an additional contribution to the subleading constant part of the entanglement entropy that comes from the gapless spinons. Though we believe it might still be possible to separate the total contribution of the constant term into a topological constant and a term that comes from the gapless spinons only. It would also be interesting to study wave functions that are expected to have non-abelian quasiparticles such as  $SU(2)_k$  quantum Hall wave functions[155]. Thirdly, since VMC techniques can be used for wave functions defined in the continuum as well, it might be interesting to study TEE of quantum Hall wave functions (and their descendants such as time-reversal invariant fractionalized topological insulators[91] ) defined directly in the continuum.

Finally, we note that one limitation of our method is that it can't be used to calculate TEE for SLs where the gauge fields are coupled to bosonic (rather than fermionic) spinons. This is because VMC techniques are not very efficient when dealing with wave functions that are written as permanents (in contrast to determinants). It would be interesting to see if the recent VMC calculation for a  $SU(2)$  symmetric bosonic SL [171] can be pushed to bigger system sizes so as to establish topological order in such wave functions.

# Chapter 9

## Quasi-particle Statistics and Braiding from Ground State Entanglement

### 9.1 Introduction

Topologically ordered states are gapped quantum phases of matter that lie beyond the Landau symmetry breaking paradigm[190]. Well known examples include fractional quantum Hall states and gapped quantum spin liquids[4, 10, 88, 102, 145, 146, 153, 158, 188, 190, 191]. These phases are not characterized by local correlations or order parameters but rather by long range entanglement in their ground-state wave functions[80]. Recently, there has been renewed interest in such states, both from a fundamental perspective, as well as with a view to applications in quantum computing[115]. At the fundamental level, topologically ordered phases display a number of unique properties. In two dimensions, emergent excitations in these states display nontrivial statistics. In Abelian topological phases, exchange of identical excitations or taking one excitation around another (braiding) leads to characteristic phase factors, that are neither bosonic nor fermionic. A further remarkable generalization of statistics occurs in non-Abelian phases where excitations introduce a degeneracy. Braiding excitations then leads to a unitary transformation on these degenerate states, which generalizes the phase factor of Abelian states.

These striking properties of topologically ordered phases are connected to excitations. An important and interesting question is whether the ground state directly encodes this information, and if so how one may access it. It is well known that topologically ordered phases feature a ground-state degeneracy that depends on the topology of the space on which they are defined. Also, ground states of such states contain a topological contribution to the quantum entanglement, the topological entanglement entropy (TEE) [53, 55, 79, 93]. In

this chapter we show that combined together, these two ground-state properties can be used to extract the generalized statistics associated with excitations in these states. We apply these insights to a chiral spin-liquid wave function, and numerically extract the semionic statistics associated with excitations. This demonstrates the promise of this approach in helping numerical studies diagnose the precise character of topological order in a particular state.

The generalized statistics of quasiparticles is formally captured by the modular  $\mathcal{S}$  and  $\mathcal{U}$  matrices, in both Abelian and non-Abelian states [38, 76, 77, 115, 191]. The element  $S_{ij}$  of the modular  $\mathcal{S}$  matrix determines the mutual statistics of  $i$ 'th quasiparticle with respect to the  $j$ 'th quasiparticle while the element  $\mathcal{U}_{ii}$  of (diagonal)  $\mathcal{U}$  matrix determines the self-statistics ('topological spin') of the  $i$ 'th quasiparticle. Note, these provide a nearly complete description of a topologically ordered phase - for instance, fusion rules that dictate the outcome of bringing together a pair of quasiparticles, are determined from the modular  $\mathcal{S}$  matrix, by the Verlinde formula[179]. Previously, Wen proposed using the non-Abelian Berry phase to extract statistics of quasiparticles[191]. However, the idea in Ref. [191] requires one to have access to an infinite set of ground states labeled by a continuous parameter, and is difficult to implement. Recently, Bais et al. also discussed extracting  $\mathcal{S}$  matrix in numerical simulations, by explicit braiding of excitations[8]. In contrast, here we will just use the set of ground states on a torus, to determine the braiding and fusing of gapped excitations.

Recall, the ground-state entanglement entropy of a two-dimensional topologically ordered phase in a disk-shaped region  $A$  with a smooth boundary of length  $L$  takes the form  $S_A = \alpha L - \gamma$ , where the universal constant  $\gamma$  is the TEE [53, 55, 79, 93]. The constant  $\gamma$  equals  $\log(D)$  where  $D = \sqrt{\sum d_i^2}$  is the "total quantum dimension" associated with the topological phase while  $d_i$  is the quantum dimension of  $i$ 'th quasiparticle type. For Abelian states  $d_i = 1$  so  $D^2$  is simply the number of quasiparticle types in the theory. This is also the ground-state degeneracy on a torus. For example, the simplest case of  $D^2 = 2$  corresponds to the chiral spin liquid or equivalently the  $\nu = 1/2$  bosonic Laughlin state[71, 72, 189]. This has, in addition to the trivial excitation, a semionic quasiparticle. Unfortunately, the total quantum dimension  $D$  only provides a partial characterization of topological order since two distinct topological phases can have same value of  $D$ . For example, the topological phase based on a  $Z_2$  gauge theory has  $D^2 = 4$ , which could also be achieved with two decoupled copies of the chiral spin liquid. However a knowledge of the modular  $\mathcal{S}$  matrix could tell these states apart.

It is sometimes stated without qualification, that TEE is a quantity solely determined by the total quantum dimension  $D$  of the underlying topological theory. However, this holds true only when the boundary of the region  $A$  consists of topologically trivial closed loops. If the boundary of region  $A$  is non-contractible, for example if one divides the torus into a pair of cylinders, generically the entanglement entropy is different for different ground states (see Figure 9.1). Indeed as shown in Ref. [26] for a class of topological states, the TEE depends on the particular linear combination of the ground states when the boundary of region  $A$  contains non-contractible loops. We will exploit this dependence to extract information about the topological phase beyond the total quantum dimension  $D$ .

At a practical level, recent progress in numerical techniques have lead to a number of

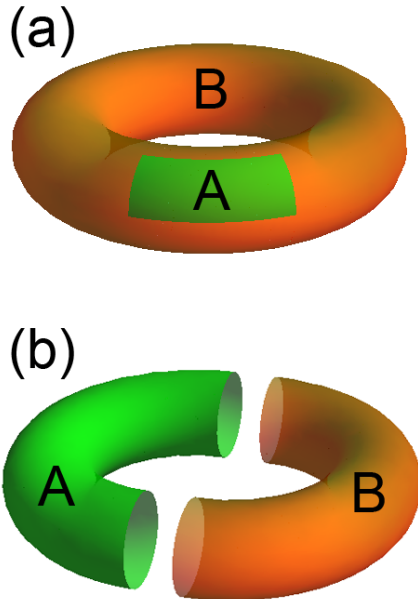


Figure 9.1. Two types of entanglement bipartitions on the torus: (a) A trivial bipartition with contractible boundaries for which the TEE  $\gamma = \log D$ , and (b) A bipartition with non-contractible boundaries, where the TEE depends on ground state.

proposals for topologically ordered spin liquid phases on the Kagome[69, 200], honeycomb[99] and square lattice with diagonal exchange[70, 182]. A number of lattice states related to the Laughlin states have also been proposed in recent numerical studies[116, 147, 164, 170, 184]. Clearly, smoking gun numerical signatures of topological order are increasingly needed. The procedure outlined here suggests that entanglement entropy could be used to numerically diagnose details of topological order beyond the total quantum dimension[42, 56, 65, 201, 204, 205, 208], which is a single number susceptible to numerical error. An elegant different approach to a more complete identification of topological order is through the study of the entanglement spectrum[95]. However we note that requires the existence of edge states and may not be applicable for topological phases like the  $Z_2$  spin liquid. Furthermore, it is possible to compute TEE using Monte Carlo techniques on relatively larger systems[65, 204, 205], as also done in this chapter, where the entanglement spectrum is not currently available.

Let us briefly summarize the key ideas involved in this work. We recall that the number of ground states on a torus corresponds to the number of distinct quasiparticle types. Intuitively, different ground states are generated by inserting appropriate fluxes ‘inside’ the cycle of the torus, which is only detected by loops circling the torus. We would like to express these quasiparticle states as a linear combination of ground states. A critical insight is that this can be done using the topological entanglement entropy for a region  $A$  that wraps around the relevant cycle of the torus. With this in hand one can readily access the modular  $\mathcal{S}$  and  $\mathcal{U}$  matrices. For example, the  $\mathcal{S}$  matrix is obtained by relating quasiparticle states associated with different cycles of the torus.

We begin by elaborating on the ground-state dependence of entanglement entropy, focusing on the case of a partition of torus into two cylinders (Section 9.2.1). We present an argument based on the strong subadditivity property of quantum information and show that the TEE per connected boundary is not identical to that for a trivial bipartition, such as a disc cut out of the torus. This is illustrated as an ‘uncertainty’ relation, between entropies for two different cylindrical bipartitions of the torus.

In Section 9.2.2 we also demonstrate this ground-state dependence numerically, and calculate the entanglement entropy for the chiral spin liquid (CSL) wave function[71, 72, 189] as different linear superpositions of the two ground states (Figure 9.4) with the Variational Monte Carlo (VMC) method[45, 58, 204, 205]. The physical origin of the ground-state dependence of TEE is made explicit by studying a  $Z_2$  toric code model[80] (Section 9.2.3). We introduce the notion of minimum entropy states (MESs), namely the ground states with minimal entanglement entropy (or maximal TEE, since the TEE always reduces the entropy) for a given bipartition. These states can be identified with the quasiparticles of the topological phase and generated by insertion of the quasiparticles into the cycle enclosed by region A. For a generic lattice wave function with finite correlation length, such as the CSL wave functions we study, a nonlocal measurement like TEE is essentially to identify this basis of MESs.

Having established the dependence of the TEE on the ground states, in Section 9.3 we detail a procedure that uses this dependence to extract the key properties of quasiparticle excitations by determining modular  $\mathcal{S}$  and  $\mathcal{U}$  matrices. The basic idea is to relate MESs for different entanglement bipartitions of the torus. The MESs, which reflect quasiparticle excitations, are determined using TEE. As an application, we extract the modular  $\mathcal{S}$  matrix of an  $SU(2)$  symmetric CSL, a lattice equivalence to a  $\nu = 1/2$  Laughlin state, through TEE calculated with a recently developed VMC scheme. For illustrative purposes, we discuss in the Appendix D how our algorithm applies to Kitaev’s toric code model[80], a zero correlation length phase, and extract the modular  $\mathcal{S}$  matrix and  $\mathcal{U}$  matrices. This chapter is reproduced from a previously submitted work[203].

## 9.2 Ground State Dependence of Topological Entanglement Entropy

Given a normalized wave function  $|\Phi\rangle$  and a partition of the system into subsystems  $A$  and  $B$ , one can trace out the subsystem  $B$  to obtain the reduced density matrix on subsystem  $A$ :  $\rho_A = Tr_B |\Phi\rangle \langle \Phi|$ . The Renyi entropies are defined as:

$$S_n = \frac{1}{1-n} \log (Tr \rho_A^n) \quad (9.1)$$

where  $n$  is an index parameter. Taking the limit  $n \rightarrow 1$ ,  $S_n$  recovers the definition of the usual von Neumann entropy. In this chapter we will often discuss the Renyi entropy with

index  $n = 2$ :  $S_2 = -\log(Tr(\rho_A^2))$  since it can be calculated most easily with the VMC method[204, 205] and at the same time, captures all the information that we are interested in.

For a gapped phase in two dimensions with topological order and a disc shaped region  $A$  with smooth boundary of length  $L_A$ , the Area Law of the Renyi entropy gives:

$$S_n = \alpha_n L_A - \gamma \quad (9.2)$$

where we have omitted the sub-leading terms. Although the coefficient  $\alpha_n$  of the leading ‘boundary law’ term is non-universal, the sub-leading constant  $\gamma$ , which is often dubbed as the TEE, is universal and a robust property of the phase of matter for which  $|\Phi\rangle$  is the ground state. When region  $A$  has a disc geometry, it has been shown that  $\gamma$  for different degenerate ground states are identical and it is also insensitive to the Renyi entropy index  $n$  [26, 36]. It equals  $\gamma = \log D$ , where  $D$  is the total quantum dimension of the model [79, 93], and offers a partial characterization of the underlying topological order.

However, when the subsystem  $A$  takes a non-trivial topology, or more precisely when the boundary of  $A$  is non-contractible, TEE contains more information[26], as we will elaborate further in this chapter. For simplicity of illustration, throughout we focus on the case when the two-dimensional space is a torus  $T_2$  and the subsystem  $A$  wraps around the  $\hat{y}$  direction of the torus and takes the geometry of a cylinder. For such a geometry, the  $n$ 'th Renyi entropy corresponding to the wave function  $|\Phi\rangle = \sum_j c_j |\Xi_j\rangle$  is given by:  $S_n = \alpha_n L_A - \gamma'_n$ , where  $|\Xi_j\rangle$  is a special basis that we will describe in detail below and  $\gamma'_n$  is given by[26]:

$$\gamma'_n(\{p_j\}) = 2\gamma + \frac{1}{n-1} \log \left( \sum_j p_j^n d_j^{2(1-n)} \right) \quad (9.3)$$

Here  $d_j \geq 1$  is the quantum dimension of the  $j$ th quasiparticle and  $p_j = |c_j|^2$ . For Abelian anyons,  $d_j = 1$ . Note,  $d_j$  shares the same subscript  $j$  as the states  $|\Xi_j\rangle$  because the states  $|\Xi_j\rangle$  can be obtained by inserting a quasiparticle with quantum dimension  $d_j$  (the ground-state degeneracy on the torus is equal to the number of distinct quasiparticles). This equation shows that the TEE for this geometry depends on the wave function through  $\{p_j\}$  as well as the Renyi index  $n$ , unlike the case with disc geometry.

What is the physical significance of the basis states  $|\Xi_j\rangle$ ? We claim that these are precisely the eigenstates of the nonlocal operators defined on the entanglement cut, which distinguish the topologically degenerate ground states. For example, in the case of the quantum Hall[26] (Section 9.2.2), these states are the eigenstates of the Wilson loop operator associated with the Chern-Simons gauge field around the hole exposed by the entanglement cut. Similarly, for a  $Z_2$  gauge theory (Section 9.2.3), these are the states with definite electric and magnetic field fluxes perpendicular to the entanglement cut. For Abelian states, which have  $d_j = 1$  for all  $j$  and are the focus of this chapter, the entanglement entropy associated with the states  $|\Xi_j\rangle$  is minimum, i.e. heuristically, the entanglement cut has the maximum ‘knowledge’ about these states. For this reason we name them Minimum Entropy States (MESs).

### 9.2.1 Strong Subadditivity and the ‘Uncertainty’ Principle of TEE

In this subsection we discuss the TEE for bipartitions of a torus into two cylinders. This can be done by slicing the torus in two distinct ways, along the vertical or horizontal directions. Intuitively, one might expect both bipartitions would have the same TEE of  $2\gamma$ , given the two disconnected boundaries of the cylinders. However, very general considerations based on strong subadditivity of von-Neumann entropy alone suggest that this expectation cannot be correct. In practice, it is known that for a wide class of topological phases, TEE of such nontrivial bipartitions indeed depends on the ground state selected[26]. Here we do not address ground-state dependence, rather we demonstrate that TEE cannot be identical to its value for trivial bipartitions. It invokes strong subadditivity, a deep property of quantum information[119]. This will allow us to come up with an uncertainty principle, which constrains the amount of information we have when we cut the torus in two orthogonal directions. Its advantage is that it assumes almost nothing about the phase, except that it is gapped.

Consider the ground-state wave function of a gapped phase in two dimensions and three non-overlapping subregions  $A, B, C$ . The von-Neumann entropies  $S$  follow the strong subadditivity condition[119]:

$$S_{ABC} + S_B - S_{AB} - S_{BC} \leq 0 \quad (9.4)$$

Note, this is only known to hold for von-Neumann entropies, not Renyi entropies in general. Now, consider a torus with subregions  $A, B, C$  as shown in the Figure 9.2. Let us decompose the entropy into a part that arises from local contributions and a non-local TEE  $S = S^{\text{local}} + S^{\text{topo}}$ . For a subregion with the topology of a disc, the TEE is expected to be  $S^{\text{topo}} = -\gamma$ . Quite generally one can argue that  $\gamma \geq 0$  utilizing the strong subadditivity condition[93]. For subregions defined on a simply connected surface, such as a disc, the TEE is proportional to the number of connected components of the boundary. If this was also true for the torus, we would expect  $S_{AB}^{\text{topo}} = S_{BC}^{\text{topo}} = -2\gamma$  (since they have a pair of boundaries). We now show this cannot be a consistent assignment of TEE on the torus.

In order to isolate the topological part of the entropy, we assume that the regions  $A$  and  $C$  are well separated compared to the correlation length of the gapped ground state. Then, the local contributions cancel in the combination above:  $S_{ABC}^{\text{local}} + S_B^{\text{local}} - S_{AB}^{\text{local}} - S_{BC}^{\text{local}} \rightarrow 0$ . This can be argued following Refs. [79, 93]. For example, consider a local deformation near region  $A$ ’s boundary far away from the other regions. This change will be in  $S_{ABC}^{\text{local}}$ , but a nearly identical contribution will also appear in  $S_{AB}^{\text{local}}$ , since it only differs by the addition of a distant region. These will cancel in the combination above. Thus, we can rewrite the Eqn. 9.4 as:

$$S_{ABC}^{\text{topo}} + S_B^{\text{topo}} - S_{AB}^{\text{topo}} - S_{BC}^{\text{topo}} \leq 0 \quad (9.5)$$

This inequality implies the TEEs expected from the disc is not legal for the torus.

For regions where the boundary is topologically trivial and contractible (such as  $ABC$  or  $B$ ), one expects the TEE to be independent of the surface on which they are defined, and hence  $S_{ABC}^{\text{topo}} = S_B^{\text{topo}} = -\gamma$ . Only regions  $AB$  and  $BC$ , whose boundaries wrap around the

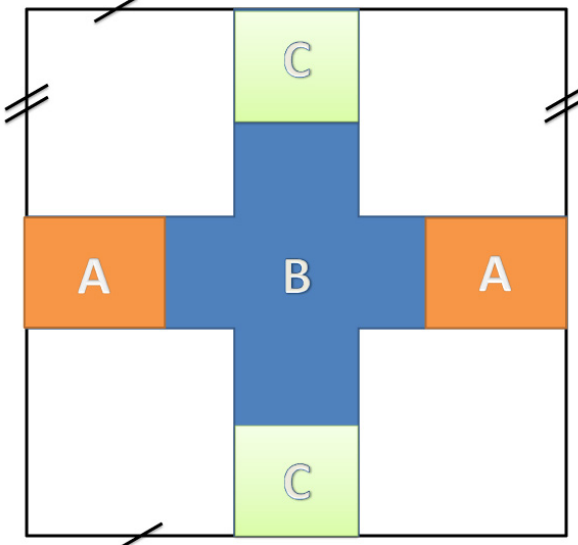


Figure 9.2. A torus (the top and bottom sides and left and right sides are identified). Subregions  $A$ ,  $B$ ,  $C$  are defined as shown. Regions  $A$  and  $C$  are assumed to be well separated as compared to the correlation length. The regions  $AB$  and  $BC$  correspond to bipartitions of the torus into cylinders in orthogonal directions.

torus, are sensitive to the topology of the space they are defined on. Their TEEs satisfy:

$$\gamma_{BC} + \gamma_{AB} \leq 2\gamma \quad (9.6)$$

where we have defined  $S_{AB(BC)}^{\text{topo}} = -\gamma_{AB(BC)}$ . Clearly this does not allow both the TEEs to be  $2\gamma$ . In fact if one of them attains its maximal disc value, the other must vanish. Note, the TEE reduces the total entropy. Thus, when the entropy of a cut along one of the cycles of the torus attains its minimum value, i.e. we have most knowledge about the state on the cut, then along the orthogonal direction, the entropy associated with a cut must attain its maximal value, implying our knowledge is the least. Therefore this can be thought of as an uncertainty relation, between cuts that wrap around different directions of the torus.

### 9.2.2 Ground State Dependence of TEE in a Chiral Spin Liquid

In this subsection, to illustrate the state dependence of TEE, we study the entanglement properties in a lattice model of an  $SU(2)$  spin-symmetric CSL on a torus. The CSL has the same topological order as the half filled Landau level  $\nu = 1/2$  Laughlin state[71, 72, 157, 189] of bosons (these bosons can be thought of as residing at the location of spin up moments), and has two-fold degenerate ground states on the torus. The topological order in CSL can be confirmed by calculating its topological entanglement entropy (TEE) numerically using Monte Carlo and verifying that it is non-zero and agrees with the field theoretical predictions[204, 205]. We note that here we are working with a generic wave function in this phase defined on a lattice, rather than with idealized zero correlation length states or

the topological field theory. This will introduce new conceptual issues - in particular, the connection between MESs and lattice ground states will be discussed.

We begin by reporting the results of a numerical experiment. We extract TEE of linear combinations of the two ground states of the CSL, and show that it indeed depends systematically on the chosen linear combination, when the entanglement cut wraps around the torus. We will then predict theoretically the dependence and find excellent agreement as shown in Figure 9.4.

### Numerical study of ground state dependence of TEE in Gutzwiller projected CSL states

Wave functions of an SU(2) spin symmetric CSL are obtained in the slave particle construction. We write the spins as bilinear in fermions  $\vec{S} = \frac{1}{2} f_\sigma^\dagger [\vec{\sigma}]_{\sigma\sigma'} f_{\sigma'}$  and assume a chiral d-wave state for the fermions. Operationally, the spin wave functions are obtained by Gutzwiller projection of a  $d_{x^2-y^2} + id_{xy}$  superconductor to one fermion per site. More technical details regarding this wave function are in Chapter 8.3. We consider the system on a torus. Before projection, one can write down different fermion states, by choosing periodic or anti-periodic boundary conditions along  $\hat{x}$  and  $\hat{y}$  directions. These boundary conditions are invisible to the spin degrees of freedom which are bilinear in the fermions and lead to degenerate ground states[145]. We denote the ground states by the mean field fluxes in  $\hat{x}$  and  $\hat{y}$  directions as  $|\varphi_1, \varphi_2\rangle$ ,  $\varphi_{1,2} = 0, \pi$ . The two fold degeneracy of the CSL implies that only two of the four ground states  $|0, 0\rangle$ ,  $|\pi, 0\rangle$ ,  $|0, \pi\rangle$ ,  $|\pi, \pi\rangle$  are linearly independent. Here we consider linear combinations of  $|0, \pi\rangle$  and  $|\pi, 0\rangle$ , which we have numerically checked to be indeed orthogonal for the system sizes that we consider:

$$|\Phi(\phi)\rangle = \cos \phi |0, \pi\rangle + \sin \phi |\pi, 0\rangle \quad (9.7)$$

We calculated TEE for the state  $|\Phi\rangle$  using VMC method and Gutzwiller projected wave functions based on Eqn. 8.10. An efficient VMC algorithm which allows to study a linear combination of Gutzwiller projected wave functions was developed and detailed in Appendix C. To our knowledge, this is the first numerical study to accomplish this.

The geometry and partition of the system are shown in Figure 9.3b. The total system size is 12 lattice spacings in both directions with rectangles  $A$  and  $B$  being  $6 \times 4$  and rectangle  $C$   $12 \times 4$ . Note that the subsystems  $AC$ ,  $BC$ ,  $AB$ ,  $C$  and  $ABC$  all wrap around  $\hat{y}$  direction so that their TEE will all be equal (and denoted  $\gamma'$ ). This is the quantity we wish to access. For contractible subsystems  $A$  and  $B$  it remains the same  $\gamma$  as that expected for a region with a single boundary, cut out of a topologically trivial surface (such as a bigger disc). We use the construction due to Kitaev and Preskill[79] and effectively isolate the topological contributions in the limit of small correlation length, by evaluating the combination of entropies  $S_A + S_B + S_C - S_{AB} - S_{AC} - S_{BC} + S_{ABC}$ . This combination

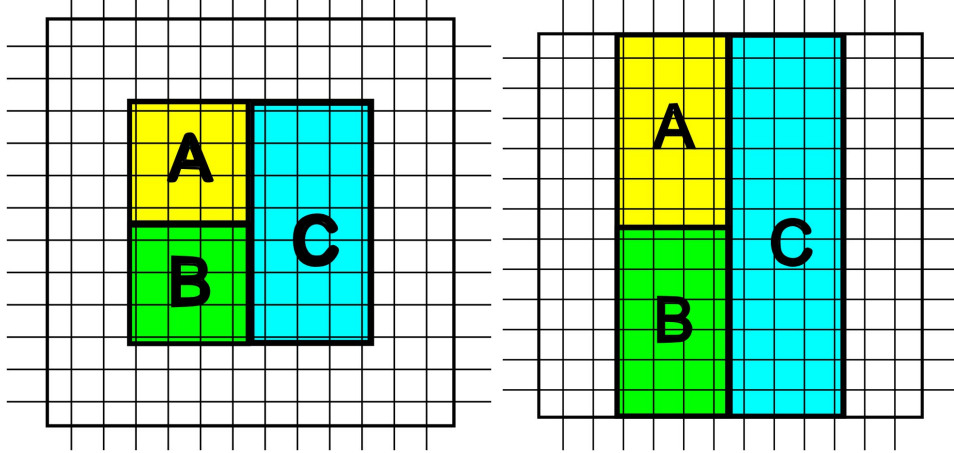


Figure 9.3. The separation of the system into subsystem  $A$ ,  $B$ ,  $C$  and environment, periodic or antiperiodic boundary condition is employed in both  $\hat{x}$  and  $\hat{y}$  directions. a: The subsystem  $ABC$  is an isolated square and the measured TEE has no ground-state dependence. b: The subsystem  $ABC$  takes a non-trivial cylindrical geometry and wraps around the  $\hat{y}$  direction, and TEE may possess ground-state dependence.

is related to the TEE by:

$$\begin{aligned}
 -2\gamma + \gamma' &= S_A + S_B + S_C \\
 &\quad - S_{AB} - S_{AC} - S_{BC} + S_{ABC} \\
 &= 2S_A - 2S_{AC} + S_{ABC}
 \end{aligned} \tag{9.8}$$

In the second line we have exploited symmetries of the construction to reduce the problem to calculation of the Renyi entropy  $S_2$  of three regions  $A$ ,  $AC$  and  $ABC$  for each  $\phi$ . To measure  $S_2$  numerically, we calculated the expectation value of a  $\text{Swap}_A$  operator, see Ref. [204, 205] and Section 8.2 for an elaboration of the method used. Our results for  $2\gamma - \gamma'(\phi)$  corresponding to different linear combinations parameterized by  $\phi$  are shown in Figure 9.4. This is one of the main results of this chapter.

We note the TEE strongly depends on the particular linear combination chosen. The zero of the curve implies that the TEE  $\gamma' = 2\gamma$ , intuitive value for an entanglement cut with two boundaries. The corresponding state is the MES. We note that the MES occurs at a nontrivial angle. Understanding this requires connecting the lattice states and the field theory which is done below. We predict this angle to be  $0.125\pi$  and the overall TEE dependence to be Eqn. 9.18, which is plotted as the solid curve Figure 9.4, in rather good agreement with the numerical data.

### Theoretical evaluation of ground state dependence of TEE in CSL wave functions

A calculation of ground-state dependence of TEE involves two steps. In the first step, we ask the following question: given a state expressed as a linear combination of MESs, what is

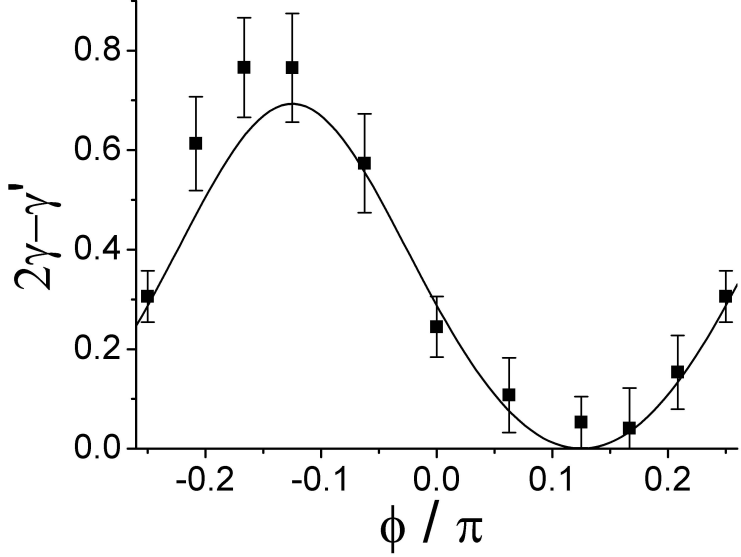


Figure 9.4. Numerically measured TEE  $2\gamma - \gamma'$  for a CSL ground state from linear combination  $|\Phi\rangle = \cos\phi|0, \pi\rangle + \sin\phi|\pi, 0\rangle$  as a function of  $\phi$  with VMC simulations using geometry in Figure 9.3b. The solid curve is the theoretical value from Eqn. 9.18. The periodicity is  $\pi/2$ .

the expected TEE? For the CSL, this question has already been answered by Ref. [26] that TEE for a state  $|\psi\rangle = a_1|1\rangle + a_2|2\rangle$  is:

$$\gamma' - 2\gamma = \log(|a_1|^4 + |a_2|^4) \quad (9.9)$$

where  $|1\rangle, |2\rangle$  are MESs for cutting the torus in the direction in question.

Second, we need to understand the relation between the MES and the physical states that appear in the Gutzwiller wave function. In general it appears that the only way to identify MESs in a generic wave function is by calculating the TEE. However, when the lattice model has additional symmetry, that can also be used to identify MESs. Here, we have a  $12 \times 12$  system defined on a square lattice and we will exploit the  $\pi/2$  rotation symmetry to establish a connection between the flux states  $|\varphi_1, \varphi_2\rangle$  of the Gutzwiller ansatz and the MESs.

The Gutzwiller projected ground states of the CSL,  $|0, 0\rangle$  and  $|\pi, \pi\rangle$  are clearly invariant under a  $\pi/2$  rotation symmetry upto a phase factor. A simple calculation shows that the  $|0, 0\rangle$  state acquires phase factor  $-1$  while the  $|\pi, \pi\rangle$  state acquires no phase under rotation. Similarly, the states  $\frac{1}{\sqrt{2}}(|0, \pi\rangle \pm |\pi, 0\rangle)$  acquire a phase  $\pm 1$  under rotation. Having established the transformation of lattice states under rotation, we now study how the MESs in the field theory respond to rotations. We will see that  $\pi/2$  rotation in the basis of the MESs is described by the modular  $\mathcal{S}$  matrix. The eigenvectors of the modular  $\mathcal{S}$  matrix will then be identified with lattice states that are rotation eigenstates.

The CSL has the same topological order as the half filled Landau level  $\nu = 1/2$  Laughlin

state[71, 72, 157, 189] of bosons. The field theory describing the topological order of a  $\nu = 1/k$  Laughlin state is described by the following Chern-Simons action. Note, here only the very long wavelength degrees of freedom are retained:

$$S = \int \frac{k}{4\pi} a_\mu \partial_v a_\lambda \epsilon^{\mu\nu\lambda} \quad (9.10)$$

One can define the Wilson loop operators  $T_1 = e^{i\theta_1} = e^{i \oint a_x dx}$  and  $T_2 = e^{i\theta_2} = e^{i \oint a_y dy}$  around the two distinct cycles of the torus. In terms of  $\theta_i$ , the action is given by:

$$S = i \frac{k}{2\pi} \int dt \theta_1 \dot{\theta}_2 \quad (9.11)$$

which implies that at the operator level  $[\theta_1, \theta_2] = i \frac{2\pi}{k}$  or:

$$T_1 T_2 = T_2 T_1 e^{2\pi i / k} \quad (9.12)$$

Owing to the above relation, there are  $k$  orthogonal ground states  $|\psi_m\rangle$  that can be chosen to transform under  $T_i$  as:

$$\begin{aligned} T_2 |\psi_m\rangle &= e^{2\pi i(m-1)/k} |\psi_m\rangle \\ T_1 |\psi_m\rangle &= |\psi_{m+1}\rangle \end{aligned} \quad (9.13)$$

In the case of a CSL phase,  $k = 2$ . Let us label the two degenerate ground states as  $(1, 0)^T$  and  $(0, 1)^T$ , which are eigenstates of  $T_2$ :

$$\begin{aligned} T_2 (1, 0)^T &= (1, 0)^T \\ T_2 (0, 1)^T &= -(0, 1)^T \\ T_1 (1, 0)^T &= (0, 1)^T \\ T_1 (0, 1)^T &= (1, 0)^T \end{aligned} \quad (9.14)$$

The last two equations are due to the commutation relation  $T_1 T_2 = -T_2 T_1$ . It follows that the eigenstates of  $T_1$  are  $(1, 1)^T / \sqrt{2}$  and  $(1, -1)^T / \sqrt{2}$ .

The significance of the  $T_{1,2}$  eigenstates is that they are MESs[26], for cuts whose boundaries are parallel to the loops used to define  $T_{1,2}$ . This is because eigenstates of these loop operators have a fixed value of flux enclosed within the relevant cycle of the torus, which minimizes the entanglement entropy for a parallel cut.

Now consider a  $\pi/2$  rotation, under which  $\theta_1 \rightarrow \theta_2$  and  $\theta_2 \rightarrow -\theta_1$  so  $T_1 \rightarrow T_2$  and  $T_2 \rightarrow T_1^{-1} = T_1$ . Thus, the matrix representing the effect of  $\pi/2$  rotation for CSL in  $T_2$  eigenstate basis is:

$$\mathcal{S} = \begin{pmatrix} \frac{1}{\sqrt{2}} & \frac{1}{\sqrt{2}} \\ \frac{1}{\sqrt{2}} & -\frac{1}{\sqrt{2}} \end{pmatrix} \quad (9.15)$$

Note that we have used the symbol  $\mathcal{S}$  for the above matrix because it is indeed the modular  $\mathcal{S}$  matrix of the Chern-Simons topological quantum field theory corresponding to a CSL. We recall that the modular  $\mathcal{S}$  matrix transforms the eigenstates of one Wilson loop operator  $T_2$  to those of  $T_1$ . We will return to the discussion of deriving  $\mathcal{S}$  matrix for CSL state using the entanglement properties of the ground states in Section 9.3.1. Here we restrict ourselves to the calculation of TEE for the CSL.

Since we are interested in the entanglement entropy with respect to a cut with non-contractible boundaries, such as the one shown in Figure 9.1b, let us represent all our states in the basis of the eigenstates of  $T_2$ , i.e. the states  $(0, 1)$  and  $(1, 0)$ . Then, by matching eigenstates of the  $\mathcal{S}$  matrix in the above basis and rotation eigenstates of the lattice problem, we conclude:

$$\begin{aligned} |\pi, 0\rangle &= \left( \sin \frac{\pi}{8}, \cos \frac{\pi}{8} \right)^T \\ |0, \pi\rangle &= \left( \cos \frac{\pi}{8}, -\sin \frac{\pi}{8} \right)^T \end{aligned} \quad (9.16)$$

We can now expand the general linear combination state  $|\Phi(\phi)\rangle$  in MESs:

$$\begin{aligned} |\Phi\rangle &= \cos \phi |0, \pi\rangle + \sin \phi |\pi, 0\rangle \\ &= \left( \cos \left( \phi - \frac{\pi}{8} \right), \sin \left( \phi - \frac{\pi}{8} \right) \right)^T \end{aligned} \quad (9.17)$$

Then, according to Eqn. 9.3, theoretically one expects the following expression for TEE:

$$2\gamma - \gamma' = \log \frac{4}{3 + \sin(4\phi)} \quad (9.18)$$

which is compared with the numerical data in Figure 9.4. The MES occur at the value of  $\phi = \pi/8$  (modulo  $\pi/2$ ).

### 9.2.3 Ground State Dependence of TEE in the Toric Code Model

In this subsection we use the Kitaev's Toric code model[80] as a pedagogical example to understand ground-state dependence of TEE and the nature of the MESs for a  $Z_2$  gauge theory.

Consider the toric code Hamiltonian of spins defined on the links of a square lattice[80]:

$$H = - \sum_s A_s - \sum_p B_p \quad (9.19)$$

where  $s$  and  $p$  represent the links spanned by star and plaquette as shown in the Figure 9.5, and  $A_s = \prod_{j \in s} \sigma_j^x$ ,  $B_p = \prod_{j \in p} \sigma_j^z$ . Since all individual terms in the Hamiltonian commute with each other, ground states are constructed from the simultaneous eigenstates of all  $A_s$

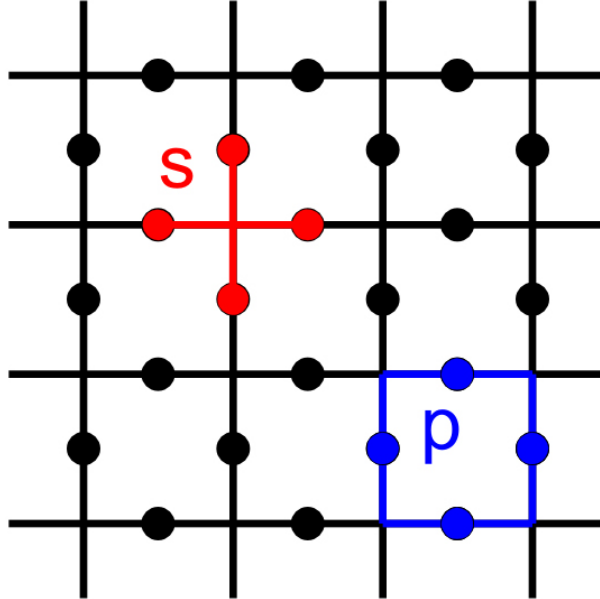


Figure 9.5. Illustration of a lattice of the toric code model, the links spanned by star and plaquette are highlighted in red and blue, respectively.

and  $B_p$ . Define the operator  $W^z(C)$  associated with a set of closed curves  $C$  on the bonds of the lattice, as follows:

$$W^z(C) = \prod_{j \in C} \sigma_j^z \quad (9.20)$$

Then the ground state is an equal superposition of all possible loop configurations:  $\sum_C W^z(C)|\text{vac}_x\rangle$ , where  $|\text{vac}_x\rangle$  is a state with  $\sigma_x = -1$  on every site. The closed loops are interpreted as electric field lines of the  $Z_2$  gauge theory. We now consider two geometries, first the cylinder and then the torus. The former case has a pair of degenerate ground states, and is the simplest setting to demonstrate state dependence of TEE.

### Cylinder geometry

On a cylinder, the Hamiltonian in Eqn. 9.19 leads to a pair of degenerate ground states (the  $A_s$  part of the Hamiltonian is suitably modified at the boundary of the cylinder to only include three links). The two normalized ground states  $|\xi_0\rangle, |\xi_1\rangle$ , are given by equal superpositions of electric field loop configurations which have an even and odd winding number around the cylinder respectively (see Figure 9.6). Consider now partitioning the cylinder into two cylindrical regions  $A$  and  $B$ . Then the Schmidt decomposition of these

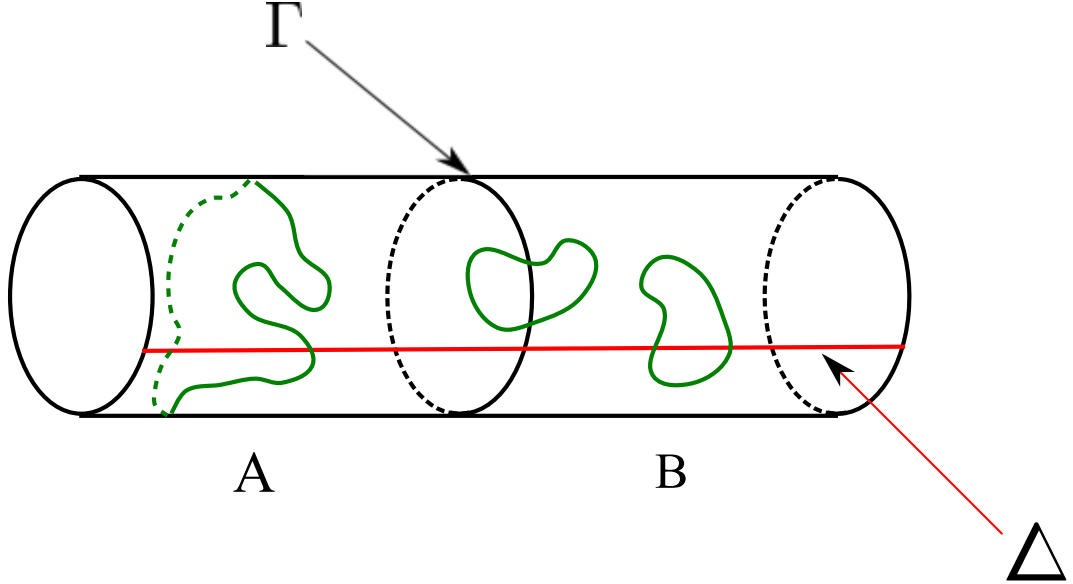


Figure 9.6. A snapshot of the ground state on the cylinder. Closed-loop strings (“ $Z_2$  electric fields”) can wrap around the cylinder. The ground states are doubly degenerate, corresponding to even and odd winding number sectors. The total number of string crossings the cut  $\Delta$  equals the winding number, modulo 2. The number of string crossings at the boundary  $\Gamma$  is even in the degenerate ground states.

ground states can be written as:

$$\begin{aligned} |\xi_0\rangle &= \frac{1}{\sqrt{2N_q}} \sum_{\{q_l\}} (|\Psi_{\{q_l\},0}^A\rangle |\Psi_{\{q_l\},0}^B\rangle + |\Psi_{\{q_l\},1}^A\rangle |\Psi_{\{q_l\},1}^B\rangle) \\ |\xi_1\rangle &= \frac{1}{\sqrt{2N_q}} \sum_{\{q_l\}} (|\Psi_{\{q_l\},0}^A\rangle |\Psi_{\{q_l\},1}^B\rangle + |\Psi_{\{q_l\},1}^A\rangle |\Psi_{\{q_l\},0}^B\rangle) \end{aligned} \quad (9.21)$$

where the  $N_q$  distinct configurations represented by  $\{q_l\}$  denotes the electric field configurations at the cut. The number of field lines crossing the cut is always even, since the ground state is composed of closed loops. For trivial bipartitions, this exhausts all terms in the Schmidt decomposition[93]. However, given that the boundary of the cut is non-contractible, the additional index 0, 1 appears which counts the parity of electric field winding around the cylinder, within a partition. These are correlated between the two partitions, for the fixed winding number ground states. This is the key difference from a trivial bipartition, leading to the ground-state dependence of TEE.

We now calculate the entanglement entropy associated with such a cut for an arbitrary linear combination of these two ground states  $|\Psi\rangle = c_0|\xi_0\rangle + c_1|\xi_1\rangle$ , with unit norm. Using Eqn. 9.21 one can easily verify:

$$\begin{aligned} |\Psi\rangle &= \frac{1}{\sqrt{2N_q}} \sum_{\{q_l\}} [(c_0 + c_1)|\Psi_{\{q_l\},+}^A\rangle |\Psi_{\{q_l\},+}^B\rangle \\ &\quad + (c_0 - c_1)|\Psi_{\{q_l\},-}^A\rangle |\Psi_{\{q_l\},-}^B\rangle] \end{aligned} \quad (9.22)$$

where  $|\Psi_{\{q_l\},\pm}^{A(B)}\rangle = \left(|\Psi_{\{q_l\},0}^{A(B)}\rangle \pm |\Psi_{\{q_l\},1}^{A(B)}\rangle\right)/\sqrt{2}$ .

For a Schmidt decomposition  $|\Psi\rangle = \sum_a \sqrt{\lambda_a} |\Psi_a^A\rangle |\Psi_a^B\rangle$  the  $n$ th Renyi entropy is given by:  $S_n = \frac{1}{1-n} \log (\sum_a \lambda_a^n)$ . We arrive at:

$$S_n = \frac{1}{1-n} \log N_q^{1-n} [p_+^n + p_-^n] \quad (9.23)$$

where  $p_\pm = |c_0 \pm c_1|^2/2$ . Recognizing that the closed loop constraint leads to  $N_q = 2^{L-1}$ , where  $L$  is the length of the cut, and using the definition of TEE in Eqn. 9.2 we have:

$$\gamma'_n = \log 2 - \frac{1}{1-n} \log (p_+^n + p_-^n) \quad (9.24)$$

Thus, for the electric field winding eigenstates  $|\xi_{0,1}\rangle$  where  $p_\pm = 1/2$ , the TEE vanishes. However, for their equal superpositions when one of  $p_+$  or  $p_-$  vanishes, the TEE attains its maximal value  $\log 2$ . These are eigenstates of the Wilson loop operator that encircles the cylinder and measures the  $Z_2$  magnetic flux (vison number) threading it. An example of such a flux operator is  $F = \prod_{j \in Q} \sigma_j^z$ , where  $Q$  is a closed curve that loops once around the cylinder, such as the boundary  $\Gamma$  in Figure 9.6. Since TEE reduces the entanglement entropy, the maximum TEE states correspond to MESs. Why these MESs are eigenstates of flux through the cylinder for this particular cut? The number of electric field lines crossing the boundary  $\Gamma$  is always even. This constraint carries some information and hence lowers the entropy by bringing in the standard TEE of  $\log 2$ . On the other hand, the topology of the cut boundary  $\Gamma$  allows for a determination of which magnetic flux sector the cylinder is in. A state that is not an eigenstate of magnetic flux through the cylinder leads to a loss of information and hence a positive contribution to the total entanglement entropy (and reduces TEE). This suggests that the MESs are eigenstates of loop operators which can be defined parallel to the cut  $\Gamma$ . This is further substantiated by the result for the torus case discussed below, where they are simultaneous eigenstates of magnetic flux enclosed by the cut and electric flux penetrating the cut.

## Torus geometry

The four degenerate ground states are distinguished by the even-odd parity of the winding number of electric field lines around the two cycles of the torus. The operator  $W^z(C)$ , which generates the set of closed loops  $C$  can be used to write the ground states:

$$|\xi_{ab}\rangle = \sum_C W_{ab}^z(C) |\text{vac}_x\rangle \quad (9.25)$$

where the subscript  $a$  ( $b$ ) takes on binary values 0, 1 and denotes whether the loops  $C$  belong to the even or odd winding number sectors along the  $\hat{x}$  ( $\hat{y}$ ) direction, and  $|\text{vac}_x\rangle$  is a state with  $\sigma_x = -1$  on every site. The four ground states cannot be mixed by any local operator

and hence realize a  $Z_2$  topological order. Let us consider a ground state as the following linear combination:

$$|\Psi\rangle = \sum_{a,b=0,1} c_{a,b} |\xi_{ab}\rangle \quad (9.26)$$

We are interested in calculating entanglement entropy for the state  $|\Psi\rangle$  corresponding to the partition shown in the Figure 9.1b and the dependence of TEE on parameters  $c_{a,b}$ . After straightforward algebra (see details in Appendix D.1), one finds the following expression for subsystem A with boundaries of length  $L$ :

$$S_n = L\log(2) - \gamma'_n \quad (9.27)$$

where:

$$\gamma'_n = 2\log(2) - \frac{1}{1-n} \log \sum_{j=1}^4 p_j^n \quad (9.28)$$

and:

$$\begin{aligned} p_1 &= \frac{|c_{00} + c_{01}|^2}{2} \\ p_2 &= \frac{|c_{00} - c_{01}|^2}{2} \\ p_3 &= \frac{|c_{10} + c_{11}|^2}{2} \\ p_4 &= \frac{|c_{10} - c_{11}|^2}{2} \end{aligned} \quad (9.29)$$

This is indeed consistent with Eqn. 9.3, given that  $\gamma = \log D = \log 2$  and  $d_j = 1$  for an Abelian topological order with  $D^2 = 4$  degenerate ground states. Further, Eqn. 9.28 readily leads to the following four MESSs:

$$\begin{aligned} |\Xi_1\rangle &= \frac{1}{\sqrt{2}}(|\xi_{00}\rangle + |\xi_{01}\rangle) \\ |\Xi_2\rangle &= \frac{1}{\sqrt{2}}(|\xi_{00}\rangle - |\xi_{01}\rangle) \\ |\Xi_3\rangle &= \frac{1}{\sqrt{2}}(|\xi_{10}\rangle + |\xi_{11}\rangle) \\ |\Xi_4\rangle &= \frac{1}{\sqrt{2}}(|\xi_{10}\rangle - |\xi_{11}\rangle) \end{aligned} \quad (9.30)$$

What is the physical significance of these four states being the MESSs? Similar to the cylinder geometry case, these states are the simultaneous eigenstates of Wilson loop operators that encircles the torus and measures the  $Z_2$  magnetic and electric fluxes threading it, as shown in Table 9.1 and Figure 9.7. We leave more detailed algebra to Appendix D.1.

MES	$T_y$	$F_y$	quasiparticle
$\Xi_1$	0	0	1
$\Xi_2$	1	0	$m$
$\Xi_3$	0	1	$e$
$\Xi_4$	1	1	$em$

Table 9.1. List of  $Z_2$  magnetic flux  $T_y$ ,  $Z_2$  electric flux  $F_y$  and corresponding quasiparticle of Wilson loop operator for the four MESs  $|\Xi_\alpha\rangle$  of the toric code with system geometry in Figure 9.1b. The definitions of  $T_y$  and  $F_y$  are in Appendix D.1.

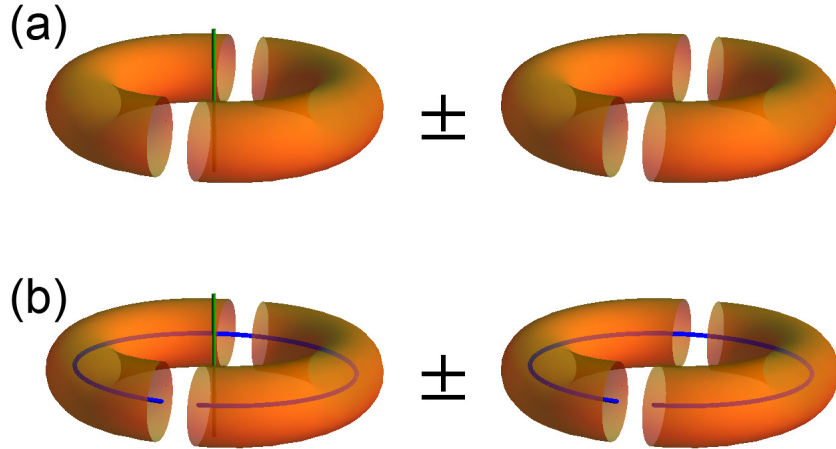


Figure 9.7. The four minimum entropy states of the  $Z_2$  topological phase corresponding to the bipartition shown in the figure expressed as linear combinations of the four magnetic flux states. The magnetic  $\pi$  flux is represented by the thick blue and green lines.

When  $\gamma'_n$  is maximized, the corresponding  $S_n$  is minimized, providing the maximum possible information about a given state. Since the cut is made along  $\hat{y}$ , it can measure the  $Z_2$  magnetic and electric fluxes directed parallel to  $\hat{x}$ . Hence the MES  $|\Xi_\alpha\rangle$  with definite magnetic and electric flux sectors, maximizes the TEE with  $\gamma_{topo} = 2 \log(2)$ , a contribution of  $\log(2)$  from each of the two boundaries. As one linearly superposes different MESs  $|\Xi_\alpha\rangle$ , the information obtained from measuring magnetic and electric sectors becomes scrambled; especially, at the extreme case of equal superposition of  $|\Xi_\alpha\rangle$ , all information about the global quantum numbers has been lost and we have  $\gamma' = 0$ . This offers another example where MESs are the eigenstates of loop operators defined on the cylinder from the entanglement cut.

## 9.3 Extracting Statistics from Topological Entanglement Entropy

The modular  $\mathcal{S}$  and  $\mathcal{U}$  matrices describe the action of certain modular transformations on the degenerate ground states of the topological quantum field theory. On the other hand, the braiding and statistics of quasiparticles are encoded in the  $\mathcal{S}$  and  $\mathcal{U}$  matrices. For Abelian phases, the  $ij$ 'th entry of the  $\mathcal{S}$  matrix corresponds to the phase the  $i$ 'th quasiparticle acquires when it encircles the  $j$ 'th quasiparticle. The  $\mathcal{U}$  matrix is diagonal and the  $ii$ 'th entry corresponds to the phase the  $i$ 'th quasiparticle acquires when it is exchanged with an identical one. Since the MESs are the eigenstates of the nonlocal operators defined on the entanglement cut, the MESs are the canonical basis for defining  $\mathcal{S}$  and  $\mathcal{U}$ . The modular matrices are just certain unitary transformations of the MES basis. As argued in Appendix D.2, the  $\mathcal{S}$  matrix acts on MESs as an operator that implements  $\pi/2$  rotation while the  $\mathcal{U}\mathcal{S}$  matrix corresponds to  $2\pi/3$  rotation of MESs.

### 9.3.1 Modular $\mathcal{S}$ Matrix of CSL from TEE

Let's consider the CSL wave functions studied in Section 9.2.2, and assume that we did not have any information about the individual quantum dimensions or the modular  $\mathcal{S}$  matrix. The only information that is provided is the two-fold degenerate ground-state wave functions  $|\pi, 0\rangle$  and  $|0, \pi\rangle$ . We construct the linear combination  $|\Phi\rangle$  as Eqn. 9.17 and calculate its TEE for a non-trivial bipartition as Figure 9.1b on a  $\pi/2$  rotation symmetric lattice. Consequently, we get the  $2\gamma - \gamma'$  dependence on parameter  $\phi$  in Figure 9.4.

We notice that the minimum of the  $2\gamma' - \gamma$  attained is approximately zero. According to Eqn. 9.3, this implies that at least one of the quantum dimensions  $d_i$  should be 1. Since the total quantum dimension  $D = \sqrt{d_0^2 + d_{1/2}^2} = \sqrt{2}$ , this implies that  $d_0 = d_{1/2} = 1$ . Also, we see that the MES lies at  $\phi \approx 0.14\pi$  by fitting Figure 9.4 to Eqn. 9.3.

For system with square geometry the  $\mathcal{S}$  matrix describes the action of  $\pi/2$  rotation on the MESs. Since the two states  $|0, \pi\rangle$  and  $|\pi, 0\rangle$  transform into each other under  $\pi/2$  rotation, this implies that in the basis  $\{|0, \pi\rangle, |\pi, 0\rangle\}$ , the modular  $\mathcal{S}$  matrix is given by the Pauli matrix  $\sigma_x$ . To change the basis to MESs, we just need a unitary transformation  $V$  that rotates  $|0, \pi\rangle | \pi, 0\rangle$  basis to the MESs basis. The  $V$  is determined by the fact that one needs to rotate  $|0, \pi\rangle | \pi, 0\rangle$  basis by an angle  $\approx 0.14\pi$  to obtain MES (this is the numerically determined value, the exact value being  $\pi/8$ ). Therefore:

$$\mathcal{S} = V^\dagger \begin{pmatrix} 0 & 1 \\ 1 & 0 \end{pmatrix} V \quad (9.31)$$

where:

$$V \approx \begin{pmatrix} \cos(0.14\pi) & -\sin(0.14\pi)e^{i\varphi} \\ \sin(0.14\pi) & \cos(0.14\pi)e^{i\varphi} \end{pmatrix} \quad (9.32)$$

from the two MESSs:  $(\cos(0.14\pi), \sin(0.14\pi))^T$  and  $(-\sin(0.14\pi), \cos(0.14\pi))^T$  and  $\varphi$  is an undecided phase. This yields the following value for the approximate modular  $\mathcal{S}$  matrix:

$$\mathcal{S} \approx \begin{pmatrix} \sin(0.28\pi) & \cos(0.28\pi)e^{i\varphi} \\ \cos(0.28\pi)e^{-i\varphi} & -\sin(0.28\pi) \end{pmatrix} \quad (9.33)$$

The existence of an identity particle requires positive real entries in the first row and column and implies  $\varphi = 0$ , which gives:

$$\mathcal{S} \approx \begin{pmatrix} 0.77 & 0.63 \\ 0.63 & -0.77 \end{pmatrix} \quad (9.34)$$

Comparing this result with the exact expression in Eqn. 9.15, we observe that even though the  $\mathcal{S}$  matrix obtained using our method is approximate, some of the more important statistics can be extracted rather exactly. The above  $\mathcal{S}$  matrix tells us that the quasiparticle corresponding to  $d_0 = 1$  does not acquire any phase when it goes around any other particle and corresponds to an identity particle as expected, while the quasiparticle corresponding to  $d_{1/2} = 1$  has semion statistics since it acquires a phase of  $\pi$  when it encircles another identical particle. Numerical improvements can further reduce the error in pinpointing the MES and thereby leading to a more accurate value of the  $\mathcal{S}$  matrix. As another application, we study the action of modular transformation on the MESSs  $|\Xi_\alpha\rangle$  for the  $Z_2$  gauge theory in Appendix D.3.

### 9.3.2 Algorithm for Extracting Modular $\mathcal{S}$ Matrix from TEE

In the last subsection and Appendix D.3 we calculated the modular  $\mathcal{S}$  matrices for the CSL and  $Z_2$  toric code model respectively using the transformation properties of the basis states  $|\xi_{ab}\rangle$  under  $\pi/2$  rotation transformations  $\mathcal{R}$  and translating it into the canonical basis of MESSs  $|\Xi_i\rangle$ :  $\mathcal{S} = U^\dagger \mathcal{R} U$ . However, such  $\pi/2$  rotation symmetry is not necessary. Even without symmetry, it is possible to obtain the  $\mathcal{S}$  matrix by studying the modular transformation between certain nontrivial pair of sets of MESSs.

Starting from the definition, the modular  $\mathcal{S}$  matrix has the following expression:

$$\mathcal{S}_{\alpha\beta} = \frac{1}{D} \left\langle \Xi_\alpha^{\hat{x}} \middle| \Xi_\beta^{\hat{y}} \right\rangle \quad (9.35)$$

Here  $D$  is the total quantum dimension and  $\hat{x}$  and  $\hat{y}$  are two directions on a torus. Eqn. 9.35 is just a unitary transformation between the particle states along different directions. In the case of a square system as in the last subsection, the  $\mathcal{S}$  matrix acts as a  $\pi/2$  rotation on the MES basis  $|\Xi_\beta^{\hat{y}}\rangle$ . In general, however,  $\hat{x}$  and  $\hat{y}$  do not need to be geometrically orthogonal, and the system does not need to be rotationally symmetric, as long as the loops defining  $|\Xi_\alpha^{\hat{x}}\rangle$  and  $|\Xi_\beta^{\hat{y}}\rangle$  interwind with each other. Therefore, the modular  $\mathcal{S}$  matrix can be derived even without any presumed symmetry of the given wave functions. Note that there

is an undetermined phase for each  $|\Xi_{\alpha}^{\hat{x}}\rangle$  and  $|\Xi_{\beta}^{\hat{y}}\rangle$ , therefore a phase freedom between the rows (columns), which may be fixed by the existence of an identity particle.

Let's start with the two primitive vectors  $w_1$  and  $w_2$  and determine the transformation of the MESs of  $w_2$  to those of  $w'_2$  given by:

$$\begin{aligned} w'_1 &= n_1 w_1 + m_1 w_2 \\ w'_2 &= n_2 w_1 + m_2 w_2 \end{aligned} \quad (9.36)$$

with  $n_1 m_2 - m_1 n_2 = 1$  by definition of the modular transformation. We restrict  $n_2 = -1$ , which means the cross product:

$$w_2 \times w'_2 = -w_2 \times w_1 = w_1 \times w_2 = A \quad (9.37)$$

$A$  is the surface area of the torus.

The corresponding modular matrix can be expanded as:

$$\begin{aligned} \begin{pmatrix} n_1 & 1 - n_1 m_2 \\ -1 & m_2 \end{pmatrix} &= \begin{pmatrix} 1 & -n_1 \\ & 1 \end{pmatrix} \begin{pmatrix} & 1 \\ -1 & \end{pmatrix} \begin{pmatrix} 1 & -m_2 \\ & 1 \end{pmatrix} \\ &= U^{-n_1} S U^{-m_2} \end{aligned} \quad (9.38)$$

Correspondingly, according to Appendix D.2 the transformation:

$$\mathcal{R} = \mathcal{U}^{-n_1} S \mathcal{U}^{-m_2} \quad (9.39)$$

Because  $\mathcal{U}$  matrix is diagonal by definition, its left (right) matrix products only adds an additional phase factor to each row (column) and can be eliminated. Therefore, without any argument on the symmetry, the generalized algorithm:

1. Given a set of ground-state wave functions  $|\xi_{\alpha}\rangle$ , calculate the TEE of an entanglement bipartition along  $w_2$  direction, for a linear combination  $|\Phi\rangle = \sum c_{\alpha} |\xi_{\alpha}\rangle$ . Search for the minimum of TEE  $2\gamma - \gamma'$  in the  $c_{\alpha}$  parameter space. That gives one MES  $|\Xi_{\beta}\rangle$  and the corresponding quantum dimension  $2 \log(d_{\beta}) = 2\gamma - \gamma'$ . Note that the existence of an identity particle ensures at least one minimum TEE  $2\gamma - \gamma' = 0$ .
2. iterate step 1 but with  $c_{\alpha}$  in the parameter space orthogonal to all previous obtained MESs  $|\Xi_{\beta}\rangle$ . Continue this process until we have the expressions for all  $|\Xi_{\beta}\rangle$ . This gives a unitary transformation matrix  $U_1$  with the  $\alpha\beta$ 'th entry being  $c_{\alpha\beta}$ , which changes the basis from  $|\xi_{\alpha}\rangle$  to  $|\Xi_{\beta}\rangle$ . Note that there is a relative  $U(1)$  phase degree of freedom for each  $|\Xi_{\beta}\rangle$ .
3. Repeat step 1 and step 2 but with the entanglement cut along  $w'_2$  direction, which satisfies Eqn. 9.36 and Eqn. 9.37, and obtains the unitary transformation matrix  $U_2$ .
4. The modular  $\mathcal{S}$  matrix is given by  $U_2^{-1} U_1$  except for an undetermined phase for each MES corresponding to a row or a column. The existence of an identity particle that obtains trivial phase encircling any quasiparticle helps to fix the relative phase between different MESs, requiring the entries of the first row and column to be real and positive. This completely defines the modular  $\mathcal{S}$  matrix.

The above algorithm is able to extract the modular transformation matrix  $\mathcal{S}$  and hence braiding and mutual statistics of quasiparticle excitations just using the ground-state wave functions as an input. Further, there is no loss of generality for non-Abelian phases, which can be dealt by enforcing the orthogonality condition in step 2 which guarantees that one obtains states with quantum dimensions  $d_\alpha$  in an increasing order.

In Appendix D.3 we take the square lattice toric code model as an example once again, but without presuming any symmetry of the system.

### 9.3.3 Extracting Other Modular Matrices from TEE

In Appendix D.3, we calculate the  $\mathcal{U}$  matrix for the  $Z_2$  toric code model, given the simple action of  $\mathcal{U}$  on  $|\xi_{ab}\rangle$ . Though we were unable to find a general algorithm for the  $\mathcal{U}$  matrix, as we did for the the  $\mathcal{S}$  matrix in the last subsection, in the presence of certain symmetries  $\mathcal{U}$  can indeed be extracted given a set of ground-state wave functions  $|\xi_\alpha\rangle$ . This is achieved by first calculating the action  $\mathcal{R}$  on the states  $|\xi_\alpha\rangle$  under this symmetry operation, and then translating it into the action on MESs. Specifically, the corresponding modular matrix is given by  $U^\dagger \mathcal{R} U$ , where the unitary matrix  $U$  is obtained through the first two steps of the algorithm in the last subsection.

The aforementioned symmetry to extract  $\mathcal{S}$  matrix is the  $\pi/2$  rotation, as shown in Section 9.3.1 and the first example in Appendix D.3, but it may be generalized to symmetries such as rotation of other angles and even reflection symmetry (see Appendix D.2). More interestingly, when the symmetry operation  $\mathcal{R}$  is a  $2\pi/3$  rotation, one gets the  $\mathcal{US}$  matrix. Hence, if one starts with an arbitrary basis  $|\xi_\alpha\rangle$  for the degenerate ground-state manifold of a topological order, the problem of  $\mathcal{S}$  and  $\mathcal{U}$  matrices can be reduced to the transformation property of chosen basis states  $|\xi_\alpha\rangle$  under  $\pi/2$  and  $2\pi/3$  rotations and the unitary transformation that translates  $|\xi_\alpha\rangle$  basis to the MESs  $|\Xi_\alpha\rangle$ . To illustrate this point, we extract the  $\mathcal{US}$  matrix for the  $Z_2$  gauge theory in Appendix D.3 by putting the  $Z_2$  toric code on triangular lattice which has  $2\pi/3$  rotation symmetry.

## 9.4 Conclusion

In this chapter, we studied two topologically ordered phases, the chiral spin liquid (CSL) and the  $Z_2$  spin liquid using VMC method for Gutzwiller projected wave functions numerically and the  $Z_2$  toric code model analytically, and showed that the topological entanglement entropy (TEE) depends on the chosen ground state when the entanglement bipartition is topologically nontrivial. We also determined the minimum entropy states (MESs) and explained their physical significance.

As an application of the physical significance of MESs, we suggested an algorithm for extracting the modular transformation matrices that determine the statistics such as quasi-

particle self and mutual statistics and individual quantum dimensions. These matrices also determine the central charge of the edge state modulo 8 [77]. Given the ground states, this algorithm determines the topological order to a large extent. We note that Wen proposed a different way to extract  $\mathcal{S}$  and  $\mathcal{U}$  matrices by calculating the non-abelian Berry phase[191] which in practice may be difficult to implement, especially on a lattice, since it requires calculating the degenerate ground states  $\psi_n$  of the system as function of the modular parameter  $\tau = \omega_2/\omega_1$  and calculating the derivatives such as  $\langle \psi_n(\tau) | \partial_\tau | \psi_m(\tau) \rangle$ .

We note that there may be cases where the  $\pi/2$  and  $2\pi/3$  rotations of the MESs may not be exactly identifiable with the modular  $\mathcal{S}$  and  $\mathcal{U}\mathcal{S}$  matrices respectively. This may happen, for example, when the particles have an internal angular momentum which may cause the wave function to acquire an additional phase upon rotation, over and above the phase due to underlying topological structure. If the MESs correspond to spin-singlet spin-liquid wave functions (such as CSL studied in this chapter) and/or string-net models (such as toric code model) where there is no such internal structure, there should not be such additional phase. Further, since all MESs are locally same, they should all acquire same extra phase due to any local physics and therefore, the extra phase may be separable from the topological phase.

For quantum Hall systems, because of the bulk-edge correspondence, the fusion algebra and topological spin of the bulk quasiparticles also determine the fusion rules and scaling dimensions for the primary fields in the chiral CFT at the edge. Therefore, in the context of quantum Hall systems, the entanglement entropy of the ground-state manifold determines robust features of the fields in the corresponding edge CFT.

It would also be interesting to consider generalization of the methods developed in this chapter to higher dimensions. Discrete gauge theories furnish the best known theories with long-range entanglement in  $D \geq 3$  dimensions and akin to  $D = 2$ , they again support degenerate ground states on the torus. In a recent paper[48], it was shown that these theories again have non-zero TEE that is proportional to  $\log(|G|)$ , the number of elements in the gauge group. A simple generalization of the method developed in this chapter shows that TEE for bipartition that has non-contractible boundaries will again depend on the ground state, and one will again find certain MESs that have the maximum knowledge of the quantum numbers associated with an entanglement cut. Yet we are not aware of simple generalization of modular transformations to higher dimensions, the meaning of the matrix that relates MESs for orthogonal entanglement cuts in higher dimensions requires further investigation.

# Bibliography

- [1] Jason Alicea. Majorana fermions in a tunable semiconductor device. *Phys. Rev. B*, 81:125318, Mar 2010.
- [2] B. L. Altshuler, A. G. Aronov, and B. Z. Spivak. The aaronov-bohm effect in disordered conductors. *JETP Lett.*, 33:94, 1981.
- [3] B. L. Altshuler, L. B. Ioffe, and A. J. Millis. Low-energy properties of fermions with singular interactions. *Phys. Rev. B*, 50:14048–14064, Nov 1994.
- [4] P. W. ANDERSON. The resonating valence bond state in  $la_2cuo_4$  and superconductivity. *Science*, 235(4793):1196–1198, 1987.
- [5] Yoichi Asada, Keith Slevin, and Tomi Ohtsuki. Numerical estimation of the  $\beta$  function in two-dimensional systems with spin-orbit coupling. *Phys. Rev. B*, 70:035115, Jul 2004.
- [6] Y. Avishai and B. Horovitz. Phase transition of the aharonov-bohm periodicity in metallic cylinders. *Phys. Rev. B*, 35:423–426, Jan 1987.
- [7] J. E. Avron, R. Seiler, and B. Simon. Homotopy and quantization in condensed matter physics. *Phys. Rev. Lett.*, 51:51–53, Jul 1983.
- [8] F. A. Bais and J. C. Romers. The modular S-matrix as order parameter for topological phase transitions. *ArXiv e-prints*, August 2011.
- [9] L. Balents, M. P. A. Fisher, and S. M. Girvin. Fractionalization in an easy-axis kagome antiferromagnet. *Phys. Rev. B*, 65:224412, May 2002.
- [10] Leon Balents. Spin liquids in frustrated magnets. *Nature*, 464(7286):199–208, March 2010.
- [11] J. H. Bardarson, P. W. Brouwer, and J. E. Moore. Aharonov-bohm oscillations in disordered topological insulator nanowires. *Phys. Rev. Lett.*, 105:156803, Oct 2010.
- [12] J. H. Bardarson, J. Tworzydlo, P. W. Brouwer, and C. W. J. Beenakker. One-parameter scaling at the dirac point in graphene. *Phys. Rev. Lett.*, 99:106801, Sep 2007.
- [13] B. Andrei Bernevig, Taylor L. Hughes, and Shou-Cheng Zhang. Quantum spin hall effect and topological phase transition in hgte quantum wells. *Science*, 314(5806):1757–1761, 2006.

- [14] B. Andrei Bernevig and Shou-Cheng Zhang. Quantum spin hall effect. *Phys. Rev. Lett.*, 96:106802, Mar 2006.
- [15] Matthew S. Block, D. N. Sheng, Olexei I. Motrunich, and Matthew P. A. Fisher. Spin bose-metal and valence bond solid phases in a spin-1/2 model with ring exchanges on a four-leg triangular ladder. *Phys. Rev. Lett.*, 106:157202, Apr 2011.
- [16] Alonso Botero and Benni Reznik. Bcs-like modewise entanglement of fermion gaussian states. *Physics Letters A*, 331(1-2):39 – 44, 2004.
- [17] Noah Bray-Ali, Letian Ding, and Stephan Haas. Topological order in paired states of fermions in two dimensions with breaking of parity and time-reversal symmetries. *Phys. Rev. B*, 80:180504, Nov 2009.
- [18] D. Carpentier, P. Le Doussal, and T. Giamarchi. Stability of the bragg glass phase in a layered geometry. *EPL (Europhysics Letters)*, 35(5):379, 1996.
- [19] H. Casini and M. Huerta. Universal terms for the entanglement entropy in 2+1 dimensions. *Nuclear Physics B*, 764:183, 2007.
- [20] Claudio Castelnovo and Claudio Chamon. Topological order and topological entropy in classical systems. *Phys. Rev. B*, 76:174416, Nov 2007.
- [21] V. Chandrasekhar, M. J. Rooks, S. Wind, and D. E. Prober. Observation of aharonov-bohm electron interference effects with periods  $\frac{h}{e}$  and  $\frac{h}{2e}$  in individual micron-size, normal-metal rings. *Phys. Rev. Lett.*, 55:1610–1613, Oct 1985.
- [22] Y. L. Chen, J.-H. Chu, J. G. Analytis, Z. K. Liu, K. Igarashi, H.-H. Kuo, X. L. Qi, S. K. Mo, R. G. Moore, D. H. Lu, M. Hashimoto, T. Sasagawa, S. C. Zhang, I. R. Fisher, Z. Hussain, and Z. X. Shen. Massive dirac fermion on the surface of a magnetically doped topological insulator. *Science*, 329(5992):659–662, 2010.
- [23] J. Ignacio Cirac and Germán Sierra. Infinite matrix product states, conformal field theory, and the haldane-shastry model. *Phys. Rev. B*, 81:104431, Mar 2010.
- [24] A. Croy, R. A. Roemer, and M. Schreiber. Localization of electronic states in amorphous materials: recursive Green’s function method and the metal-insulator transition at  $E_{\text{F}}=0$ . *eprint arXiv:cond-mat/0602300*, February 2006.
- [25] Eric Dennis, Alexei Kitaev, Andrew Landahl, and John Preskill. Topological quantum memory. *Journal of Mathematical Physics*, 43(9):4452–4505, 2002.
- [26] Shiying Dong, Eduardo Fradkin, Robert G. Leigh, and Sean Nowling. Topological entanglement entropy in chern-simons theories and quantum hall fluids. *Journal of High Energy Physics*, 2008(05):016, 2008.
- [27] Volovik G. E. Chiral anomaly and the law of conservation of momentum in 3he-a. *JETP Lett.*, 43:551, 1986.

- [28] Tohru Eguchi, Peter B. Gilkey, and Andrew J. Hanson. Gravitation, gauge theories and differential geometry. *Physics Reports*, 66(6):213 – 393, 1980.
- [29] J. P. Eisenstein, K. B. Cooper, L. N. Pfeiffer, and K. W. West. Insulating and fractional quantum hall states in the first excited landau level. *Phys. Rev. Lett.*, 88:076801, Jan 2002.
- [30] J.P. Eisenstein, R.L. Willett, H.L. Stormer, L.N. Pfeiffer, and K.W. West. Activation energies for the even-denominator fractional quantum hall effect. *Surface Science*, 229(1-3):31 – 33, 1990.
- [31] J. Eisert, M. Cramer, and M. B. Plenio. *Colloquium* : Area laws for the entanglement entropy. *Rev. Mod. Phys.*, 82:277–306, Feb 2010.
- [32] Andrew M. Essin, Joel E. Moore, and David Vanderbilt. Magnetoelectric polarizability and axion electrodynamics in crystalline insulators. *Phys. Rev. Lett.*, 102:146805, Apr 2009.
- [33] Andrew M. Essin, Ari M. Turner, Joel E. Moore, and David Vanderbilt. Orbital magnetoelectric coupling in band insulators. *Phys. Rev. B*, 81:205104, May 2010.
- [34] Lukasz Fidkowski. Entanglement spectrum of topological insulators and superconductors. *Phys. Rev. Lett.*, 104:130502, Apr 2010.
- [35] Lukasz Fidkowski and Alexei Kitaev. Effects of interactions on the topological classification of free fermion systems. *Phys. Rev. B*, 81:134509, Apr 2010.
- [36] Steven T. Flammia, Alioscia Hamma, Taylor L. Hughes, and Xiao-Gang Wen. Topological entanglement rényi entropy and reduced density matrix structure. *Phys. Rev. Lett.*, 103:261601, Dec 2009.
- [37] Eduardo Fradkin, Elbio Dagotto, and Daniel Boyanovsky. Physical realization of the parity anomaly in condensed matter physics. *Phys. Rev. Lett.*, 57:2967–2970, Dec 1986.
- [38] Philippe Di Francesco, P. Mathieu, and D. Sénéchal. *Conformal Field Theory*. Graduate Texts in Contemporary Physics. Springer, 1997.
- [39] Liang Fu and C. L. Kane. Topological insulators with inversion symmetry. *Phys. Rev. B*, 76:045302, Jul 2007.
- [40] Liang Fu and C. L. Kane. Superconducting proximity effect and majorana fermions at the surface of a topological insulator. *Phys. Rev. Lett.*, 100:096407, Mar 2008.
- [41] Liang Fu, C. L. Kane, and E. J. Mele. Topological insulators in three dimensions. *Phys. Rev. Lett.*, 98:106803, Mar 2007.
- [42] Shunsuke Furukawa and Grégoire Misguich. Topological entanglement entropy in the quantum dimer model on the triangular lattice. *Phys. Rev. B*, 75:214407, Jun 2007.

- [43] M. Gijs, C. Van Haesendonck, and Y. Bruynseraede. Resistance oscillations and electron localization in cylindrical mg films. *Phys. Rev. Lett.*, 52:2069–2072, Jun 1984.
- [44] Dimitri Gioev and Israel Klich. Entanglement entropy of fermions in any dimension and the widom conjecture. *Phys. Rev. Lett.*, 96:100503, Mar 2006.
- [45] Claudius Gros. Physics of projected wavefunctions. *Annals of Physics*, 189(1):53 – 88, 1989.
- [46] Tarun Grover and T. Senthil. Topological spin hall states, charged skyrmions, and superconductivity in two dimensions. *Phys. Rev. Lett.*, 100:156804, Apr 2008.
- [47] Tarun Grover, N. Trivedi, T. Senthil, and Patrick A. Lee. Weak mott insulators on the triangular lattice: Possibility of a gapless nematic quantum spin liquid. *Phys. Rev. B*, 81:245121, Jun 2010.
- [48] Tarun Grover, Ari M. Turner, and Ashvin Vishwanath. Entanglement entropy of gapped phases and topological order in three dimensions. *Phys. Rev. B*, 84:195120, Nov 2011.
- [49] F. D. M. Haldane. Fractional quantization of the hall effect: A hierarchy of incompressible quantum fluid states. *Phys. Rev. Lett.*, 51:605–608, Aug 1983.
- [50] F. D. M. Haldane. Exact jastrow-gutzwiller resonating-valence-bond ground state of the spin-(1/2 antiferromagnetic heisenberg chain with  $1/r^2$  exchange. *Phys. Rev. Lett.*, 60:635–638, Feb 1988.
- [51] B. I. Halperin. Statistics of quasiparticles and the hierarchy of fractional quantized hall states. *Phys. Rev. Lett.*, 52:1583–1586, Apr 1984.
- [52] B. I. Halperin, Patrick A. Lee, and Nicholas Read. Theory of the half-filled landau level. *Phys. Rev. B*, 47:7312–7343, Mar 1993.
- [53] A. Hamma, R. Ionicioiu, and P. Zanardi. Ground state entanglement and geometric entropy in the kitaev’s model. *Phys. Lett. A*, 337:22, 2005.
- [54] A. Hamma, W. Zhang, S. Haas, and D. A. Lidar. Entanglement, fidelity, and topological entropy in a quantum phase transition to topological order. *Phys. Rev. B*, 77:155111, Apr 2008.
- [55] Alioscia Hamma, Radu Ionicioiu, and Paolo Zanardi. Bipartite entanglement and entropic boundary law in lattice spin systems. *Phys. Rev. A*, 71:022315, Feb 2005.
- [56] Masudul Haque, Oleksandr Zozulya, and Kareljan Schoutens. Entanglement entropy in fermionic Laughlin states. *Phys. Rev. Lett.*, 98:060401, Feb 2007.
- [57] M. Z. Hasan and C. L. Kane. *Colloquium : Topological insulators*. *Rev. Mod. Phys.*, 82:3045–3067, Nov 2010.

- [58] Matthew B. Hastings, Iván González, Ann B. Kallin, and Roger G. Melko. Measuring renyi entanglement entropy in quantum monte carlo simulations. *Phys. Rev. Lett.*, 104:157201, Apr 2010.
- [59] Friedrich W. Hehl, Yuri N. Obukhov, Jean-Pierre Rivera, and Hans Schmid. Relativistic analysis of magnetoelectric crystals: Extracting a new 4-dimensional p odd and t odd pseudoscalar from cr<sub>2</sub>o<sub>3</sub> data. *Physics Letters A*, 372(8):1141 – 1146, 2008.
- [60] J. S. Helton, K. Matan, M. P. Shores, E. A. Nytko, B. M. Bartlett, Y. Yoshida, Y. Takano, A. Suslov, Y. Qiu, J.-H. Chung, D. G. Nocera, and Y. S. Lee. Spin dynamics of the spin-1/2 kagome lattice antiferromagnet zncu<sub>3</sub>(OH)<sub>6</sub>cl<sub>2</sub>. *Phys. Rev. Lett.*, 98:107204, Mar 2007.
- [61] K.H. Hoffmann and A. Meyer. *Parallel Algorithms and Cluster Computing*. Lecture Notes in Computational Science and Engineering. Springer-Verlag, 2006.
- [62] Christoph Holzhey, Finn Larsen, and Frank Wilczek. Geometric and renormalized entropy in conformal field theory. *Nuclear Physics B*, 424(3):443 – 467, 1994.
- [63] D. Hsieh, D. Qian, L. Wray, Y. Xia, Y. S. Hor, R. J. Cava, and M. Z. Hasan. A topological dirac insulator in a quantum spin hall phase. *Nature*, 452(7190):970–974, April 2008.
- [64] D. Hsieh, Y. Xia, L. Wray, D. Qian, A. Pal, J. H. Dil, J. Osterwalder, F. Meier, G. Bihlmayer, C. L. Kane, Y. S. Hor, R. J. Cava, and M. Z. Hasan. Observation of unconventional quantum spin textures in topological insulators. *Science*, 323(5916):919–922, 2009.
- [65] Sergei V. Isakov, Matthew B. Hastings, and Roger G. Melko. Topological entanglement entropy of a bose-hubbard spin liquid. *Nat Phys*, 7(10):772–775, October 2011.
- [66] D. A. Ivanov and T. Senthil. Projected wave functions for fractionalized phases of quantum spin systems. *Phys. Rev. B*, 66:115111, Sep 2002.
- [67] R. Jackiw and P. Rossi. Zero modes of the vortex-fermion system. *Nuclear Physics B*, 190(4):681 – 691, 1981.
- [68] J.D. Jackson. *Classical Electrodynamics*. Wiley, 1999.
- [69] H. C. Jiang, Z. Y. Weng, and D. N. Sheng. Density matrix renormalization group numerical study of the kagome antiferromagnet. *Phys. Rev. Lett.*, 101:117203, Sep 2008.
- [70] H.-C. Jiang, H. Yao, and L. Balents. Spin Liquid Ground State of the Spin-1/2 Square  $J_1 - J_2$  Heisenberg Model. *ArXiv e-prints*, December 2011.
- [71] V. Kalmeyer and R. B. Laughlin. Equivalence of the resonating-valence-bond and fractional quantum hall states. *Phys. Rev. Lett.*, 59:2095–2098, Nov 1987.

- [72] Vadim Kalmeyer and R. B. Laughlin. Theory of the spin liquid state of the heisenberg antiferromagnet. *Phys. Rev. B*, 39:11879–11899, Jun 1989.
- [73] C. L. Kane and E. J. Mele. Quantum spin hall effect in graphene. *Phys. Rev. Lett.*, 95:226801, Nov 2005.
- [74] C. L. Kane and E. J. Mele.  $Z_2$  topological order and the quantum spin hall effect. *Phys. Rev. Lett.*, 95:146802, Sep 2005.
- [75] Mehdi Kargarian and Gregory A. Fiete. Topological phases and phase transitions on the square-octagon lattice. *Phys. Rev. B*, 82:085106, Aug 2010.
- [76] Esko Keski-Vakkuri and Xiao-Gang Wen. The ground state structure and modular transformations of fractional quantum hall states on a torus. *Int. J. Mod. Phys. B*, 25:4227, Nov 1993.
- [77] Alexei Kitaev. Anyons in an exactly solved model and beyond. *Annals of Physics*, 321(1):2 – 111, 2006. January Special Issue.
- [78] Alexei Kitaev. Periodic table for topological insulators and superconductors. *AIP Conference Proceedings*, 1134(1):22–30, 2009.
- [79] Alexei Kitaev and John Preskill. Topological entanglement entropy. *Phys. Rev. Lett.*, 96:110404, Mar 2006.
- [80] A.Yu. Kitaev. Fault-tolerant quantum computation by anyons. *Annals of Physics*, 303(1):2 – 30, 2003.
- [81] Steven A. Kivelson, Daniel S. Rokhsar, and James P. Sethna. Topology of the resonating valence-bond state: Solitons and high- $T_c$  superconductivity. *Phys. Rev. B*, 35:8865–8868, Jun 1987.
- [82] Israel Klich. Lower entropy bounds and particle number fluctuations in a fermi sea. *Journal of Physics A: Mathematical and General*, 39(4):L85, 2006.
- [83] Mahito Kohmoto, Bertrand I. Halperin, and Yong-Shi Wu. Diophantine equation for the three-dimensional quantum hall effect. *Phys. Rev. B*, 45:13488–13493, Jun 1992.
- [84] Markus Konig, Steffen Wiedmann, Christoph Brune, Andreas Roth, Hartmut Buhmann, Laurens W. Molenkamp, Xiao-Liang Qi, and Shou-Cheng Zhang. Quantum spin hall insulator state in hgte quantum wells. *Science*, 318(5851):766–770, 2007.
- [85] Andreas M Lauchli, Emil J Bergholtz, and Masudul Haque. Entanglement scaling of fractional quantum hall states through geometric deformations. *New Journal of Physics*, 12(7):075004, 2010.
- [86] R. B. Laughlin. Anomalous quantum hall effect: An incompressible quantum fluid with fractionally charged excitations. *Phys. Rev. Lett.*, 50:1395–1398, May 1983.

- [87] Dung-Hai Lee. Surface states of topological insulators: The dirac fermion in curved two-dimensional spaces. *Phys. Rev. Lett.*, 103:196804, Nov 2009.
- [88] Patrick A Lee. From high temperature superconductivity to quantum spin liquid: progress in strong correlation physics. *Reports on Progress in Physics*, 71(1):012501, 2008.
- [89] Sung-Sik Lee. Low-energy effective theory of fermi surface coupled with u(1) gauge field in 2 + 1 dimensions. *Phys. Rev. B*, 80:165102, Oct 2009.
- [90] Sung-Sik Lee and Patrick A. Lee. U(1) gauge theory of the hubbard model: Spin liquid states and possible application to  $\kappa$ -(BEDT-TTF)<sub>2</sub> $\%mathrm{Cu_2(CN)_3}$ . *Phys. Rev. Lett.*, 95:036403, Jul 2005.
- [91] Michael Levin and Ady Stern. Fractional topological insulators. *Phys. Rev. Lett.*, 103:196803, Nov 2009.
- [92] Michael Levin and Xiao-Gang Wen. Fermions, strings, and gauge fields in lattice spin models. *Phys. Rev. B*, 67:245316, Jun 2003.
- [93] Michael Levin and Xiao-Gang Wen. Detecting topological order in a ground state wave function. *Phys. Rev. Lett.*, 96:110405, Mar 2006.
- [94] Michael A. Levin and Xiao-Gang Wen. String-net condensation: a physical mechanism for topological phases. *Phys. Rev. B*, 71:045110, Jan 2005.
- [95] Hui Li and F. D. M. Haldane. Entanglement spectrum as a generalization of entanglement entropy: Identification of topological order in non-abelian fractional quantum hall effect states. *Phys. Rev. Lett.*, 101:010504, Jul 2008.
- [96] T. Li. Antiferromagnetic long range order in the uniform resonating valence bond state on square lattice. *ArXiv e-prints*, December 2011.
- [97] Andreas W. W. Ludwig, Matthew P. A. Fisher, R. Shankar, and G. Grinstein. Integer quantum hall transition: An alternative approach and exact results. *Phys. Rev. B*, 50:7526–7552, Sep 1994.
- [98] Roman M. Lutchyn, Jay D. Sau, and S. Das Sarma. Majorana fermions and a topological phase transition in semiconductor-superconductor heterostructures. *Phys. Rev. Lett.*, 105:077001, Aug 2010.
- [99] Z. Y. Meng, T. C. Lang, S. Wessel, F. F. Assaad, and A. Muramatsu. Quantum spin liquid emerging in two-dimensional correlated dirac fermions. *Nature*, 464(7290):847–851, April 2010.
- [100] Max A. Metlitski, Carlos A. Fuertes, and Subir Sachdev. Entanglement entropy in the  $o(n)$  model. *Phys. Rev. B*, 80:115122, Sep 2009.
- [101] G. Misguich, D. Serban, and V. Pasquier. Quantum dimer model on the kagome lattice: Solvable dimer-liquid and ising gauge theory. *Phys. Rev. Lett.*, 89:137202, Sep 2002.

- [102] R. Moessner and S. L. Sondhi. Resonating valence bond phase in the triangular lattice quantum dimer model. *Phys. Rev. Lett.*, 86:1881–1884, Feb 2001.
- [103] Roger S. K. Mong, Andrew M. Essin, and Joel E. Moore. Antiferromagnetic topological insulators. *Phys. Rev. B*, 81:245209, Jun 2010.
- [104] Gregory Moore and Nicholas Read. Nonabelions in the fractional quantum hall effect. *Nuclear Physics B*, 360(2-3):362 – 396, 1991.
- [105] J. E. Moore and L. Balents. Topological invariants of time-reversal-invariant band structures. *Phys. Rev. B*, 75:121306, Mar 2007.
- [106] Joel E. Moore. The birth of topological insulators. *Nature*, 464(7286):194–198, March 2010.
- [107] Joel E. Moore, Ying Ran, and Xiao-Gang Wen. Topological surface states in three-dimensional magnetic insulators. *Phys. Rev. Lett.*, 101:186805, Oct 2008.
- [108] Olexei I. Motrunich. Variational study of triangular lattice spin-1/2 model with ring exchanges and spin liquid state in  $\kappa$ -(ET)<sub>2</sub>cu<sub>2</sub>(CN)<sub>3</sub>. *Phys. Rev. B*, 72:045105, Jul 2005.
- [109] V. Mourik, K. Zuo, S. M. Frolov, S. R. Plissard, E. P. A. M. Bakkers, and L. P. Kouwenhoven. Signatures of majorana fermions in hybrid superconductor-semiconductor nanowire devices. *Science*, 2012.
- [110] David F. Mross, John McGreevy, Hong Liu, and T. Senthil. Controlled expansion for certain non-fermi-liquid metals. *Phys. Rev. B*, 82:045121, Jul 2010.
- [111] Shuichi Murakami. Phase transition between the quantum spin hall and insulator phases in 3d: emergence of a topological gapless phase. *New Journal of Physics*, 9(9):356, 2007.
- [112] Shuichi Murakami, Naoto Nagaosa, and Shou-Cheng Zhang. Dissipationless quantum spin current at room temperature. *Science*, 301(5638):1348–1351, 2003.
- [113] Shuichi Murakami, Naoto Nagaosa, and Shou-Cheng Zhang. Spin-hall insulator. *Phys. Rev. Lett.*, 93:156804, Oct 2004.
- [114] M. Nakahara. *Geometry, topology, and physics*. Graduate student series in physics. Institute of Physics Publishing, 2003.
- [115] Chetan Nayak, Steven H. Simon, Ady Stern, Michael Freedman, and Sankar Das Sarma. Non-abelian anyons and topological quantum computation. *Rev. Mod. Phys.*, 80:1083–1159, Sep 2008.
- [116] Titus Neupert, Luiz Santos, Claudio Chamon, and Christopher Mudry. Fractional quantum hall states at zero magnetic field. *Phys. Rev. Lett.*, 106:236804, Jun 2011.

- [117] Spivak B. Z. Shklovskii B. I. Nguyen, V. L. Aaronov-bohm oscillations with normal and superconducting flux quanta in hopping conductivity. *JETP Lett.*, 41:42, 1985.
- [118] K.-K. Ni, S. Ospelkaus, M. H. G. de Miranda, A. Pe'er, B. Neyenhuis, J. J. Zirbel, S. Kotochigova, P. S. Julienne, D. S. Jin, and J. Ye. A high phase-space-density gas of polar molecules. *Science*, 322(5899):231–235, 2008.
- [119] M.A. Nielsen and I.L. Chuang. *Quantum Computation and Quantum Information*. Quantum Computation and Quantum Information. Cambridge University Press, 2010.
- [120] Akinori Nishide, Alexey A. Taskin, Yasuo Takeichi, Taichi Okuda, Akito Kakizaki, Toru Hirahara, Kan Nakatsuji, Fumio Komori, Yoichi Ando, and Iwao Matsuda. Direct mapping of the spin-filtered surface bands of a three-dimensional quantum spin hall insulator. *Phys. Rev. B*, 81:041309, Jan 2010.
- [121] Kentaro Nomura, Mikito Koshino, and Shinsei Ryu. Topological delocalization of two-dimensional massless dirac fermions. *Phys. Rev. Lett.*, 99:146806, Oct 2007.
- [122] Yoshihiko Okamoto, Minoru Nohara, Hiroko Aruga-Katori, and Hidenori Takagi. Spin-liquid state in the  $s = 1/2$  hyperkagome antiferromagnet  $\text{na}_4\text{ir}_3\text{o}_8$ . *Phys. Rev. Lett.*, 99:137207, Sep 2007.
- [123] Yuval Oreg, Gil Refael, and Felix von Oppen. Helical liquids and majorana bound states in quantum wires. *Phys. Rev. Lett.*, 105:177002, Oct 2010.
- [124] Masaki Oshikawa and T. Senthil. Fractionalization, topological order, and quasiparticle statistics. *Phys. Rev. Lett.*, 96:060601, Feb 2006.
- [125] S. Ospelkaus, K.-K. Ni, M. H. G. de Miranda, B. Neyenhuis, D. Wang, S. Kotochigova, P. S. Julienne, D. S. Jin, and J. Ye. Ultracold polar molecules near quantum degeneracy. *Faraday Discuss.*, 142:351–359, 2009.
- [126] W. Pan, J.-S. Xia, V. Shvarts, D. E. Adams, H. L. Stormer, D. C. Tsui, L. N. Pfeiffer, K. W. Baldwin, and K. W. West. Exact quantization of the even-denominator fractional quantum hall state at  $\nu = 5/2$  landau level filling factor. *Phys. Rev. Lett.*, 83:3530–3533, Oct 1999.
- [127] Stefanos Papanikolaou, Kumar S. Raman, and Eduardo Fradkin. Topological phases and topological entropy of two-dimensional systems with finite correlation length. *Phys. Rev. B*, 76:224421, Dec 2007.
- [128] Arun Paramekanti and J B Marston.  $\text{Su} ( n )$  quantum spin models: a variational wavefunction study. *Journal of Physics: Condensed Matter*, 19(12):125215, 2007.
- [129] Arun Paramekanti, Mohit Randeria, and Nandini Trivedi. Testing for  $Z_2$  topological order in variational wave functions for spin liquids. *Phys. Rev. B*, 71:094421, Mar 2005.
- [130] Hailin Peng, Keji Lai, Desheng Kong, Stefan Meister, Yulin Chen, Xiao-Liang Qi, Shou-Cheng Zhang, Zhi-Xun Shen, and Yi Cui. Aharonov-bohm interference in topological insulator nanoribbons. *Nat Mater*, 9(3):225–229, March 2010.

- [131] Ingo Peschel. Calculation of reduced density matrices from correlation functions. *Journal of Physics A: Mathematical and General*, 36(14):L205, 2003.
- [132] Ingo Peschel. On the reduced density matrix for a chain of free electrons. *Journal of Statistical Mechanics: Theory and Experiment*, 2004(06):P06004, 2004.
- [133] Ingo Peschel and Viktor Eisler. Reduced density matrices and entanglement entropy in free lattice models. *Journal of Physics A: Mathematical and Theoretical*, 42(50):504003, 2009.
- [134] M. K. Phani, Joel L. Lebowitz, and M. H. Kalos. Monte carlo studies of an fcc ising antiferromagnet with nearest- and next-nearest-neighbor interactions. *Phys. Rev. B*, 21:4027–4037, May 1980.
- [135] Frank Pollmann, Erez Berg, Ari M. Turner, and Masaki Oshikawa. Symmetry protection of topological phases in one-dimensional quantum spin systems. *Phys. Rev. B*, 85:075125, Feb 2012.
- [136] Frank Pollmann, Ari M. Turner, Erez Berg, and Masaki Oshikawa. Entanglement spectrum of a topological phase in one dimension. *Phys. Rev. B*, 81:064439, Feb 2010.
- [137] Xiao-Liang Qi, Taylor L. Hughes, S. Raghu, and Shou-Cheng Zhang. Time-reversal-invariant topological superconductors and superfluids in two and three dimensions. *Phys. Rev. Lett.*, 102:187001, May 2009.
- [138] Xiao-Liang Qi, Taylor L. Hughes, and Shou-Cheng Zhang. Topological field theory of time-reversal invariant insulators. *Phys. Rev. B*, 78:195424, Nov 2008.
- [139] Xiao-Liang Qi and Shou-Cheng Zhang. Spin-charge separation in the quantum spin hall state. *Phys. Rev. Lett.*, 101:086802, Aug 2008.
- [140] Xiao-Liang Qi and Shou-Cheng Zhang. The quantum spin hall effect and topological insulators. *Physics Today*, 63(1):33–38, 2010.
- [141] Xiao-Liang Qi and Shou-Cheng Zhang. Topological insulators and superconductors. *Rev. Mod. Phys.*, 83:1057–1110, Oct 2011.
- [142] S. Raghu, Xiao-Liang Qi, C. Honerkamp, and Shou-Cheng Zhang. Topological mott insulators. *Phys. Rev. Lett.*, 100:156401, Apr 2008.
- [143] Ying Ran, Ashvin Vishwanath, and Dung-Hai Lee. Spin-charge separated solitons in a topological band insulator. *Phys. Rev. Lett.*, 101:086801, Aug 2008.
- [144] Ying Ran, Yi Zhang, and Ashvin Vishwanath. One-dimensional topologically protected modes in topological insulators with lattice dislocations. *Nat Phys*, 5(4):298–303, April 2009.
- [145] N. Read and B. Chakraborty. Statistics of the excitations of the resonating-valence-bond state. *Phys. Rev. B*, 40:7133–7140, Oct 1989.

- [146] N. Read and Subir Sachdev. Large-  $N$  expansion for frustrated quantum antiferromagnets. *Phys. Rev. Lett.*, 66:1773–1776, Apr 1991.
- [147] N. Regnault and B. Andrei Bernevig. Fractional chern insulator. *Phys. Rev. X*, 1:021014, Dec 2011.
- [148] Raffaele Resta and David Vanderbilt. Theory of polarization: A modern approach. 105:31–68, 2007.
- [149] Ivan D. Rodriguez and German Sierra. Entanglement entropy of integer quantum hall states. *Phys. Rev. B*, 80:153303, Oct 2009.
- [150] Daniel S. Rokhsar and Steven A. Kivelson. Superconductivity and the quantum hard-core dimer gas. *Phys. Rev. Lett.*, 61:2376–2379, Nov 1988.
- [151] Rahul Roy. Topological phases and the quantum spin hall effect in three dimensions. *Phys. Rev. B*, 79:195322, May 2009.
- [152] Shinsei Ryu and Tadashi Takayanagi. Aspects of holographic entanglement entropy. *JHEP*, 0608:045, 2006.
- [153] Subir Sachdev. Kagome and triangular-lattice heisenberg antiferromagnets: Ordering from quantum fluctuations and quantum-disordered ground states with unconfined bosonic spinons. *Phys. Rev. B*, 45:12377–12396, Jun 1992.
- [154] Jay D. Sau, Roman M. Lutchyn, Sumanta Tewari, and S. Das Sarma. Generic new platform for topological quantum computation using semiconductor heterostructures. *Phys. Rev. Lett.*, 104:040502, Jan 2010.
- [155] Burkhard Scharfenberger, Ronny Thomale, and Martin Greiter. Non-abelian statistics and a hierarchy of fractional spin liquids in spin- $s$  antiferromagnets. *Phys. Rev. B*, 84:140404, Oct 2011.
- [156] Andreas P. Schnyder, Shinsei Ryu, Akira Furusaki, and Andreas W. W. Ludwig. Classification of topological insulators and superconductors in three spatial dimensions. *Phys. Rev. B*, 78:195125, Nov 2008.
- [157] Darrell F. Schroeter, Eliot Kapit, Ronny Thomale, and Martin Greiter. Spin hamiltonian for which the chiral spin liquid is the exact ground state. *Phys. Rev. Lett.*, 99:097202, Aug 2007.
- [158] T. Senthil and Matthew P. A. Fisher.  $Z_2$  gauge theory of electron fractionalization in strongly correlated systems. *Phys. Rev. B*, 62:7850–7881, Sep 2000.
- [159] T. Senthil and O. Motrunich. Microscopic models for fractionalized phases in strongly correlated systems. *Phys. Rev. B*, 66:205104, Nov 2002.
- [160] T. Senthil, Ashvin Vishwanath, Leon Balents, Subir Sachdev, and Matthew P. A. Fisher. Deconfined quantum critical points. *Science*, 303(5663):1490–1494, 2004.

- [161] Shankar, R. Applications of topology to the study of ordered systems. *J. Phys. France*, 38(11):1405–1412, 1977.
- [162] D. Yu. Sharvin and Yu. V. Sharvin. Magnetic-flux quantization in a cylindrical film of a normal metal. *JETP Lett.*, 34:272, 1981.
- [163] B. Sriram Shastry. Exact solution of an  $S = 1/2$  heisenberg antiferromagnetic chain with long-ranged interactions. *Phys. Rev. Lett.*, 60:639–642, Feb 1988.
- [164] D.N. Sheng, Zheng-Cheng Gu, Kai Sun, and L. Sheng. Fractional quantum hall effect in the absence of landau levels. *Nat Commun*, 2:389, July 2011.
- [165] Y. Shimizu, K. Miyagawa, K. Kanoda, M. Maesato, and G. Saito. Spin liquid state in an organic mott insulator with a triangular lattice. *Phys. Rev. Lett.*, 91:107001, Sep 2003.
- [166] Anjana Sinha and Rajkumar Roychoudhury. Dirac equation in (1+1)-dimensional curved space-time. *International Journal of Theoretical Physics*, 33:1511–1522, 1994. 10.1007/BF00670693.
- [167] A. Douglas Stone and Y. Imry. Periodicity of the aharonov-bohm effect in normal-metal rings. *Phys. Rev. Lett.*, 56:189–192, Jan 1986.
- [168] Kai Sun, Zhengcheng Gu, Hosho Katsura, and S. Das Sarma. Nearly flatbands with nontrivial topology. *Phys. Rev. Lett.*, 106:236803, Jun 2011.
- [169] B. Swingle. Renyi entropy, mutual information, and fluctuation properties of Fermi liquids. *ArXiv e-prints*, July 2010.
- [170] Evelyn Tang, Jia-Wei Mei, and Xiao-Gang Wen. High-temperature fractional quantum hall states. *Phys. Rev. Lett.*, 106:236802, Jun 2011.
- [171] Tiamhock Tay and Olexei I. Motrunich. Variational study of  $J_1$ - $J_2$  heisenberg model on kagome lattice using projected schwinger-boson wave functions. *Phys. Rev. B*, 84:020404, Jul 2011.
- [172] Jeffrey C. Y. Teo, Liang Fu, and C. L. Kane. Surface states and topological invariants in three-dimensional topological insulators: Application to  $\text{bi}_{1-x}\text{sb}_x$ . *Phys. Rev. B*, 78:045426, Jul 2008.
- [173] D. J. Thouless, M. Kohmoto, M. P. Nightingale, and M. den Nijs. Quantized hall conductance in a two-dimensional periodic potential. *Phys. Rev. Lett.*, 49:405–408, Aug 1982.
- [174] Luca F. Tocchio, Alberto Parola, Claudius Gros, and Federico Becca. Spin-liquid and magnetic phases in the anisotropic triangular lattice: The case of  $\kappa$ -(ET)<sub>2</sub>X. *Phys. Rev. B*, 80:064419, Aug 2009.
- [175] D. C. Tsui, H. L. Stormer, and A. C. Gossard. Two-dimensional magnetotransport in the extreme quantum limit. *Phys. Rev. Lett.*, 48:1559–1562, May 1982.

- [176] Ari M. Turner, Yi Zhang, Roger S. K. Mong, and Ashvin Vishwanath. Quantized response and topology of magnetic insulators with inversion symmetry. *Phys. Rev. B*, 85:165120, Apr 2012.
- [177] Ari M. Turner, Yi Zhang, and Ashvin Vishwanath. Entanglement and inversion symmetry in topological insulators. *Phys. Rev. B*, 82:241102, Dec 2010.
- [178] David Vanderbilt and R. D. King-Smith. Electric polarization as a bulk quantity and its relation to surface charge. *Phys. Rev. B*, 48:4442–4455, Aug 1993.
- [179] Erik Verlinde. Fusion rules and modular transformations in 2d conformal field theory. *Nuclear Physics B*, 300(0):360 – 376, 1988.
- [180] G.E. Volovik. *The Universe in a Helium Droplet*. International Series of Monographs on Physics. Oxford University Press, 2009.
- [181] Xiangang Wan, Ari M. Turner, Ashvin Vishwanath, and Sergey Y. Savrasov. Topological semimetal and fermi-arc surface states in the electronic structure of pyrochlore iridates. *Phys. Rev. B*, 83:205101, May 2011.
- [182] L. Wang, Z.-C. Gu, F. Verstraete, and X.-G. Wen. Spin-liquid phase in spin-1/2 square J\_1-J\_2 Heisenberg model: A tensor product state approach. *ArXiv e-prints*, December 2011.
- [183] Yi-Fei Wang, Zheng-Cheng Gu, Chang-De Gong, and D. N. Sheng. Fractional quantum hall effect of hard-core bosons in topological flat bands. *Phys. Rev. Lett.*, 107:146803, Sep 2011.
- [184] Yi-Fei Wang, Hong Yao, Zheng-Cheng Gu, Chang-De Gong, and D. N. Sheng. Non-abelian quantum hall effect in topological flat bands. *Phys. Rev. Lett.*, 108:126805, Mar 2012.
- [185] Zhong Wang, Xiao-Liang Qi, and Shou-Cheng Zhang. Equivalent topological invariants of topological insulators. *New Journal of Physics*, 12(6):065007, 2010.
- [186] R. A. Webb, S. Washburn, C. P. Umbach, and R. B. Laibowitz. Observation of  $\frac{h}{e}$  aharonov-bohm oscillations in normal-metal rings. *Phys. Rev. Lett.*, 54:2696–2699, Jun 1985.
- [187] X. G. Wen. Gapless boundary excitations in the quantum hall states and in the chiral spin states. *Phys. Rev. B*, 43:11025–11036, May 1991.
- [188] X. G. Wen. Mean-field theory of spin-liquid states with finite energy gap and topological orders. *Phys. Rev. B*, 44:2664–2672, Aug 1991.
- [189] X. G. Wen, Frank Wilczek, and A. Zee. Chiral spin states and superconductivity. *Phys. Rev. B*, 39:11413–11423, Jun 1989.

- [190] X.G. Wen. *Quantum Field Theory Of Many-body Systems: From The Origin Of Sound To An Origin Of Light And Electrons*. Oxford Graduate Texts. Oxford University Press, 2004.
- [191] Xiao-Gang Wen. Topological orders in rigid states. *Int. J. Mod. Phys. B*, 4:239, Feb 1990.
- [192] Xiao-Gang Wen. Quantum orders and symmetric spin liquids. *Phys. Rev. B*, 65:165113, Apr 2002.
- [193] R. Willett, J. P. Eisenstein, H. L. Störmer, D. C. Tsui, A. C. Gossard, and J. H. English. Observation of an even-denominator quantum number in the fractional quantum hall effect. *Phys. Rev. Lett.*, 59:1776–1779, Oct 1987.
- [194] Michael M. Wolf. Violation of the entropic area law for fermions. *Phys. Rev. Lett.*, 96:010404, Jan 2006.
- [195] Congjun Wu, B. Andrei Bernevig, and Shou-Cheng Zhang. Helical liquid and the edge of quantum spin hall systems. *Phys. Rev. Lett.*, 96:106401, Mar 2006.
- [196] J. S. Xia, W. Pan, C. L. Vicente, E. D. Adams, N. S. Sullivan, H. L. Stormer, D. C. Tsui, L. N. Pfeiffer, K. W. Baldwin, and K. W. West. Electron correlation in the second landau level: A competition between many nearly degenerate quantum phases. *Phys. Rev. Lett.*, 93:176809, Oct 2004.
- [197] Y. Xia, D. Qian, D. Hsieh, L. Wray, A. Pal, H. Lin, A. Bansil, D. Grauer, Y. S. Hor, R. J. Cava, and M. Z. Hasan. Observation of a large-gap topological-insulator class with a single dirac cone on the surface. *Nat Phys*, 5(6):398–402, June 2009.
- [198] Cenke Xu and J. E. Moore. Stability of the quantum spin hall effect: Effects of interactions, disorder, and  $F_2$  topology. *Phys. Rev. B*, 73:045322, Jan 2006.
- [199] Minoru Yamashita, Norihito Nakata, Yoshinori Senshu, Masaki Nagata, Hiroshi M. Yamamoto, Reizo Kato, Takasada Shibauchi, and Yuji Matsuda. Highly mobile gapless excitations in a two-dimensional candidate quantum spin liquid. *Science*, 328(5983):1246–1248, 2010.
- [200] Simeng Yan, David A. Huse, and Steven R. White. Spin-liquid ground state of the  $s = 1/2$  kagome heisenberg antiferromagnet. *Science*, 332(6034):1173–1176, 2011.
- [201] Hong Yao and Xiao-Liang Qi. Entanglement entropy and entanglement spectrum of the kitaev model. *Phys. Rev. Lett.*, 105:080501, Aug 2010.
- [202] Haijun Zhang, Chao-Xing Liu, Xiao-Liang Qi, Xi Dai, Zhong Fang, and Shou-Cheng Zhang. Topological insulators in bi2se3, bi2te3 and sb2te3 with a single dirac cone on the surface. *Nat Phys*, 5(6):438–442, June 2009.
- [203] Y. Zhang, T. Grover, A. Turner, M. Oshikawa, and A. Vishwanath. Quasi-particle Statistics and Braiding from Ground State Entanglement. *ArXiv e-prints*, November 2011.

- [204] Yi Zhang, Tarun Grover, and Ashvin Vishwanath. Entanglement entropy of critical spin liquids. *Phys. Rev. Lett.*, 107:067202, Aug 2011.
- [205] Yi Zhang, Tarun Grover, and Ashvin Vishwanath. Topological entanglement entropy of  $z_2$  spin liquids and lattice Laughlin states. *Phys. Rev. B*, 84:075128, Aug 2011.
- [206] Yi Zhang, Ying Ran, and Ashvin Vishwanath. Topological insulators in three dimensions from spontaneous symmetry breaking. *Phys. Rev. B*, 79:245331, Jun 2009.
- [207] Yi Zhang and Ashvin Vishwanath. Anomalous Aharonov-Bohm conductance oscillations from topological insulator surface states. *Phys. Rev. Lett.*, 105:206601, Nov 2010.
- [208] O. S. Zozulya, M. Haque, K. Schoutens, and E. H. Rezayi. Bipartite entanglement entropy in fractional quantum Hall states. *Phys. Rev. B*, 76:125310, Sep 2007.

# Appendix A

## Effective Hamiltonian on a Curved Topological Insulator Surface

The effective Hamiltonian for a TI surface has the form of a Dirac equation:  $H = \vec{p} \cdot \vec{\sigma}$  when the spin and momentum are parallel and  $H = \mathbf{e}_3 \cdot (\vec{p} \times \vec{\sigma})$  when they are perpendicular, where  $\mathbf{e}_3$  is the normal direction of the surface. Both the momentum and spin are confined to the surface. More generally, when the angle between spin and momentum is  $\theta$  the effective Hamiltonian is:

$$H = (\mathbf{e}_1 \cdot \vec{\sigma} \cos \theta + \mathbf{e}_2 \cdot \vec{\sigma} \sin \theta) (\mathbf{e}_1 \cdot \vec{p}) + (\mathbf{e}_2 \cdot \vec{\sigma} \cos \theta - \mathbf{e}_1 \cdot \vec{\sigma} \sin \theta) (\mathbf{e}_2 \cdot \vec{p}) \quad (\text{A.1})$$

where  $\mathbf{e}_1$  and  $\mathbf{e}_2$  are orthogonal directions in plane.

One would tends to apply the same Hamiltonian to a curved surface. However, here we claim the effective Hamiltonian on an arbitrary shaped TI surface is:

$$H = (\mathbf{e}_1 \cdot \vec{\sigma} \cos \theta + \mathbf{e}_2 \cdot \vec{\sigma} \sin \theta) (\mathbf{e}_1 \cdot \vec{p}) + (\mathbf{e}_2 \cdot \vec{\sigma} \cos \theta - \mathbf{e}_1 \cdot \vec{\sigma} \sin \theta) (\mathbf{e}_2 \cdot \vec{p}) + \frac{\hbar}{2} \left( \frac{1}{R_1} + \frac{1}{R_2} \right) \sin \theta + \frac{i\hbar}{2} (\vec{\sigma} \cdot \mathbf{e}_3) \left( \frac{1}{R_1} + \frac{1}{R_2} \right) \cos \theta \quad (\text{A.2})$$

where  $\mathbf{e}_1$  and  $\mathbf{e}_2$  are tangent vectors of the surface with radius of curvature  $R_1$  and  $R_2$ , respectively, and  $\mathbf{e}_3$  is the normal vectors.  $\theta$  is the constant angle between spin and momentum in the corresponding flat surface effective theory. Note when the surface is flat, the last two terms vanish and the Hamiltonian goes back to the one describing the flat surface mode.

An intuitive derivation of the curved TI surface effective Hamiltonian Eqn. A.2 is to ensure hermiticity and anticommutation relation  $\{H, \vec{\sigma} \cdot \mathbf{e}_3\} = 0$  since the spin is in the surface plane. With the relations:

$$\begin{aligned} (\mathbf{e}_i \cdot \vec{p}) \mathbf{e}_j &= i\hbar \delta_{ij} \mathbf{e}_3 / R_i \\ (\mathbf{e}_i \cdot \vec{p}) \mathbf{e}_3 &= -i\hbar \mathbf{e}_i / R_i \\ (\vec{\sigma} \cdot \hat{A}) (\vec{\sigma} \cdot \hat{B}) &= \hat{A} \cdot \hat{B} + i\hat{\sigma} \cdot (\hat{A} \times \hat{B}) \end{aligned} \quad (\text{A.3})$$

for  $i = 1, 2$ , the terms arising from the space curvature are canceled by the inclusion of the connection form.

For a general and systematical formalism of defining curved space-time Dirac theories, we consider inclusion of the connection form for a curved spacetime[28, 114, 166], and then specializing to our case of interest where only the space is curved.

Consider flat (2+1)-dimensional spacetime. We work with Euclidean time, so  $x^0 = \tau = it$ , and  $\hbar = c = 1$ . Then, the massless Dirac equation reads:  $(\sum_{a=0}^2 \gamma_a \partial_a) \Psi = 0$ . The matrices satisfy the anticommutation relations:  $\{\gamma_a, \gamma_b\} = 2\delta_{ab}$ , where the right hand side is the Kronecker delta function, due to the Euclidean spacetime. The  $\gamma$  matrices can just be taken as the Pauli matrices, and we can write this as a three vector  $\gamma = (\gamma_0, \gamma_1, \gamma_2)$ .

Now consider a curved spacetime, defined by coordinates  $x^\mu$  metric  $g_{\mu\nu}$ , where the indices take values  $\in \{0, 1, 2\}$ . It is always possible to define a triad of vectors  $\epsilon_\mu$ , with three components each, such that  $g_{\mu\nu} = \epsilon_\mu \cdot \epsilon_\nu$ . One can define also a dual frame  $\epsilon^\mu$  such that  $\epsilon^\mu \cdot \epsilon_\nu = \delta_\nu^\mu$ , the Kronecker delta function. (This is like the relation between bases in real space and reciprocal space, for a crystal). Now, the generalization of the Gamma matrices can be defined as:  $\gamma^\mu = \epsilon^\mu \cdot \gamma$ , or in component form  $\gamma^\mu = \sum_{a=0}^2 \epsilon_a^\mu \gamma_a$ . The Dirac equation in curved space takes the form:

$$\gamma^\mu (\partial_\mu + \Gamma_\mu) \Psi = 0 \quad (\text{A.4})$$

where  $\partial_\mu = \partial/\partial x^\mu$ , and summation over repeated indices is assumed from here on. The  $\Gamma_\mu$  matrices are the spin-connections, the main objects of interest here. They are given most compactly by the formula:

$$\Gamma_\mu = \frac{1}{4} \gamma_\nu \nabla_\mu \gamma^\nu \quad (\text{A.5})$$

$$\nabla_\mu \gamma^\nu = \partial_\mu \gamma^\nu + \Gamma_{\mu\lambda}^\nu \gamma^\lambda \quad (\text{A.6})$$

$$\Gamma_{\mu\lambda}^\nu = \frac{1}{2} g^{\nu\alpha} (\partial_\mu g_{\alpha\lambda} + \partial_\lambda g_{\mu\alpha} - \partial_\alpha g_{\mu\lambda}) \quad (\text{A.7})$$

where the Eqn. A.5 relates the spin connection to the covariant derivative  $\nabla_\mu$ . This is defined via the usual Christoffel symbols,  $\Gamma_{\mu\lambda}^\nu$  (Eqn. A.7), which in turn are defined from the metric via the standard formula (Eqn. A.7). The spin connection can be shown to satisfy the equation:

$$[\Gamma_\mu, \gamma^\nu] = \partial_\mu \gamma^\nu + \Gamma_{\mu\lambda}^\nu \gamma^\lambda \quad (\text{A.8})$$

which indicates that it is responsible for parallel transport of spinors.

We now specialize to the case when only space is curved. Then, we expect the metric tensor can be brought into the form  $g_{00} = 1$ ;  $g_{0i} = 0$ , where the Latin indices  $i, j, k \dots$  will take on values  $\in \{1, 2\}$ . This can be arranged if  $\epsilon^0$  is unit modulus and orthogonal to the other two tangent vectors. Note also, the only non-vanishing Christoffel symbols are ones with all Latin indices  $\Gamma_{jk}^i$ . Similarly the temporal spin connection vanishes  $\Gamma_0 = 0$ . To read off the Hamiltonian, we write the Dirac equation as  $\partial\Psi/\partial\tau = -H\Psi$ , where  $H = \gamma_0 [\gamma_i (\partial_i + \Gamma_i)]$ . We therefore identify  $\beta = \gamma_0$ , and using  $\beta^2 = 1$ ,  $\gamma^i = -i\beta\alpha^i$ . Substituting this into Eqn. A.5, we obtain:

$$\Gamma_i = -\frac{1}{4} (\beta \partial_i \beta + \alpha_k \partial_i \alpha^k + \Gamma_{ik}^j \alpha_j \alpha^k) \quad (\text{A.9})$$

Actually, an even simpler form for the spin connection is:

$$\Gamma_i = -\frac{1}{2}\beta\partial_i\beta \quad (\text{A.10})$$

To derive this we first show the spin connection  $\Gamma_i$  is in the tangent plane, i.e. it can be expressed in terms of  $\alpha_i$ . We write equations for  $\alpha_i$ :

$$[\Gamma_i, \alpha^j] = \partial_i\alpha^j + \Gamma_{ik}^j\alpha^k \quad (\text{A.11})$$

which can be derived from Eqn. A.8 and the definition  $\alpha^j = i\beta\gamma^j$ . We have mentioned before that  $[\partial_i\mathbf{e}^j]_{\parallel} = -\Gamma_{ik}^j\mathbf{e}^k$ , therefore we can check that the right hand side corresponding to the vector  $\partial_i\mathbf{e}^j + \Gamma_{ik}^j\mathbf{e}^k$  has no components in the plane and corresponds to the surface normal. Hence  $\Gamma_i$  only has components in the tangent plane.

Then we consider the zeroth component  $\gamma^0 = \beta$  use Eqn. A.8:

$$[\Gamma_i, \beta] = \partial_i\beta \quad (\text{A.12})$$

since all the relevant Christoffel symbols vanish. The commutator can be written as  $2\beta\Gamma_i = -\partial_i\beta$  which gives us the desired result Eqn. A.10.

To see this algebraically, we consider the inner product with a general in plane vector  $\mathbf{e}_l$ , which gives:

$$\mathbf{e}_l \cdot \partial_i\mathbf{e}^j + \Gamma_{il}^j \quad (\text{A.13})$$

where we used  $\mathbf{e}^k \cdot \mathbf{e}_l = \delta_l^k$ . This can be shown to be zero. The critical input in this derivation is that  $\partial_i\mathbf{e}_j = \partial_j\mathbf{e}_i$ , which is only true because these are tangent vectors, derived by differentiating the three-dimensional coordinates of the surface  $\mathbf{e}_i = \partial\mathbf{r}/\partial x^i$ . See Ref. [87] for an alternate elegant formalism applied to quantized Hall states on a TI surface.

We note identical results are obtained if we choose the basis vectors as a fixed linear combination of tangent vectors: i.e. if  $\mathbf{e}'_1 = \cos\theta\mathbf{e}_1 + \sin\theta\mathbf{e}_2$  and  $\mathbf{e}'_2 = -\sin\theta\mathbf{e}_1 + \cos\theta\mathbf{e}_2$ . In particular, a natural choice is  $\theta = \pi/2$ , which gives a Dirac Hamiltonian in flat space of the form  $H = -iv_F\hbar(\sigma_y\partial_x - \sigma_x\partial_y)$ .

We now discuss a general argument which fixes the half integer offset of momentum quantization, and goes beyond the particular Dirac model chosen. Note, by time reversal invariance fixes this offset to be  $\pi$  or zero. In the latter case, a gapless one-dimensional mode is present that is protected by time reversal symmetry. Now consider a slightly different geometry, an annular cylinder with radii  $R_1, R_2$ . Take  $R_2 \rightarrow \infty$  so we now have a hollow inner cylinder. If we now shrink the inner radius  $R_1 \rightarrow 0$ , one just obtains the bulk topological insulator. Hence, we must have that the modes on the inner cylinder were gapped, which implies  $\pi$  phase shift. Note, although the cylinder is 'flat' in the sense it has vanishing Gaussian curvature, a nonzero spin connection leads to the Berry's phase of  $\pi$ . It is in this sense that we refer to this phase as being surface curvature induced - strictly it refers to a topological property of the surface (i.e. the possibility of looping around the cylinder while avoiding the inserted magnetic field).

# Appendix B

## Inversion Symmetry Models and Related Properties

### B.1 Inversion Symmetric Tight Binding Models

Tight-binding models are useful for studying inversion symmetric Hamiltonians. In general, the Hamiltonian is:

$$H = - \sum_{i,j,\mathbf{R},\Delta} t_{ij}(\Delta) c_i^\dagger(\mathbf{R} + \Delta) c_j(\mathbf{R}) \quad (\text{B.1})$$

where  $c_i$  is the creation operator for the  $i^{\text{th}}$  orbital. If there are  $N_{\text{even}}$  even orbitals  $|s_i\rangle$  and  $N_{\text{odd}}$  odd orbitals  $|p_i\rangle$ , then for a Bloch wave function  $\psi_{a\mathbf{k}}$  of the  $a^{\text{th}}$  band, inversion maps  $\mathbf{k} \rightarrow -\mathbf{k}$  and  $\phi_i \rightarrow I_{ij}\phi_j$ , where  $I_{ij}$  is a diagonal matrix of  $N_{\text{even}} + 1$  and  $N_{\text{odd}} - 1$ .

There is a simple criterion to determine the parities of the states at the TRIMs: if a state is parity odd, then all its  $s$ -wave components vanish; if it is parity even, all  $p$ -wave components vanish. Generically, it is enough to check a single  $s$ -wave component:

$$\begin{aligned} \eta_a(\kappa) &= +1 \text{ if } \langle s_1 | \psi_{a\kappa} \rangle \neq 0 \\ \eta_a(\kappa) &= -1 \text{ if } \langle s_1 | \psi_{a\kappa} \rangle = 0 \end{aligned} \quad (\text{B.2})$$

If a component is exactly zero, it is reasonable to assume that it is forbidden by the inversion symmetry.

In momentum space Eqn. B.1 can be written as  $\sum_{ij} c_i^\dagger(\mathbf{k}) c_j(\mathbf{k}) H_{ij}(\mathbf{k})$ . The Hamiltonian used to illustrate the entanglement-rule in Figure 5.2 can be built from two subsystems  $H_1$  and  $H_2$ , whose occupied states' parities are given by the upper and lower signs in Figure 5.2a, respectively. Both Hamiltonians can be gapped because their sets of signs satisfy the constraint  $\prod_\kappa \eta_\kappa = 1$  on their own.

Each Hamiltonians can be constructed with one even orbital  $|s_r\rangle$  and one odd orbital  $|p_r\rangle$ , so the inversion operator  $I = \sigma_Z$ . A inversion symmetric must commute with  $I$ , so

its diagonal matrix elements are inversion even and the off-diagonal matrix elements are inversion odd.

The Hamiltonians can be combined together by a small mixing between the two subsystems. The example Hamiltonian has the form:

$$H(\mathbf{k}) = \begin{pmatrix} H_1(\mathbf{k}) & t\mathbf{1} \\ t\mathbf{1} & H_2(\mathbf{k}) \end{pmatrix}. \quad (\text{B.3})$$

where:

$$\begin{aligned} H_1 &= A_{\mathbf{k}}\sigma_z + B_{\mathbf{k}}\sigma_x + C_{\mathbf{k}}\sigma_y \\ H_2 &= D_{\mathbf{k}}\sigma_z + E_{\mathbf{k}}\sigma_x + F_{\mathbf{k}}\sigma_y \end{aligned} \quad (\text{B.4})$$

and:

$$\begin{aligned} A_{\mathbf{k}} &= (1 - \cos(k_x))\cos(k_y) + (1 + \cos(k_x))\cos(k_y - k_z) \\ B_{\mathbf{k}} &= (1 - \cos(k_x))\sin(k_y) + (1 + \cos(k_x))\sin(k_y - k_z) \\ C_{\mathbf{k}} &= \sin(k_x), E_{\mathbf{k}} = -\sin(k_x), F_{\mathbf{k}} = \sin(k_z) \\ D_{\mathbf{k}} &= \cos(k_x) + \cos(k_z) - 1 \end{aligned} \quad (\text{B.5})$$

The parities of the occupied states at TRIM  $\kappa$  of  $H_1$  and  $H_2$  are equal to the signs shown in Figure 5.2. The corresponding inversion center is  $\frac{1}{2}\hat{x}$ , which is a necessary choice because the entanglement spectrum is obtained by separating the system between two planes of atoms.

## B.2 “Frozen” Crystals

In this Appendix we determine the subset of the  $n_o(\kappa)$  vectors space corresponding to the “frozen” crystals. Define  $\mathbf{f}_d$  as the primitive vectors for systems with a single electron in each unit cell displaced by  $\mathbf{d}$  from the Bravais lattice. For each of the eight polarizations  $\mathbf{d}$ , the numbers of odd parity states at TRIMs are  $\mathbf{f}_d(\kappa) \equiv 1 + \frac{\kappa}{\pi} \cdot 2\mathbf{d}$  (modulo 2) for odd orbitals. For nonzero TRIM  $\mathbf{f}_d$  contains four zeros and four ones, and  $\mathbf{f}_0(\kappa) = 1$ .

The goal is to determine which vectors are integer linear combinations of the  $\mathbf{f}_d$ ’s. It is easier to solve in a  $\mathbb{Z}^8$  coordinate system. Once a basis  $\mathbf{v}_1 \dots \mathbf{v}_8$  for  $\mathbb{Z}^8$  is found, if  $n_1\mathbf{v}_1, n_2\mathbf{v}_2, \dots, n_8\mathbf{v}_8$  is a basis for the frozen vectors, the criteria that  $\mathbf{n}_o = a_1\mathbf{v}_1 + \dots + a_8\mathbf{v}_8$  corresponds a “frozen” crystal is that  $a_i$  is a multiple of  $n_i$ .

To find the basis, take an  $8 \times 8$  matrix whose columns are the  $\mathbf{f}_d$ ’s. Perform column operations including adding or subtracting columns or changing the sign of a column until the vectors become divisible by integers  $n_1, n_2, \dots$ . These operations do not change the lattice spanned by the  $\mathbf{f}_d$ ’s. The algorithm is described by the classification theorem for finitely generated Abelian groups.

This leads to the following basis:  $\mathbf{m}_0$ ,  $\mathbf{m}_x$ ,  $2\mathbf{m}_{xy}$ ,  $4\mathbf{m}_{xyz}$  and their permutations. Here  $\mathbf{m}_0$  is the vector with ones at all corners of the cube,  $\mathbf{m}_x$  is the vector with ones on the

$\kappa_x = \pi$  plane and zeros elsewhere,  $\mathbf{m}_{xy}$  is the vector with ones on the  $\kappa_x = \kappa_y = \pi$  edge, and  $\mathbf{m}_{xyz}$  is the vector with a one at the  $\kappa_x = \kappa_y = \kappa_z = \pi$  vertex .

In a similar demonstration,  $\mathbf{m}_0$ ,  $\mathbf{m}_i$ ,  $\mathbf{m}_{ij}$  and  $\mathbf{m}_{xyz}$  span all combinations of 8 integers. Therefore any vector  $\mathbf{n}_o$  can be decomposed as:

$$\mathbf{n}_o = a_0 \mathbf{m}_0 + \sum_i a_i \mathbf{m}_i + \sum_{i < j} a_{ij} \mathbf{m}_{ij} + a_{xyz} \mathbf{m}_{xyz} \quad (\text{B.6})$$

where  $a_{ij}$  is an even integer and  $a_{xyz}$  is a multiple of four. Combining the  $a_0$  and  $a_i$ , the even part of  $a_{ij}$  and the 4 multiple contained in  $a_{xyz}$  forms a vector in the frozen lattice. The displacement between this site and  $\mathbf{n}_o$  has the form of Eqn. 5.13. The concise statement of this result is that the quotient of  $\mathbb{Z}^8$  by the span of the  $\mathbf{f}$ 's is  $\mathbb{Z}_2^3 \times \mathbb{Z}_4$ .

### B.3 Monopoles and Weyl Points

Consider a Hamiltonian where the  $a^{\text{th}}$  and  $a + 1^{\text{st}}$  bands are nearly degenerate at  $\mathbf{k}_0$ , then all states except the two nearly degenerate states are unimportant, the spectrum can be described by a  $2 \times 2$  matrix:

$$\mathcal{H}(\mathbf{k}) = \begin{pmatrix} E_0 + A(\mathbf{k}) & B(\mathbf{k}) \\ B^*(\mathbf{k}) & E_0 + C(\mathbf{k}) \end{pmatrix}. \quad (\text{B.7})$$

where the eigenvalues are degenerate if  $A(\mathbf{k}) = C(\mathbf{k})$  and  $B(\mathbf{k}) = 0$ . Since  $B$  is complex, this gives three equations and three variables, generically, so point solutions may be found in three-dimensional space. The degeneracy point at  $\mathbf{k}_W$  is call the Weyl point.

At the Weyl point there are magnetic monopoles in the Berry magnetic fields  $\mathbf{B}_a$  and  $\mathbf{B}_{a+1}$  of the two bands[180]. The Weyl point has a handedness  $\delta = \pm 1$ , which determines the charge of the monopoles. Bands  $a$  and  $a + 1$  have opposite monopole charge:

$$\begin{aligned} Q_a &= 2\pi\delta \\ Q_{a+1} &= -2\pi\delta. \end{aligned} \quad (\text{B.8})$$

This monopole and anti-monopole are glued together at the  $\mathbf{k}_W$  but they do not annihilate because they are monopoles in different “magnetic” fields.

To understand why the monopoles exist, write the Hamiltonian in terms of Pauli matrices and expand the coefficients to linear order in  $\mathbf{k}$ :

$$H(\mathbf{k}) \approx E_0 + \mathbf{v}_0 \cdot \mathbf{k} + \sum_{i=1}^3 (\mathbf{v}_i \cdot \mathbf{k} \sigma_i) \quad (\text{B.9})$$

and the handedness is defined by:

$$\delta = \text{sign}[\mathbf{v}_1 \cdot (\mathbf{v}_2 \times \mathbf{v}_3)]. \quad (\text{B.10})$$

Define the oblique coordinate system  $K_i = (\mathbf{k} - \mathbf{k}_W) \cdot \mathbf{v}_i$ ,  $K_3 = K \cos \theta$ ,  $K_1 = K \sin \theta \cos \phi$ ,  $K_2 = K \sin \theta \sin \phi$ . The eigenvectors of the Hamiltonian are  $\psi_{a+1} = (\cos \frac{1}{2}\theta e^{-i\phi}, \sin \frac{1}{2}\theta)$  and  $\psi_a = (\sin \frac{1}{2}\theta e^{-i\phi}, -\cos \frac{1}{2}\theta)$ .

The Berry magnetic field in band  $a$  is defined as  $\mathbf{B}_a = \text{curl} \mathbf{A}_a$  where  $\mathbf{A}_a$  is defined in Eqn. 5.16. The Berry connections for the eigenstates are  $A_{a+1}(\mathbf{K}) = \frac{1}{2} \cot \frac{\theta}{2} \hat{\phi}$  and  $A_a(\mathbf{K}) = \frac{1}{2} \tan \frac{\theta}{2} \hat{\phi}$ . These fields are the vector potentials for Dirac monopoles[68]. These monopoles have fluxes of  $\mathbf{B}_{a+1} = -2\pi$  and  $\mathbf{B}_a = 2\pi$  along the  $K_3$  axis respectively. Note that if  $\delta = -1$  the oblique coordinate system is left-handed, then because magnetic flux is a pseudoscalar, the signs of the monopoles will change. This directly leads to Eqn. B.8.

Next we show that the curves defined by  $s_a(\mathbf{k}) = 0$  and  $s_{a+1}(\mathbf{k}) = 0$  merge with one another at the Weyl point. The function  $s_a(\mathbf{k})$  is defined as  $\langle s | \psi_{a\mathbf{k}} \rangle = \langle s | \uparrow \rangle \langle \uparrow | \psi_{a\mathbf{k}} \rangle + \langle s | \downarrow \rangle \langle \downarrow | \psi_{a\mathbf{k}} \rangle$ .  $|\uparrow\rangle = (1, 0)$  and  $|\downarrow\rangle = (0, 1)$  are the only two important states in the effective theory near  $\mathbf{k}_W$ . Parameterize these overlaps via:

$$\begin{pmatrix} \langle \uparrow | s \rangle \\ \langle \downarrow | s \rangle \end{pmatrix} = A \begin{pmatrix} \cos \frac{\alpha}{2} e^{-i\beta} \\ \sin \frac{\alpha}{2} \end{pmatrix}. \quad (\text{B.11})$$

then  $s^a(\mathbf{k}) = 0$  if  $\theta = \alpha$  and  $\phi = \beta$  and  $s^{a+1}(\mathbf{k}) = 0$  if  $\theta = \pi - \alpha$  and  $\phi = \pi + \beta$ . The two curves meet at the Dirac point from opposite directions.

Now we prove that when an even and odd parity state at a TRIM pass through the Fermi energy in opposite directions, a pair of monopoles are created or annihilated. In the effective Hamiltonian Eqn. B.7 for this problem, the top and bottom components represent the even and odd parity states respectively. Then inversion  $I_0 = \sigma_z$ , and since  $I_0 H(\mathbf{k}) I_0^{-1} = H(-\mathbf{k})$ , the diagonal entries have to be even and the off-diagonal entries have to be odd functions of  $\mathbf{k}$ .

We study how the dispersions change when the gap  $\Delta = A(0) - C(0)$  changes sign. Because the trace of  $H(\mathbf{k})$  only gives a constant shift to the dispersion, it is safe to assume  $A(\mathbf{k}) = \frac{\Delta}{2} + f(\mathbf{k}) = -C(\mathbf{k})$  where  $f$  is a function quadratic in  $\mathbf{k}$  at lowest order.  $B(\mathbf{k})$  is a linear function of  $\mathbf{k}$ , so we may choose a coordinate system  $B(\mathbf{k}) = K_1 - iK_2$ . The dispersion is:

$$E = \pm \sqrt{\left(\frac{\Delta}{2} + f(\mathbf{k})\right)^2 + K_1^2 + K_2^2} \quad (\text{B.12})$$

where the Weyl points are  $K_{W1} = K_{W2} = 0$  and  $\Delta = -2f(K_{W3}, 0, 0) = -2\alpha K_{W3}^2$ ,  $\alpha > 0$ . Thus, there are two band-touching points when  $\Delta$  is negative and no crossings when  $\Delta$  is positive. So if  $\Delta$  changes from positive to negative, two monopoles appear and vice versa. The distance from the origin to the crossings is proportional to the square root of  $\Delta$ . Expand the Hamiltonian to linear order around one of the  $\mathbf{k}_W$ 's to find the form of the Hamiltonian for the Weyl modes, it gives  $\alpha K_{W3}(K_3 - K_{W3})\sigma_z + K_1\sigma_x + K_2\sigma_y$ . The two cone points have opposite handedness since  $K_{W3}$  has opposite signs, which is consistent with the fact that the monopole charge has to be conserved.

## B.4 Inversion Symmetry in Entanglement Spectra

First, we will show how to construct the paired functions  $F_{i\mathbf{k}_\perp}(x)$  in Eqn. 6.21. Let us split the wave function into two parts  $x > 0$  and  $x < 0$ , Then the correlation function has four parts:

$$\hat{C} = \begin{pmatrix} \hat{C}_R & \hat{C}_{LR} \\ \hat{C}_{LR}^\dagger & \hat{C}_L \end{pmatrix} \quad (\text{B.13})$$

Since  $\hat{C}$  only has eigenvalues 1 and 0,  $\hat{C}^2 = \hat{C}$ , which gives matrix equation  $\hat{C}_{LR}(\mathbf{1} - \hat{C}_R) = \hat{C}_L \hat{C}_{LR}$ . Given an eigenfunction  $f_i^R$  of  $\hat{C}_R$  with eigenvalue  $p_i$  one can obtain an eigenvector of  $\hat{C}_L$  with eigenvalue  $1 - p_i$  via a unitary transformation  $\hat{M} = \frac{1}{\sqrt{\hat{C}_L - \hat{C}_L^2}} \hat{C}_{LR}$ :

$$f_i^L(x) = [\hat{M} f_i^R](x) = \frac{1}{\sqrt{p_i(1-p_i)}} \sum_{x'>0} \hat{C}_{LR}(x, x') \phi_i^R(x'). \quad (\text{B.14})$$

the pre-factor is a normalization. Then the entanglement modes for the left and right sides of the systems  $f_i^L$  and  $f_i^R$  can be paired up to give the occupied states' wave functions of the entire system  $F$  in Eqn. 5.25 and 6.21, the eigenstates of  $\hat{C}$  with eigenvalue 1.

The expression for the Schmidt weights has an intuitive relationship to the  $F$ 's. Since each  $F$  has unit occupancy, a term in the Schmidt decomposition is obtained when a decision is made about the probability of electrons appearing on the left or right half, see Figure 6.8b. The Schmidt coefficients  $\lambda_\alpha^2$  are thus given by a Bernoulli distribution  $\prod_{j \in A_R} p_j \prod_{j \in A_L} (1-p_j)$ , equivalent to Eqn. 6.13.

The transformation  $\mathcal{I}_S$ :  $f_{i,\kappa_\perp}^R \rightarrow f_{i,-\kappa_\perp}^R$  can be expressed in terms of the correlation function  $\hat{C}$ . Since  $\hat{M}$  maps the right half to the left half of the system, combined with inversion symmetry  $\hat{I}$  it gives the transformation  $\mathcal{I}_S = \hat{I} \hat{M}$  in Section 5.5 and 6.5, which transforms the entanglement spectrum of the right half back into itself. It is unitary, and changes the sign of  $\mathbf{k}_\perp$  as well as  $p_i - \frac{1}{2}$ , since it anti-commutes with  $\hat{C}_R - \frac{1}{2}$ .

The transformation  $\mathcal{I}_S$  has the same properties as a two-dimensional ‘‘CRT’’ symmetry for the space parallel to the cut:  $C$  is the particle-hole symmetry,  $R$  is the  $180^\circ$  rotation and  $T$  is the time-reversal symmetry, although the system generally does not have those symmetries on their own;  $C$  changes the sign of the ‘‘energy’’ and all three operators change the sign of the momentum, and the product is also unitary.

Next we prove that the number of Fermi arcs through a TRIM equals to  $\Delta N_e(\kappa_\perp)$  modulo 2. To show this, we use the  $k \cdot p$  effective Hamiltonian for zero entanglement ‘‘energy’’ states at  $\kappa_\perp$  and determine the dispersion vary away from  $\kappa_\perp$ . Generically, all the states at the TRIM have the same  $\mathcal{I}_e$  parity, then particle-hole symmetry implies that the effective Hamiltonian is odd in  $\mathbf{k}_\perp$  in leading order, hence  $H(\mathbf{k}_\perp) = |k|(A_x \cos \theta + A_y \sin \theta)$  in polar coordinates. The dispersion has a cone-shaped structure  $\epsilon_i(k, \theta) = |k|f_i(\theta)$  where  $f_i(\theta)$  are the eigenvalues of the polar Hamiltonian  $A_x \cos \theta + A_y \sin \theta$ , the zeros of which denote the Fermi arcs through the TRIM.

The particle-hole symmetry implies that the bands come in pairs satisfying  $\epsilon_i(\mathbf{k}_\perp) = -\epsilon_{i'}(-\mathbf{k}_\perp)$ , in other words,  $f_i(\theta + \pi) = -f_{\Delta N_e + 1 - i}(\theta)$ . This relates the dispersions  $f_i$  in

pairs, except for the case when  $\Delta N_e$  is odd, where the mode in the middle  $f_{\frac{1}{2}(\Delta N_e+1)}$  is related to itself. This mode changes sign from 0 to  $\pi$  due to symmetry, so it crosses 0 an odd number  $2k+1$  of times between 0 to  $\pi$ , and another  $2k+1$  times between  $\pi$  to  $2\pi$ , corresponding to  $2k+1$  arcs through the TRIM. All other pairs of modes  $f_i$  and  $f_{\Delta N_e+1-i}$  give an even number of arcs. Thus, the parity of the number of Fermi arcs is equal to the parity of  $\Delta N_e$ .

Next we prove that  $(\mathcal{IM})^2$  only depends on the topological phase of an insulator characterized by  $\delta$  and the difference between the numbers of particles on two halves in a Schmidt state  $2k$ . To do so, we start with the inversion transformation of the ground-state wave function of a finite system with parity  $(-1)^P$ . The products in the Schmidt decomposition Eqn. 6.1 have to be anti-symmetrized due to fermion statistics:

$$\Phi_\alpha(\mathbf{r}_i) = |\alpha R\rangle|\alpha L\rangle \equiv A.S.\{\Phi_{\alpha R}(\mathbf{r}_1, \mathbf{r}_2, \dots, \mathbf{r}_{\frac{N}{2}+k})\Phi_{\alpha L}(\mathbf{r}_{\frac{N}{2}+k+1}, \dots, \mathbf{r}_N)\} \quad (\text{B.15})$$

where “A.S.” means to anti-symmetrize in all the variables. The inversion of this wave function is:

$$\Phi_\alpha(-\mathbf{r}_i) = A.S.\{\Phi_{\alpha R}(-\mathbf{r}_1, \dots, -\mathbf{r}_{\frac{N}{2}+k})\Phi_{\alpha L}(-\mathbf{r}_{\frac{N}{2}+k+1}, \dots, -\mathbf{r}_N)\} \quad (\text{B.16})$$

The inversion of the factor corresponding to the right side of the system  $\mathcal{I}\Phi_{\alpha R}(\mathbf{r}_i) = \Phi_{\alpha R}(-\mathbf{r}_i)$  is a wave function on the left side. So we can compare Eqn. B.16 to:

$$|\mathcal{I}\Phi_{\alpha L}\rangle|\mathcal{I}\Phi_{\alpha R}\rangle = A.S.\{\Phi_{\alpha L}(-\mathbf{r}_1, \dots, -\mathbf{r}_{\frac{N}{2}-k})\Phi_{\alpha R}(-\mathbf{r}_{\frac{N}{2}-k+1}, \dots, -\mathbf{r}_N)\} \quad (\text{B.17})$$

which differs from Eqn. B.16 only in the coordinates labels. The parity of the permutation is  $(-1)^{(\frac{N}{2}-k)(\frac{N}{2}+k)} = (-1)^{\frac{N}{2}-k}$ :

$$\mathcal{I}|\Phi_{\alpha R}\rangle|\Phi_{\alpha L}\rangle = (-1)^{\frac{N}{2}-k}|\mathcal{I}\Phi_{\alpha L}\rangle|\mathcal{I}\Phi_{\alpha R}\rangle \quad (\text{B.18})$$

The parity of the ground state of a noninteracting insulator  $(-1)^P$  is equivalent to the parity of the maximum weight terms in the Schmidt decomposition. Assume there are  $\delta$  pairs of zero “energy” states  $\frac{1}{\sqrt{2}}(r_i^\dagger + l_i^\dagger)$ , each pair has the same parity  $\pi_i = \pm 1$ ,  $r_i \leftrightarrow \pi_i l_i$ . Then all the maximum weight states of the Schmidt decomposition are contained in  $\prod_{i=1}^{\delta} (r_{2i-1}^\dagger + \pi_i l_{2i-1}^\dagger)(r_{2i}^\dagger + \pi_i l_{2i}^\dagger)|S_R\rangle|S_L\rangle$ . By Eqn. B.18, the parity of  $|S_R\rangle|S_L\rangle$  is  $(-1)^{\frac{N}{2}-\delta}$  and zero “energy” states map to themselves, so the parity of the maximum weight terms as well as the ground-state wave function is also  $(-1)^{\frac{N}{2}-\delta}$ .

Consider a generic term  $|\Phi_\alpha\rangle = |\Phi_{\alpha R}\rangle|\Phi_{\alpha L}\rangle$  of the Schmidt decomposition: apply inversion to the Schmidt decomposition maps one term to another except for a factor of  $(-1)^P$ , so  $(-1)^{P+\frac{N}{2}-k}|\mathcal{I}\Phi_{\alpha L}\rangle|\mathcal{I}\Phi_{\alpha R}\rangle$  is also a term in the Schmidt decomposition. Since  $\mathcal{M}$  is defined to map each left-hand Schmidt state to its partner in the Schmidt decomposition, i.e. it maps  $|\Phi_{\alpha L}\rangle$  to  $|\Phi_{\alpha R}\rangle$  and  $\mathcal{I}|\Phi_{\alpha R}\rangle$  to  $(-)^{P+\frac{N}{2}-k}\mathcal{I}|\Phi_{\alpha L}\rangle = (-1)^{\delta+k}\mathcal{I}|\Phi_{\alpha L}\rangle$ ,  $(\mathcal{M}\mathcal{I})^2$  gives  $(-1)^{\delta+k}$ .

# Appendix C

## Algorithms and Benchmarks for Variational Monte Carlo Method

### C.1 Benchmarks

We benchmarked our algorithm for three problems: Free spinless fermions hopping on a one-dimensional chain of  $L = 200$  sites at half filling with  $L_A$  up to 100 sites, (see Figure C.1) and free spinless fermions on an  $18 \times 18$  square lattice at half filling with the linear size  $L_A$  up to 7 sites (see Figure C.2). We find very good agreement with the exact results that we calculated using the correlation matrix technique[133].

We also considered Dirac-like electronic dispersion, by studying a nearest neighbor hopping model on the honeycomb (graphene) lattice. We calculate entanglement entropy by our Monte Carlo technique and the exact correlation matrix technique[133]. A 64 site lattice was considered (32 unit cells), and the region A was a rectangle of size  $L_A \times L_A/2$  unit cells. For  $L_A = 2$ , we obtained  $S_2 = 1.4487 \pm 0.00023$  from Monte Carlo, very close to the exact value of  $S_2 = 1.4486$ . For  $L_A = 4$  Monte Carlo obtained  $S_2 = 3.2369 \pm 0.0016$ , while the exact result is  $S_2 = 3.2375$ . The area law can be readily verified for this free Dirac fermion theory by going to large sizes.

### C.2 Marshall Sign Rule for Gutzwiller Projected Wave Functions

For a bipartite lattice with  $t_{rr'}$  non-zero and real only for the opposite sublattices, one can prove that the wave function satisfies the Marshall sign rule. To see this, one can perform the particle-hole transformation:  $f_{r\uparrow} = \tilde{f}_{r\uparrow}$  but  $f_{r\downarrow} = \epsilon_r \tilde{f}_{r\downarrow}^\dagger$  where  $\epsilon_r = +/ -$  for  $A/B$  sublattice. For bipartite hoppings this leaves  $H_{MF}$  unchanged. Thus the wave function in this new basis is given by filling the Fermi sea:  $|\psi\rangle = \prod_{(k,\epsilon_k < 0)} \tilde{f}_{\uparrow k}^\dagger \tilde{f}_{\downarrow k}^\dagger |\Omega\rangle$  where  $|\Omega\rangle$  is the vacuum for the  $\tilde{f}_\sigma$  particles.

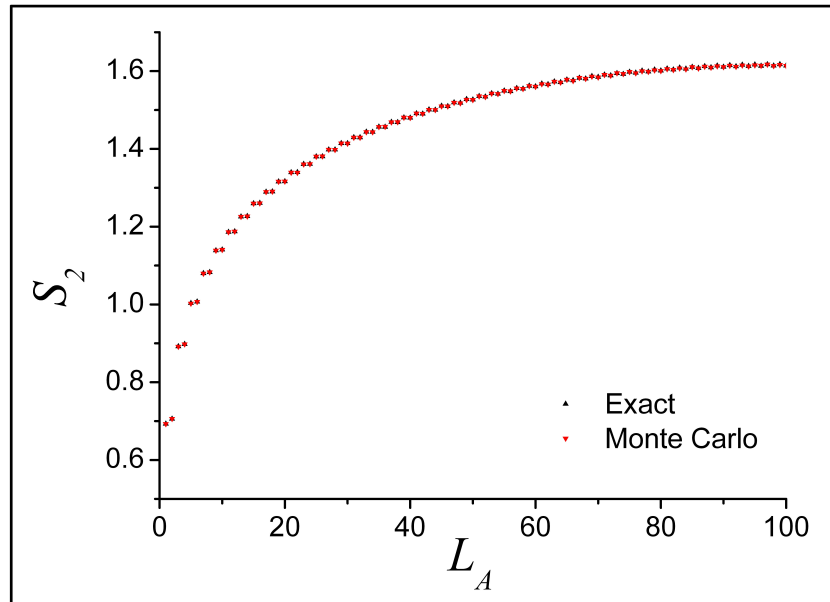


Figure C.1. Comparison of the exact result for Renyi entropy with that calculated using the Monte Carlo method described in the paper for free spinless fermions on a one-dimensional lattice consisting of 200 sites.

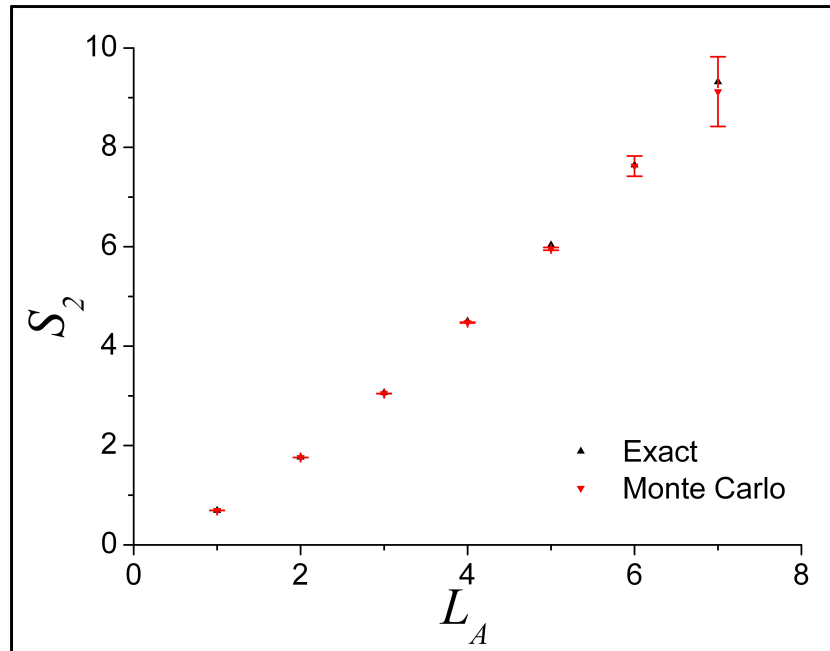


Figure C.2. Comparison of the exact result for Renyi entropy with that calculated using the Monte Carlo method described in the paper for free spinless fermions on a two-dimensional square lattice of size  $18 \times 18$ .

After projection, a spin wave function is conveniently expressed in terms of an amplitude for spin configurations with up spins at specified locations:  $\psi(r_1, r_2, \dots, r_{N/2}) = \langle r_1 r_2 \dots r_{N/2} | \psi \rangle$ . The spin raising operator:  $S_r^+ = f_{\uparrow r}^\dagger f_{\downarrow r} = \epsilon_r \tilde{f}_{\uparrow r}^\dagger \tilde{f}_{\downarrow r}^\dagger$  lets us write the basis states:  $|r_1 r_2 \dots r_{N/2}\rangle = \left[ \prod_{i=1}^{N/2} \epsilon_{r_i} \right] \tilde{f}_{\uparrow r_i}^\dagger \tilde{f}_{\downarrow r_i}^\dagger |\Omega\rangle$ , i.e. one creates a pair of  $\tilde{f}$  fermions at the up spin locations. Thus the wave function is:

$$\psi(r_1, r_2, \dots, r_{N/2}) = \prod_{i=1}^{N/2} \epsilon_{r_i} [Det(\mathcal{M})]^2 \quad (\text{C.1})$$

where  $\mathcal{M}_{ij} = e^{ik_i \cdot r_j}$  and  $k_i$  are momenta inside the Fermi sea with  $\epsilon_k < 0$ . With real hoppings, the determinant is real, hence the wave function satisfies Marshall sign rule.

### C.3 Sign Trick for Entanglement Entropy Calculation

The Renyi entropy of a wave function  $\phi(a, b)$  (where  $a$  ( $b$ ) is the configuration of subsystem A (B)) is:

$$e^{-S_2} = \langle Swap_A \rangle = \frac{1}{N^2} \sum_{aa'bb'} \phi^*(a, b) \phi(a', b) \phi^*(a', b') \phi(a, b') \quad (\text{C.2})$$

Defining configurations  $\alpha_1 = a, b$ ,  $\alpha_2 = a', b'$  and  $\beta_1 = a', b$ ,  $\beta_2 = a, b'$ , this can be rewritten as:

$$\begin{aligned} \langle Swap_A \rangle &= \left[ \sum_{\alpha_1 \alpha_2} \rho_{\alpha_1} \rho_{\alpha_2} |f(\alpha_1, \alpha_2)| \right] \left[ \sum_{\alpha_1 \alpha_2} \tilde{\rho}_{\alpha_1, \alpha_2} e^{i\phi(\alpha_1, \alpha_2)} \right] \\ &= \langle Swap_{A,mod} \rangle \langle Swap_{A,sign} \rangle \end{aligned} \quad (\text{C.3})$$

Here  $f(\alpha_1, \alpha_2) = \frac{\phi_{\beta_1} \phi_{\beta_2}}{\phi_{\alpha_1} \phi_{\alpha_2}}$  and  $\rho_{\alpha_i} = |\phi_{\alpha_i}|^2 / \sum_{\alpha_i} |\phi_{\alpha_i}|^2$ . The first factor,  $\langle Swap_{A,mod} \rangle$ , is related to the Renyi entropy of the modulus wave function  $|\phi(a, b)|$  and poses no sign problem.

The second term,  $\langle Swap_{A,sign} \rangle$ , calculates the expectation value of the phase factor  $e^{i\phi(\alpha_1, \alpha_2)}$  where  $\phi(\alpha_1, \alpha_2) = \arg[\phi_{\alpha_1}^* \phi_{\alpha_2}^* \phi_{\beta_1} \phi_{\beta_2}]$  with the probability distribution:

$$\tilde{\rho}_{\alpha_1, \alpha_2} = \frac{|\phi_{\alpha_1} \phi_{\alpha_2} \phi_{\beta_1} \phi_{\beta_2}|}{\sum_{\alpha_1 \alpha_2} |\phi_{\alpha_1} \phi_{\alpha_2} \phi_{\beta_1} \phi_{\beta_2}|} \quad (\text{C.4})$$

We note that the calculation of  $\langle Swap_{A,sign} \rangle$ , which is the time consuming step, enjoys two simplifications compared to the original expression for  $\langle Swap_A \rangle$ . First, the swapped configurations that do not belong to the Hilbert space (for example, that do not maintain  $S_z = 0$  constraint) are automatically rejected since the probability distribution function is proportional to the amplitudes for the swapped configurations  $|\phi_{\beta_1} \phi_{\beta_2}|$ . A second advantage is specific to the case of Gutzwiller projected wave functions. Even though the swapped configurations would generally differ significantly from the original configurations, the ratio

$\frac{\tilde{\rho}(\alpha'_1, \alpha_2)}{\tilde{\rho}(\alpha_1, \alpha_2)}$  of probability distribution functions for two neighboring Monte Carlo steps (assuming  $\alpha_1 \rightarrow \alpha'_1$  and  $\beta_1 \rightarrow \beta'_1$  for the sake of argument) can be calculated using just the ratio of determinants (as in the conventional variational Monte Carlo method), since  $\tilde{\rho}(\alpha_1, \alpha_2)$  is proportional to the amplitude of the original as well as the swapped configuration.

Furthermore, we will see in our problem of interest that calculating these two parts separately we obtain  $\langle Swap_A \rangle = \langle Swap_{A,mod} \rangle \langle Swap_{A,sign} \rangle$  with much smaller error bars. This is because both terms turn out to be of similar magnitude. Hence  $\langle Swap_{A,sign} \rangle$  is not as small a quantity as  $\langle Swap_A \rangle$  itself and can be calculated more accurately.

## C.4 Method for Linear Combinations of Wave Functions

To calculate TEE for wave functions of different linear combinations, it is important to establish a VMC algorithm for wave function as  $|\Phi\rangle = \cos\phi|\Phi_1\rangle + \sin\phi|\Phi_2\rangle$ , where we assume  $|\Phi_1\rangle$  and  $|\Phi_2\rangle$  are properly normalized. In our case,  $|\Phi_1\rangle$  and  $|\Phi_2\rangle$  are two degenerate ground states,  $\langle\alpha|\Phi_1\rangle$  and  $\langle\alpha|\Phi_2\rangle$  are single Slater determinants products for each configuration  $|\alpha\rangle$ , making  $\langle\alpha|\Phi\rangle$  a sum of two Slater determinants products. However, it may also be generalized to the situation of any wave functions.

In the VMC scenario, the central quantity to evaluate in each Monte Carlo step is the ratio of  $\langle\alpha'|\Phi\rangle / \langle\alpha|\Phi\rangle$ , which now has the form:

$$\frac{\langle\alpha'|\Phi\rangle}{\langle\alpha|\Phi\rangle} = \frac{\cos\phi\langle\alpha'|\Phi_1\rangle + \sin\phi\langle\alpha'|\Phi_2\rangle}{\cos\phi\langle\alpha|\Phi_1\rangle + \sin\phi\langle\alpha|\Phi_2\rangle} \quad (\text{C.5})$$

It is usually much less costly to calculate ratio of  $\langle\alpha'|\Phi_1\rangle / \langle\alpha|\Phi_1\rangle$  and  $\langle\alpha'|\Phi_2\rangle / \langle\alpha|\Phi_2\rangle$  if  $|\alpha\rangle$  and  $|\alpha'\rangle$  are locally different. For our case, when  $|\alpha\rangle$  and  $|\alpha'\rangle$  differ only by one spin (or electron) exchange, a much less costly and more accurate algorithm may be implemented for the ratio of determinants with only one different row or column. Unfortunately, after linear superposing different  $|\Phi_i\rangle$ , Eqn. C.5 no longer has such a privilege.

However, one can re-express Eqn. C.5 as:

$$\frac{\langle\alpha'|\Phi\rangle}{\langle\alpha|\Phi\rangle} = \frac{a + bc \cdot \tan\phi}{1 + c \cdot \tan\phi} \quad (\text{C.6})$$

where:

$$\begin{aligned} a &= \langle\alpha'|\Phi_1\rangle / \langle\alpha|\Phi_1\rangle \\ b &= \langle\alpha'|\Phi_2\rangle / \langle\alpha|\Phi_2\rangle \end{aligned} \quad (\text{C.7})$$

are again ratio of determinants and can be effectively evaluated, and:

$$c = \langle\alpha|\Phi_2\rangle / \langle\alpha|\Phi_1\rangle \quad (\text{C.8})$$

can be efficiently kept track of with  $c' = a^{-1}bc$  whenever the update  $|\alpha\rangle \rightarrow |\alpha'\rangle$  is accepted in a Monte Carlo step. In practice, numerical check should be included to make sure error for  $c$  does not accumulate too much after a certain number of Monte Carlo steps.

This algorithm may be easily generalized to the linear combination of  $n$  wave functions, with the computational cost only  $n$  times that for a single wave functions.

# Appendix D

## Minimum Entropy States and Modular Matrices of $Z_2$ Gauge Theory

### D.1 Minimum Entropy States of the Toric Code Model on Dividing Torus

In this appendix we Schmidt-decompose the individual Toric code ground states  $|\Psi\rangle$  in Eqn. 9.26 for the bipartition of a torus in Figure 9.1b. It is helpful to introduce a virtual cut  $\Delta$  which wraps around the torus in the  $\hat{x}$  direction, and define  $|\Psi_{\{q_l\},b}^{A(B)}\rangle$  as the normalized equal superposition of all the possible configurations of closed-loop strings  $C$  in the subsystem  $A$  ( $B$ ) with the partition boundary condition specified by  $\{q_l = 0, 1\}$ ,  $l = 1, 2, \dots, L$  (so  $L$  is the total length of the boundary), and the number of crossings of the virtual cut  $\Delta$  modulo 2 equals  $b = 0, 1$ . The four ground states may now be expanded as:

$$|\xi_{ab}\rangle = \frac{1}{\sqrt{2N_q}} \sum_{\{q_l\} \in a} (|\Psi_{\{q_l\},0}^A\rangle |\Psi_{\{q_l\},b}^B\rangle |\Psi_{\{q_l\},1}^A\rangle |\Psi_{\{q_l\},(b+1) \text{ mod } 2}^B\rangle) \quad (\text{D.1})$$

Here  $\{q_l\} \in a = 0$  (1) denotes that the only even (odd) number of crossings are allowed at the boundary  $\Gamma_1$  (the number of crossings at the other boundary  $\Gamma_2$  must be same modulo 2).  $N_q = 2^{L-2}$  equals the total number of valid boundary conditions  $\{q_l\} \in a$  in each parity sector.

We calculate entanglement entropy using the reduced density matrix. Here,  $\rho^A =$

$\text{tr}_B|\Psi\rangle\langle\Psi|$  is readily calculated:

$$\begin{aligned}
\rho^A &= \frac{1}{2N_q} \sum_{\{q_l\} \in \text{even}} \left[ (|c_{00}|^2 + |c_{01}|^2) (|\Psi_{\{q_l\},0}^A\rangle\langle\Psi_{\{q_l\},0}^A| + |\Psi_{\{q_l\},1}^A\rangle\langle\Psi_{\{q_l\},1}^A|) \right. \\
&\quad \left. + 2 \text{Real}(c_{00}^* c_{01}) (|\Psi_{\{q_l\},0}^A\rangle\langle\Psi_{\{q_l\},1}^A| + |\Psi_{\{q_l\},1}^A\rangle\langle\Psi_{\{q_l\},0}^A|) \right] \\
&\quad + \frac{1}{2N_q} \sum_{\{q_l\} \in \text{odd}} \left[ (|c_{10}|^2 + |c_{11}|^2) (|\Psi_{\{q_l\},0}^A\rangle\langle\Psi_{\{q_l\},0}^A| + |\Psi_{\{q_l\},1}^A\rangle\langle\Psi_{\{q_l\},1}^A|) \right. \\
&\quad \left. + 2 \text{Real}(c_{10}^* c_{11}) (|\Psi_{\{q_l\},0}^A\rangle\langle\Psi_{\{q_l\},1}^A| + |\Psi_{\{q_l\},1}^A\rangle\langle\Psi_{\{q_l\},0}^A|) \right] \\
&= \frac{1}{2N_q} \sum_{\{q_l\} \in \text{even}} \left[ |c_{00} + c_{01}|^2 |\Psi_{\{q_l\},+}^A\rangle\langle\Psi_{\{q_l\},+}^A| + |c_{00} - c_{01}|^2 |\Psi_{\{q_l\},-}^A\rangle\langle\Psi_{\{q_l\},-}^A| \right] \\
&\quad + \frac{1}{2N_q} \sum_{\{q_l\} \in \text{odd}} \left[ |c_{10} + c_{11}|^2 |\Psi_{\{q_l\},+}^A\rangle\langle\Psi_{\{q_l\},+}^A| + |c_{10} - c_{11}|^2 |\Psi_{\{q_l\},-}^A\rangle\langle\Psi_{\{q_l\},-}^A| \right] \quad (\text{D.2})
\end{aligned}$$

Here  $|\Psi_{\{q_l\},\pm}^A\rangle = \frac{1}{\sqrt{2}} \left( |\Psi_{\{q_l\},0}^A\rangle \pm |\Psi_{\{q_l\},1}^A\rangle \right)$  and hold the orthogonal condition.

From the above expression, it immediately follows that the Renyi entanglement entropy  $S_n$  is given by Eqn. 9.28:

$$\begin{aligned}
S_n &= \frac{1}{1-n} \log (Tr \rho_A^n) \\
&= \frac{1}{1-n} \log \left( \left( \frac{1}{2N_q} \right)^n \cdot N_q \left( \sum_{j=1}^4 (2p_j)^n \right) \right) \\
&= \log N_q + \frac{1}{1-n} \log \sum_{j=1}^4 p_j^n \\
&= L \log 2 - \left( 2 \log 2 + \frac{1}{n-1} \log \sum_{j=1}^4 p_j^n \right) \quad (\text{D.3})
\end{aligned}$$

where  $p_j$  are defined in Eqn. 9.29.

To understand the nature of the corresponding MES above and in Eqn. 9.30, we first discuss the quasiparticle excitations of the Toric code model. Imagine acting a string operator defined on the links of the lattice:

$$W^z(O) = \prod_{j \in O} \sigma_j^z \quad (\text{D.4})$$

Now  $W^z(O)|\text{vac}_x\rangle$  is an excited states and still an eigenstate of  $A_s$  and  $B_p$ , with  $A_s = -1$  at the two ends of  $O$ . We may regard them as electric charge quasiparticles that cost a finite energy to create and the string connecting them as an electric field line. To return to the ground state, the electric charges need to be annihilated with each other. One way to do this is to wrap the open string  $O$  parallel to  $\hat{x}$  around the cycle of the torus.  $O$  becomes a closed loop  $C$ , yet this changes the parity of electric field winding number along  $\hat{x}$ . We define the

electric charge loop operator that insert an additional electric field in the  $\hat{x}(\hat{y})$  direction by the above procedure as a  $Z_2$  electric flux insertion operator  $T_x(T_y)$ :

$$\begin{aligned} T_x|\xi_{1b}\rangle &= |\xi_{0b}\rangle \\ T_x|\xi_{0b}\rangle &= |\xi_{1b}\rangle \\ T_y|\xi_{a1}\rangle &= |\xi_{a0}\rangle \\ T_y|\xi_{a0}\rangle &= |\xi_{a1}\rangle \end{aligned} \quad (\text{D.5})$$

There is also a magnetic field, which determines the phase of the electric charge as it moves. In particular, when there is a magnetic field along the  $\hat{y}$  direction of the torus of 1(0) total flux modulo 2, the electric charge picks up a  $-(+)$  sign traveling around the loop around the  $\hat{x}$  direction, and similarly for the magnetic field along the  $\hat{x}$  direction. Denoting the insertion operator of such  $Z_2$  magnetic flux as  $F_y$  and  $F_x$ , the loop operators of the magnetic charge (vison), we have:

$$\begin{aligned} T_x F_y &= -F_y T_x \\ T_y F_x &= -F_x T_y \end{aligned} \quad (\text{D.6})$$

They suggest that  $T_x(T_y)$  is the magnetic flux measuring operator in the  $\hat{y}(\hat{x})$  direction and  $F_x(F_y)$  is the electric flux measuring operator in the  $\hat{y}(\hat{x})$  direction. Note that both electric and magnetic flux are defined modulo 2 in correspondence with the  $Z_2$  gauge theory. After simple algebra:

$$\begin{aligned} F_y|\xi_{ab}\rangle &= (-1)^a|\xi_{ab}\rangle \\ F_x|\xi_{ab}\rangle &= (-1)^b|\xi_{ab}\rangle \end{aligned} \quad (\text{D.7})$$

Compare Eqn. D.5 and D.7 with Eqn. 9.30, we arrive at the conclusions listed in Table 9.1.

## D.2 Modular Transformations

The  $\mathcal{S}$  and  $\mathcal{U}$  matrices describe the action of modular transformations on the degenerate ground states of the topological quantum field theory on a torus. For Abelian phases, the  $ij$ 'th entry of the  $\mathcal{S}$  matrix corresponds to the phase the  $i$ 'th quasiparticle acquires when it encircles the  $j$ 'th quasiparticle. The  $\mathcal{U}$  matrix is diagonal and the  $ii$ 'th entry corresponds to the phase the  $i$ 'th quasiparticle acquires when it is exchanged with an identical one. Let us first review the geometric meaning of these transformations. Labeling our system by complex coordinates  $z = x + iy$ , the torus may be defined by the periodicity of  $\omega_1$  and  $\omega_2$  along the two directions  $\hat{e}_1$  and  $\hat{e}_2$  (need not to be orthogonal) i.e.  $z \equiv z + \omega_1 \equiv z + \omega_2$ . Now consider a transformation:

$$\begin{pmatrix} \omega_1 \\ \omega_2 \end{pmatrix} \rightarrow \begin{pmatrix} \omega'_1 \\ \omega'_2 \end{pmatrix} = \begin{pmatrix} a & b \\ c & d \end{pmatrix} \begin{pmatrix} \omega_1 \\ \omega_2 \end{pmatrix} \quad (\text{D.8})$$

where  $a, b, c, d \in \mathbb{Z}$ . Since our system lives on a lattice, the inverse of the above matrix should again have integer components, hence the determinant  $ad - bc = 1$ . One can show that matrices with these properties form a group, called  $SL(2, \mathbb{Z})$ . Interestingly, all the elements in this group can be obtained by a successive application of the following two generators of  $SL(2, \mathbb{Z})$ :

- $S = \begin{pmatrix} 0 & 1 \\ -1 & 0 \end{pmatrix}$ . This transformation corresponds to  $\omega_1 \rightarrow \omega_2$  and  $\omega_2 \rightarrow -\omega_1$  and therefore, for a square geometry corresponds to rotation of the system by  $90^\circ$ .
- $U = \begin{pmatrix} 1 & 1 \\ 0 & 1 \end{pmatrix}$ . Under this transformation  $\omega_1 \rightarrow \omega'_1 = \omega_1 + \omega_2$  and  $\omega_2 \rightarrow \omega'_2 = \omega_2$ . Consider a loop on the torus with winding numbers  $n_1$  and  $n_2$  along  $\omega_1$  and  $\omega_2$  directions. By definition of the  $U$  transformation, the winding numbers in the transformed basis:

$$\begin{aligned} & n_1\omega_1 + n_2\omega_2 \\ &= n_1(\omega'_1 - \omega'_2) + n_2\omega'_2 \\ &= n'_1\omega'_1 + n'_2\omega'_2 \end{aligned} \tag{D.9}$$

where  $n'_1 = n_1$  and  $n'_2 = n_2 - n_1$  are the winding numbers along the  $\omega'_1$  and  $\omega'_2$  directions.

The transformation properties of the resulting MESs under modular transformations would yield the desired  $\mathcal{S}$  and  $\mathcal{U}$  matrices. Further, for a symmetry transformation of  $F(S, U)$  on  $(\omega_1, \omega_2)^T$ , the corresponding modular transformation on MESs would yield the modular  $\mathcal{F}(\mathcal{S}, \mathcal{U})$  matrix.

In the main text, we have obtained  $\mathcal{S}$  and  $\mathcal{U}$  matrices for the toric code model from the action of these transformations on the basis states  $|\xi_{ab}\rangle$ . We now show that one can also obtain the  $\mathcal{U}\mathcal{S}$  matrix by studying the action of  $2\pi/3$  rotation  $R_{2\pi/3}$  on the MESs (provided that  $R_{2\pi/3}$  is symmetry of the model). To see this, consider a triangular lattice that is defined by two lattice vectors (complex numbers)  $\omega_1, \omega_2$  with  $\omega_1 = (1, 0)$  and  $\omega_2 = (1/2, \sqrt{3}/2)$ . The transformation of our interest is the transformation of  $\omega_1, \omega_2$  under  $R_{2\pi/3}$  rotation:  $\omega_1 \rightarrow \omega'_1 = -\omega_1 + \omega_2$  and  $\omega_2 \rightarrow \omega'_2 = -\omega_1$ . Therefore, one can write the  $R_{2\pi/3}$ -matrix:

$$R_{2\pi/3} = \begin{pmatrix} -1 & 1 \\ -1 & 0 \end{pmatrix} \tag{D.10}$$

This matrix belongs to the group  $SL(2, \mathbb{Z})$  and simple algebra shows that  $R_{2\pi/3} = \mathcal{U}\mathcal{S}$ . One may also check that  $R_{2\pi/3}^3 = 1$  as one might expect. Therefore, knowing the action of  $R_{2\pi/3}$  on the MESs would lead to the  $\mathcal{U}\mathcal{S}$  matrix.

### D.3 Modular Matrices of $Z_2$ Gauge Theory from Minimum Entropy States

Let's study the action of modular transformation on the MESs  $|\Xi_\alpha\rangle$  for the  $Z_2$  gauge theory in Section 9.2.3 and compare the resulting modular matrices with the known results.

First consider a  $\pi/2$  rotation symmetric square sample. Under  $\pi/2$  rotation,  $|\xi_{ab}\rangle \rightarrow |\xi_{ba}\rangle$ . According to Eqn. 9.30, the transformation for the MESs  $|\Xi_\alpha\rangle$  for cuts along  $\hat{y}$ :

$$\begin{aligned} |\Xi_1\rangle &\rightarrow \frac{1}{2} (|\Xi_1\rangle + |\Xi_2\rangle + |\Xi_3\rangle + |\Xi_4\rangle) \\ |\Xi_2\rangle &\rightarrow \frac{1}{2} (|\Xi_1\rangle + |\Xi_2\rangle - |\Xi_3\rangle - |\Xi_4\rangle) \\ |\Xi_3\rangle &\rightarrow \frac{1}{2} (|\Xi_1\rangle - |\Xi_2\rangle + |\Xi_3\rangle - |\Xi_4\rangle) \\ |\Xi_4\rangle &\rightarrow \frac{1}{2} (|\Xi_1\rangle - |\Xi_2\rangle - |\Xi_3\rangle + |\Xi_4\rangle) \end{aligned} \quad (\text{D.11})$$

Hence, the modular  $\mathcal{S}$  matrix is given by:

$$\mathcal{S} = \frac{1}{2} \begin{pmatrix} 1 & 1 & 1 & 1 \\ 1 & 1 & -1 & -1 \\ 1 & -1 & 1 & -1 \\ 1 & -1 & -1 & 1 \end{pmatrix} \quad (\text{D.12})$$

This is exactly what one expects from the topological quantum field theory corresponding to the zero correlation length deconfined-confined  $Z_2$  gauge theory. There are four flavors of quasiparticles in the spectrum:  $1, m, e, em$ , as we have shown in Table 9.1. The electric charge  $e$  and magnetic charge (vison)  $m$  both have self-statistics of a boson and pick up a phase of  $\pi$  when they encircle each other (and as a corollary, the same phase when they encircle  $em$ ). By studying  $\mathcal{S}$ , one gets the self and mutual statistics for quasiparticles encircling each other.

In Section 9.3.2 we further show that symmetry is not required to determine the  $\mathcal{S}$  matrix. In Eqn. 9.30 we have shown the MESs for cuts along  $w_2 = \hat{y}$  direction:

$$\begin{aligned} |\Xi_1\rangle &= \frac{e^{i\varphi_1}}{\sqrt{2}} (|\xi_{00}\rangle + |\xi_{01}\rangle) \\ |\Xi_2\rangle &= \frac{e^{i\varphi_2}}{\sqrt{2}} (|\xi_{00}\rangle - |\xi_{01}\rangle) \\ |\Xi_3\rangle &= \frac{e^{i\varphi_3}}{\sqrt{2}} (|\xi_{10}\rangle + |\xi_{11}\rangle) \\ |\Xi_4\rangle &= \frac{e^{i\varphi_4}}{\sqrt{2}} (|\xi_{10}\rangle - |\xi_{11}\rangle) \end{aligned} \quad (\text{D.13})$$

where  $\varphi_i$  are undetermined phases for MESs  $|\Xi_i\rangle$ . The unitary matrix  $U_1$  connecting the  $w_2$

MESs and the electric flux states:

$$U_1 = \frac{1}{\sqrt{2}} \begin{pmatrix} e^{i\varphi_1} & e^{i\varphi_2} \\ e^{i\varphi_1} & -e^{i\varphi_2} \\ & e^{i\varphi_3} & e^{i\varphi_4} \\ & e^{i\varphi_3} & -e^{i\varphi_4} \end{pmatrix} \quad (\text{D.14})$$

On the other hand, it is straightforward to verify that for loops along  $w'_2 = -\hat{x} + \hat{y}$  direction, which satisfies our requirement Eqn. 9.37, the corresponding MESs:

$$\begin{aligned} |\Xi'_1\rangle &= \frac{e^{i\varphi'_1}}{\sqrt{2}}(|\xi_{00}\rangle + |\xi_{11}\rangle) \\ |\Xi'_2\rangle &= \frac{e^{i\varphi'_2}}{\sqrt{2}}(|\xi_{00}\rangle - |\xi_{11}\rangle) \\ |\Xi'_3\rangle &= \frac{e^{i\varphi'_3}}{\sqrt{2}}(|\xi_{01}\rangle + |\xi_{10}\rangle) \\ |\Xi'_4\rangle &= \frac{e^{i\varphi'_4}}{\sqrt{2}}(|\xi_{01}\rangle - |\xi_{10}\rangle) \end{aligned} \quad (\text{D.15})$$

again  $\varphi'_i$  are undetermined phases for MESs  $|\Xi'_i\rangle$ . The unitary matrix  $U_2$  connecting the  $w'_2$  MESs and the electric flux states:

$$U_2 = \frac{1}{\sqrt{2}} \begin{pmatrix} e^{i\varphi'_1} & e^{i\varphi'_2} & e^{i\varphi'_3} & e^{i\varphi'_4} \\ & e^{i\varphi'_3} & e^{i\varphi'_4} & -e^{i\varphi'_4} \\ e^{i\varphi'_1} & -e^{i\varphi'_2} & e^{i\varphi'_3} & -e^{i\varphi'_4} \end{pmatrix} \quad (\text{D.16})$$

Combining Eqn. D.14 and D.16, we can write down the modular  $\mathcal{S}$  matrix as:

$$\begin{aligned} \mathcal{S} &= U_2^{-1} U_1 \\ &= \frac{1}{2} \begin{pmatrix} e^{i(\varphi_1-\varphi'_1)} & e^{i(\varphi_2-\varphi'_1)} & e^{i(\varphi_3-\varphi'_1)} & -e^{i(\varphi_4-\varphi'_1)} \\ e^{i(\varphi_1-\varphi'_2)} & e^{i(\varphi_2-\varphi'_2)} & -e^{i(\varphi_3-\varphi'_2)} & e^{i(\varphi_4-\varphi'_2)} \\ e^{i(\varphi_1-\varphi'_3)} & -e^{i(\varphi_2-\varphi'_3)} & e^{i(\varphi_3-\varphi'_3)} & e^{i(\varphi_4-\varphi'_3)} \\ e^{i(\varphi_1-\varphi'_4)} & -e^{i(\varphi_2-\varphi'_4)} & -e^{i(\varphi_3-\varphi'_4)} & -e^{i(\varphi_4-\varphi'_4)} \end{pmatrix} \end{aligned} \quad (\text{D.17})$$

To ensure the existence of an identity particle in accord with the first row and column, we impose the conditions:

$$\varphi'_1 = \varphi'_2 = \varphi'_3 = \varphi'_4 = \varphi_1 = \varphi_2 = \varphi_3 = \varphi_4 + \pi \quad (\text{D.18})$$

This leads to the following modular  $\mathcal{S}$  matrix:

$$\mathcal{S} = \frac{1}{2} \begin{pmatrix} 1 & 1 & 1 & 1 \\ 1 & 1 & -1 & -1 \\ 1 & -1 & 1 & -1 \\ 1 & -1 & -1 & 1 \end{pmatrix} \quad (\text{D.19})$$

which is indeed the correct result for  $Z_2$  toric code.

Now consider the transformation corresponding to  $\mathcal{U}$  matrix as described in Appendix D.2, where  $n'_1 = n_1$  and  $n'_2 = n_2 - n_1$  are the winding numbers along the  $\omega'_1$  and  $\omega'_2$  directions. Using this expression and Eqn. 9.30, the transformation for MESs from  $w_2$  cut to  $w'_2$  cut:

$$\begin{aligned} |\Xi_1\rangle &\rightarrow |\Xi_1\rangle \\ |\Xi_2\rangle &\rightarrow |\Xi_2\rangle \\ |\Xi_3\rangle &\rightarrow |\Xi_3\rangle \\ |\Xi_4\rangle &\rightarrow -|\Xi_4\rangle \end{aligned} \quad (\text{D.20})$$

This leads to the following modular  $\mathcal{U}$  matrix:

$$\mathcal{U} = \begin{pmatrix} 1 & 0 & 0 & 0 \\ 0 & 1 & 0 & 0 \\ 0 & 0 & 1 & 0 \\ 0 & 0 & 0 & -1 \end{pmatrix} \quad (\text{D.21})$$

Again, this is what is expected from the  $Z_2$  gauge theory. The sign of  $-1$  on the last entry of the diagonal corresponds to the fermionic self statistics of the *em* while the positive signs correspond to the bosonic self statistics of  $1, e$  and  $m$  particles.

To see a more generic example to derive the  $\mathcal{U}$  matrix from rotation symmetry, we first define the toric code on a triangular lattice, with system dimensions such that the  $2\pi/3$  rotation is a symmetry of the system. The Hamiltonian is same as Eqn. 9.19 with the star  $s$  denoting six links emanating from a vertex while the plaquette  $p$  now involves three links. We again denote the four degenerate ground states on a torus as  $|\xi_{ab}\rangle$  with  $a, b = 0, 1$  denoting the parity of electric field along the non-contractible cycles. The relation between the MESs  $|\Xi_\alpha\rangle$  and the states  $|\xi_{ab}\rangle$  remains unchanged (Eqn. 9.30). The calculation for the transformation under  $2\pi/3$  proceeds analogously to that for  $\pi/2$  rotation and one finds:

$$\begin{aligned} R_{2\pi/3}|\xi_{00}\rangle &= |\xi_{00}\rangle \\ R_{2\pi/3}|\xi_{01}\rangle &= |\xi_{10}\rangle \\ R_{2\pi/3}|\xi_{10}\rangle &= |\xi_{11}\rangle \\ R_{2\pi/3}|\xi_{11}\rangle &= |\xi_{01}\rangle \end{aligned} \quad (\text{D.22})$$

Translating the action of  $R_{2\pi/3}$  on the states  $|\xi_\alpha\rangle$  to that on states  $|\Xi_\alpha\rangle$ , one finds:

$$\mathcal{U}\mathcal{S} = \frac{1}{2} \begin{pmatrix} 1 & 1 & 1 & 1 \\ 1 & 1 & -1 & -1 \\ 1 & -1 & 1 & -1 \\ -1 & 1 & 1 & -1 \end{pmatrix} \quad (\text{D.23})$$

Combining the expression and the  $\mathcal{S}$  matrix, one obtains as expected:

$$\mathcal{U} = \begin{pmatrix} 1 & 0 & 0 & 0 \\ 0 & 1 & 0 & 0 \\ 0 & 0 & 1 & 0 \\ 0 & 0 & 0 & -1 \end{pmatrix} \quad (\text{D.24})$$